

**CHARACTERISATION OF THE
TORSIONAL BEHAVIOUR OF
TITANIUM METAL MATRIX COMPOSITE SHAFTS**

Yaw Chuan Lee, BEng (Hons.)

**Thesis submitted to the University of Nottingham
for the degree of Doctor of Philosophy**

June 2008

ABSTRACT

Titanium Metal Matrix Composites (TiMMC) have been gaining momentum in the aerospace applications in the past two decades. The advantages of TiMMC include superior stiffness-to-weight and strength-to-weight ratios, compared to conventional aerospace steels. The low pressure shaft in the aeroengine is one of the components that could benefit from the superior material properties of TiMMC. Potentially, the use of TiMMC could provide a combination of higher torque density (higher torque for a given diameter) and lower weight for these shafts. However, little has been done to investigate the torsional behaviour of TiMMC shafts.

This thesis investigates the torsional behaviour of TiMMC shafts with different fibre orientations, through experimental tests. A material database was established for the TiMMC system used for each fibre orientation. Further to that, a comprehensive failure investigation was carried out on the tested specimens in order to understand the failure mechanisms. Samples from the fractured specimens were polished and etched to study their microstructure and internal features.

Numerical models were developed to predict the global orthotropic elastic material properties of TiMMC using the unit cell concept. The material properties were then used in the tube models which predict the shear moduli for different fibre orientations. The results were validated with the experimental test results.

To minimise weight, aeroengine shafts aim to have thin walls, which could result in buckling instability. Numerical models were therefore developed, to investigate the buckling behaviour of TiMMC shafts. Hill's potential function in ABAQUS was used, which define the anisotropic yield behaviour, using user-defined stress ratios.

As a result of this research, the understanding of the torsional behaviour of TiMMC has been strengthened.

ACKNOWLEDGEMENTS

I would like to express my deepest gratitude to my supervisors, Prof. Thomas Hyde and Dr. Edward Williams, for their endless support and guidance throughout the course of my PhD. This work would not have been possible without their help and encouragement at various stages during the research. I am also grateful with the guidance provided by Dr. William Robotham at the early stage in my PhD, who had done preliminary studies on this subject.

Also, this research would not be possible without the financial support from the European Commission, who funded the VITAL program. I would like to offer my sincere thanks to Dr. John Pursell, Dr. Phillip Doorbar, Scott Wood and Simon Nelson from Rolls-Royce plc, who contribute valuable technical advice and discussions during this research. I am also grateful to received advices from David Murgatroyd and Stephen Flitcroft of TISICS Ltd. for the procedure of cutting and polishing techniques of samples.

I would also like to acknowledge the assistance given by Barrie Hanson, John Chapman and Graham Malkinson, who are technical staff within the School of Mechanical, Materials and Manufacturing Engineering. The experimental work would not be smooth without their contributions.

Finally, I would like to thank all my friends and colleagues who accompanied me throughout the course of my studies over the years in UK. My endless gratitude goes to my family and relatives, who show so much love and care throughout my studies. Nothing will be possible without my parents, for bringing me to this world, who ensure my well-being and a fruitful life.

TABLE OF CONTENTS

ABSTRACT	i
ACKNOWLEDGEMENTS	iii
TABLE OF CONTENTS	iv
NOMENCLATURE	x
CHAPTER 1 - INTRODUCTION	
1.1 Background	1-1
1.2 Objectives	1-3
1.3 Methodology	1-3
1.4 Structure of Thesis	1-4
CHAPTER 2 - LITERATURE REVIEW	
2.1 Introduction	2-1
2.2 TiMMC Systems	2-2
2.2.1 Ti-6-4/SCS6	2-3
2.2.2 Ti-15-3/SCS6	2-5
2.2.3 Ti-6-2-4-2/SCS6	2-6
2.2.4 Ti-6-4/SM1140+	2-7
2.2.5 Ti-6-4/SM1240	2-9
2.3 Manufacturing Routes	2-10
2.3.1 Foil-Fibre-Foil Method	2-11
2.3.2 Plasma Spray Method	2-12
2.3.3 Matrix Coated Fibre Method	2-12
2.4 Mechanical Characteristics	2-15
2.4.1 Behaviour under Uniaxial Loading	2-16
2.4.2 Behaviour under Biaxial Loading	2-22

2.5	Reaction Zone and Interface	2-24
2.6	Micromechanical Modelling	2-26
2.7	Summary	2-30

CHAPTER 3 - EXPERIMENTAL RESULTS

3.1	Introduction	3-1
3.2	Design of Specimens	3-2
3.3	Equipment and Testing Method	3-4
3.3.1	Test Rig, Specimens and Adapters	3-4
3.3.2	Loading Method and Load Pattern	3-8
3.3.3	Measurements from Tests	3-10
3.4	Dimensional Check of Specimens	3-12
3.5	Analysis of Test Results	3-14
3.5.1	Torque vs. Twist	3-15
3.5.2	MMC Shear Stress vs. Shear Strain	3-16
3.5.2.1	<i>Shear Strain for MMC</i>	3-16
3.5.2.2	<i>Shear Stress for MMC</i>	3-18
3.5.3	Shear Strength at Knee of MMC	3-21
3.5.4	Effective MMC Shear Modulus	3-22
3.5.5	Ultimate Shear Strength of MMC	3-22
3.6	Correction of Test Results	3-23
3.6.1	Actual Torque Load and Twist	3-23
3.6.2	Strain Gauge Transverse Sensitivity	3-24
3.7	Test Results	3-26
3.7.1	Room Temperature Tests	3-27
3.7.1.1	<i>Monolithic 1 (Machined from Solid Ti-6-4)</i>	3-27
3.7.1.2	<i>Monolithic 2 (HIPped Solid Ti-6-4)</i>	3-29
3.7.1.3	<i>UTC1 (0° Fibre Orientation)</i>	3-29
3.7.1.4	<i>UTC 5 ($\pm 30^\circ$ Fibre Orientation)</i>	3-31
3.7.1.5	<i>UTC 6 (-30° Fibre Orientation)</i>	3-32
3.7.1.6	<i>UTC 7 ($+30^\circ$ Fibre Orientation)</i>	3-34
3.7.1.7	<i>UTC 8 ($\pm 45^\circ$ Fibre Orientation)</i>	3-35

3.7.1.8	<i>UTC 9 (-45° Fibre Orientation)</i>	3-37
3.7.1.9	<i>UTC 10 (+45° Fibre Orientation)</i>	3-38
3.7.2	Elevated Temperature Tests (350°C)	3-40
3.7.2.1	<i>Monolithic 2 (HIPped Solid Ti-6-4)</i>	3-40
3.7.2.2	<i>UTC 3 (0° Fibre Orientation)</i>	3-42
3.7.2.3	<i>UTC 11 (±45° Fibre Orientation)</i>	3-44
3.7.2.4	<i>UTC 12 (-45° Fibre Orientation)</i>	3-45
3.7.2.5	<i>UTC 13 (+45° Fibre Orientation)</i>	3-47
3.8	Discussions	3-48
3.8.1	Effective MMC Shear Modulus	3-51
3.8.2	Shear Strength at Knee of MMC	3-52
3.8.3	Ultimate Shear Strength of MMC	3-53
3.8.4	Ductility	3-56
3.9	Summary	3-58

CHAPTER 4 - FAILURE INVESTIGATION AND MATERIAL STUDIES

4.1	Introduction	4-1
4.2	Damage Evolutions	4-1
4.2.1	Room Temperature Test	4-3
4.2.1.1	<i>UTC1 (0° Fibre Orientation)</i>	4-3
4.2.1.2	<i>UTC5 (±30° Fibre Orientation)</i>	4-4
4.2.1.3	<i>UTC6 (-30° Fibre Orientation)</i>	4-5
4.2.1.4	<i>UTC7 (+30° Fibre Orientation)</i>	4-7
4.2.1.5	<i>UTC8 (±45° Fibre Orientation)</i>	4-8
4.2.1.6	<i>UTC9 (-45° Fibre Orientation)</i>	4-10
4.2.1.7	<i>UTC10 (+45° Fibre Orientation)</i>	4-11
4.2.2	Elevated Temperature Test (350°C)	4-13
4.2.2.1	<i>UTC3 (0° Fibre Orientation)</i>	4-13
4.2.2.2	<i>UTC11 (±45° Fibre Orientation)</i>	4-14
4.2.2.3	<i>UTC12 (-45° Fibre Orientation)</i>	4-15
4.2.2.4	<i>UTC13 (+45° Fibre Orientation)</i>	4-15

4.3	Fracture Surfaces Studies	4-16
4.3.1	UTC1 (0° Fibre Orientation)	4-17
4.3.2	UTC3 (0° Fibre Orientation)	4-20
4.3.3	UTC5 ($\pm 30^\circ$ Fibre Orientation)	4-22
4.3.4	UTC6 (-30° Fibre Orientation)	4-24
4.3.5	UTC7 ($+30^\circ$ Fibre Orientation)	4-26
4.3.6	UTC8 ($\pm 45^\circ$ Fibre Orientation)	4-28
4.3.7	UTC9 (-45° Fibre Orientation)	4-30
4.3.8	UTC10 ($+45^\circ$ Fibre Orientation)	4-33
4.3.9	UTC11 ($\pm 45^\circ$ Fibre Orientation)	4-34
4.3.10	UTC12 (-45° Fibre Orientation)	4-36
4.3.11	UTC13 ($+45^\circ$ Fibre Orientation)	4-37
4.4	SEM Imaging	4-39
4.4.1	Imaging of Polished Samples	4-40
4.4.1.1	<i>UTC1 (0° Fibre Orientation)</i>	4-40
4.4.1.2	<i>UTC3 (0° Fibre Orientation)</i>	4-41
4.4.1.3	<i>UTC5 ($\pm 30^\circ$ Fibre Orientation)</i>	4-43
4.4.1.4	<i>UTC6 (-30° Fibre Orientation)</i>	4-44
4.4.1.5	<i>UTC7 ($+30^\circ$ Fibre Orientation)</i>	4-45
4.4.1.6	<i>UTC8 ($\pm 45^\circ$ Fibre Orientation)</i>	4-46
4.4.1.7	<i>UTC9 (-45° Fibre Orientation)</i>	4-47
4.4.1.8	<i>UTC10 ($+45^\circ$ Fibre Orientation)</i>	4-48
4.4.1.9	<i>UTC11 ($\pm 45^\circ$ Fibre Orientation)</i>	4-49
4.4.1.10	<i>UTC12 (-45° Fibre Orientation)</i>	4-49
4.4.1.11	<i>UTC13 ($+45^\circ$ Fibre Orientation)</i>	4-50
4.4.2	Microstructural Studies	4-51
4.5	Energy-dispersive X-ray Analysis	4-54
4.5.1	Line Scanning	4-54
4.5.2	Chemical Mapping	4-58
4.6	Summary	4-60

CHAPTER 5 - PREDICTION OF TIMMC MATERIAL PROPERTIES USING FINITE ELEMENT METHOD

5.1	Introduction	5-1
5.2	Prediction of Global Orthotropic Elasticity	5-1
5.3	Unit Cell Models	5-2
5.3.1	Unidirectional 0° Unit Cell Model	5-5
5.3.1.1	<i>SC03 Unit Cell Model</i>	5-5
5.3.1.2	<i>ABAQUS Unit Cell Model</i>	5-11
5.3.1.3	<i>Predicted orthotropic material properties for MMC</i>	5-19
5.3.2	Cross-ply ±45° Unit Cell Model	5-20
5.3.2.1	<i>ABAQUS Model</i>	5-22
5.3.2.2	<i>SC03 Model</i>	5-25
5.4	Tube Models	5-27
5.4.1	ABAQUS Parametric Tube Model	5-27
5.4.2	Cyclic Symmetry Tube Model	5-34
5.4.2.1	<i>ABAQUS Cyclic Symmetry Tube Model</i>	5-34
5.4.2.2	<i>SC03 Cyclic Symmetry Tube Model</i>	5-36
5.5	Validation with Experimental Results	5-41
5.6	Summary	5-44

CHAPTER 6 - TIMMC TORSIONAL BUCKLING ANALYSIS USING FINITE ELEMENT METHOD

6.1	Introduction	6-1
6.2	Analysis Algorithms	6-3
6.2.1	Elastic Buckling (Eigenvalue Algorithm)	6-3
6.2.2	Elastic-Plastic Buckling (Riks Algorithm)	6-5
6.3	Analysis Approach	6-7
6.3.1	Design and Model Generation	6-7
6.3.2	Elements	6-10
6.3.3	Material Models	6-11
6.3.3.1	<i>Elasticity Material Model</i>	6-11
6.3.3.2	<i>Plasticity Material Model</i>	6-12

6.3.4	Imperfections	6-18
6.3.5	Boundary Conditions	6-20
6.3.6	Loading	6-20
6.3.6.1	<i>EV Analysis</i>	6-20
6.3.6.2	<i>Riks Analysis</i>	6-20
6.3.7	Monitoring the Analysis	6-21
6.4	Results and Discussions	6-23
6.4.1	Analysis of Results	6-23
6.4.2	Effect of Shear Stress Ratios	6-24
6.4.3	Effect of Fibre Orientation	6-26
6.5	Summary	6-31

CHAPTER 7 - CONCLUSIONS AND FUTURE WORK

7.1	Introduction	7-1
7.2	Conclusions	7-2
7.3	Future Works	7-6
7.3.1	Fatigue Tests	7-6
7.3.2	Buckling Tests	7-8
7.3.3	Further Development on Numerical Models	7-8
7.4	Future Prospects of TiMMC Technology	7-9

REFERENCES

APPENDIX A – Drawing of Shaft Tooling

APPENDIX B – Relation between Direct Strain and Shear Strain

APPENDIX C – Definition of Material Orientation in SC03

APPENDIX D – Conversion of Nominal Stress-Strain to True Stress-Strain in ABAQUS

NOMENCLATURE

T	Instantaneous torque
T_{total}	Total torque
$T_{Section}$	Torque carried by cross section
T_{MMC}	Torque carried by MMC layer
T_{inner}	Torque carried by inner cladding
T_{outer}	Torque carried by outer cladding
$T_{cladding}$	Torque carried by cladding
T_{Knee}	Torque at knee on stress-strain curve
F	Force/Load
F_{T0°	Force of 0° torque actuator
F_{T180°	Force of 180° torque actuator
R_{ave}	Average reaction force
R_{left}	Reaction force at left face
R_{bottom}	Reaction force at bottom face
$J_{section}$	Polar moment of inertia for cross section
J_{MMC}	Polar moment of inertia for MMC layer
J_{inner}	Polar moment of inertia for inner cladding
J_{outer}	Polar moment of inertia for outer cladding
$J_{cladding}$	Polar moment of inertia for cladding
E_1	Young's modulus at 1 direction

E_2	Young's modulus at 2 direction
E_3	Young's modulus at 3 direction
E_x	Young's modulus at x direction
E_y	Young's modulus at y direction
E_z	Young's modulus at z direction
ν_{12}	Poisson's ratio at 12 direction
ν_{13}	Poisson's ratio at 13 direction
ν_{23}	Poisson's ratio at 23 direction
ν_{xy}	Poisson's ratio at xy direction
ν_{yz}	Poisson's ratio at yz direction
ν_{zx}	Poisson's ratio at zx direction
G_{12}	Shear modulus at 12 direction
G_{13}	Shear modulus at 13 direction
G_{23}	Shear modulus at 23 direction
G_{31}	Shear modulus at 31 direction
G_{xy}	Shear modulus at xy direction
G_{yz}	Shear modulus at yz direction
G_{zx}	Shear modulus at zx direction
G_{Ti}	Shear modulus of titanium matrix
G_{MMC}	Shear modulus of MMC layer
$G_{adapter}$	Shear modulus of adapter
G_{eff}	Bulk effective shear modulus

τ_{MMC}	Mean shear stress of MMC layer
τ_i	Mean shear stress of inner cladding
τ_o	Mean shear stress of outer cladding
$\tau_{Knee,MMC}$	Shear stress of MMC layer at knee on stress-strain curve
τ_{12}	Shear stress at 12 direction
τ_{13}	Shear stress at 13 direction
τ_{23}	Shear stress at 23 direction
τ_{bulk}	Bulk shear stress
γ	Shear strain/Rotation
γ_{bulk}	Bulk shear strain
γ_{OD}	Shear strain at outer diameter
γ_{MMC}	Mean shear strain of MMC layer
γ_i	Mean shear strain for inner cladding
γ_o	Mean shear strain for outer cladding
γ_{12}	Shear strain at 12 direction
γ_{13}	Shear strain at 13 direction
γ_{23}	Shear strain at 23 direction
ϵ_{bulk}	Bulk direct strain
ϵ_{max}	Maximum direct strain
ϵ_{nom}	Nominal strain
ϵ_{0°	Direct strain of 0° strain gauges
ϵ_{45°	Direct strain of 45° strain gauges

ε_{315°	Direct strain of 315° strain gauges
ε_1	Strain at channel 1 (strain at 315° strain gauges)
ε_2	Strain at channel 2 (strain at 0° strain gauges)
ε_3	Strain at channel 3 (strain at 45° strain gauges)
$\hat{\varepsilon}_1$	Indicated direct strain at channel 1
$\hat{\varepsilon}_2$	Indicated direct strain at channel 2
$\hat{\varepsilon}_3$	Indicated direct strain at channel 3
ν_0	Poisson's ratio of the material on which the manufacturer's gauge factor was measured
K_t	Transverse sensitivity coefficient for strain gauges
σ^0	Reference stress
τ^0	Reference yield stress
σ_{nom}	Nominal stress
σ_{11}	Stress at 11 direction
σ_{22}	Stress at 22 direction
σ_{33}	Stress at 33 direction
σ_{12}	Stress at 12 direction
σ_{23}	Stress at 23 direction
σ_{31}	Stress at 31 direction
R_{11}	Stress ratio at 11 direction
R_{22}	Stress ratio at 22 direction
R_{33}	Stress ratio at 33 direction
R_{12}	Stress ratio at 12 direction

R_{23}	Stress ratio at 23 direction
R_{31}	Stress ratio at 31 direction
$\bar{\sigma}_{11}$	Yield stress at 11 direction
$\bar{\sigma}_{22}$	Yield stress at 22 direction
$\bar{\sigma}_{33}$	Yield stress at 33 direction
$\bar{\sigma}_{12}$	Yield stress at 12 direction
$\bar{\sigma}_{23}$	Yield stress at 23 direction
$\bar{\sigma}_{31}$	Yield stress at 31 direction
θ	Orientation angle/Angle
θ_{total}	Total twist (cross-head)
$\theta_{specimen}$	Specimen twist
θ_{PS}	Plain section twist
$R_{cross-head}$	Radius of cross-head
R_o	Outer diameter radius
R_b	Outer radius of MMC layer
R_a	Inner radius of MMC layer
R_i	Inner diameter radius
R_{PS}	Radius of plain section
L_{eq}	Equivalent length
L_{PS}	Plain section length
S_{T0°	Distance 0° torque actuator moved
S_{T180°	Distance 180° torque actuator moved

δ	Change of length
L	Length
$D_{transition1}$	Diameter of transition 1 section (tube model)
S_1	Tangential displacement of point 1
S_2	Tangential displacement of point 2
A	Surface area
A_{left}	Surface area of left face
A_{bottom}	Surface area of bottom face
α	Coefficient of thermal expansion
P	Hydrostatic pressure
D	Width of 0° unit cell
H	Height of 0° unit cell
K	General factor
A_1	Coefficient
A_2	Coefficient
A_N	Coefficient
u_i^P	Nodal variable at node P , degree of freedom i
u_j^Q	Nodal variable at node Q , degree of freedom j
u_k^R	Nodal variable at node R , degree of freedom k
U_1	Displacement in 1 direction
U_2	Displacement in 2 direction
U_3	Displacement in 3 direction
H_2	Height in 2-direction

M_z	Moment about z-axis
σ	Traction (SC03 cyclic symmetry tube model)
r	Effective radius of applied traction (SC03 cyclic symmetry tube model)

INTRODUCTION

1.1 Background

The research within this project was co-funded by the European Commission (EC), within the sixth framework program for research and technological development, to reduce aircraft engine noise and CO₂ emissions. The program, which has the acronym VITAL (EnVIronmenTALly Friendly Aero Engine), is a four-year program (2005-2008) with a total budget of €90M.

The VITAL program comprised of a number of sub-projects (SP) with the areas of research emphasis being on whole engine assessment, fan modules, booster module, structures, low pressure shaft, low pressure turbine and installation. Each sub-project can be divided into a number of work-packages (WP). The shaft research carried out within this project was assigned to WP5.2 within SP5 for the low pressure (LP) shaft. In WP5.2, the overall objective was to increase the torque by using MMC (Metal Matrix Composites) technology. The specific objectives for WP5.2 will be presented in section 1.2. For further details regarding the VITAL program, refer to [1].

In the past few decades, the demand for increased performance from aeroengines has increased significantly, requiring higher thrust, higher torque, increased efficiency and higher operating temperatures. The mechanical power transmission systems must carry high fluctuating torques, while at the same time they must be light and have a diameter as small as possible. This has the effect

of reducing the drag which then increases the aeroengine efficiency. The VITAL program required a shaft technology which is able to transmit a higher torque without increasing either the diameter of the shaft or the overall weight of the aeroengine. However, it is not currently possible to fulfil these conditions and demands without the introduction of new technologies using novel materials.

Titanium Metal Matrix Composites (TiMMC), which comprise of titanium matrix reinforced with embedded continuous monofilament silicon carbide (SiC) fibres are being considered as strong candidates, and have been gaining use in aerospace applications in the past two decades. The advantages of TiMMC include superior stiffness-to-weight and strength-to-weight ratios compared to conventional aerospace steels. Potentially, the use of TiMMC can improve the torque density (higher torque for a given diameter) for shafts. The design of shafts can be optimised by altering the fibre orientation and fibre volume fraction.

However, relatively little fundamental research has been carried out to improve the understanding of the torsional behaviour of TiMMC shafts; this is due to the prohibitively high cost, and the complexity associated with the manufacture and analysis. What is required is an analysis method which can be used to predict the material properties, for a TiMMC shaft of a given size, fibre volume fraction and fibre orientation. Testing of TiMMC tubes with different fibre orientations can also enhance the understanding of the material and its failure mechanisms. Furthermore, it is necessary to test specimens at elevated temperature because the temperatures of some parts of an aeroengine, in service, which may use TiMMC are relatively high.

1.2 Objectives

The main objective within the VITAL program is to develop a more environmentally friendly aeroengine that can reduce noise by 6 decibels and CO₂ emissions by 7%. Further to that, VITAL aims to develop innovative technical solutions which can reduce the weight of the aeroengine, thereby reducing both fuel consumption and CO₂ emissions.

Within WP5.2, the ability of MMC technologies to provide practical solutions in shaft applications is investigated. The aims are:-

- Optimisation of MMC structures, through fibre orientation and fibre volume fraction, for high torque applications,
- Development of stress analysis methods,
- Understanding of the characteristics of TiMMC, composite material,
- Evaluate the capability of MMC technology in applications to shaft up to the point of manufacturing a demonstration shaft.

1.3 Methodology

Within this project, the Finite Element (FE) analysis method was used to predict the material properties for TiMMC. ABAQUS, a commercial FE package, and SC03, a Rolls-Royce internal FE package, were used to develop the numerical models. Comparing the results from these FE packages enabled an assessment to establish which package gives the best predictions.

Using the numerical models, the following areas of interest were investigated:-

- Prediction of global orthotropic elastic material properties for MMC for a given fibre volume fraction

- Effective MMC shear modulus prediction of MMC shafts with different fibre orientations
- Torsional buckling behaviour of MMC shafts

1.4 Structure of Thesis

The structure and the contents of the thesis are summarized below.

The literature relevant to the field was reviewed in Chapter 2. Of particular interest, is the TiMMC system used within this project, and the torsional characterisation of the material by various researchers.

In Chapter 3, details of the experimental work, including the design of the specimens and the testing methods, is presented. The experimental results obtained from the TiMMC tube tests with different fibre orientations, at both room and elevated temperature, are also presented. Key results, which include the effective shear modulus, ultimate shear strength and the ductility, are discussed.

Following the experimental work, comprehensive failure investigations of the tested specimens were carried out, and the results are presented in Chapter 4. Samples from the specimens were polished and etched which enable detailed study of the microstructure, fibre regularity, fibre orientation and fibre spacing. Based on the studies of the fractured plane and surfaces, the failure mechanisms for each fibre orientation were described.

Chapter 5 discusses the development of the numerical models, using the FE method. Unit cell models were used to predict the global orthotropic elastic material properties of the MMC for a given fibre orientation. Then, the material

properties was used to define the MMC core layer for the tube models to predict the effective MMC shear modulus for different fibre orientations. The results obtained were compared with the experimental results presented in Chapter 3 and the comparisons were discussed.

Chapter 6 describes the methodology developed for the torsional buckling analysis of TiMMC, using FE method. Eigenvalue (EV) and Riks algorithms were used to predict the complete buckling characteristics, including the post-buckling response. Key results such as the buckling peak load and failure mode shapes are presented and discussed.

Chapter 7 contains a summary of the key findings of all of the work presented in the thesis. The main conclusions, based on the work, are stated and suggestions for future work within the VITAL program are described. Finally, the prospects for the use of TiMMC technology in the future are described.

CHAPTER 2

LITERATURE REVIEW

2.1 Introduction

In correlation to the objective within WP5.2, this project aims to assess the TiMMC technology to shaft application. This will realize the main objective of the VITAL program which is to reduce the aircraft noise and CO₂ emissions using advanced technologies and materials. Hence, the emphasis of this project was based on the characterisation of the torsional behaviour of shafts using TiMMC technology. Titanium matrix, Ti-6-4, reinforced with SiC fibres, SCS6, was selected as the TiMMC system for this research.

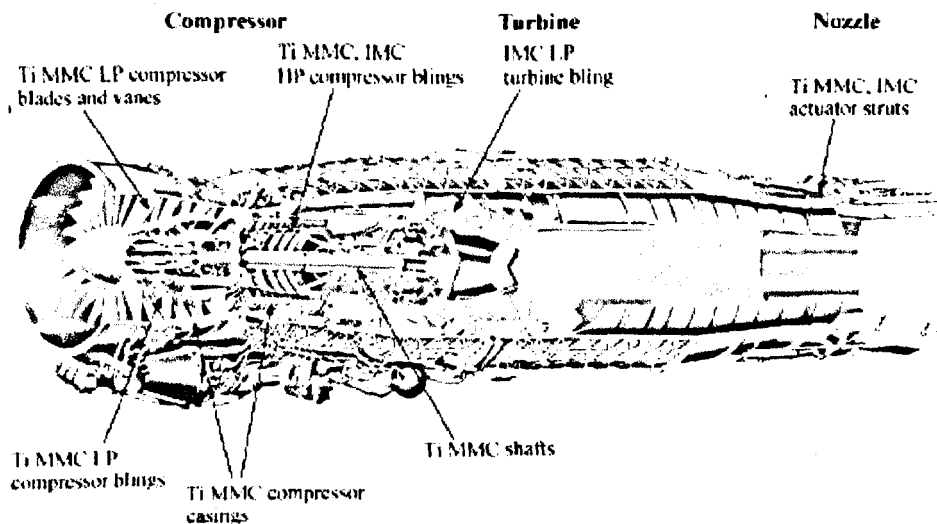


Figure 2.1 Potential TiMMC applications for military aeroengine [2]

TiMMC is lightweight, has superior stiffness-to-weight and strength-to-weight ratios compared to conventional aerospace steels. Other materials properties for TiMMC are better than those of monolithic titanium. For example, Ti-6-4/SCS6 remain strong at elevated temperatures, up to 350°C [2], and this is a key factor

in them being considered as candidates for advanced aeroengine shafts. The limitation of the operating temperature of the TiMMC components is mainly restricted by the matrix material. Therefore, the applications in an aeroengine fall within the compressor section where parts such as blings (bladed rings), blades, vanes and casings are considered as the potential candidates. Military aeroengines as well as commercial aeroengines may benefit from the superior properties of this material compared to conventional aerospace steels. Figure 2.1 shows the potential applications for TiMMC in military aeroengine.

The research within the TiMMC subject is very broad, covering experimental work, material studies, development of numerical and analytical models, and component design. However, the literature review will concentrate on the experimental work and numerical models relevant to this project. In particular, attention was paid to the literature which involved Ti-6-4/SCS6 system. The first batch of the VITAL phase 1 tube specimens were manufactured by QinetiQ, and the remaining specimens were manufactured by TISICS Ltd. Therefore, other TiMMC systems might be relevant, where they are manufactured by both companies using the same manufacturing route.

2.2 TiMMC Systems

TiMMC is a composite that contains a titanium matrix reinforced with ceramic fibres. Different combinations of titanium matrix and fibres can be used, depending on the particular application. Some matrix materials are capable of higher temperatures and some have higher strengths. Different fibres also have their own architecture and they can be varied according to the physical conditions to which the constituent materials are to be subjected to. The

particular combination of matrix and reinforcement leads to superior material properties, tailored to a particular application. Fibre volume fraction and fibre orientation can also be altered to suit the applications. TiMMC are generally classified into three categories, i.e., particulate reinforced, whisker or short fibre-reinforced and monofilament reinforced composites. The latter is the category of interest here.

The TiMMC system used within this research is Ti-6-4/SCS6. In general, titanium alloy has a low density of 4505 kg/m^3 , which is approximately half that of aerospace steels. The following sub-sections describe the various TiMMC systems available.

2.2.1 Ti-6-4/SCS6

Ti-6-4/SCS6 is currently one of the most popular TiMMC systems, where Ti-6-4 is the most widely used titanium grade in the aerospace industry, and SCS6 fibres was readily available, and has been in the market for decades.

Ti-6-4 is a two phase α - β titanium alloy, containing 6% aluminium and 4% vanadium. At low temperature, it has a Hexagonal Closed Pack (HCP) crystal structure, while at temperature above 882°C , it has a Body Centred Cubic (BCC) crystal structure. Aluminium is an alpha stabilizing element which increases the temperature at which α transforms to β . On the other hand, vanadium is a beta stabilizing element which lowers the phase transformation temperature, enable β to be stable at room temperature [3]. Ti-6-4 has a moderately high tensile strength, good fatigue resistance with intermediate fracture toughness and excellent corrosion resistance [4].

SCS6 is a monofilament SiC fibre developed by Specialty Materials Inc. within the SCS family. This fibre has excellent strength, high heat and corrosion resistance. As the reinforcement for MMC, it is high in strength, stiffness and lightweight and extremely effective for high temperature applications compared to monolithic material.

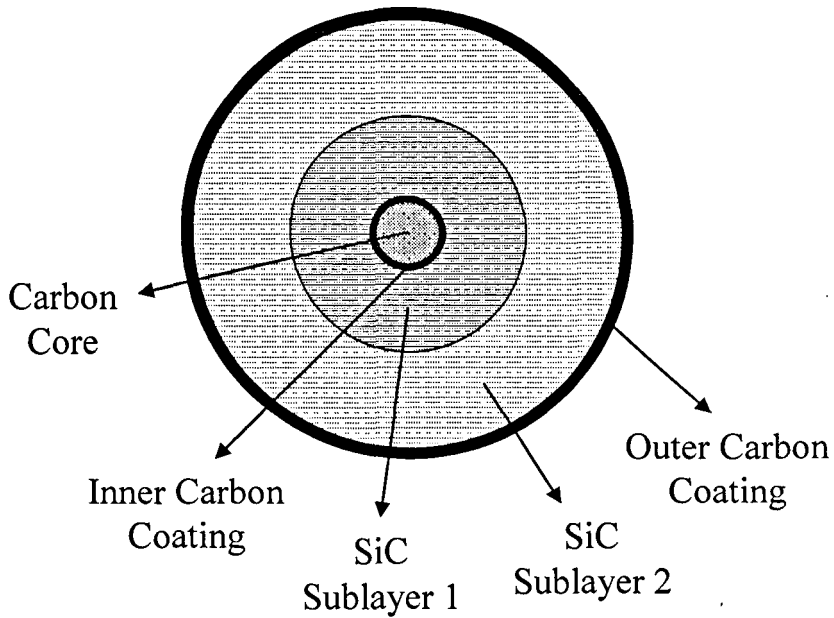


Figure 2.2 Schematic diagram of SCS6 fibre structure

The fibre is made of a carbon core, $33\mu\text{m}$ in diameter, surrounded by a soft pyrolytic inner carbon coating approximate $3\mu\text{m}$ thick. On top of these are two sublayers of SiC-based deposit, the first sublayer is $24\mu\text{m}$ thick consisting of 11% of carbon and 89% of SiC and the second sublayer is $22\mu\text{m}$ thick consisting of near pure SiC deposit. The outermost structure is a carbon coating, which is $3.5\mu\text{m}$ thick, consisting of 35% SiC and 65% pyrolytic carbon [5]. A schematic diagram of the SCS6 fibre is shown in Figure 2.2.

The relatively thick outer carbon coating minimizes the handling damage to the fibre surface, and acts as a compliant layer to accommodate the difference in

coefficient of thermal expansion (CTE) between the fibre and matrix [6]. Further to that, the coating is not totally consumed due to the reaction between the fibre and matrix during the high temperature and pressure consolidation process. The thick coating also prevents the cracks that occur at the fibre matrix reaction zone, under loading, to act as a stress raiser at the fibre surface [5].

The continuous SCS6 fibres are produced using the chemical vapour deposition (CVD) method. The deposition of SiC and coating on the carbon core is completed within the same CVD reactor with different deposition gases and temperature at different stages. Detail of the CVD process on SCS6 fibres was reported elsewhere [6]. Detail microstructure study of SCS6 can also be found here [7, 8].

2.2.2 Ti-15-3/SCS6

Ti-15-3 reinforced with SCS6 fibres was a popular TiMMC system in the late 80s and early 90s and many investigations were carried out. Ti-15-3 titanium alloy contains 15% vanadium, 3% aluminium, 3% tin and 3% chromium. It is a metastable β titanium alloy due to the large addition of the beta stabilizing element, vanadium [3]. Although not extensively used, it is the most versatile grade of titanium alloy offering the highest strength to weight ratio combined with high toughness and good fatigue resistance [9]. The Young's modulus and shear modulus of Ti-15-3 (91 GPa and 33.4 GPa [10] respectively) are lower than those for Ti-6-4 (106 GPa and 46 GPa (IMI datasheet), respectively).

Lissenden and co-workers [10-14] did extensive research on Ti-15-3 reinforced with SCS6 fibres, to understand the material behaviour under combined loading. Tubular specimens were used where biaxial loading (axial and torsion) and

multiaxial loading (axial, torsion and internal pressure) were applied at different load levels.

The area of work can be split into two major parts. First, the experimental work involved investigation in the stiffness degradation of the material, material responses under imperfect bonding, responses under the presence of damage and microstructural evaluation. The other area involved development of interfacial constitutive relations between fibre and matrix and micromechanical modelling to predict the multiaxial response of Ti-15-3/SCS6 [11]. Although, the titanium alloy used was different to the one used in this project, the work done by Lissenden and co-workers were most appreciated and complimented, since not much experimental work has been done on TiMMC, using tubular specimens. The findings from the experimental work were most valuable and will be further presented in section 2.4.2.

Mechanical responses of Ti-15-3/SCS6 were also characterised, at both room and elevated temperature up to 650°C by Newaz et al. [15] using coupon specimens. Unidirectional-ply (0° & 90°) and cross-ply ($\pm 45^\circ$) laminates were tensile tested to obtain the inelastic deformation characteristics.

2.2.3 Ti-6-2-4-2/SCS6

As mentioned earlier, the limitation of operating temperature of TiMMC components is mainly restricted by the matrix material. Therefore, in the past 5 years, Ti-6-2-4-2 titanium alloy reinforced with SCS6 fibres has been gaining momentum. Ti-6-2-4-2 is a near- α titanium alloy containing 6% aluminium, 2% tin, 4% zirconium and 2% molybdenum. It performs well at temperatures up

to 500-550°C [2], whereas Ti-6-4 is limited to 350°C. Therefore, this TiMMC system suits the environment at the rear of the aeroengine which is hotter.

ONERA (Office National d'Etudes et de Recherches Aérospatiales) as one of the VITAL partners within WP5.2, had carried out an extensive research on this TiMMC system. Cylindrical specimens (fibres at longitudinal direction) and transverse coupon specimens made from Ti-6-2-4-2 reinforced with SCS6 fibres were tested under cyclic and fatigue loading [16]. Larger tubular specimens with fibre orientation at 0°, 25° and 45° were also tested under cyclic and fatigue torque loading.

Duda et al. had studied the reaction zone formed between the fibre coating and the matrix of Ti-6-2-4-2 reinforced with SCS6 processed by a fast liquid route [17]. It was found that the carbon was diffused into the matrix and formed a reaction zone of titanium carbide. The mechanism of the formation of the reaction zone and effect of heat treatment were also investigated. Although the heat treatment increases the thickness of the titanium carbide layer, it enables the classical near α microstructure to be recovered, from the eutectic microstructure. Moreover, the brittleness of the titanium carbide layer in the eutectic zone is significantly lessened.

2.2.4 Ti-6-4/SM1140+

Another variant of SiC fibres has been developed in the 90s by Defence Evaluation Research Agency (DERA, now QinetiQ) called Sigma fibres. The more well-known SiC fibres in this Sigma family are SM1140+ and SM1240. The main difference between these fibres is the fibre coating. Since then, these fibres created more interest in MMC, subsequently, different TiMMC systems

using these fibres were investigated. Ti-6-4 is the most widely used titanium alloy being the main candidate for research. This section describes various works on Ti-6-4/SM1140+ TiMMC system and section 2.2.5 describes the work on Ti-6-4/SM1240 TiMMC system.

The SM 1140+ fibre has a tungsten core, 15 μm in diameter, surrounded by a reaction zone of 120nm thick. This reaction zone consists of two different layers which is the carbide (inner reaction layer, W_2C) and the silicide (outer reaction layer, WSi_2). On top of the reaction zone is the SiC deposit which is 40 μm thick. Finally, the outermost layer of the fibre is the carbon coating, which is 5 μm thick. Details of the microstructure for SM1140+ fibre can be found in [18]. A schematic diagram of the SM1140+ fibre is shown in Figure 2.3.

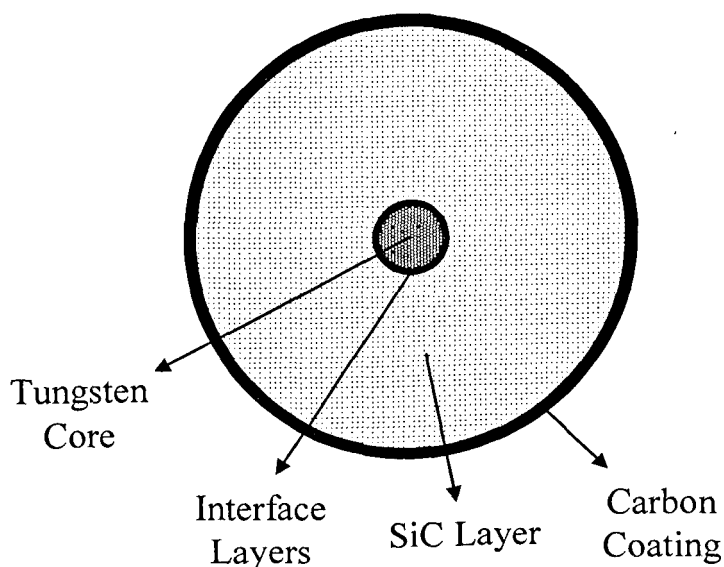


Figure 2.3 Schematic diagram of SM1140+ fibre structure

Comparing with the carbon coating in SCS6 fibre (3.5 μm thick), SM1140+ has a thicker carbon coating. The reason to have such a thick carbon coating is to prevent crack propagation from the fibre to the matrix [19]. It was found that the

failure of a SM1140+ and SM1240 composites, occurs at the interface, between the tungsten core and the SiC layer and travel outwards, under longitudinal tensile loading [20]. Hence, the thick coating suppresses the propagation from the already damaged fibre, to the neighbouring fibre through the matrix.

On the other hand, Thomas et al. [21] had tensile tested numerous 0° Ti-6-4/SM1140+ and un-reinforced coupon specimens. It was found that the MMC yield at a similar stress levels to the un-reinforced specimen, implying that the yielding of MMC is dominated by the matrix material. Also, the failure strain of the MMC is greater (~1%) than the virgin SM1140+ fibres (~0.8%). This is due to the load transfer mechanism by the matrix and thermal residual stresses in the MMC as a result of difference in CTE.

In-Situ investigation of the transverse behaviour of Ti-6-4/SM1140+ had been carried out using coupon specimens by Wu and co-workers [22]. The experimental results confirmed that debonding started at the interface between the fibre and matrix even at low stress levels. Premature microdebonding at surface positions, start at stress level as low as ~51 MPa, because of undulations. Further to that, interface which do not contain visible defect prior of loading, start to debond at a stress level of ~130 MPa. These microcracks extend along the interface under further loading, and gradually coalesce with each other, leading to full debonding. Complete debonding of all interfaces was reported to occur at a stress level of ~257 MPa.

2.2.5 Ti-6-4/SM1240

SM1240 fibre is similar to the SM1140+ fibre except for the fibre coating. A 1.3µm thick carbon coating is deposited on the SiC layer, follow by a 1.3µm

thick coating of titanium boride (TiB_x). A schematic diagram of the SM1240 fibre is shown in Figure 2.4.

The reason to have the titanium boride layer is to delay the attack due to thermal exposure on the underlying carbon layer, in which it acts as a sacrificial layer and subsequently converted to titanium monoboride [19]. Matrix embrittlement was found on the Ti-6-4/SM1140+ MMC due to diffusion of carbon into the matrix. However, the boron-rich outer layer on a Ti-6-4/SM1240 MMC appears to prevent this from happening. Nonetheless, Thomas et al. [21] found that there is no significant difference in the tensile properties of Ti-6-4/SM1140+ and Ti-6-4/SM1240, suggesting the tensile properties of both fibres are similar.

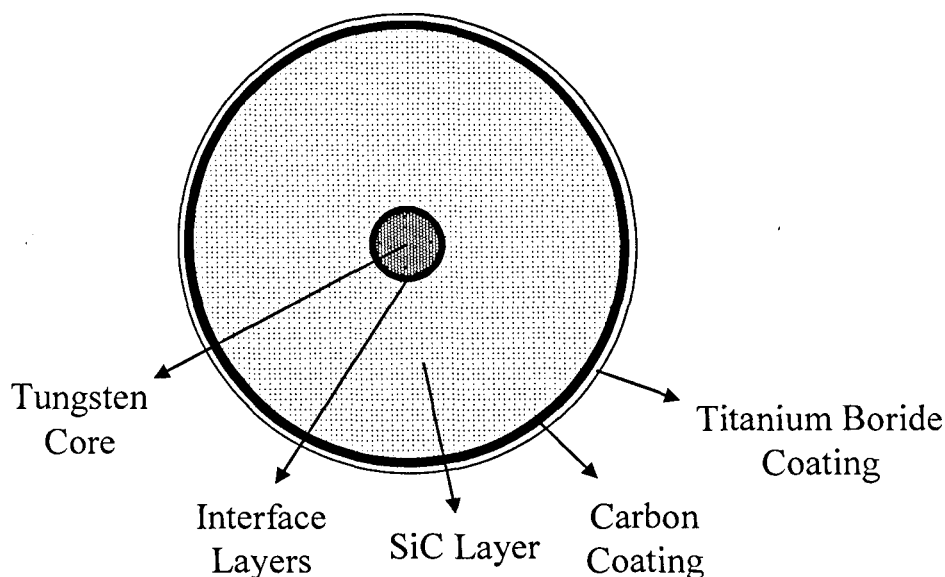


Figure 2.4 Schematic diagram of SM1240 fibre structure

2.3 Manufacturing Routes

Aerospace and automobile components made from titanium alloy reinforced with continuous monofilament SiC fibres, can be fabricated using a number of manufacturing routes. The most common routes to date are the matrix coated

fibre (MCF), foil-fibre-foil (FFF) and plasma spray (PS) methods. Note that the tube specimens tested within this project were fabricated by QinetiQ, using the MCF method and the following sub-sections describe the procedure.

2.3.1 Foil-Fibre-Foil Method

FFF method is the most well known and established method in fabricating TiMMC components. Using this method, the SiC fibres are placed between the metal foils, and hot pressed at high temperature and pressure together, to form a fully dense product. In general, during the process, the fibres are held together by an organic binder to avoid movement of fibres. The organic binder is then driven off during the degassing stage follow by hot pressing [23].

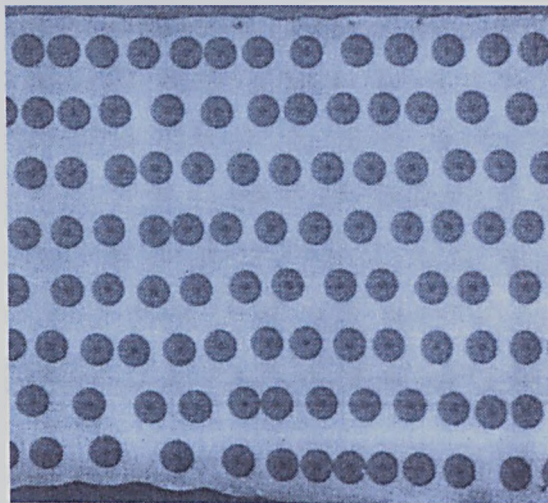


Figure 2.5 TiMMC made using FFF method [23]

However, the movement of fibres are still inevitable and touching fibres are often reported in the consolidated product. Figure 2.5 shows an example. Touching fibres promote crack grow at the interface region and severely degrade the MMC performance. Other drawbacks of this method include poor fibre distribution and high debulking during consolidation. Moreover, the inflexibility

of metal foils restricts the complexity of the component shapes [2]. Nonetheless, this method is most suitable in manufacturing flat products.

2.3.2 Plasma Spray Method

PS is an alternate method, where semi-liquid metal droplets are sprayed onto a single layer of SiC fibres, wound on a drum. The sheets are then stacked and consolidated as in the FFF method. The advantage of this method compared to the FFF method is better fibre distribution [23], as shown in Figure 2.6. However, impact damage was reported on the fibre and its coating, during the high speed spraying which makes this method unpopular.

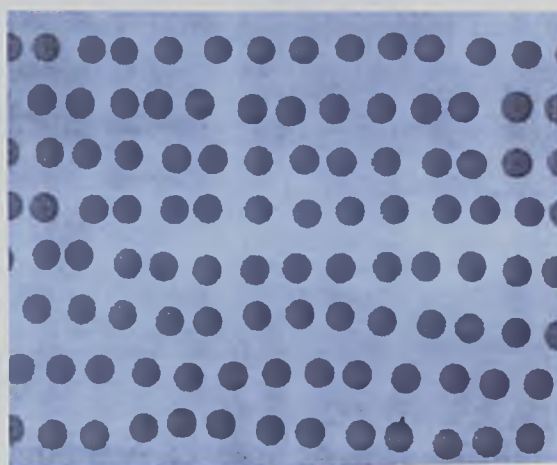


Figure 2.6 TiMMC made using PS method [23]

2.3.3 Matrix Coated Fibre Method

To overcome the disadvantages of the above fabrication methods, a new processing method called MCF was developed. MCF method utilizes the EBPVD (Electron Beam Physical Vapour Deposition) technique, which pre-coat the SiC fibre with a thick layer of matrix material before consolidation. The fibres are then laid-up on the die or tooling and hot pressed. The matrix material

of the final component is provided entirely by the matrix coating, hence, no metal foils or powder are needed. Therefore, the thickness of the matrix coating determines the fibre volume fraction of the final product.

During the EBPVD process, the fibre is passed continuously through a vapour cloud above the molten pool of matrix material. The matrix material is then deposited on the fibre surface where the vapour condensed. Figure 2.7 shows a schematic diagram of a typical EBPVD process, where fibres are held in a drum rotate above the vapour cloud.

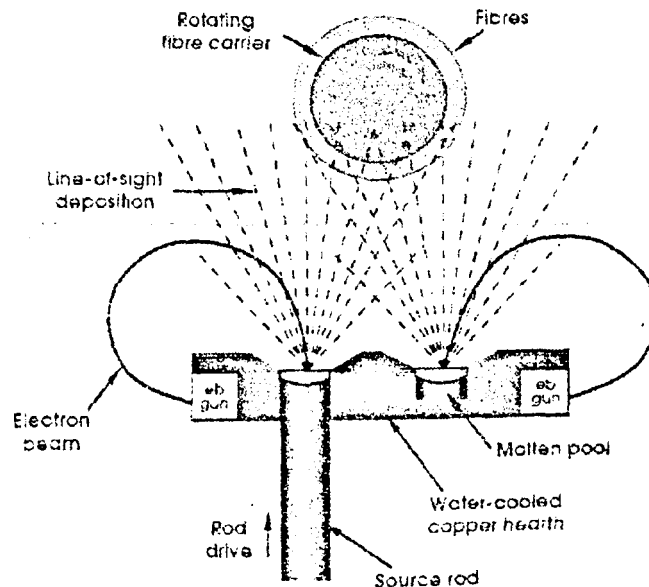


Figure 2.7 Schematic diagram of a laboratory scale twin-source electron beam evaporation fibre coating apparatus [24]

In general, the MCF is either consolidated by hot isostatic pressing (HIPping) or vacuum pressing. The fibres are bundled together, vacuum degassed and sealed in the tooling before the HIPping cycle. During the HIPping cycle, temperature and pressure are applied simultaneously. The consolidation of MCF consists of three stages; rapid plastic yielding, followed by power law creep and elimination

of micro-voids. Full consolidation is achieved when all the voids/pores disappeared. Typical parameters for a HIPping cycle for TiMMC are a temperature of 900°C and a pressure of 100 MPa for 1 hour. Ward-Close et al. [24] carried out a parametric study on the parameters for the HIPping process. It was found that, increasing the pressure reduces the consolidation time. However, using higher pressure increases the likelihood of damage to the fibre.

The advantages of using the MCF method compared to other methods are as follows:-

- Better fibre distribution and uniformity compared to FFF and PS methods
- MCF suited the filament winding on round components such as shafts, rings and discs
- Near net shape of consolidated product resulting in minimum machining
- Coated matrix protects the fibre during handling and consolidation process
- Very high fibre volume fraction up to 80% is possible

Peng [25] also studied the densification behaviour of MCF during the consolidation process. It was found that the superplastic deformation is the primary mechanism for the densification of TiMMC.

Figure 2.8 summarizes the various manufacturing routes for TiMMC component.

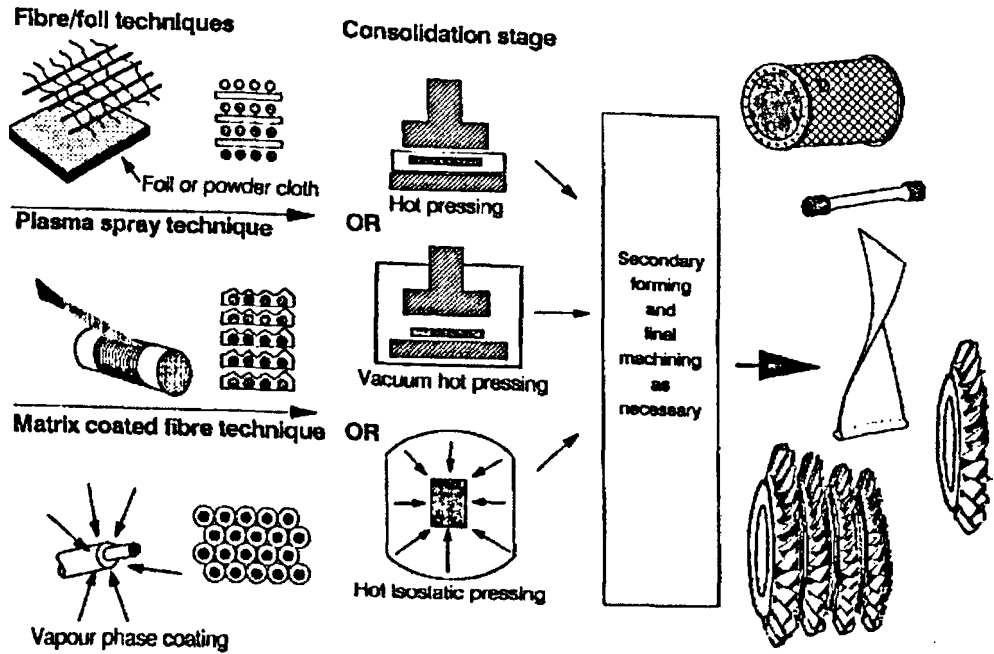


Figure 2.8 Manufacturing routes for TiMMC [2]

2.4 Mechanical Characteristics

Since the introduction of TiMMC two decades ago, a substantial amount of investigation has been carried out to understand the material characteristics. Different kinds of experiments (tension, torsion, fibre pull-out/push-in) were carried out, to characterise the material. High temperature testing is also necessary as TiMMC is a potential application in aerospace industry.

TiMMC coupon specimens with different fibre orientation/lay-up are commonly used due to its cheap cost and ease of fabrication. Tensile properties, such as Young's modulus, yield strength and ultimate strength are measured, along with the study of failure mechanisms and microstructures. The material properties could be used to develop constitutive and analytical models.

On the other hand, TiMMC tubular specimens with different fibre orientation/lay-up are tested to understand its torsional behaviour. However, the

fabrication of this kind of specimen is difficult, due to a more complex process compared to flat coupon specimens. It is reported in [13] that fibre damage was observed prior to testing. The cost of tubular specimens is higher, partly because trials are often needed to ensure the encapsulation method does not fail during the HIPping process.

In general, the mechanical characterisation of TiMMC can be divided into uniaxial and torsional behaviours.

2.4.1 Behaviour under Uniaxial Loading

It is well known that TiMMC has great strength and elastic modulus in the fibre direction compared to the monolithic matrix material. For typical monolithic titanium alloy, the ultimate strength and Young's modulus are 1020 MPa and 106 GPa, respectively. However, when the load is applied to MMC in the off axis directions, the strengths are severely degraded, as most of the load is taken by the matrix. Sun et al. have carried out an extensive experimental program to characterise Ti-6-4/SCS6 using coupon specimens with different fibre orientations at both room and elevated temperature up to 316°C [26, 27]. Off-axis stress-strain curves were also obtained from the tests.

In [27], the specimens with fibre volume fraction of 40% were tension tested at room temperature. The fibre orientations of the specimens include 0°, 5°, 10°, 15°, 30°, 45°, 60° and 90°. For convenience, the experimental results were plotted in a graph shown in Figure 2.9.

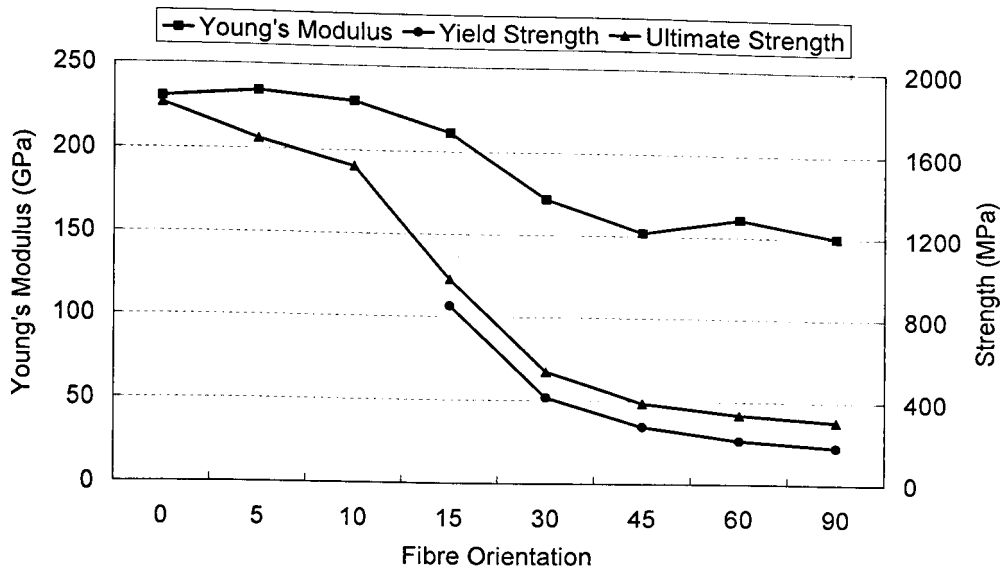


Figure 2.9 Coupon specimens test results (Ti-6-4/SCS6, $V_f = 40\%$), data obtained from [27]

The Young's moduli remain relatively unchanged from 0° to 10° , but it dropped substantially from 10° to 30° and stabilise from 45° to 90° . When the fibre orientation angle is large ($>45^\circ$), the characteristics are dominated by the matrix material. Similar observation was found on the ultimate strength, when the fibre orientation angle is small, good strength was achieved; vice versa, when the fibre orientation angle is large ($>30^\circ$), the ultimate strength degraded severely. However, no yield points were identified for the specimens with small fibre orientation angle ($<15^\circ$), as the specimens remained elastic up to failure. Though, the trend is similar to the ultimate strength.

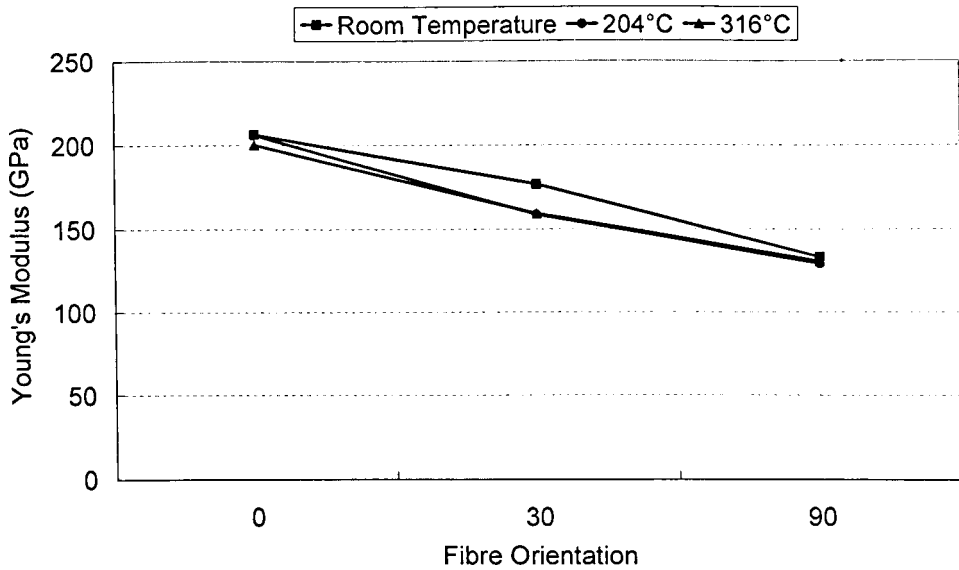


Figure 2.10 Young's moduli of coupon specimens (Ti-6-4/SCS6, $V_f = 35\%$), data obtained from [26]

Further to the above work, similar coupon specimens were tested at elevated temperature at 204°C and 316°C [26]. The fibre volume fraction for the later work is 35%. Figure 2.10 and Figure 2.11 show the measured Young's moduli and ultimate strength, respectively, for fibre orientations 0°, 30° and 90° at different test temperature. It is found that, regardless of the fibre orientation, the Young's moduli remain relatively unchanged up to 316°C. The trend is similar to the previous work where increasing the fibre orientation angle decreases the Young's moduli steadily. However, more substantial strength degradation was observed when the specimens are tested at high temperature. Similar to results from previous work, the strength decrease sharply when the fibre orientation angle is greater than 30°.

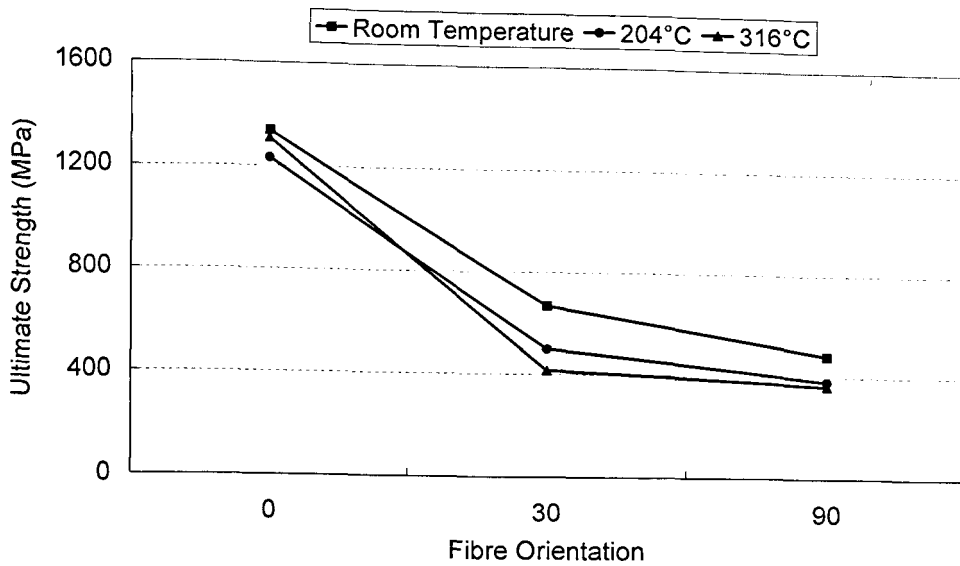


Figure 2.11 Ultimate strength of coupon specimens (Ti-6-4/SCS6, $V_f = 35\%$), data obtained from [26]

The work from Sun et al. forms the fundamental understanding of the TiMMC mechanical behaviour. Although the torsional behaviour of TiMMC is dissimilar to the uniaxial behaviour (due to the stress state), understanding of the uniaxial behaviour comprehends the torsional behaviour (biaxial stress state) of TiMMC.

Li et al. [28] investigated the longitudinal and transverse tensile behaviour of Ti-6-4/SM1240 TiMMC system. The specimens, which have a fibre volume fraction of 34%, were tested under monotonic and cyclic loading at room temperature. For the cyclic loading case, each specimen was unloaded at different strain levels and then subsequently reloaded to higher strain levels until failure.

For the monotonic loading case in the longitudinal direction, a knee on the stress-strain curve was observed, as shown in Figure 2.12. As a result of this knee, reduction in the modulus was measured. This characteristic is thought to

be due to fibre breakage and matrix plasticity. For the cyclic loading case, unloading beyond strain level of 0.4% produce strain offset, indicating the matrix is linear elastic until 0.4% strain level. The strain accumulation is due to the matrix plasticity.

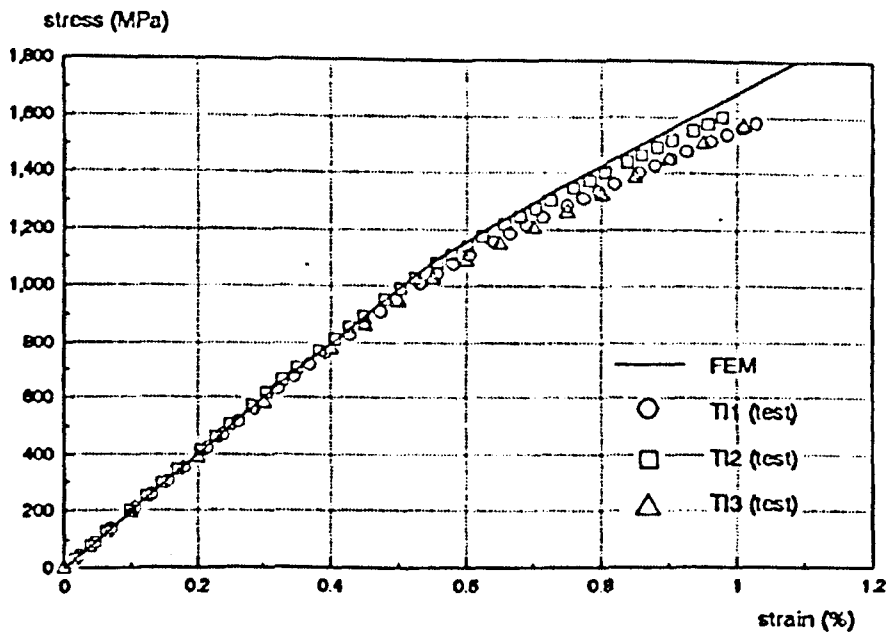


Figure 2.12 Monotonic tension test at longitudinal direction [28]

For the monotonic loading case in the transverse direction, the stress-strain curve can be characterised as three linear parts, connected by two nonlinear transition regions (knees). It is reported in [29], that the knee on the transverse stress-strain curve is due to interface debonding. At low stress level, the fibre and matrix remain elastic. The first knee occurs when the interface debonding taken place. Once the debonding process finished, the matrix still deforms elastically indicated by the second linear part. The second knee is due to the matrix yielding and subsequently matrix strain hardening represents by the final linear part. The strain to failure for this kind of test is large as the behaviour is dominated by the

matrix material. For the cyclic loading case, nonlinearity on the unloading and reloading curves is observed. This phenomenon results from the opening and closing of the interface. Hysteresis loop on the stress-strain curve is attributed by the friction of the debonded interface. Once the matrix yields, a wider loop is observed due to the addition of matrix plasticity.

Cotterill et al. [30] studied the transverse tensile properties of Ti-6-4/SM1140+TiMMC system under monotonic loading. Similar observations on the transverse stress-strain curve were found, but the curve was characterised by five distinct regions as shown in Figure 2.13. Pre-stress the specimen, above the stress level of interface debonding, results in decrease performance in subsequent transverse tensile properties. This implies that the interfacial strength plays an important role on TiMMC transverse behaviour. Again, nonlinearity on the unloading and reloading curves is observed, due to the non-homogeneous straining of the matrix material, where “holes” are created by the debonded interfaces.

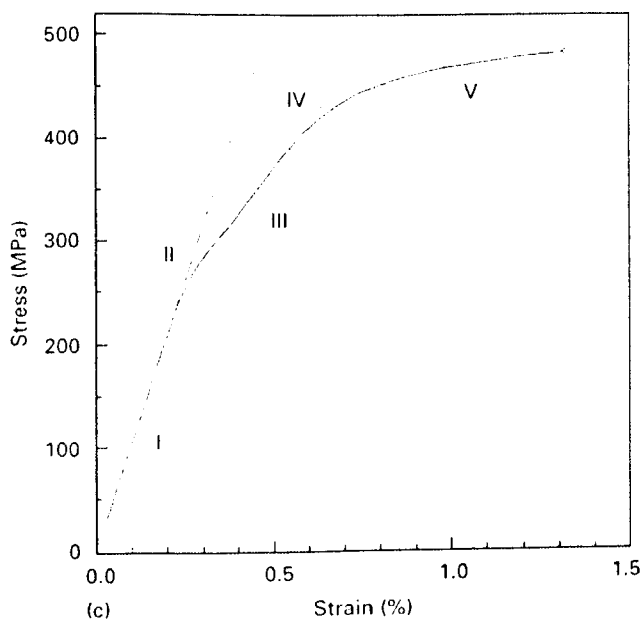


Figure 2.13 Typical stress-strain characteristics for transverse tensile test [30]

2.4.2 Behaviour under Biaxial Loading

As mentioned earlier, there are very few studies of the torsional behaviour of TiMMC in the literature. Nonetheless, Lissenden and co-workers have done a considerable amount of research on the Ti-15-3/SCS6 TiMMC system using tubular specimens.

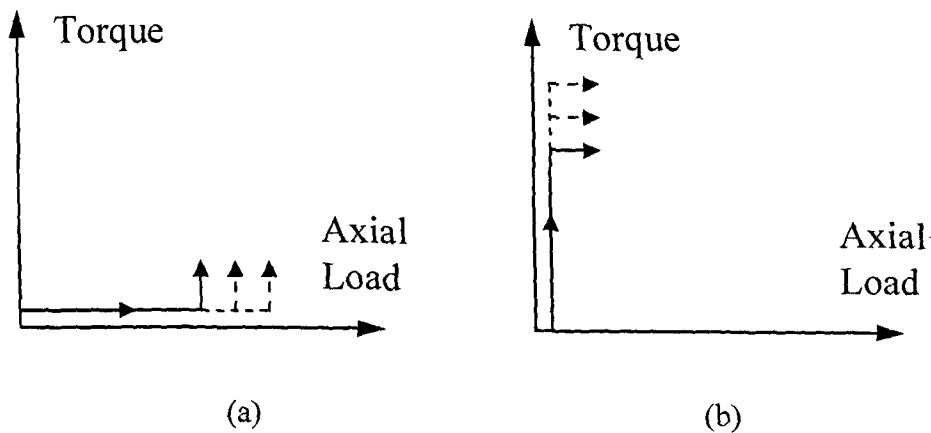


Figure 2.14 Biaxial loading types (a) type I (b) type II

Two types of fibre orientation were considered, they are unidirectional 0° and cross-ply 45° . All specimens have a fibre volume fraction of 40%, and were tested at room temperature. Two types of biaxial loading were considered, named type I (axial load dominated) and type II (torsional load dominated) as shown in Figure 2.14. In type I loading, a series of axial tensile load was applied along the tube axis and at the peak of each cycle, an increment of torsional load was applied. For type II loading, a series of torsional load was applied and at the peak of each cycle, an increment of axial tensile load was applied. These kinds of loadings introduce a biaxial stress state, and subsequently the axial and shear responses were assessed.

In [10], Lissenden et al. investigated the stiffness characteristics of Ti-15-3/SCS6 tubes (0° & $\pm 45^\circ$) at different load levels using type I and II loadings. The response of the 0° tube under type I loading was linear up to failure which shows no stiffness degradation, and the measured axial modulus is 216 GPa. For type II loading, the torsional response becomes nonlinear and exhibits an elastic-perfectly plastic behaviour at a higher torque level. This characteristic is said to be associated with the matrix yielding and interfacial damage. The measured shear modulus is 52.3 GPa.

The response of the $\pm 45^\circ$ tube under type I loading can be characterised by 3 parts. First, at lower load, the response is linear and elastic with no strain accumulation. Then, stiffness degradation is observed with no axial strain growth during the torsional portion of the loading. However, there is only a small amount of permanent strain when the material is completely unloaded, which is associated to interfacial slippage. Final part of the response shows further axial stiffness degradation with axial strain accumulation during the torsional portion of the load cycle. At the final part of the response, hysteresis is seen on the stress-strain curve. They suspected that this is due to the frictions caused by the opening and closing of the debonded interfaces, in addition to the kinematic hardening effects of the matrix. Due to the load capacity of the machine, it is unable to cause yield or failure on the $\pm 45^\circ$ tube under type II test. The measured axial and shear moduli are 120 GPa and 64.5 GPa, respectively. Clearly, the $\pm 45^\circ$ tube is stronger under the torque dominated loading, while the 0° tube is stronger at the axial dominated loading.

Further to that, detail metallographic studies are carried out on the as-fabricated and post-tested tube specimens [13]. For the as-fabricated 0° tube, radial cracks were observed in the carbon coating or at the reaction zone. The cracks appeared to initiate from the carbon core and propagate radially towards the outer diameter of the fibre. For the as-fabricated $\pm 45^\circ$ tube, large amounts of debonded fibres from the matrix were observed, which occur between the reaction zone and carbon coating. Note that, the tubes were produced using the FFF process, therefore, the fibre distribution is poor and the product is prone to damage. For the post-tested specimens, interface debonding, radial cracking and matrix plasticity are the main failure modes under both types of loading.

Although Lissenden et al. used a different TiMMC system and fibre volume fraction; their investigations give an insight into the likely behaviour of the TiMMC under torsional loading. This includes both the elastic and inelastic responses, for both fibre orientations, under axial or torsion dominated combined loads. The results suggest that if TiMMC is to be used in aerospace applications, different lay-up need to be considered which can resist axial, torque and bending loads, as very often, an aerospace component subjects to multiaxial loadings.

2.5 Reaction Zone and Interface

It is well known that a reaction zone exists between the fibre coating and matrix for TiMMC. The formation of the reaction zone occurs during the HIPping process and subsequent heat treatment, and its nature differs with different TiMMC systems due to the coating [6]. It is important, however difficult, to understand the properties of the reaction zone in order to determine the mechanical properties of TiMMC. Excessive chemical reaction, results in fibre

surface degradation leading to a loss in mechanical properties. For TiMMC subjected to transverse loading, it is particularly important as the reaction zone strongly affect the interfacial strength.

It is reported in [31], that for Ti-6-4/SCS6 TiMMC system, the reaction zone contain two layers. The first layer, titanium carbide, TiC, forms at the outer carbon coating. The second layer is the titanium silicide, Ti_5Si_3 , forms around the TiC. It is said that this reaction zone is brittle, and if too thick, will affect the transverse strength of TiMMC [24]. The thickness of the reaction zone can be controlled through the HIPping process.

Several researchers have attempted to measure the interface mechanical properties of TiMMC. Indentation technique was used by Yang et al. [32] to quantify the interfacial mechanical properties for various titanium alloy reinforced with SCS6. Debond strength is determine from the indentation test, of which it is the stress level where fibre/matrix interfacial sliding is detected. The specimen is then indented in the reverse direction to determine the frictional strength. For Ti-6-4/SCS6, the measured debond and frictional strengths are 155.9 MPa and 87.5 MPa, respectively. It was found that interface layers, between the carbon coating and TiC, as well as Ti_5Si_3 layer and matrix material, were separated during the indentation for Ti-6-4/SCS6. Annealing at 800°C for 50 and 100 hours sees slight increase in debond strength and frictional strength.

On the other hand, Wang et al. [33] attempted to determine the effective Young's modulus of the interphase, using a micro-mechanics measurement technique called Speckle Interferometry with Electron Microscopy (SIEM), under transverse tensile test. The effective Young's modulus was found to be

between 20 to 30 GPa which is one order lower than the SiC and matrix material.

2.6 Micromechanical Modelling

Mechanical characterisation of TiMMC is the best method to fully understand its behaviour. However, due to the high fabrication cost of this type of material, it is not possible for all researchers to investigate its material properties through material testing. Micromechanical modelling is an alternative, which allows a better understanding of the interaction between each constituent material at a micromechanics level. It also allows the prediction of the material properties for the resultant TiMMC. FE method is the most commonly used method for this purpose.

As it is impossible to model every fibre within the material, a common approach is to obtain a representative volume element (RVE), often called a unit cell, from the bulk material. The RVE for a unidirectional TiMMC is shown in Figure 2.15, where it is assumed the fibre packing array is periodic, and the RVE is obtained based on the periodicity argument [34]. It is well known that the hexagonal fibre packing array is more realistic than the square fibre packing array, but the RVE shown is applicable to both [35]. Li et al. [29] have also demonstrated the importance of modelling the coating in the model, for better understanding of the material behaviour. Further to that, Aghdam et al. [36] and Xie et al. [34] have attempted to model the interphase layer by assuming its properties based on those of fibre, coating and matrix. Aghdam assumed the interphase properties to be average of the fibre/coating or coating/matrix. Due to the difficulty in measuring the properties of the interphase layer, the only

solution at present is to assume its material properties and compare to the experimental results.

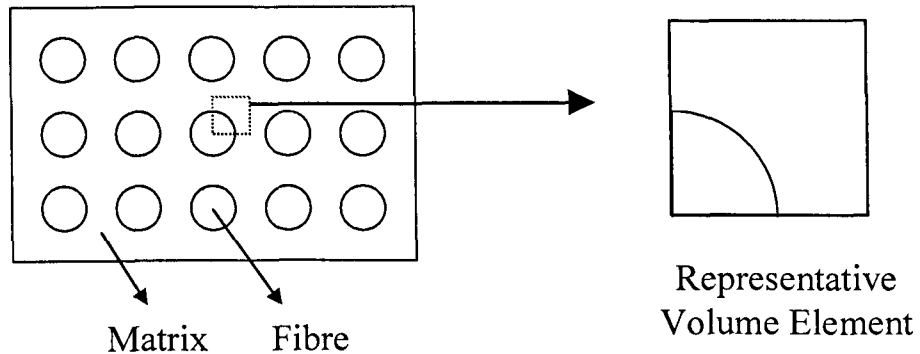


Figure 2.15 Representative volume element for unidirectional TiMMC

Because of the poor performance of TiMMC in the transverse direction, a significant amount of micromechanical modelling has been carried out by many researchers to understand its transverse behaviour [29, 34, 36-38]. The main concern is the interfacial strength between the fibre and matrix, where fibre debonding from the matrix results in crack propagation and early failure. The other concern is the thermal residual stress developed due to mismatch of the CTE between the fibre and matrix. Therefore, the residual stress affects the interfacial strength, and consequently the transverse properties of TiMMC.

As the composite cools from the processing temperature ($\sim 900^\circ\text{C}$), residual stress is created at the interphase. Li et al. [35] and Nimmer et al. [37] modelled the residual stress state of Ti-6-4/SCS6 using the RVE illustrated in Figure 2.15, by using linear elastic material properties for the fibre and elastic-plastic material properties for the matrix. The CTE of the matrix ($\alpha = 10.8 \times 10^{-6}/^\circ\text{C}$) is significantly larger than the fibre ($\alpha = 4.5 \times 10^{-6}/^\circ\text{C}$) [35]. As a result, cooling from the processing temperature to room temperature, compressive stress is

developed at the fibre radial direction, while tensile stress is developed at the axial and hoop direction in the matrix. However, the radial compressive residual stress is beneficial to the transverse behaviour, since it delays interface debonding [35]. Although this can be seen as an advantage, residual stress relaxation results in lower stress and strain to interface debonding if the TiMMC component operates at elevated temperature in service, as is often the case.

In addition to the residual stress modelling, Nimmer et al. [37] also characterised the transverse stress strain behaviour, which included residual stress before application of load. They assumed two cases for the interface, either a weak or a strong interface using contact-surface formulation with different coefficient of friction. Three test temperatures were considered, room temperature, 315°C and 427°C. Their numerical results were compared with experimental test data. Relatively good agreement between the numerical and experimental results was achieved for the transverse stress-strain behaviour for all temperatures for weak interface. Comparison of the transverse stress-strain behaviour at room temperature is shown in Figure 2.16, where the numerical model assumed a weak interface with a coefficient of friction of 0.3. Tri-linear characteristic is observed where the first knee corresponds to the fibre-matrix separation, confirmed by the edge replica experiments taken at various stage of the test. The compressive radial residual stress at the interface, will behave like a composite with finite interface strength, in which the tensile load need to overcome. The results from Nimmer imply that the interface strength is very low or close to zero.

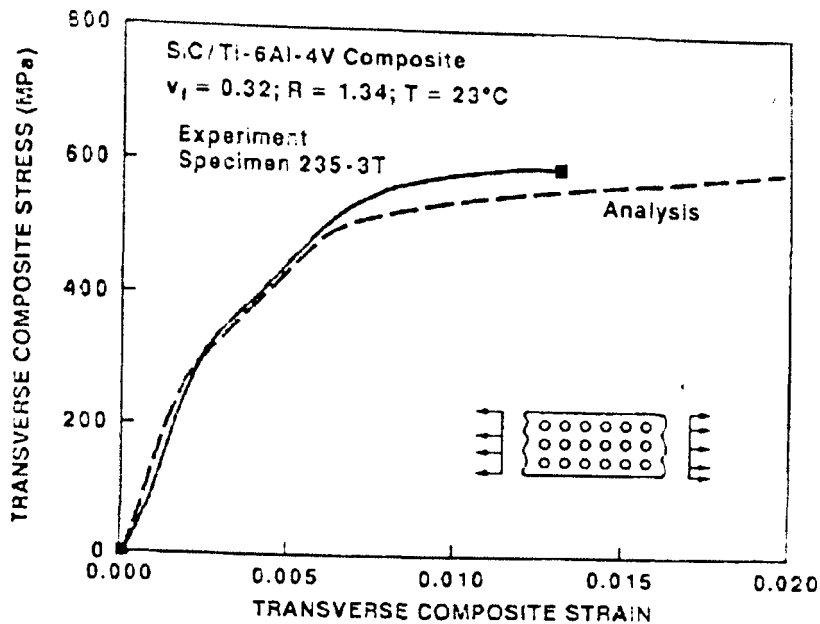


Figure 2.16 Comparison of transverse stress-strain behaviour at room temperature [37]

Li et al. [29] demonstrated the importance of modelling the carbon coating for SCS6 fibre as a separate material phase, unlike Nimmer's model. The carbon coating affects the transverse tensile behaviour and residual stress. However, the exact material properties for the carbon coating are not known. It is reported in [5] that the carbon coating consists of 65% carbon and 35% SiC, so Li estimated the carbon coating properties by weighting the contributions of carbon and SiC. This is supported by the evidence from chemical composition profiles that both carbon and SiC on the carbon coating exist throughout. The SiC is assumed to be isotropic and the carbon is transversely isotropic, therefore, the resultant properties for the carbon coating are also transversely isotropic.

It was found that the CTE of the carbon coating is highly anisotropic, which have CTE of $18.7 \times 10^{-6}/^\circ\text{C}$ and $4.1 \times 10^{-6}/^\circ\text{C}$, at radial direction and axial/hoop directions, respectively. Hence, as the composite cools from the processing

temperature, large compressive residual stress is developed at the axial and hoop direction. Due to the very high CTE at the radial direction, the residual stress is reduced significantly, which results in early debonding under transverse loading. The FE model shows that the compressive radial stress at the interface is reduced by 10~20% at 0° to the loading direction, as a result of the presence of the carbon coating. It was also found that the interface failure initiated at the interface between the fibre and coating under transverse loading. The maximum principal stress criterion is used by Li to determine the interface failure.

Xie et al. [34] attempted to model the transverse tensile and longitudinal shear response of TiMMC using the RVE. The interface is treated as an independent phase with its own material properties. It is assumed that the interphase layer has the same modulus and CTE as the matrix, but the strength is taken as a percentage K of the matrix; 1%, 35% and 100% were used for K . It demonstrated that, the strength of interface has a significant effect on the transverse tensile and longitudinal shear responses. Comparing with the experimental results from a transverse tension test from the literature, Xie showed that interface strength with 35% of matrix strength gives good correlation.

2.7 Summary

Due to the superior properties of TiMMC compared to the monolithic material and conventional aerospace steels, it has become one of the strong candidates for aeroengine applications. Its temperature capability and low density proved to be beneficial, which enable designers to optimize the TiMMC technology, to develop low emission and efficient aeroengine. However, prior to the current

study, very little research has been carried out to characterise the torsional behaviour of TiMMC for shaft applications. Nonetheless, the findings from this project proved to be valuable, which will attract more interest in this field.

Various titanium alloys reinforced with SiC fibres have been presented, which show the vast variety of TiMMC systems available currently. Furthermore, the significant amounts of research carried out by various researchers enable the author to have an insight of each TiMMC system. The advancement of manufacturing routes results in better quality TiMMC component, as this material is very sensitive to any damage prior of loading, which will significantly reduce its performance.

As the fundamental studies of this material, coupon specimens are often used, where TiMMC with different fibre orientation is tested under uniaxial loading. It is well known that the material remains strong in the longitudinal fibre direction. Hence, research has concentrated on understanding the transverse behaviour, which is the weakest when loading in this direction. With this knowledge, further characterisation of the material subjected to multiaxial loading can be carried out. To the author's best knowledge, only Lissenden and co-workers have published the results of investigations to understand the torsional behaviour of TiMMC using unidirectional and cross-ply laminate tubular specimens. The findings from Lissenden et al. are beneficial to this project.

Not only is the macroscopic behaviour important, the interaction between the constituent materials, especially those at the interface, proved to be vital to the material behaviour. Thermal residual stress is created during the cool down of the composite from the processing temperature, due to CTE mismatch between

the fibre and matrix. The large compressive radial stress at the matrix, act as a clamping force, which delays the interface debonding under transverse loading. However, residual stress relaxation leads to early debonding at lower stress and strain.

Modelling at a micromechanics level using RVE is very popular among researchers. Again, modelling of TiMMC under transverse tensile loading is the major scope, due to its weakness in this direction. Interface elements and contact elements have been used to simulate the debonding process using FE method. It is also important to model each constituent material, such as the coating and reaction zone, as independent phases. However, due to the lack of material properties, estimated values were used and compared with the experimental results.

To realize TiMMC technology in an aeroengine for shaft applications, not only does it need to resist the torque load, but also the axial and bending loads. Hence, a complete understanding is necessary, but it is not available from the literature. This thesis forms a basis for characterising the torsional behaviour of TiMMC shafts.

CHAPTER 3

EXPERIMENTAL RESULTS

3.1 Introduction

This chapter describes the experimental work on torsional test of MMC tubular specimens. The areas covered include, design and manufacture of the specimens, inspection and instrumentation, and testing of the specimens. Test results for each specimen will be presented in this chapter which will be used to validate the finite element models described in detail in Chapter 5.

Design of the specimens and VITAL phase 1 test matrix are also presented. In order to facilitate the testing, various coupling components were designed and manufactured to fit the specimen onto the shaft test rig. Most of the specimens were inspected using X-Ray method, CT Scan (Computerised Tomography Scan) to quantify if defects existed in the specimens prior to testing. The inspections also allow accurate information of the location of MMC core layer and thicknesses of inner and outer cladding. Then, a decision can be made on the size of bore based on this information, where the machining work will not damage the fibres. The measurement on cladding and MMC thicknesses are also used to calculate the effective MMC shear modulus. Each specimen is then instrumented with electrical resistance strain gauges before the test.

The shaft test rig and load profile used during the test will be described. The major aims of the test program were to obtain the effective shear modulus, ultimate shear strength of MMC and the shear stress vs. shear strain curves for the MMC layer of each specimen. The specimens were tested at both room

temperature and 350°C; the latter being the temperature identified by VITAL partners for the operation of the LP shaft. The strain measured from the test was corrected for strain gauges' transverse sensitivity to obtain accurate results. This correction was necessary as the specimens experienced biaxial strain fields under pure torsion.

3.2 Design of Specimens

Initially, the combination of fibre and matrix that was to have been used within VITAL was Ti-6-4 reinforced with Sigma SM2156 fibre. However, after a few discussions with Roll-Royce and QinetiQ, it was decided to substitute the fibre with SCS6 fibre which is developed by Textron Specialty Material. This was because SM2156 fibre was not fully developed. SCS6 fibre was readily available and has been in the market for decades.

Under work package 5.2 in VITAL, the test program is divided into 3 phases. Phase 1 and Phase 2 consists of 21 lab-scale tube specimens, of which 13 were for monotonic torsion test and the remaining for fatigue torsion test. Phase 3 consists of 3 buckling specimens, which are larger in size compared to the lab-scale specimens. Finally, a TiMMC demonstrator shaft of 1.2 metres length will be produced to assess the manufacturability.

However, due to delayed delivery of Phase 1 specimens, only the results from VITAL Phase 1 were available for inclusion in this thesis. These specimens have a fibre volume fraction of 35% were tested at either room temperature or 350°C, as per test matrix shown in Table 3.1. The specimens were initially to be manufactured by QinetiQ Ltd, but they decided to sell their TiMMC manufacturing business to a new company named TISICS Ltd. It was the delays

in transferring the manufacturing capability to the new company that caused the delays in supplying the test specimens. The drawings of the shaft tooling used to manufacture the specimens are presented in Appendix A.

Test Reference	Angle (Degree)	Number of Plies	Testing Temperature (°C)
M1	Machined from solid Ti-6-4		20
M2	HIPped solid Ti-6-4		350
UTC1	0	15	20
UTC3	0	13	350
UTC5	±30	12	20
UTC6	-30	13	20
UTC7	+30	13	20
UTC8	±45	12	20
UTC9	-45	13	20
UTC10	+45	13	20
UTC11	±45	12	350
UTC12	-45	13	350
UTC13	+45	13	350

Table 3.1 VITAL phase 1 test matrix

Note that fibres with positive orientations carry tensile loads when torque is applied to the tube. The positive orientations expressed here are measured clockwise to the tube axis as shown in Figure 3.1.

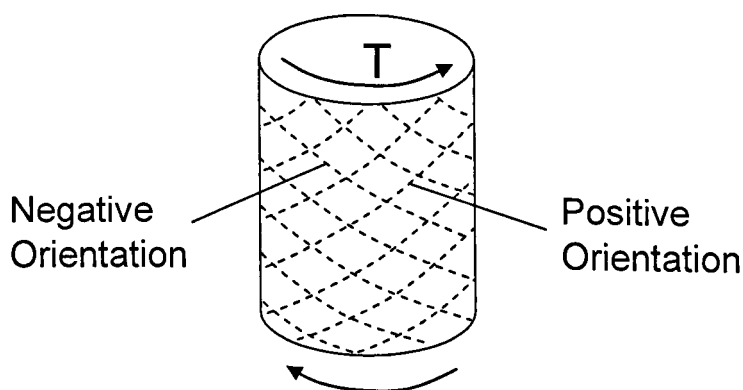


Figure 3.1 Direction of fibre orientation on tube specimen

3.3 Equipment and Testing Method

3.3.1 Test Rig, Specimens and Adapters

The shaft test rig shown in Figure 3.2 used to test the specimens is initially designed for spline specimens. Due to the smaller size of the tube specimens, new adapters and spacers were required to fit the specimen on to the rig. The specimen was positioned at the middle of the stack by connecting it to the adapters and spacers at both ends. The stack was then connected to the cross-head and the rig platform. Note that the material used for the adapters and spacers is high strength steel EN24 with a yield stress of 940 MPa.

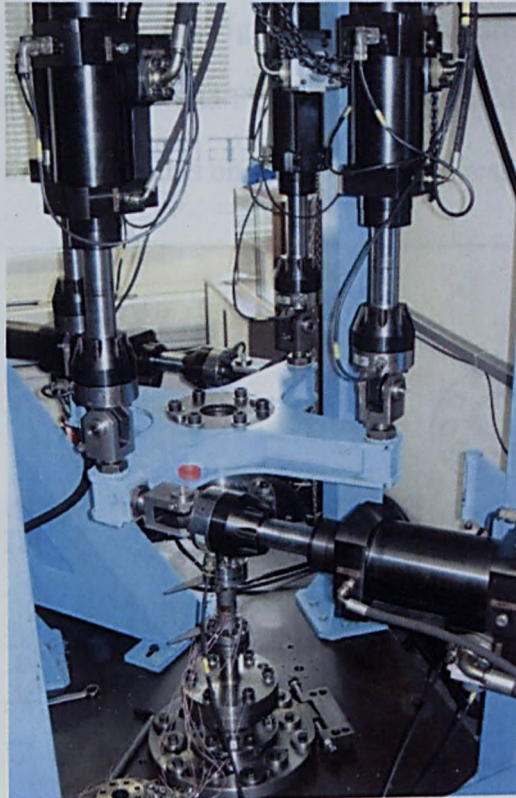


Figure 3.2 Shaft test rig

However, new adapters with different design had to be made in the middle of the test program, as the strength of the specimen was found to be much higher than anticipated. Outer diameter at the plain section of the adapters was increased

from 50mm to 80mm to give it more torque capacity. However, the increase in diameter restricted the use of fitted bolts to connect the specimen to the adapters. It was then decided to use 5 larger blind holes on the adapters, with shear pins to transfer the load from the adapter to the specimen. 5 holes on the specimen flanges were then opened up to match with the new hole arrangement on the adapters. This only applied to UTC7 and UTC8 which had been partially tested with the old adapters. All other specimens were then machined according to the new design.

Figure 3.3 and Figure 3.4 show the drawings of the tube specimen with different flange holes design; Figure 3.5 and Figure 3.6 show the drawings of the adapter with different design; Figure 3.7 and Figure 3.8 show the drawing of the spacer and arrangement of the components on the shaft test rig respectively.

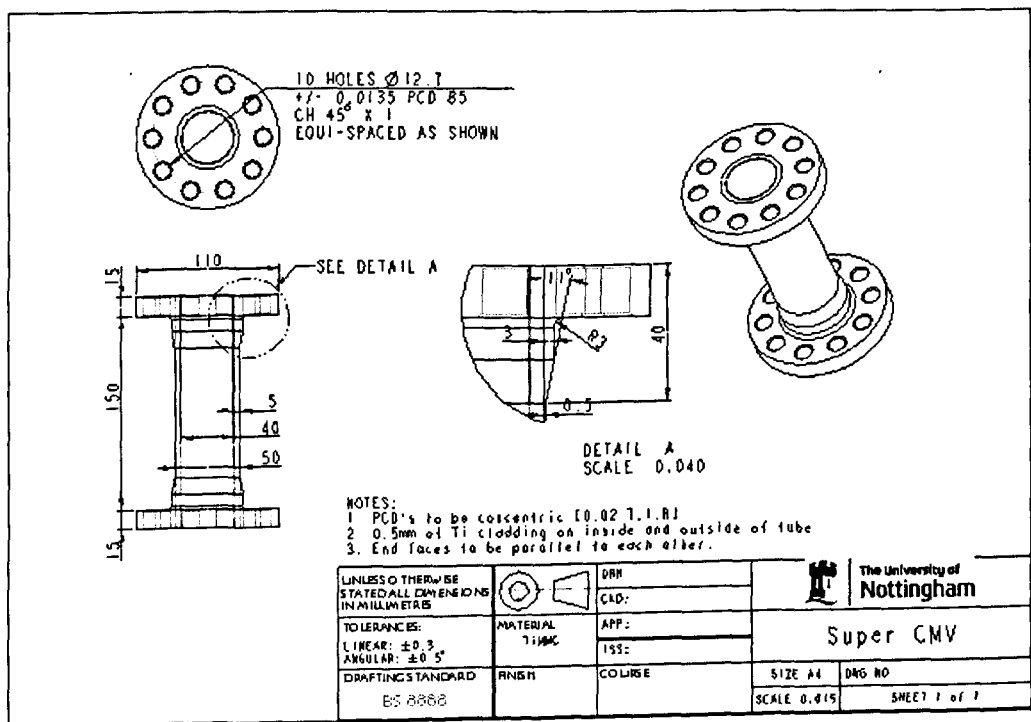


Figure 3.3 Drawing of tube specimen (1st design)

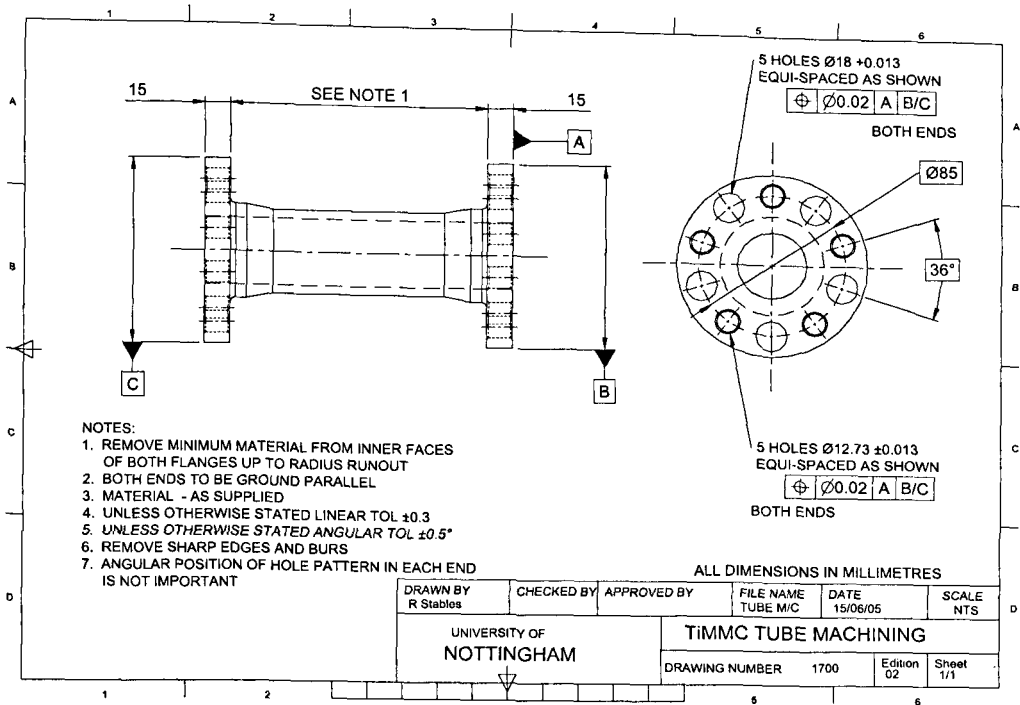


Figure 3.4 Drawing of tube specimen (2nd design)

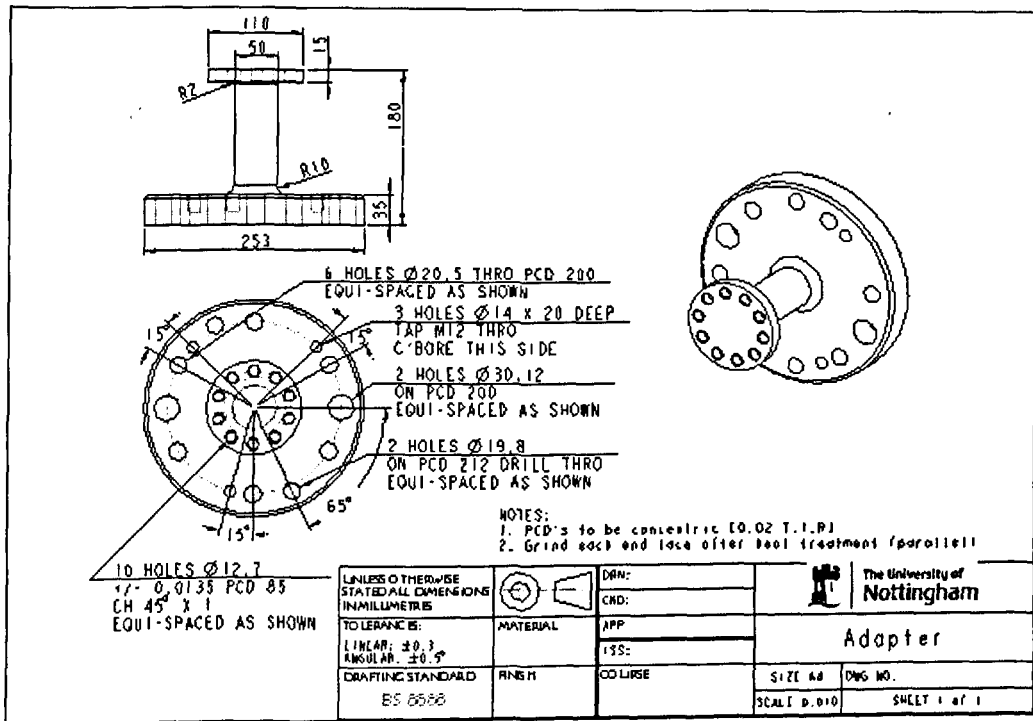


Figure 3.5 Drawing of adapter (1st design)

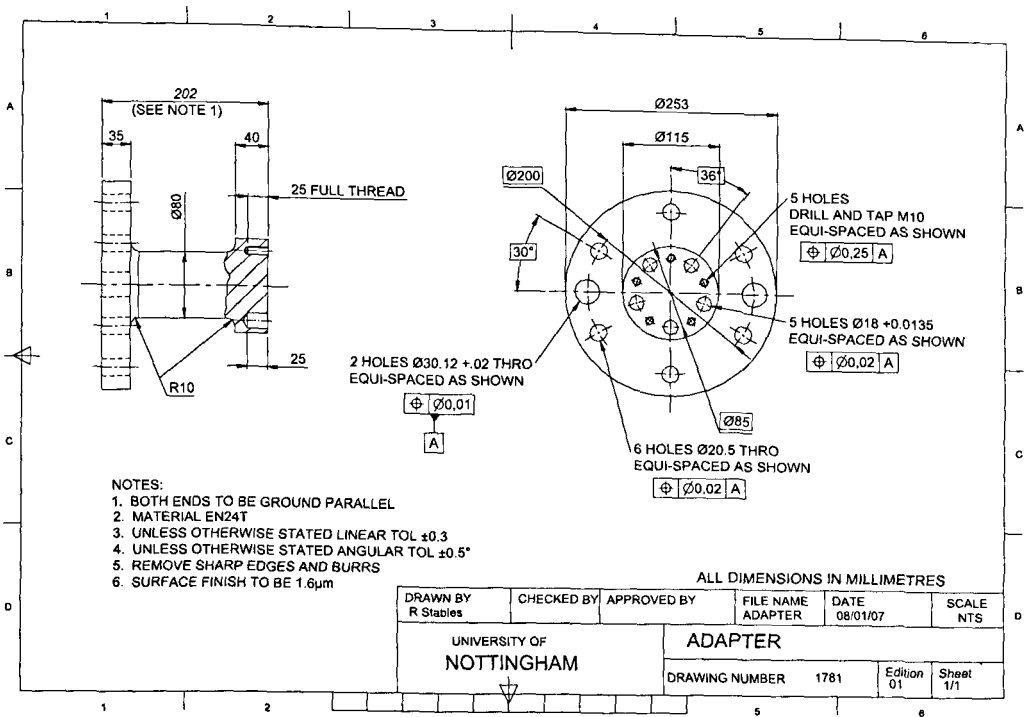


Figure 3.6 Drawing of adapter (2nd design)

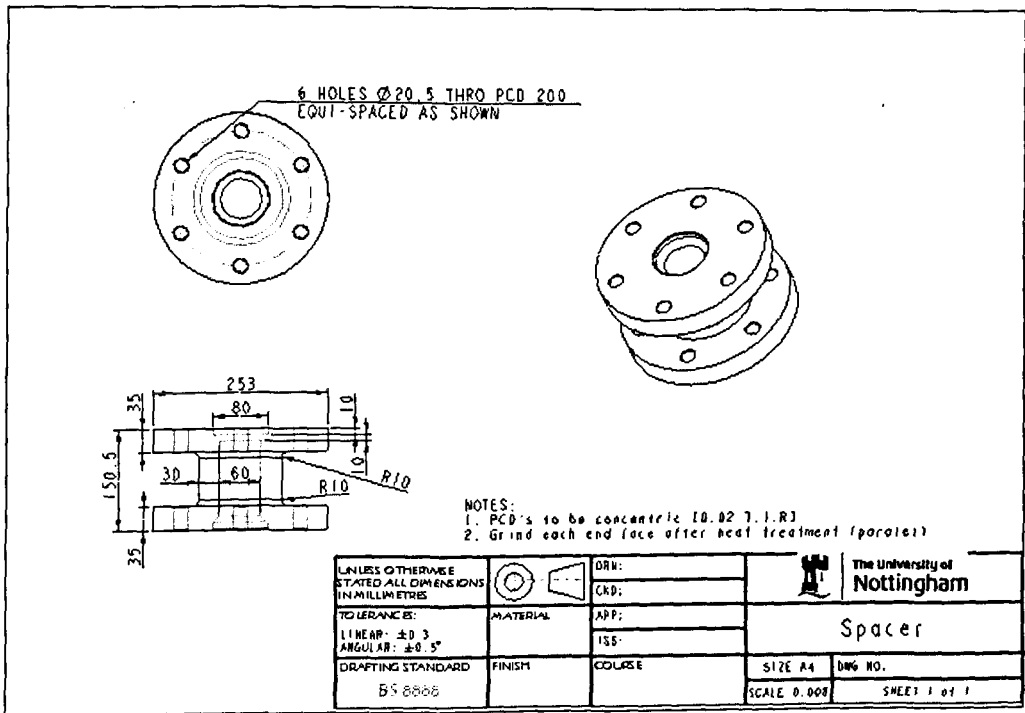


Figure 3.7 Drawing of spacer

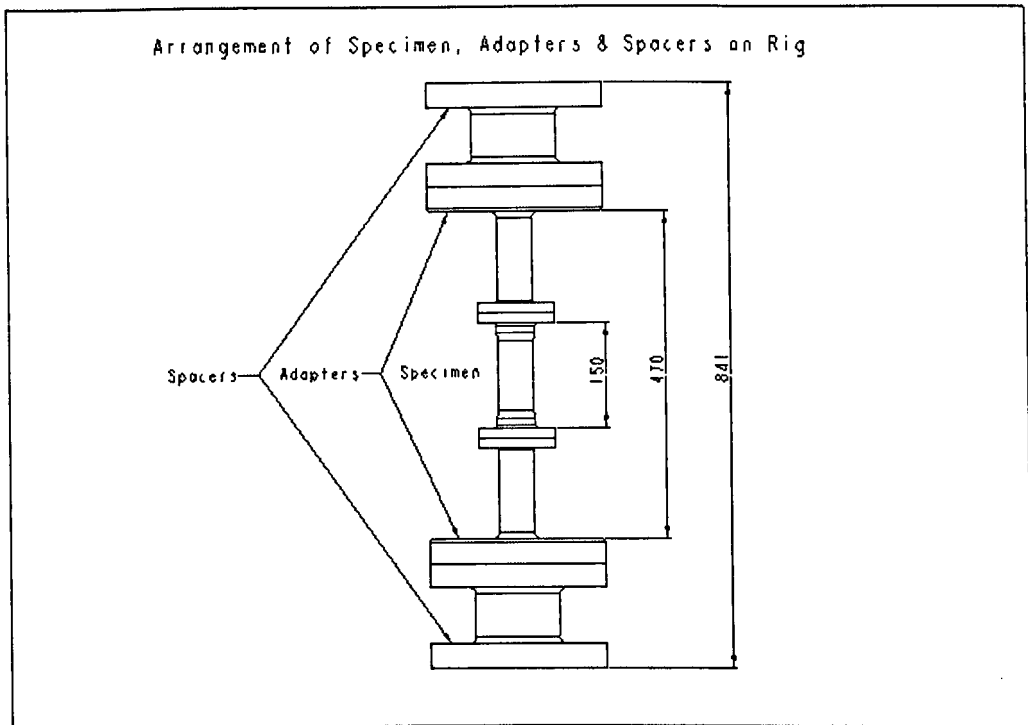


Figure 3.8 Arrangement of components on shaft test rig

3.3.2 Loading Method and Load Pattern

Repeated torsion tests were performed at different load range, in both room temperature and elevated temperature (350°C), using a purpose built shaft test rig shown in Figure 3.2. Repeated torque test from lower load to higher load was applied to the specimen to investigate its shear modulus characteristics at different load range.

The specimen was mounted vertically by connecting it to the adapters and spacers at each end as shown in Figure 3.8. The bottom spacer was fixed to the rig platform and the top spacer was bolted to the cross-head, which was connected to six actuators. Four vertical actuators can be use to provide either axial load or bending moment to the specimen as shown in the schematic diagram Figure 3.9. To provide a torque load, two actuators are connected to the cross-head in the horizontal plane. The rig can apply combinations of

static/alternating torque and axial load and constant/rotating bending moment if required. For the present work, only pure torsion was applied to the TiMMC specimens to investigate their torsional behaviour. The maximum torque load that can be generated by the rig is 20 kNm.

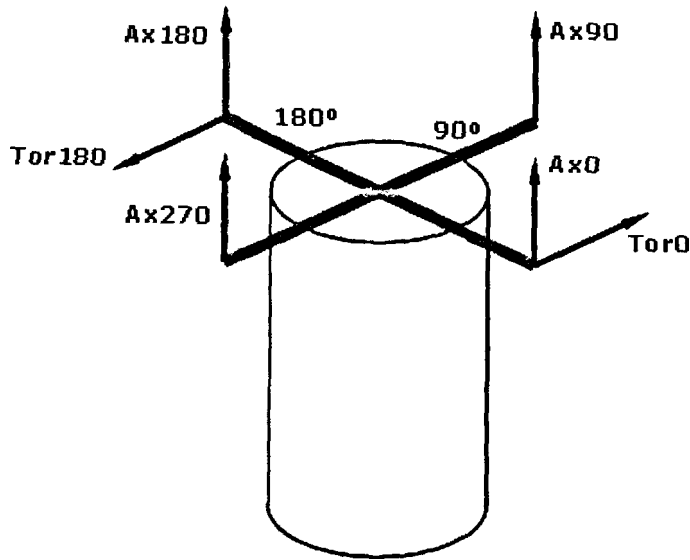


Figure 3.9 Position of actuators at the shaft test rig

The trapezoidal load profile shown in Figure 3.10 was used in the testing program in which a series of loading cycles at different load range were applied. The load was ramped up at a constant rate at 400Nm per second, then held constant for a period of time before ramping it down at the same rate. For each subsequent cycle, an incremental increase in the maximum torque of magnitude 800Nm was applied. In some cases when higher torques were applied, the twist in the specimen continued to increase throughout the hold period. These cycles were repeated with a longer dwell period at peak load to achieve a stable twist before the load increment in next cycle. This procedure was continued until the specimen failed at which time the rig automatically shuts down when the displacement exceed the limit set in the program.

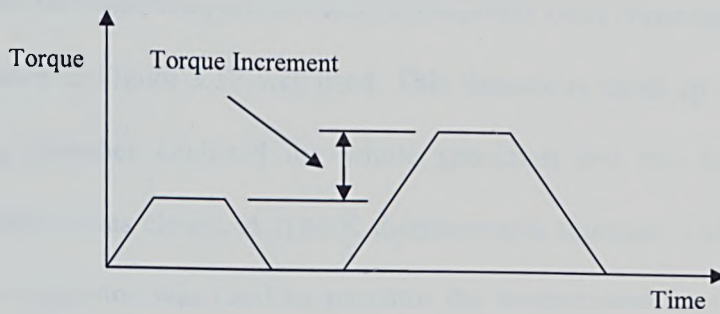


Figure 3.10 Schematic diagram of trapezoidal load profile

3.3.3 Measurements from Tests

Each load cycle during the test produced a file which contained load data from the load cells, displacement data from the Linear Variable Differential Transformers (LVDT) and strain data from the strain gauges. These data were measured and recorded for further analysis.

All of the specimens were instrumented with two sets of three-element rectangular (45 degree) strain gauges rosettes on opposite sides of the specimen as shown in Figure 3.11.

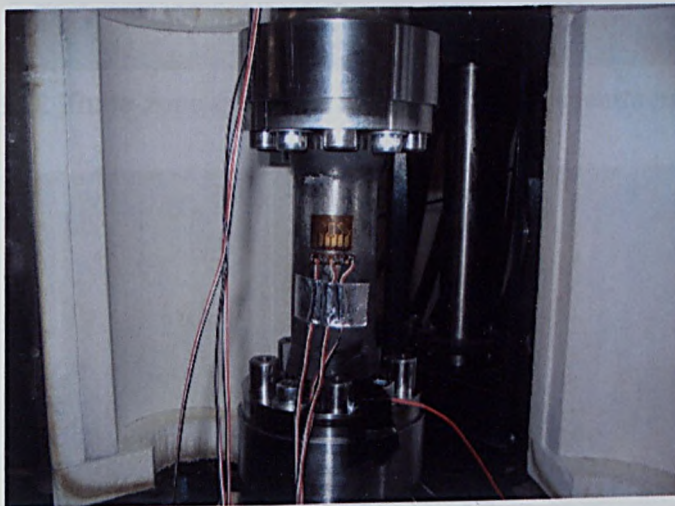


Figure 3.11 Position of strain gauges rosette (UTC10)

To facilitate the high temperature test, a purposed built three-zone split tube furnace shown in Figure 3.12 was used. This furnace is rated up to 750°C and the heating chamber enclosed the whole specimen and the flanges of the adapters when it was closed. A type-K thermocouple together with a hand-held temperature indicator was used to measure the temperature on the specimen. Figure 3.13 shows the three-zone temperature controller used to control the temperature at top, centre and bottom zones. The controller has an over-temperature protection where the furnace will automatically shut down once any of the zones exceed the temperature limit set in the over-temperature module.



Figure 3.12 Three-zone split tube furnace with test specimen (UTC3)



Figure 3.13 Three-zone temperature controller with over-temperature protection

3.4 Dimensional Check of Specimens

Monolithic Ti-6-4 tube machined from solid was supplied as per drawing and no further machining work was carried out. However, HIPped monolithic Ti-6-4 tube was supplied with a smaller bore size due to the mandrel used during the HIPping process. The mandrel is essentially the inner cladding and it is part of the finished part. Then, the specimen had its flanges ground parallel to each other and holes were drilled on the flanges. A Coordinate Measurement Machine (CMM) was used to measure the specimen geometry before installation of the strain gauges.

Ideally, each specimen should be X-ray inspected before any machining work. The reason is to avoid machining into the fibres especially when choosing the bore size. The outer diameter of each specimen at the plain section was lightly polished to obtain a better surface finish for bonding the strain gauges.

According to information from QinetiQ, UTC1 was the first tube they made and 16 plies had been laid before the HIPping process. From the experience of unidirectional matrix coated fibres (MCF) TiMMC tubes, normally 1 ply is lost to void removal, hence the total number of MMC plies for UTC1 is 15. As there were many MMC plies at the core, QinetiQ suggested having a smaller bore to avoid damage to the fibre during machining. Therefore, UTC1 had a thicker inner cladding compared to other specimens. X-ray inspection on UTC1 was only carried out after the test to measure the MMC and cladding thicknesses due to unavailability of facility. However, there is some uncertainty about the accuracy of this data because of the deformation during the test. UTC3 had not been X-ray inspected and estimation from QinetiQ regarding the cladding and

MMC thicknesses was used for calculation. UTC1 and UTC3 were specimens from the first batch of VITAL phase 1 test matrix. Specimens UTC2 and UTC4 are for VITAL phase 2 fatigue testing which will not be covered here.

UTC7 was sent to X-Tek Systems Ltd. together with UTC1 for X-ray inspection. However, this specimen was partially tested with the old adapters which were approaching its torque capacity before the specimen failed. No information was supplied by QinetiQ for UTC5 and UTC8. Based on the polished sample at plain section for UTC5, the MMC and cladding thicknesses for this cross-ply specimen was obtained. This information was also used to estimate the section thicknesses for UTC8, as both specimens have cross-ply fibre orientation and were known to have 12 MMC plies. The calculation was based on the assumption of outer diameter of 50mm and inner diameter of 40mm.

Test Ref.	Outer Diameter	Inner Diameter	Outer Cladding Thickness	Inner Cladding Thickness	MMC Thickness
M1	50.00	40.00	-	-	-
M2	50.37	36.16	-	-	-
UTC1	50.00	37.51	0.97	2.37	2.90
UTC3	50.00	40.00	0.50	1.80	2.70
UTC5	50.00	40.00	0.47	2.30	2.23
UTC6	49.75	40.15	0.48	2.04	2.28
UTC7	50.69	40.87	0.49	2.09	2.33
UTC8	50.00	40.00	0.51	2.28	2.21
UTC9	50.40	40.24	0.49	2.38	2.21
UTC10	50.40	40.08	0.49	2.45	2.22
UTC11	49.67	39.73	0.50	2.01	2.46
UTC12	50.03	39.77	0.51	2.13	2.49
UTC13	50.35	39.79	0.47	2.43	2.38

Table 3.2 Geometry of tube specimens

UTC6, UTC9 and UTC10 were sent to X-Tek System Ltd. for X-ray inspection. Measurement on these specimens prior to testing was most accurate. UTC11, UTC12 and UTC13 are the last batch of specimens from TISICS within VITAL

phase 1 test program. Due to time constraints, it was decided not to send these specimens for X-ray inspection. Dimensions of MMC and cladding thicknesses were confirmed after the specimens were tested and sectioned through Scanning Electron Microscope (SEM) imaging.

For specimens which were sent for X-ray inspection, no voids were observed within the material. Thus, the quality of the specimens was good. In general, all specimens from VITAL phase 1 have an outer diameter of 50mm, bore of 40mm and overall length of 180mm except UTC1 which has bore of 37.5mm. X-ray results for UTC7 show a much larger outer diameter and this shows the specimen already distorted after the test. However, this information was used to calculate the effective MMC shear modulus as this is the only information available. Table 3.2 shows the summary of measurement for each specimen.

3.5 Analysis of Test Results

Detailed analysis of the test results will be presented within this section. Basically, two sets of curves which are the torque vs. twist curves and MMC shear stress vs. shear strain curves were plotted. All cycles for a single specimen were plotted in the same graph to see the material behaviour at different load level. Shear strength when a knee was observed on the curves and ultimate shear strength for MMC were calculated from the test results. Furthermore, total twist and shear strain to fracture of the specimens was obtained at the point where fracture occurs. Finally, the effective MMC shear modulus was calculated based on the MMC shear stress vs. shear strain curves.

3.5.1 Torque vs. Twist

Extensive data analysis is required to convert the raw test data to useful test results. First, the torque load is the summation of the output from two torque actuators as shown in equation (3.1). The torque was calculated using the load data from the load cell multiply the length of the moment arm. The length of the moment arm is 0.4m from the centre of the cross-head to the point of acting of the actuator.

$$T_{total} = F_{T_{0^\circ}} \times R_{cross-head} + F_{T_{180^\circ}} \times R_{cross-head} \quad (3.1)$$

Twist value is equal to the linear distance travel by the rams divide by the radius of the cross-head which is 0.4m. However, 0.4m is only valid when the ram is perpendicular to the cross-head. Hence, the perpendicular distance between the centre point of the cross-head and the ram need to be calculated at each point when calculating the actual twist. This actual perpendicular distance will also be used when calculating the torque load. Detailed explanation on how to evaluate the perpendicular distance at any position of the ram is presented in section 3.6.1.

Total twist for the whole stack including the adapters and spacers is the summation of twist induced from both actuators as shown in equation (3.2). The twist from both adapters is subtracted from the total twist to obtain the twist for the specimen using equation (3.3). The section dimensions were taken from Table 3.2. The assumptions made are the twist from the spacers was neglected due to the large cross section and the adapters were within their elastic limit when the specimen failed. The shear modulus for the adapter is 80 GPa and the

length of the section is the length inside both flanges. Note that the length needed to be changed as the later tests used a different design of adapters.

$$\theta_{total} = \frac{S_{T0^\circ}}{R_{cross-head}} + \frac{S_{T180^\circ}}{R_{cross-head}} \quad (3.2)$$

$$\theta_{specimen} = \theta_{total} - 2 \times \frac{TL_{PS}}{G_{adapter} J_{section}} \quad (3.3)$$

3.5.2 MMC Shear Stress vs. Shear Strain

All TiMMC specimens are made up from MMC layer, plus inner and outer titanium cladding. To calculate the MMC shear stress vs. shear strain curve, the effect of claddings need to be subtracted from the measured values. In other words, the mean shear stress and mean shear strain of the MMC layer are required to plot the curve. The following sub-sections explain how these values were calculated.

3.5.2.1 Shear Strain for MMC

To evaluate the shear strain for MMC layer, one needs to understand how the shear strain was obtained from the strain gauge rosettes attached to the specimen. Figure 3.14 shows the three-element rectangular rosette used where three strain gauges orientated at different angle. To evaluate the shear strain, only strain gauges are orientated at 45° and 315° are needed. A positive torque load acts counter-clockwise (viewed from above) at the cross-head. Strain gauges at 315° will experience a positive strain whereas strain gauges at 45° will experience a negative strain. The shear strain is the difference between the strain at 315° and strain at 45° as shown in equation (3.5) or two times the direct strain

from 45° or 315° strain gauges. Further explanation on why the shear strain is two times the direct strain can be found in Appendix B.

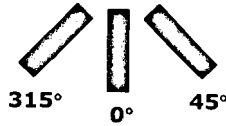


Figure 3.14 Three-element (45 degree) strain gauges rosette

$$\gamma_{OD} = \varepsilon_{315^\circ} - \varepsilon_{45^\circ} \quad (3.5)$$

However, due to the nature of the torque load, a bi-axial stress/strain field was created where the stress transverse to the strain gauges will affect the actual strain at the axial direction. Hence, the measured strain data need to be corrected for strain gauge transverse sensitivity which is presented in detail in section 3.6.2.

For some tests where there are large deformations towards the end of the test, the strain gauges exceed their strain range. Hence, no strain data was recorded beyond this point. To plot the complete shear stress vs. shear strain curves up until failure, the strain results were converted from the twist value of the specimen using equation (3.6). L_{eq} is the equivalent length of the specimen which is used as a variable to adjust the gradient of the stress strain curve. This will ensure it matches up with the gradient of the previous cycle.

$$\gamma = \frac{\theta_{PS} R_o}{L_{eq}} \quad (3.6)$$

Different sections on a MMC tube are shown in Figure 3.15. The twist angle is assumed to be the same for all layers, such that the shear strain varies linearly across the cross section with the maximum at the outer diameter. Therefore, to

calculate the mean shear strain of the MMC layer, equation (3.7) is used. Note that γ_{OD} is the shear strain after correction for strain gauges transverse sensitivity.

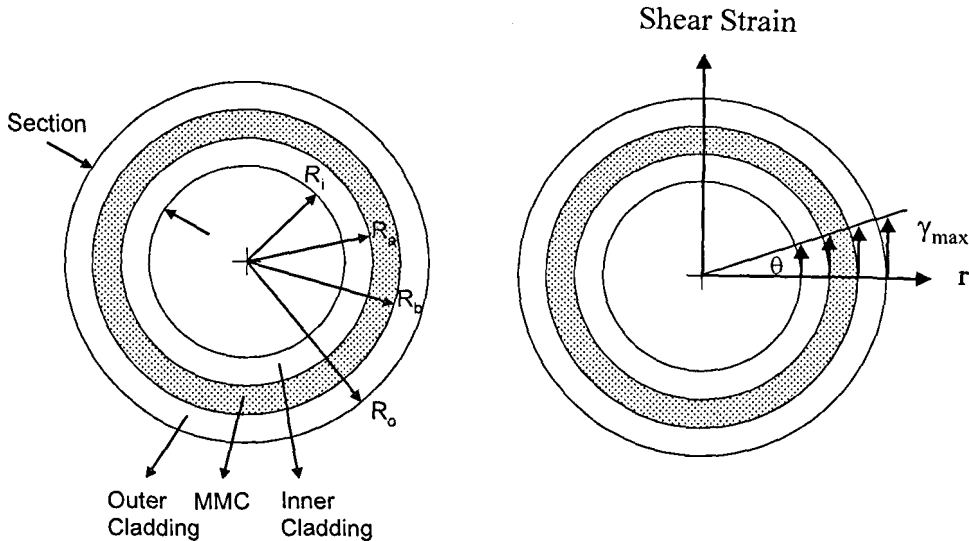


Figure 3.15 Schematic diagram of the cross section of MMC tube

$$\gamma_{MMC} = \frac{R_a + R_b}{R_o} \times \gamma_{OD} \quad (3.7)$$

3.5.2.2 Shear Stress for MMC

The procedure to obtain the mean shear strain was presented in previous section. The mean shear stress for the MMC layer is needed to plot the shear stress vs. shear strain curve. The torque imposed on the specimen and the corrected shear strain from strain gauges were used as the raw data to calculate the mean shear stress for the MMC layer.

The total torque carried by the whole section is the summation of torque carried by the inner cladding, outer cladding and MMC layer as shown in equation (3.8).

The individual torques, T_{inner} , T_{outer} and T_{MMC} are given by equations (3.9) to

(3.11), in which τ_i , τ_o and τ_{MMC} are the mean shear stress of the inner cladding, outer cladding and MMC layer respectively.

$$T_{Section} = T_{MMC} + T_{inner} + T_{outer} \quad (3.8)$$

$$T_{inner} = \int_{R_i}^{R_a} \tau_i (2\pi r) dr \times r \quad (3.9)$$

$$T_{outer} = \int_{R_b}^{R_o} \tau_o (2\pi r) dr \times r \quad (3.10)$$

$$T_{MMC} = \int_{R_a}^{R_b} \tau_{MMC} (2\pi r) dr \times r \quad (3.11)$$

As mentioned earlier, the angle of twist is the same for all section and the shear strain is linear through the section. Given the corrected shear strain measured from the strain gauges γ_{OD} , the mean shear strain for the claddings γ_i and γ_o , can be calculated using equation (3.12) and (3.13) respectively.

$$\gamma_i = \frac{R_i + R_a}{R_o} \times \gamma_{OD} \quad (3.12)$$

$$\gamma_o = \frac{R_b + R_o}{R_o} \times \gamma_{OD} \quad (3.13)$$

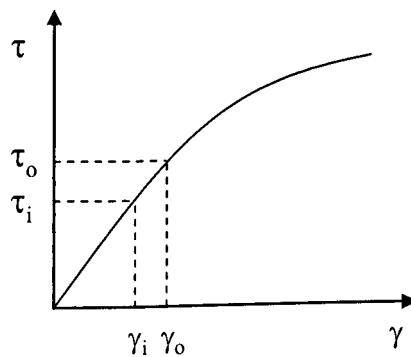


Figure 3.16 Compound shear stress vs. shear strain curve for Ti-6-4

Then, the mean shear stress for the claddings τ_i and τ_o can be obtained from the shear stress vs. shear strain curve for the cladding material. However, repeated torsion test was carried out on monolithic Ti-6-4 tubes M1 and M2 at room temperature and 350°C respectively. Curve fitting was done on the test results for M1 and M2 to give a single compound curve for each temperature. These curves are needed in order to determine the respective mean shear stress for a given mean shear strain for the claddings, as shown in Figure 3.16. The compound curves produced from the monolithic tubes will be presented in section 3.7.1.1 and 3.7.2.1.

With the mean shear stress for the inner and outer claddings, the respective carrying torque for each section can be calculated using equation (3.9) and (3.10). For a given corrected shear strain measured from the strain gauges γ_{OD} , the total torque carried by the whole section can be obtained from the torque vs. shear strain curve as shown in Figure 3.17. Using equation (3.8), the remaining torque carried by the MMC layer can be obtained. Finally, the mean shear stress for the MMC layer was calculated using equation (3.14)

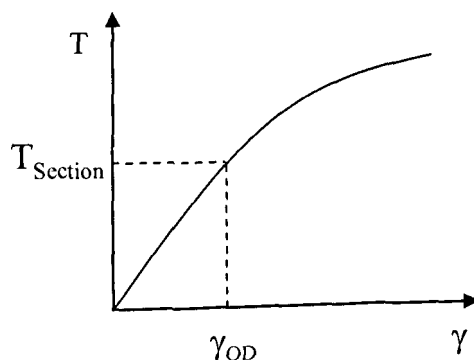


Figure 3.17 Torque vs. shear strain curve

$$\tau_{MMC} = \frac{T_{MMC}}{\int_{r_a}^{r_b} (2\pi r) dr \times r} \quad (3.14)$$

Now, the mean shear stress together with the mean shear strain for MMC layer at a given point is obtained. With this knowledge, the process is repeated at many points on the torque vs. shear strain curve to plot a complete MMC shear stress vs. shear strain curve for a cycle. Then the results from each cycle are plotted in a single graph to compare how the material behaves at different load levels.

3.5.3 Shear Strength at Knee of MMC

Shear strength at knee of MMC was calculated where a knee is observed at the torque vs. twist curve for a particular cycle. The knee is the point where the curve starts to deviate from the linear elastic portion of the curve. The knee occurs when the fibres start to debond from the matrix where additional twist was observed at lower load. Then, the torque load is obtained at this point and the shear strength was calculated.

First, the torque value when the knee observed was obtained from the torque vs. twist curve. The corresponding corrected shear strain at this torque level was obtained and used to calculate the twist at the plain section using equation (3.15). Then, the torque carried by the inner and outer claddings were calculated using equation (3.16) and (3.17) respectively with shear modulus of Ti-6-4. The remaining torque carried by the MMC layer was then obtained using equation (3.18).

$$\theta_{PS} = \frac{\gamma L_{PS}}{R_o} \quad (3.15)$$

$$T_{inner} = \frac{G_{Ti} J_{inner} \theta_{PS}}{L_{PS}} \quad (3.16)$$

$$T_{outer} = \frac{G_{Ti} J_{outer} \theta_{PS}}{L_{PS}} \quad (3.17)$$

$$T_{MMC} = T_{Knee} - T_{inner} - T_{outer} \quad (3.18)$$

Finally, with this torque value, the shear strength at knee of MMC at the outermost ply can be calculated knowing the section geometry using equation (3.19) and (3.20).

$$\tau_{Knee,MMC} = \frac{T_{MMC} R_b}{J_{MMC}} \quad (3.19)$$

$$J_{MMC} = \frac{\pi}{2} (R_b^4 - R_a^4) \quad (3.20)$$

3.5.4 Effective MMC Shear Modulus

The effective MMC shear modulus is calculated using the MMC shear stress vs. shear strain curves. The gradients of the curves at the linear portion, for each cycle before yielding occurs were obtained. The values are then averaged to get the effective MMC shear modulus for that specimen.

3.5.5 Ultimate Shear Strength of MMC

Ultimate shear strength of MMC was calculated using the MMC shear stress vs. shear strain curves. The ultimate shear strength of MMC was determined based on the maximum shear stress imposed on the specimen.

3.6 Correction of Test Results

3.6.1 Actual Torque Load and Twist

As mentioned earlier, to calculate the actual torque and actual twist, the perpendicular distance between the centre point of the cross head and the ram need to be used. The perpendicular distance of 0.4m which is the radius of the cross head is only valid when the ram is at the centre of travel. At other position of the ram, there will be some error and the error will be the greatest when the ram approaching the end of travel. Hence, the perpendicular distance need to be calculated to evaluate the actual torque and actual twist based on the position of the ram. The ram has a travel of +100mm to -100mm and the centre point 0mm indicated by the LVDT is the point where the perpendicular distance is 0.4m. Figure 3.18 shows a schematic diagram of the plan view of cross head and the position of rams. It clearly illustrates a different perpendicular distance when the ram is at different positions.

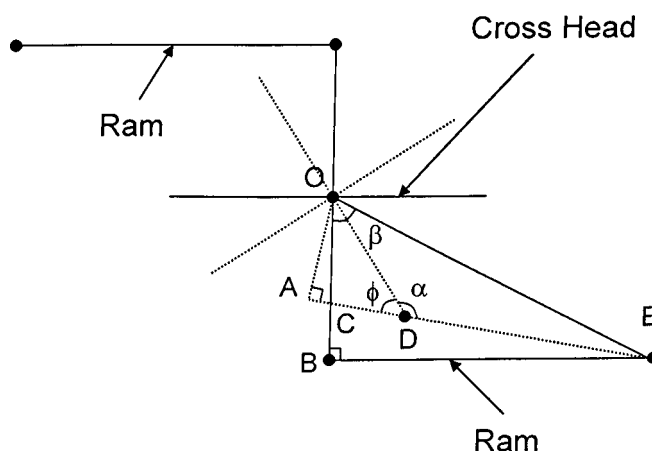


Figure 3.18 Schematic diagram of plan view of cross head and rams

First, length OE is calculated using equation (3.25) where OB is 0.4m and BE is 0.9375m. If the ram is not at its centre point of travel, the perpendicular distance

become OA instead of OB. To calculate length OA, angle ϕ need to be calculated. Angle α can be calculated using equation (3.26) where OD remain 0.4m and DE is the length based on the position of the ram. If the LVDT indicate a reading of 50mm, which the ram retract a distance of 50mm, this mean DE equal to BE minus 50mm. With angle α , angle ϕ can be calculated using equation (3.27). Finally, the perpendicular distance (OA) is calculated using equation (3.28). Thus, the actual torque and actual twist can be calculated using this perpendicular distance where it depends on the position of the rams.

$$OE = \sqrt{OB^2 + BE^2} \quad (3.25)$$

$$\alpha = \cos^{-1} \frac{DE^2 + OD^2 - OE^2}{2 \times DE \times OD} \quad (3.26)$$

$$\phi = 180^\circ - \alpha \quad (3.27)$$

$$OA = \sin \phi \times OD \quad (3.28)$$

3.6.2 Strain Gauge Transverse Sensitivity

The simplest way to calculate the shear strain is to take the difference in strain between strain gauges orientated at 45° and 315° . However, as mentioned earlier, the bi-axial stress/strain fields experienced by the strain gauges during the torque load will create a more complex strain output at the strain gauges. The indicated strain is no longer the actual strain and need to be corrected for strain gauges transverse sensitivity. The corrections are based on the technical notes TN509 from Vishay Measurements Group which is titled “Errors due to transverse sensitivity at strain gauges”.

According to the technical notes, errors in indicated strain due to transverse sensitivity are generally small. However, in bi-axial stress/strain fields characterized by extreme ratios between principal strains, the percentage error in the smaller strain can be very great if not corrected for transverse sensitivity. On the other hand, in the particular case of uniaxial stress in a material (steel) with a Poisson's ratio of 0.285, the error is zero because the gauge factor given by the manufacturer was measured in such a uniaxial stress field and already includes the effect of the Poisson strain. It is important to note that when a strain gauge is used under any conditions other than those employed in the gauge-factor calibration, there is always some degree of errors due to transverse sensitivity. In this case, where the strain gauges were used in a different material, it will exhibit transverse sensitivity error which may require correction.

Equations (3.29), (3.30) and (3.31) were used to calculate the actual strain at each channel from the measured strain. Note that the Poisson's ratio, ν_0 and the transverse sensitivity coefficient, K_t are 0.285 and -4.3%, respectively, as quoted by the manufacturer. The corresponding channel number to each strain gauge on the three-element rosette is illustrated in Figure 3.19. Hence, the actual shear strain is the difference between corrected strain value of channel 1 and channel 3 which shown is in equation (3.32).

$$\varepsilon_1 = \frac{1 - \nu_0 K_t}{1 - K_t^2} (\hat{\varepsilon}_1 - K_t \hat{\varepsilon}_3) \quad (3.29)$$

$$\varepsilon_2 = \frac{1 - \nu_0 K_t}{1 - K_t^2} [\hat{\varepsilon}_2 - K_t (\hat{\varepsilon}_1 + \hat{\varepsilon}_3 - \hat{\varepsilon}_2)] \quad (3.30)$$

$$\varepsilon_3 = \frac{1 - \nu_0 K_t}{1 - K_t^2} (\hat{\varepsilon}_3 - K_t \hat{\varepsilon}_1) \quad (3.31)$$

$$\gamma = \varepsilon_1 - \varepsilon_3 \quad (3.32)$$

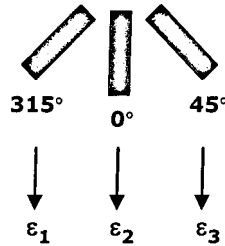


Figure 3.19 Three-element (45 degree) strain gauges rosette and the corresponding channel number

3.7 Test Results

The experimental results are presented in this section. The geometry of each tube specimen is summarized in Table 3.2 based on the estimation from QinetiQ or X-ray measurements. For specimens which have not been sent for X-ray measurement, the thicknesses for each section were confirmed through the SEM images of the tested samples. Material properties such as effective MMC shear modulus, ultimate shear strength and shear strength at knee of MMC are obtained from each test. Shear strain to fracture and total twist of the specimen at failure were also obtained to evaluate the ductility. A comprehensive failure investigation for tested specimens was carried out for each specimen and the results will be presented in Chapter 4.

3.7.1 Room Temperature Tests

This section describes the following test results.

Section	Specimen	Description
3.7.1.1	M1	Machined from Solid Ti-6-4
3.7.1.2	M2	HIPped Solid Ti-6-4
3.7.1.3	UTC1	0° Fibre Orientation
3.7.1.4	UTC5	±30° Fibre Orientation
3.7.1.5	UTC6	-30° Fibre Orientation
3.7.1.6	UTC7	+30° Fibre Orientation
3.7.1.7	UTC8	±45° Fibre Orientation
3.7.1.8	UTC9	-45° Fibre Orientation
3.7.1.9	UTC10	+45° Fibre Orientation

Table 3.3 Room temperature tests

3.7.1.1 Monolithic 1 (Machined from Solid Ti-6-4)

This specimen with test reference M1 was machined from Ti-6-4 extruded bar stock. Actual dimension of the specimen was measured using CMM and the measurement agreed well with the required dimension as per drawing.

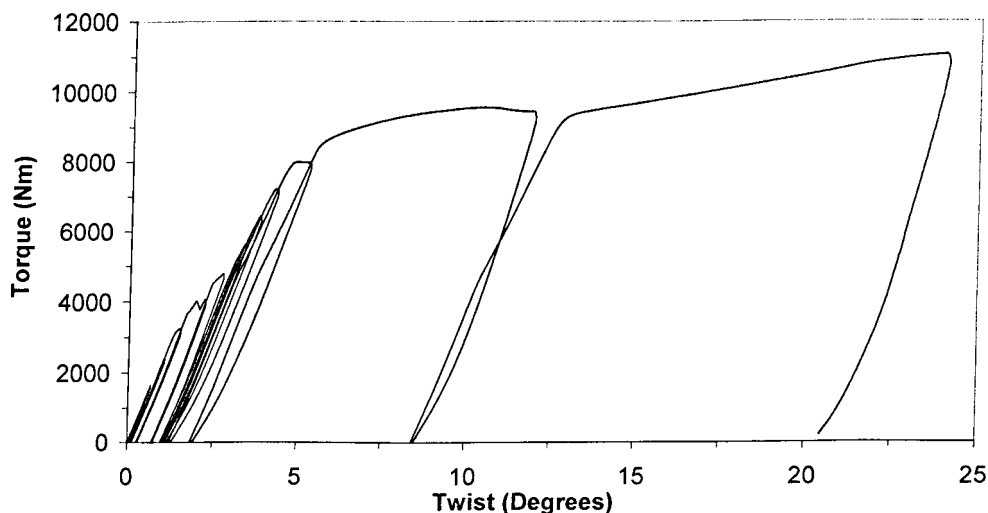


Figure 3.20 Torque vs. twist curves for M1

The torque vs. twist curves are shown in Figure 3.20. Note that apparent knees on the curves were observed at lower load. These were due to slip between the

specimen and the adapters. In later tests, the specimen was pre-load to remove the slip between the specimen and the adapters before applying the repeated torque load. They were not present in Figure 3.21.

According to the datasheet from IMI, Ti-6-4 will start to yield at a shear stress level around 530 MPa or a torque of 7781 Nm for this specimen.

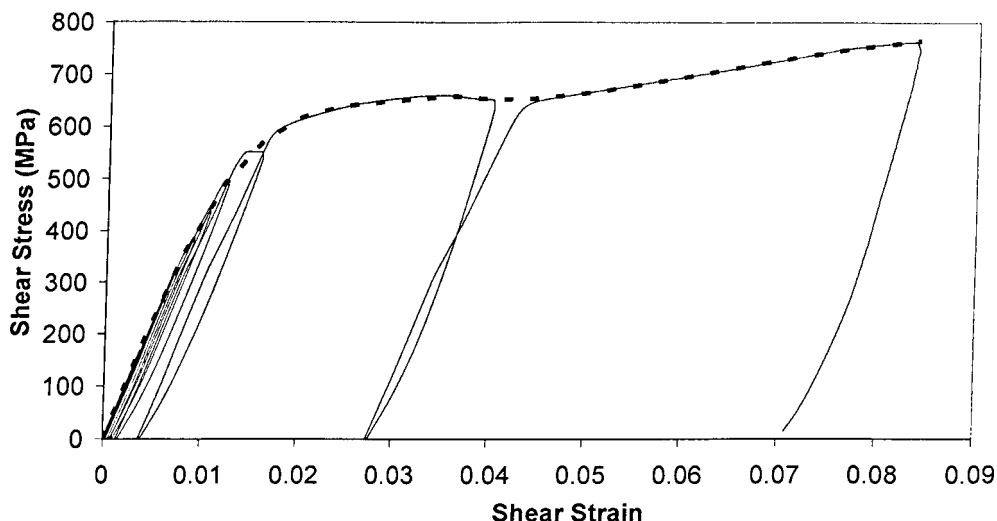


Figure 3.21 Shear stress vs. shear strain curves for M1

The dotted curve shown in Figure 3.21 is the compound curve used to determine the mean shear stress for the cladding material for a given mean shear strain. This is needed when evaluating the MMC shear stress vs. shear strain curve.

As seen from the test results, the specimen started to yield at a torque of approximately 8 kNm. Then, significant yielding occurred in the last two cycles where the load exceeds the elastic limit of the material. The material hardened as the load increased in subsequent cycles. The test is stopped as the torque actuators ran out of travel and it is decided to conclude the test at this point. The calculated averaged shear modulus is 46.4 GPa which is very similar to the value of 46 GPa quoted by IMI. The proof shear strength calculated is 497 MPa compare to the yield strength of 530 MPa quoted by IMI. The ultimate shear

strength is 763 MPa based on the maximum torque imposed on the specimen. The maximum torque applied on this specimen is approximately 11.1 kNm. Total twist on the specimen is 20.46° which shows great ductility.

3.7.1.2 Monolithic 2 (HIPped Solid Ti-6-4)

This specimen with test reference M2 is a monolithic Ti-6-4 specimen, which was manufactured through the HIPping process as used for the TiMMC specimen. This specimen was used as a benchmark to evaluate the material properties of the base material. The effect of HIPping to the material properties was also investigated. As mentioned earlier, the bore size of this specimen is slightly larger compare to other specimens. This is because of the Ti-6-4 mandrel used during the HIPping process, which form as a part of the specimen at the finished state.

Repeated torsion tests were applied to this specimen at room temperature to evaluate its shear modulus. The load level applied is below the Ti-6-4 elastic limit. The calculated averaged shear modulus is 44.1 GPa which is 5% lower than the shear modulus of the solid Ti-6-4 specimen. This is due to the smaller grain size in the microstructure as a result of the HIPping process. This is justified through the microstructure studies of the specimen which will be presented in Chapter 4. After the shear modulus characterization at room temperature, the specimen was tested to failure at 350°C.

3.7.1.3 UTC1 (0° Fibre Orientation)

This specimen with test reference UTC1 is a MMC tube with 0° fibre orientation. There are 15 MMC plies at the core layer, which is the thickest of all

specimens. The dimensions of the cross sections were estimated by QinetiQ which will be used for calculation. Repeated torsion test was carried out at room temperature.

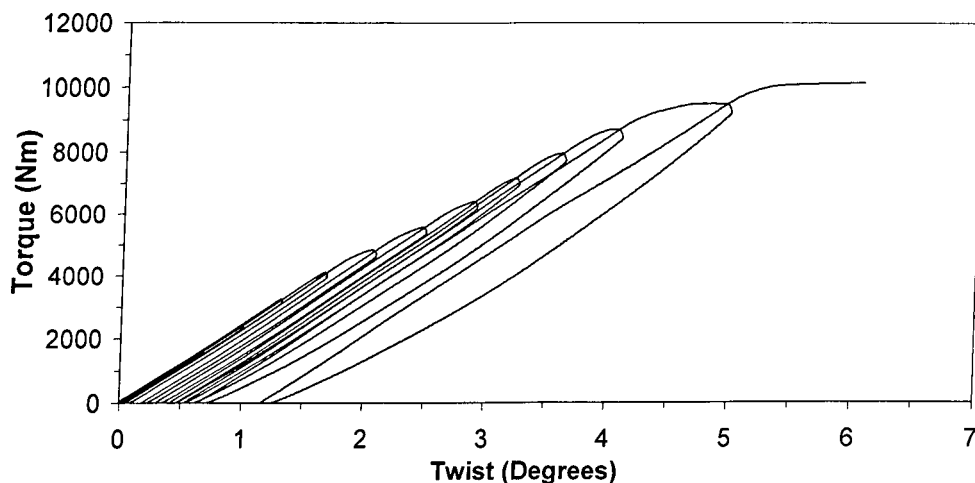


Figure 3.22 Torque vs. twist curves for UTC1

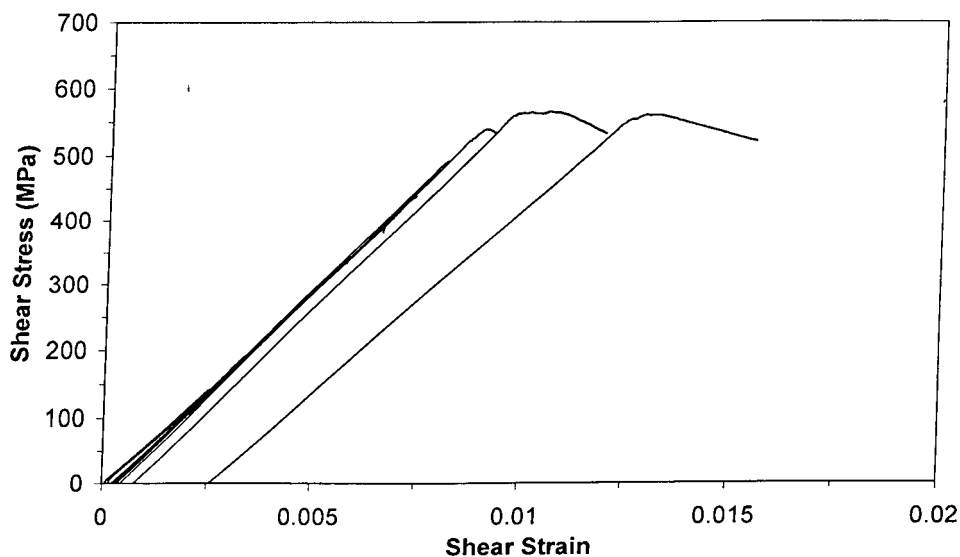


Figure 3.23 MMC shear stress vs. shear strain curves for UTC1

Figure 3.22 and Figure 3.23 show the test results of UTC1. Initial knee on the torque vs. twist curve was observed around 4.8 kNm and this is where the fibres start to debond from the matrix. The calculated shear strength at knee of MMC is 329 MPa. The specimen starts to yield significantly at the last two cycles where

the load already exceeds its elastic limit. The calculated ultimate shear strength for MMC is 564 MPa based on the maximum torque applied of 10.1 kNm. Calculated effective MMC shear modulus for UTC1 is 62.8 GPa. Total twist on the specimen at ultimate load is 6.06° and the shear strain to fracture is 1.72%.

The MMC shear stress vs. shear strain curves clearly shows a significant strain accumulation at the last two cycles. Note that at the last two cycles, the MMC shear stress is dropping but the strain is increasing during the constant torque phase. This is because the cladding can carry higher stress at these increased strain levels as seen from the compound curve. Hence, the torque/stress carried by the MMC drops. Similar phenomenon was observed on MMC shear stress vs. shear strain curves for other specimens.

3.7.1.4 UTC 5 ($\pm 30^\circ$ Fibre Orientation)

This specimen with test reference UTC5 is a MMC tube with $\pm 30^\circ$ fibre orientation. There are 12 MMC plies at the core layer and the dimensions of the cross sections were obtained through SEM on the polished sample. Repeated torsion test was carried out at room temperature.

Figure 3.24 and Figure 3.25 show the test results of UTC5. Initial knee on the torque vs. twist curves was observed around 4.5 kNm and the calculated shear strength at knee of MMC is 367 MPa. Micro yielding was observed once the fibres started to debond from the matrix. Beyond the torque level of 9 kNm, a more significant yielding of specimen was observed up until failure. Due to the torque holding period is not long enough in the last few cycles, the specimen was reloaded once more at the same target peak load. The calculated ultimate shear strength for MMC is 1027 MPa based on the maximum torque applied of

13.3 kNm. Calculated effective MMC shear modulus for UTC5 is 67.3 GPa. Total twist on the specimen at ultimate load is 10.62° and the shear strain to fracture is 3.01%.

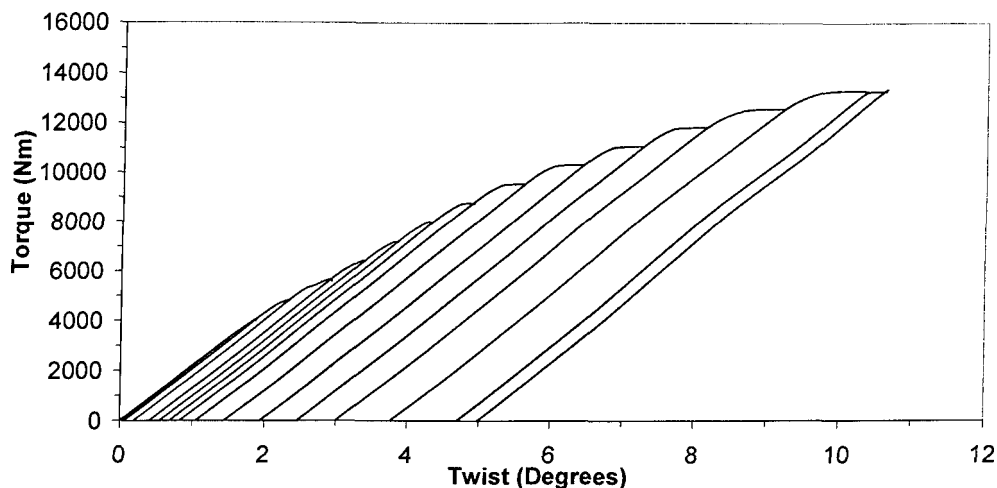


Figure 3.24 Torque vs. twist curves for UTC5

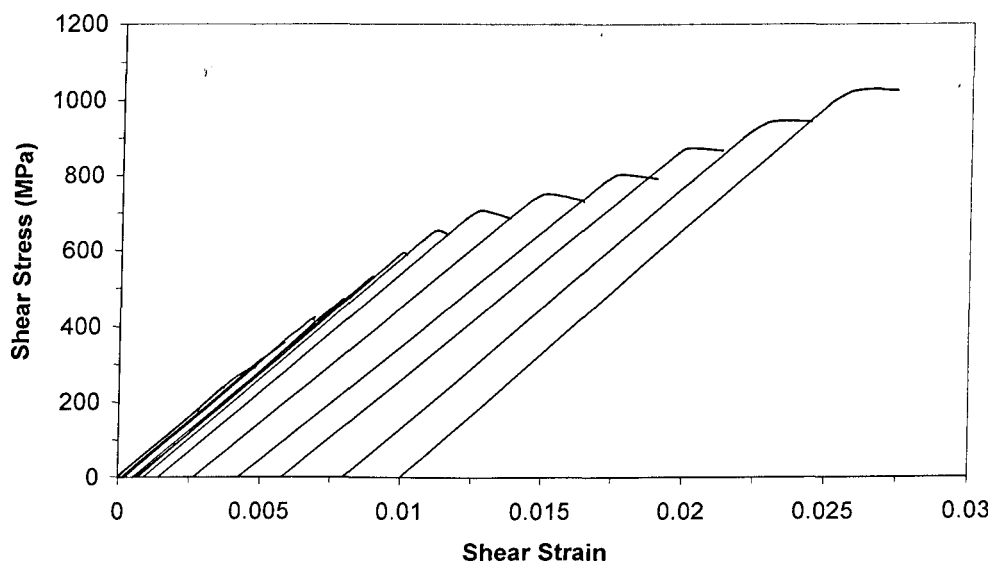


Figure 3.25 MMC shear stress vs. shear strain curves for UTC5

3.7.1.5 UTC 6 (-30° Fibre Orientation)

This specimen with test reference UTC6 is a MMC tube with -30° fibre orientation. There are 13 MMC plies at the core layer and the dimensions of the

cross sections were obtained through the X-ray measurements. Repeated torsion test was carried out at room temperature.

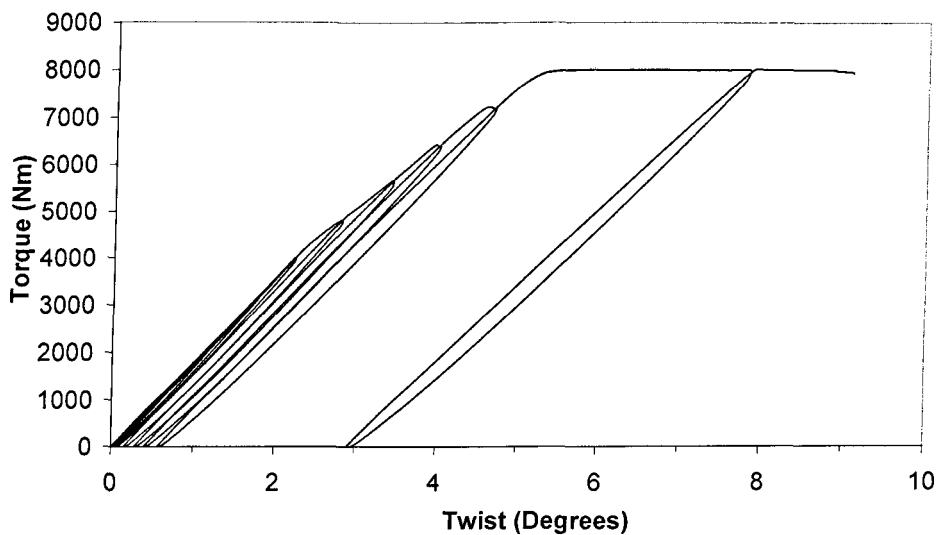


Figure 3.26 Torque vs. twist curves for UTC6

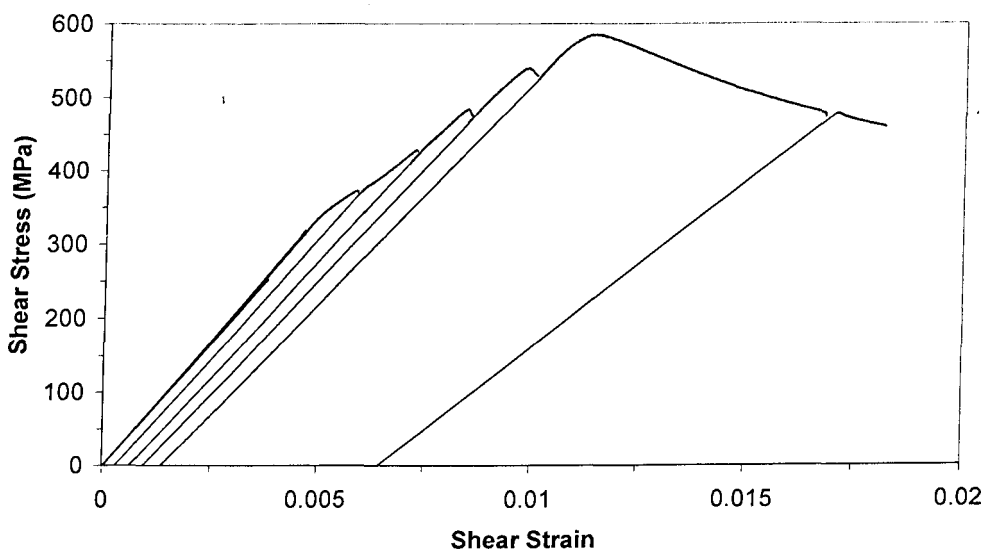


Figure 3.27 MMC shear stress vs. shear strain curves for UTC6

Figure 3.26 and Figure 3.27 show the test results of UTC6. Initial knee on the torque vs. twist curves was observed around 4.4 kNm and the calculated shear strength at knee of MMC is 385 MPa. Similar to the $\pm 30^\circ$ fibre orientation, micro yielding was observed once the fibres debonded from the matrix.

Significant yielding only observed in the last two cycles. The final cycle has the same target peak load as the penultimate cycle. The calculated ultimate shear strength for MMC is 586 MPa based on the maximum torque applied of 8 kNm. Calculated effective MMC shear modulus for UTC6 is 68.4 GPa. Total twist on the specimen at ultimate load is 9.08° and the shear strain to fracture is 2.09%.

3.7.1.6 UTC 7 (+30° Fibre Orientation)

This specimen with test reference UTC7 is a MMC tube with +30° fibre orientation. There are 13 MMC plies at the core layer and the dimensions of the cross sections were obtained through the X-ray measurements. Repeated torsion test was carried out at room temperature. Note that this specimen was not tested to failure at the first test due to the adapters approaching its torque capacity. The flange holes of the specimen is then modified to suit the new adapters before loaded to failure.

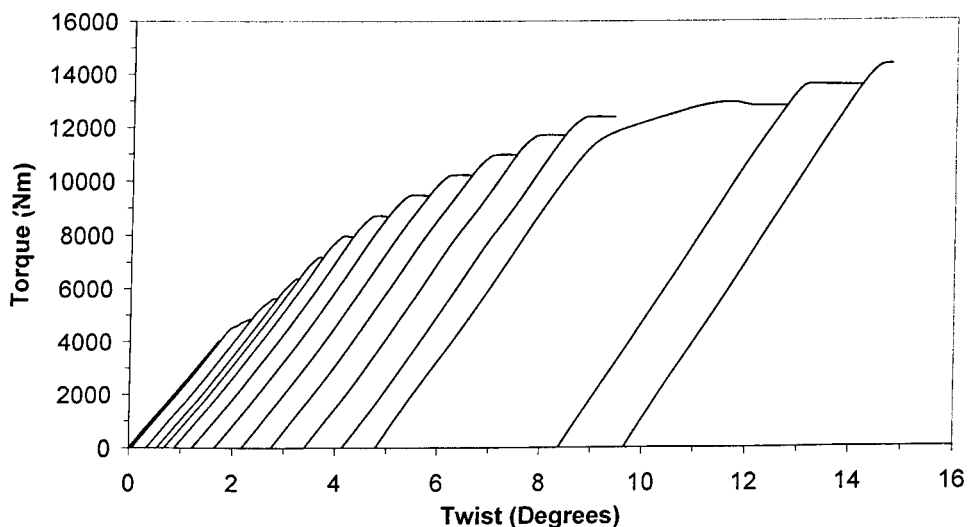


Figure 3.28 Torque vs. twist curves for UTC7

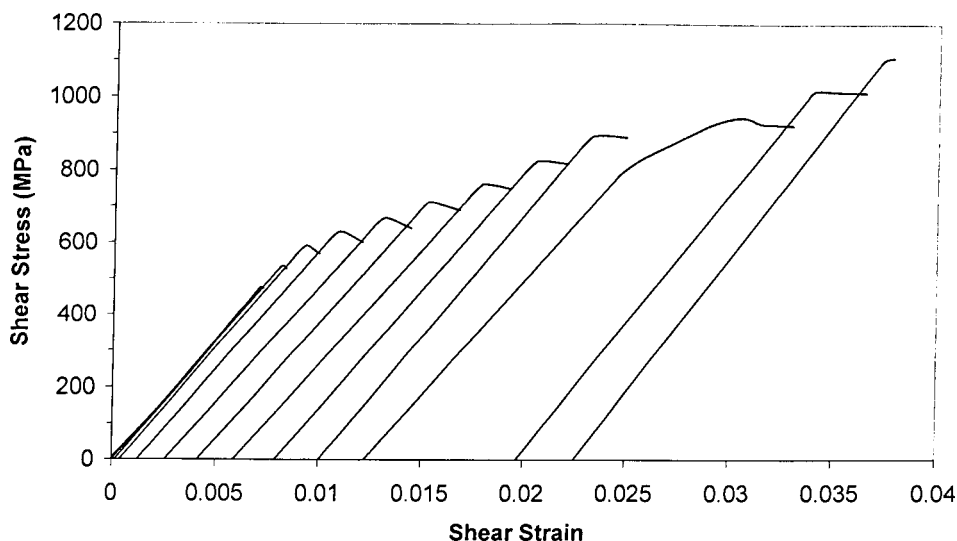


Figure 3.29 MMC shear stress vs. shear strain curves for UTC7

Figure 3.28 and Figure 3.29 show the test results of UTC7. Initial knee on the torque vs. twist curves was observed around 4500Nm and the calculated shear strength at knee of MMC is 359 MPa. The specimen plastically deformed when the load increase in the subsequent cycle. However, in the first cycle of the second test, significant plasticity and strain accumulation were observed. The calculated ultimate shear strength for MMC is 1108 MPa based on the maximum torque applied of 14.3 kNm. Calculated effective MMC shear modulus for UTC7 is 66.6 GPa. Total twist on the specimen at ultimate load is 14.75° and the shear strain to fracture is 4.04%.

3.7.1.7 UTC 8 ($\pm 45^\circ$ Fibre Orientation)

This specimen with test reference UTC8 is a MMC tube with $\pm 45^\circ$ fibre orientation. There are 12 MMC plies at the core layer and the dimensions of the cross sections were obtained through SEM on the polished sample. Repeated torsion test was carried out at room temperature. Similar to UTC7, this specimen

was not tested to failure at the first test. It is tested to failure with the new adapters in the second test.

Figure 3.30 and Figure 3.31 show the test results of UTC8. Initial knee on the torque vs. twist curves was observed around 4.7 kNm and the calculated shear strength at knee of MMC is 392 MPa. Once, the specimen passed the elastic limit of Ti-6-4, it deformed progressively from cycle to cycle up until failure. The calculated ultimate shear strength for MMC is 1189 MPa based on the maximum torque applied of 14.3 kNm. Calculated effective MMC shear modulus for UTC8 is 70.5 GPa. Total twist on the specimen at ultimate load is 10.98° and the shear strain to fracture is 2.93%.

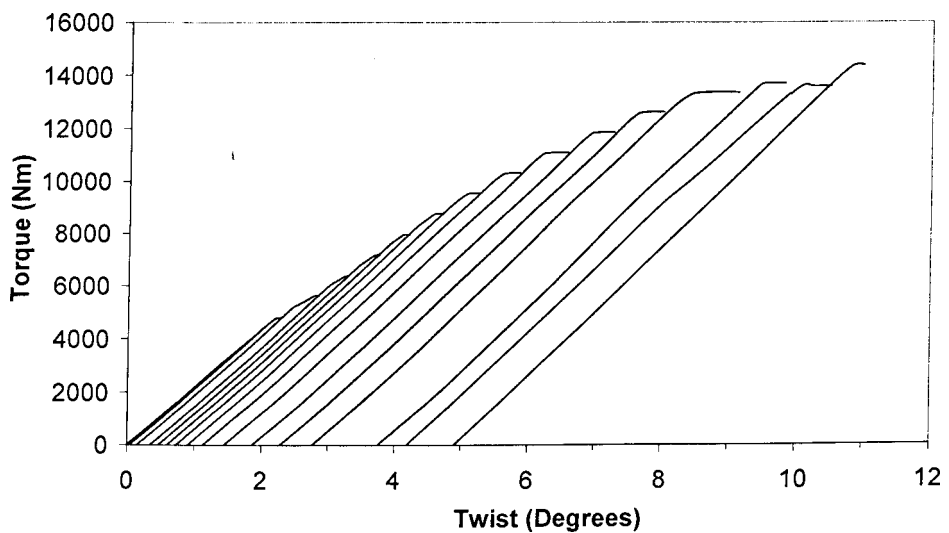


Figure 3.30 Torque vs. twist curves for UTC8

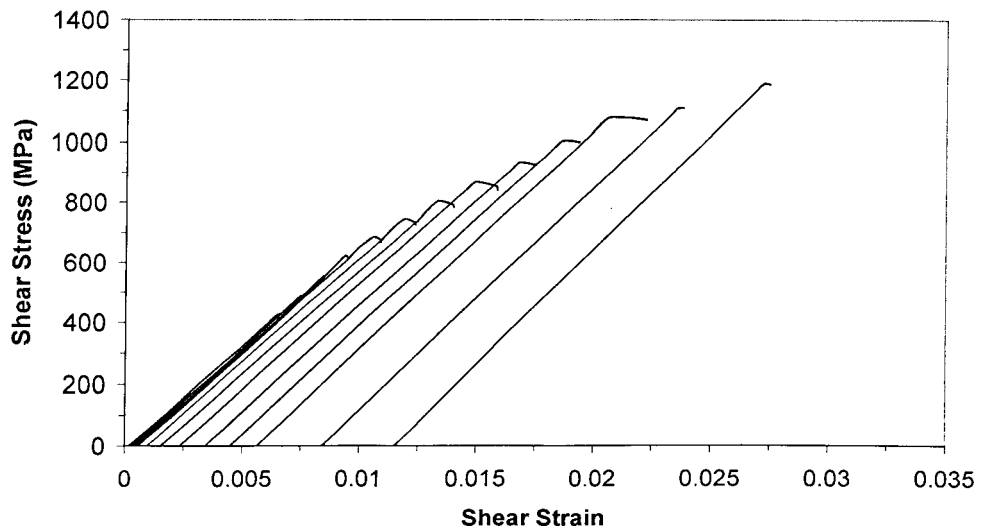


Figure 3.31 MMC shear stress vs. shear strain curves for UTC8

3.7.1.8 UTC 9 (-45° Fibre Orientation)

This specimen with test reference UTC9 is a MMC tube with -45° fibre orientation. There are 13 MMC plies at the core layer and the dimensions of the cross sections were obtained through the X-ray measurements. Repeated torsion test was carried out at room temperature.

Figure 3.32 and Figure 3.33 show the test results of UTC9. Initial knee on the torque vs. twist curves was observed around 6 kNm and the calculated shear strength at knee of MMC is 489 MPa. Very low strain and twist accumulation was observed for this specimen. From the curves, it clearly shown this specimen exhibits a bilinear behaviour. The calculated ultimate shear strength for MMC is 792 MPa based on the maximum torque applied of 10.4 kNm. Calculated effective MMC shear modulus for UTC9 is 68.6 GPa. Total twist on the specimen at ultimate load is 5.63° and the shear strain to fracture is 1.38%.

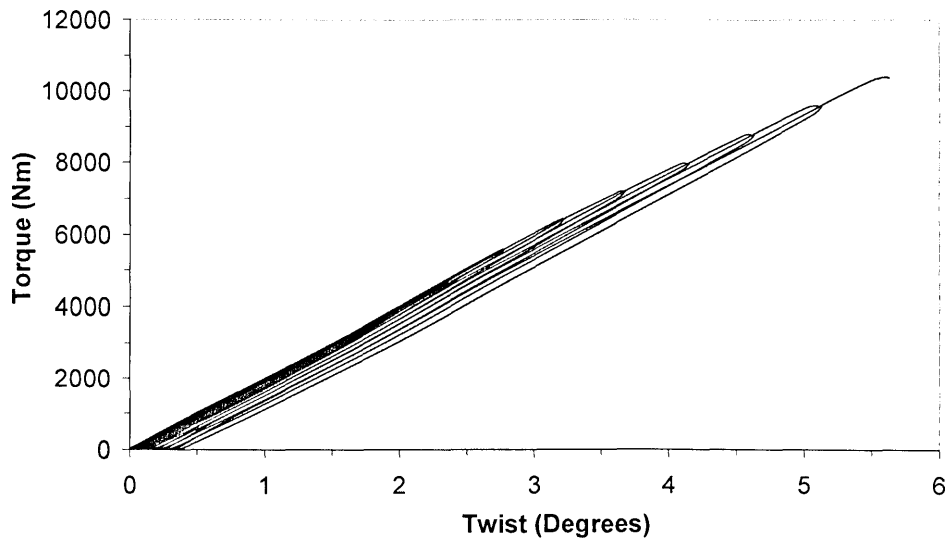


Figure 3.32 Torque vs. twist curves for UTC9

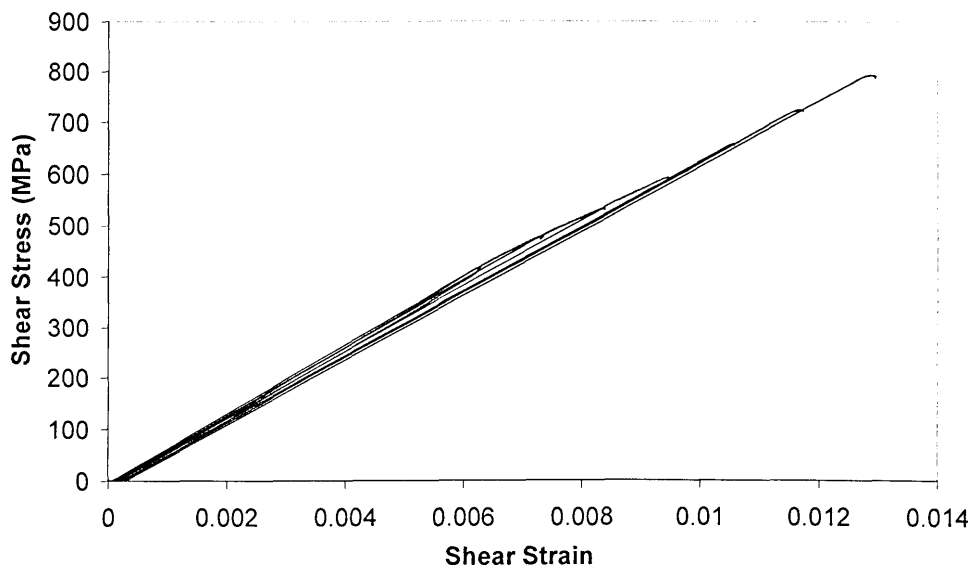


Figure 3.33 MMC shear stress vs. shear strain curves for UTC9

3.7.1.9 UTC 10 (+45° Fibre Orientation)

This specimen with test reference UTC10 is a MMC tube with +45° fibre orientation. There are 13 MMC plies at the core layer and the dimensions of the cross sections were obtained through the X-ray measurements. Repeated torsion test was carried out at room temperature.

Figure 3.34 and Figure 3.35 show the test results of UTC10. Initial knee on the torque vs. twist curves was observed around 6.3 kNm and the calculated shear strength at knee of MMC is 495 MPa. Similar to the $\pm 45^\circ$ fibre orientation the specimen deformed progressively from cycle to cycle up until failure once it passed the elastic limit of Ti-6-4. The calculated ultimate shear strength for MMC is 1248 MPa based on the maximum torque applied of 15.9 kNm. Calculated effective MMC shear modulus for UTC10 is 68.2 GPa. Total twist on the specimen at ultimate load is 12.49° and the shear strain to fracture is 3.62%.

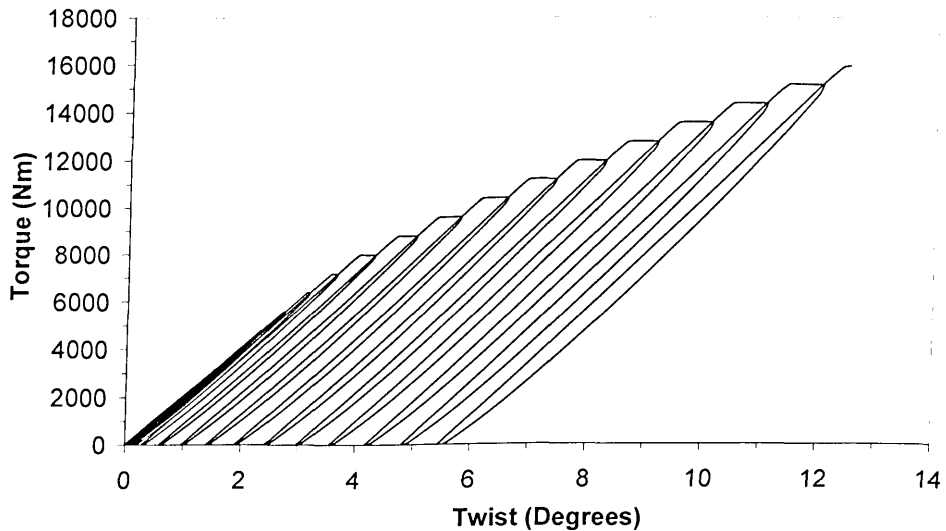


Figure 3.34 Torque vs. twist curves for UTC10

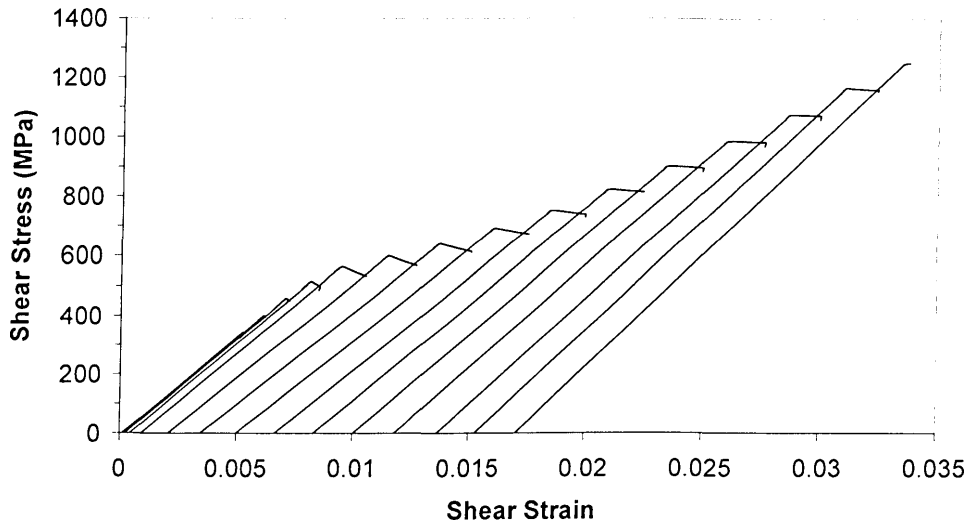


Figure 3.35 MMC shear stress vs. shear strain curves for UTC10

3.7.2 Elevated Temperature Tests (350°C)

This section describes the following test results.

Section	Specimen	Description
3.7.2.1	M2	HIPped Solid Ti-6-4
3.7.2.2	UTC3	0° Fibre Orientation
3.7.2.3	UTC11	±45° Fibre Orientation
3.7.2.4	UTC12	-45° Fibre Orientation
3.7.2.5	UTC13	+45° Fibre Orientation

Table 3.4 Elevated temperature tests (350°C)

3.7.2.1 Monolithic 2 (HIPped Solid Ti-6-4)

After stiffness characterization at room temperature, the HIPped solid Ti-6-4 specimen was tested at 350°C to failure. Figure 3.36 and Figure 3.37 show the test results of M2 at 350°C. The specimen starts to yield around 5.5 kNm. Again, significant yielding was observed beyond this point as further load applied to the specimen. The material hardened as the load increased in subsequent cycle. The test was stopped and concluded as the torque actuators ran out of travel.

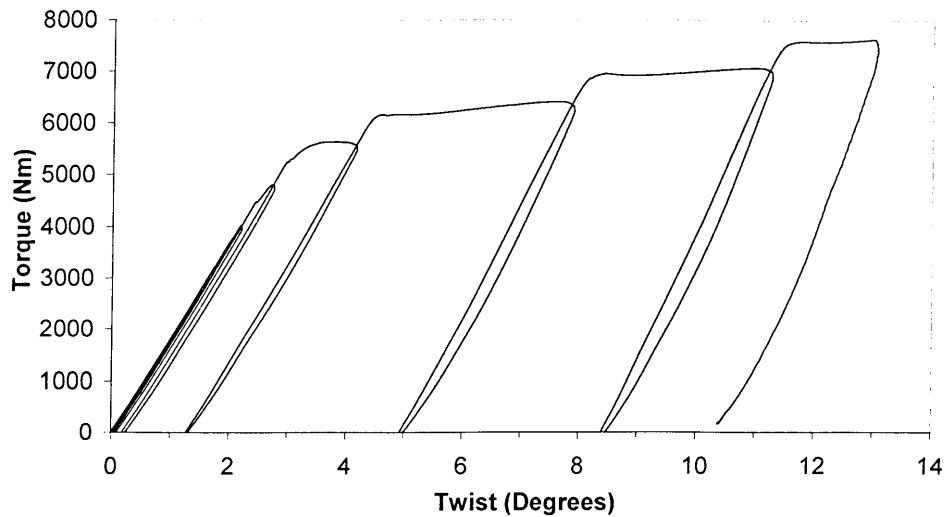


Figure 3.36 Torque vs. twist curves for M2

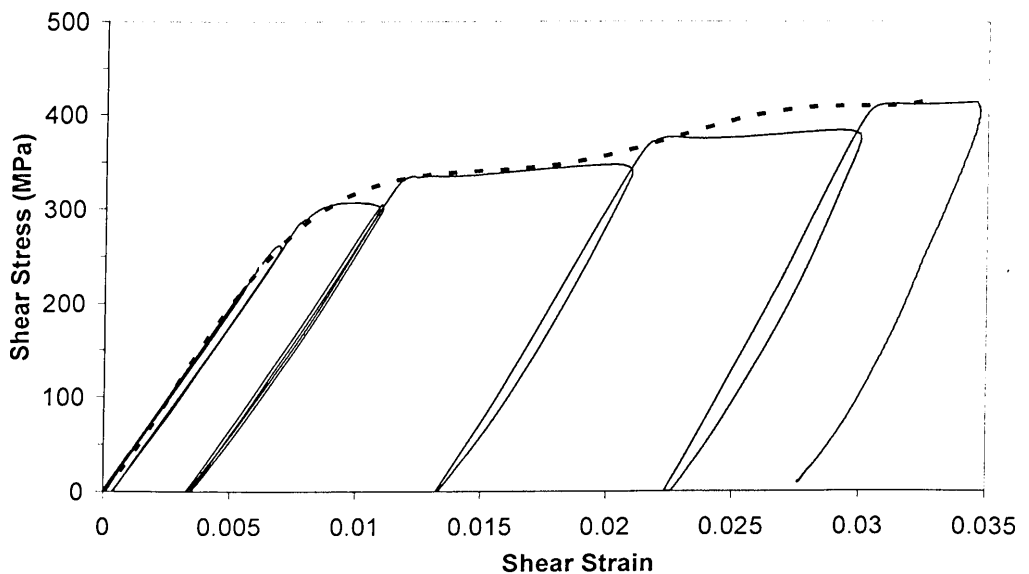


Figure 3.37 Shear stress vs. shear strain curves for M2

The proof shear strength calculated is 286 MPa compare to the yield strength of 364 MPa quoted by IMI. Clearly, the HIPping process affects the yield strength significantly. The ultimate shear strength calculated is 414 MPa based on the maximum torque imposed on the specimen. The maximum torque applied on this specimen is approximately 7.6 kNm. The compound shear stress vs. shear strain curve is shown as dotted line in Figure 3.37. This compound curve was

used to evaluate the MMC shear stress vs. shear strain curves for UTC3, UTC11, UTC12 and UTC13 tested at 350°C.

3.7.2.2 UTC 3 (0° Fibre Orientation)

This specimen with test reference UTC3 is a MMC tube with 0° fibre orientation. There are 13 MMC plies at the core layer and the dimensions of the cross sections were estimated by QinetiQ. Repeated torsion test was carried out at 350°C. It took approximate 2 hours to heat the specimen up to the target temperature where the test was launched at this point.

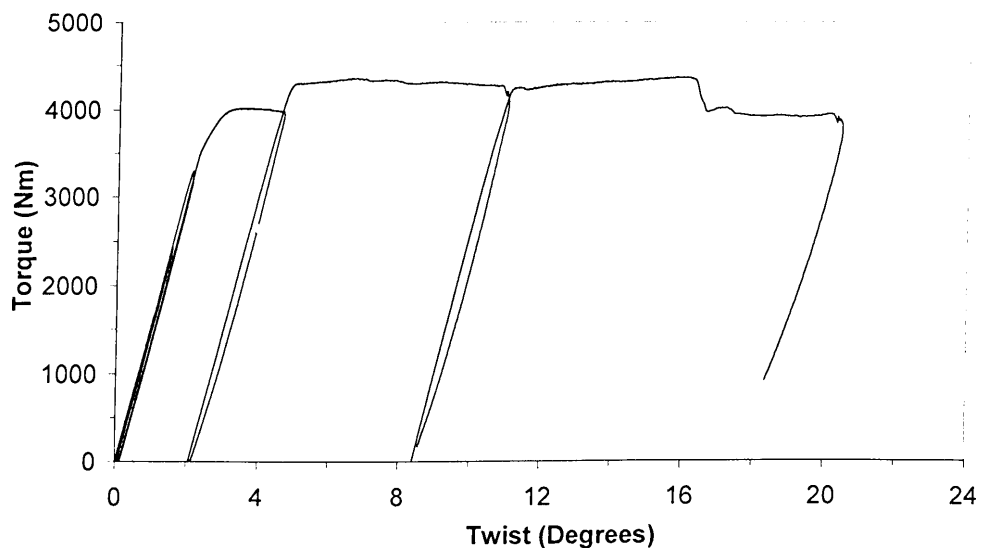


Figure 3.38 Torque vs. twist curves for UTC3

Figure 3.38 and Figure 3.39 show the test results of UTC3. Initial knee on the torque vs. twist curve was observed around 3.5 kNm. The calculated shear strength at knee of MMC is 245 MPa. The specimen starts to yield significantly at the last three cycles. At the penultimate cycle, continuous yielding of the specimen was observed before the end of the load holding period. Hence, it is decided to reload the specimen once more at the same target peak load for it to

reach equilibrium. It is at this cycle where the specimen fractured. The calculated ultimate shear strength for MMC is 256 MPa based on the maximum torque applied of 4.3 kNm. Calculated effective MMC shear modulus for UTC3 is 48.6 GPa. Total twist on the specimen at ultimate load is 20.45° and the shear strain to fracture is 5.09%.

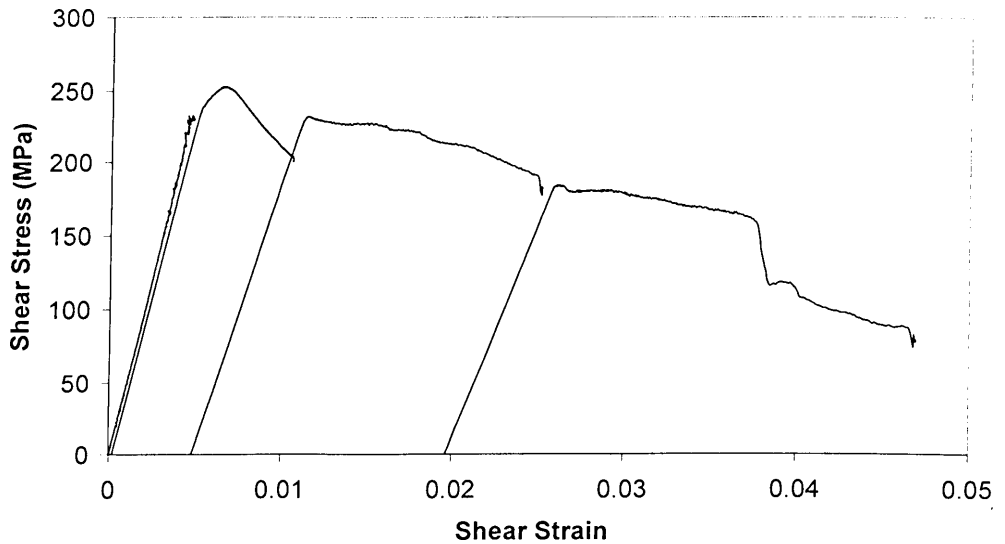


Figure 3.39 MMC shear stress vs. shear strain curves for UTC3

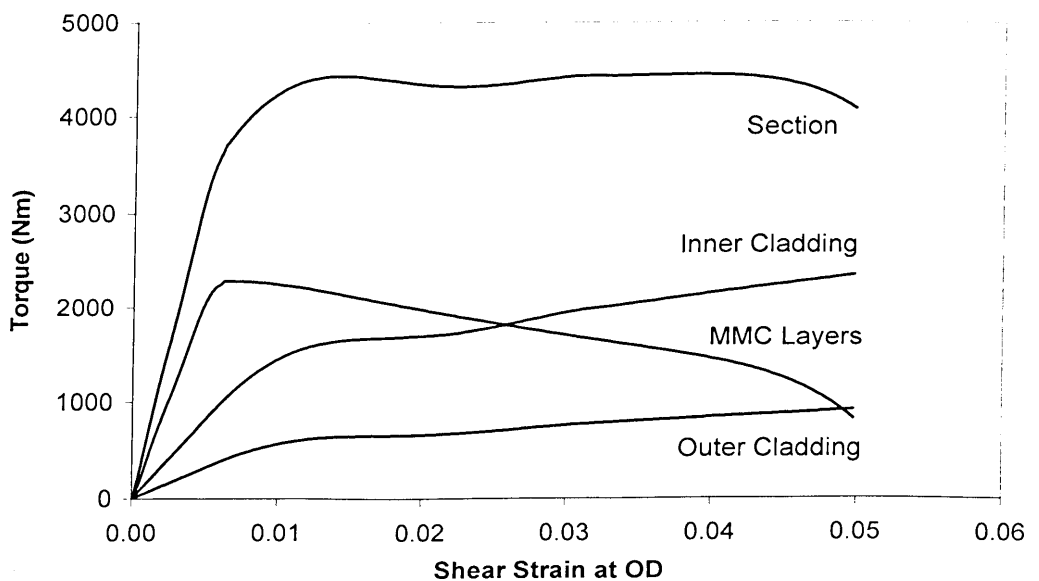


Figure 3.40 Torque vs. shear strain curves of each section for UTC3

Note that the strain signal is rather noisy for this test. No strain data was recorded for the last three cycles as the strain gauges passed their strain limit. Hence, the shear strain of the last three cycles was converted from the twist data. The torque vs. shear strain curve for each section (Figure 3.40) confirms that the MMC layer carries a reducing proportion of the overall torque once the strain exceeds the point of maximum shear stress. The torque carried by the cladding layers continues to increase through to final fracture. Hence, the MMC layer is the weakest part for this specimen. These curves shown are the compound curves from the test.

3.7.2.3 UTC 11 ($\pm 45^\circ$ Fibre Orientation)

This specimen with test reference UTC11 is a MMC tube with $\pm 45^\circ$ fibre orientation. There are 12 MMC plies at the core layer and the dimensions of the cross sections were obtained through SEM on the polished sample. Repeated torsion test was carried out at 350°C .

Figure 3.41 and Figure 3.42 show the test results of UTC11. Initial knee on the torque vs. twist curves was observed around 4.8 kNm and the calculated shear strength at knee of MMC is 413 MPa. Similar to $\pm 45^\circ$ fibre orientation specimen tested at room temperature, the specimen deformed progressively beyond the elastic limit of Ti-6-4 at 350°C up until failure. The calculated ultimate shear strength for MMC is 858 MPa based on the maximum torque applied of 9.6 kNm. Calculated effective MMC shear modulus for UTC11 is 70.4 GPa. Total twist on the specimen at ultimate load is 7.94° and the shear strain to fracture is 1.89%.

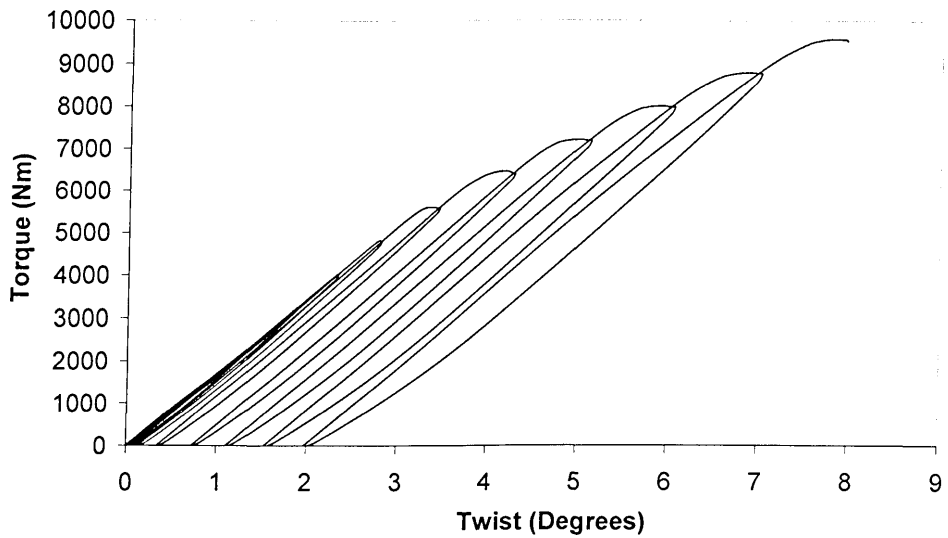


Figure 3.41 Torque vs. twist curves for UTC11

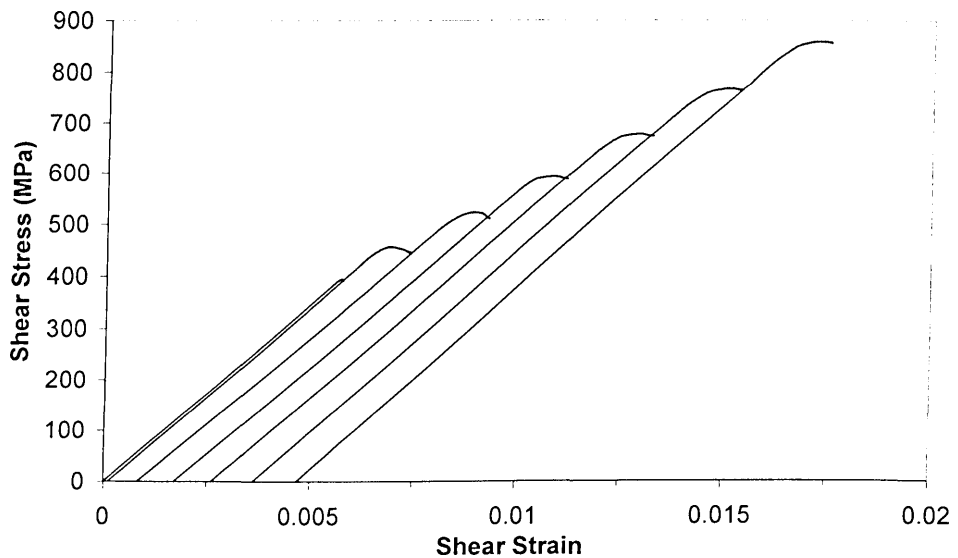


Figure 3.42 MMC shear stress vs. shear strain curves for UTC11

3.7.2.4 UTC 12 (-45° Fibre Orientation)

This specimen with test reference UTC12 is a MMC tube with -45° fibre orientation. There are 13 MMC plies at the core layer and the dimensions of the cross sections were obtained through SEM on the polished sample. Repeated torsion test was carried out at 350°C.

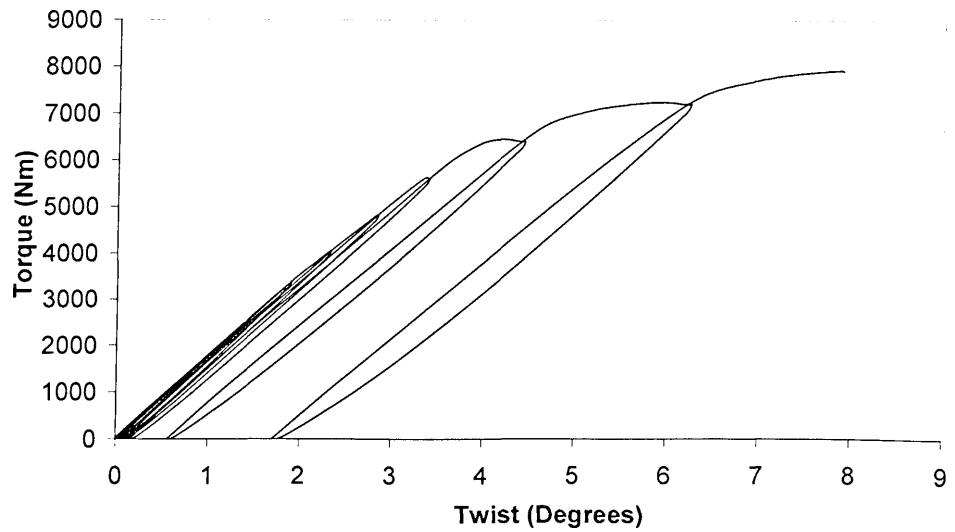


Figure 3.43 Torque vs. twist curves for UTC12

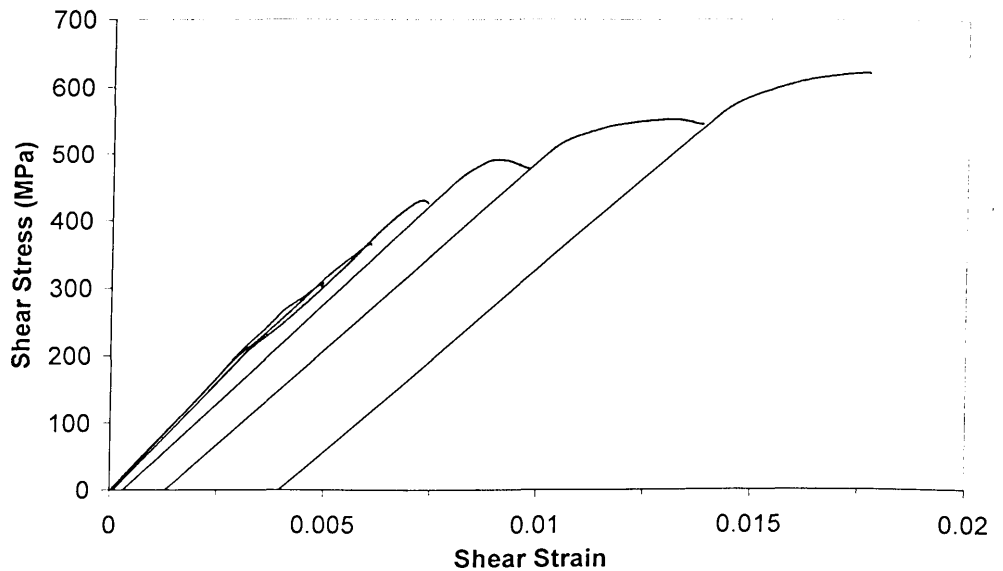


Figure 3.44 MMC shear stress vs. shear strain curves for UTC12

Figure 3.43 and Figure 3.44 show the test results of UTC12. Initial knee on the torque vs. twist curves was observed around 3.6 kNm and the calculated shear strength at knee of MMC is 296 MPa. The specimen only yields significantly in the last three cycles. Similar to the -45° fibre orientation specimen tested at room temperature, the specimen exhibits a bilinear behaviour as seen from the shear stress vs. shear strain curves. The calculated ultimate shear strength for MMC is

622 MPa based on the maximum torque applied of 7.9 kNm. Calculated effective MMC shear modulus for UTC12 is 69.8 GPa. Total twist on the specimen at ultimate load is 7.90° and the shear strain to fracture is 1.90%.

3.7.2.5 UTC 13 (+45° Fibre Orientation)

This specimen with test reference UTC13 is a MMC tube with +45° fibre orientation. There are 13 MMC plies at the core layer and the dimensions of the cross sections were obtained through SEM on the polished sample. Repeated torsion test was carried out at 350°C.

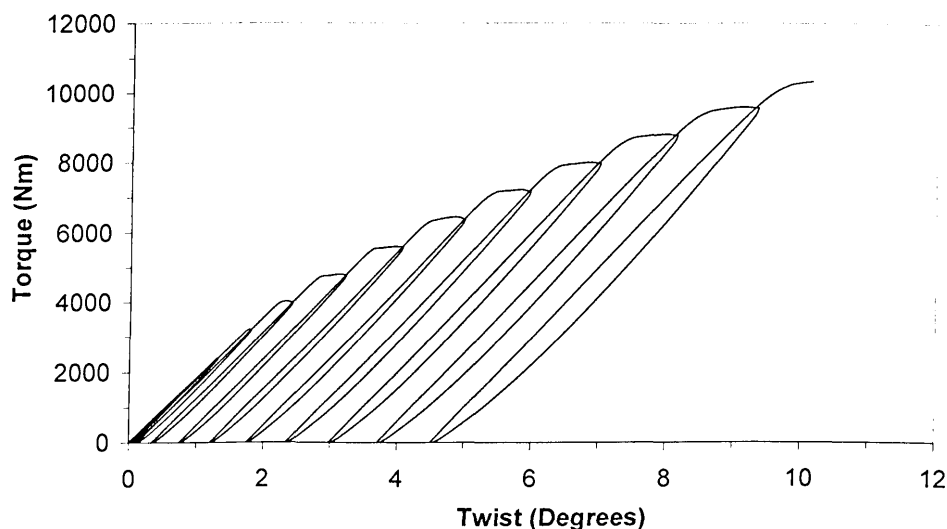


Figure 3.45 Torque vs. twist curves for UTC13

Figure 3.45 and Figure 3.46 show the test results of UTC13. Initial knee on the torque vs. twist curves was observed around 4 kNm and the calculated shear strength at knee of MMC is 317 MPa. Again, the specimen deformed progressively beyond the elastic limit of Ti-6-4 at 350°C up until failure. The calculated ultimate shear strength for MMC is 859 MPa based on the maximum torque applied of 10.3 kNm. Calculated effective MMC shear modulus for

UTC13 is 68.6 GPa. Total twist on the specimen at ultimate load is 10.14° and the shear strain to fracture is 2.84%.

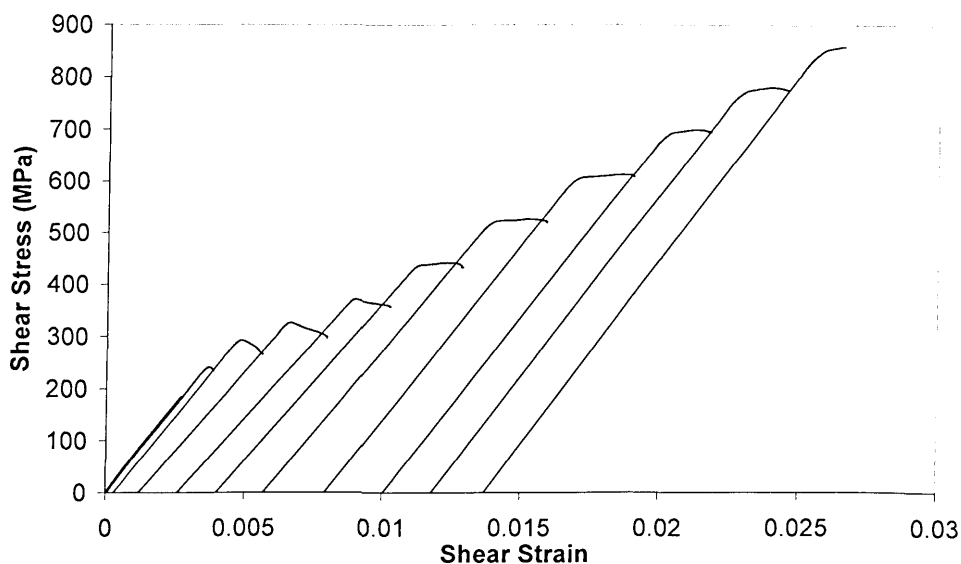


Figure 3.46 MMC shear stress vs. shear strain curves for UTC13

3.8 Discussions

Detailed discussions for the experimental results will be presented within this section. In particular, the effective MMC shear modulus, shear strength at knee and ultimate shear strength of MMC for different fibre orientation. Ductility between the specimens will also be compared through the shear strain to fracture of the specimens. Only 0° , $\pm 45^\circ$, $+45^\circ$ and -45° fibre orientation have been tested both at room temperature and elevated temperature (350°C). Therefore, the difference in material properties due to the effect of temperature will be discussed for these fibre orientations.

Table 3.5 shows a summary for the experimental results. Note that the shear modulus quoted for M1 and M2 is for the monolithic specimen. The proof shear strength and ultimate shear strength quoted is for MMC except M1 and M2. The

ultimate shear strength for M1 and M2 were calculated based on the maximum load imposed on the specimen although the specimen did not fracture.

Test Ref.	Fibre Orientation	Testing Temperature (°C)	Effective MMC Shear Modulus (GPa)	Shear Strength at Knee (MPa)	Ultimate Shear Strength (MPa)	Shear Strain to Fracture (%)	Total Twist (Degrees)
M1	-	20	46.4(*)	497	763(+)	-	20.46
M2	-	20	44.1(*)	-	-	-	-
M2	-	350	39.0(*)	286	414(+)	-	10.38
UTC1	0°	20	62.8	329	564	1.72	6.06
UTC3	0°	350	48.6	245	256	5.09	20.45
UTC5	±30°	20	67.3	367	1027	3.01	10.62
UTC6	-30°	20	68.4	385	586	2.09	9.08
UTC7	+30°	20	66.6	359	1108	4.04	14.75
UTC8	±45°	20	70.5	392	1189	2.93	10.98
UTC9	-45°	20	68.6	489	792	1.38	5.63
UTC10	+45°	20	68.2	495	1248	3.62	12.49
UTC11	±45°	350	70.4	413	858	1.89	7.94
UTC12	-45°	350	69.8	296	622	1.90	7.90
UTC13	+45°	350	68.6	317	859	2.84	10.14

Table 3.1 Summary of experimental results

* Shear modulus of Ti-6-4

+ Based on maximum load imposed on specimen

3.8.1 Effective MMC Shear Modulus

With the exception of the 0° fibre orientation at 350°C , the overall variation in shear modulus is only 12%. As seen from Table 3.5, at room temperature, specimen with 0° fibre orientation has the lowest effective MMC shear modulus. The shear modulus decreased by 23% when tested at 350°C . The decrease in shear modulus is rather significant compare to the monolithic specimen M2 which only decreased by 12% when it is tested at 350°C . Hence, temperature effect on the shear modulus for 0° specimen is significant.

For specimens with 30° fibre orientation tested at room temperature, cross-ply or uni-ply, the effective MMC shear modulus is within 3% between the maximum (-30°) and minimum ($+30^\circ$). This is similar for specimens with 45° fibre orientation, the effective MMC shear modulus is within 3% between the maximum ($\pm 45^\circ$) and minimum ($+45^\circ$). The highest effective MMC shear modulus measured is from the $\pm 45^\circ$ fibre orientation specimen, because fibres at 45° direction are aligned with the principal tensile stress for a tube subjected to pure torsion. Hence, the shear modulus will be the highest in this case. However, it can be seen that the effective MMC shear modulus does not increase greatly by changing the fibre orientation from 30° to 45° . A trend is clearly there where the effective MMC shear modulus increase from $+30^\circ$ to $+45^\circ$ and $\pm 30^\circ$ to $\pm 45^\circ$.

For specimens with 45° fibre orientation tested at 350°C , cross-ply or uni-ply, the effective MMC shear modulus is similar to those tested at room temperature. Clearly the temperature up to 350°C has no effect to the effective MMC shear modulus. This is due to the behaviour of 45° specimens are dominated by the

fibres, unlike 0° specimen which is dominated by the matrix. This is consistent with the on-axis and off-axis coupon tests done by Sun et. al. [26], which showed that the Young's Modulus remained unchanged up to 316°C .

In conclusion, for torque applications, specimens with $+45^\circ$ fibre orientation give the highest effective MMC shear modulus. The fibre lay-up does not have a significant effect on the shear modulus.

3.8.2 Shear Strength at Knee of MMC

Shear strength at knee of MMC can be referred as the debond shear strength where fibres start to debond from the matrix. As seen from Table 3.5, at room temperature, specimen with 0° fibre orientation has the lowest MMC shear strength at knee. The shear strength at knee was decreased by 25% when tested at 350°C . The decrease is smaller compared to the monolithic specimens, which decreased by almost 42% when tested at 350°C .

For specimens with 30° fibre orientation tested at room temperature, cross-ply or uni-ply, the shear strength at knee varies by 7% between the maximum (-30°) and minimum ($+30^\circ$). However, for specimens with 45° fibre orientation tested at room temperature, there is a greater variation (21%) between the maximum ($+45^\circ$) and minimum ($\pm 45^\circ$). Specimen with $+45^\circ$ fibre orientation gives the highest MMC shear strength at knee. By taking the average value of shear strength at knee for 30° and 45° fibre orientation separately, it improved by 24% changing from 30° to 45° fibre orientation.

For specimens with 45° fibre orientation tested at 350°C , the shear strength at knee of MMC varies from the highest at 413 MPa ($\pm 45^\circ$) to the lowest at 296

MPa (-45°). Interestingly, the lowest value was measured on the -45° specimen. This is due to a tensile component acting transversely to the -45° fibres causing debonding to occur at a lower load level. However, this phenomenon was not observed for -45° specimen tested at room temperature. Testing specimens with 45° fibre orientation at 350°C clearly decreases the shear strength at the knee by 25% on average compare to those tested at room temperature.

For all fibre orientations, it can be seen that the MMC shear strength at knee at room temperature falls between 330 MPa and 500 MPa; for 350°C it falls between 260 MPa and 410 MPa. However, the ultimate shear strength for MMC does not fall in such a small range and will be discuss in next section.

3.8.3 Ultimate Shear Strength of MMC

The ultimate shear strength of MMC is calculated based on maximum shear stress imposed on the MMC layer before fracture occur. The specimen with 0° fibre orientation has the lowest ultimate shear strength. At room temperature, the strength measured is 564 MPa. This decreased by 55% when tested at 350°C . Even at room temperature, the ultimate shear strength is lower than the monolithic specimen. Hence, reinforcement with fibres at 0° does not increase the strength of shafts for pure torque applications. MMC layer exhibit maximum strength when the fibres are loaded in tension, but are weak if there are tensile loads perpendicular to the fibre direction or the fibre plane is loaded in shear, as in the 0° case. Detailed discussions regarding the failure of each specimen will be presented in Chapter 4.

Figure 3.47 shows the ultimate shear strength of MMC for uni-ply fibre orientation at room temperature. The ultimate shear strength of MMC increases from 0° to $+45^\circ$ and from 0° to -45° . The increase from -30° to -45° is due to fibres at -45° experiencing an on-axis compressive load under pure torsion, which is due to the high compressive strength of the fibres. The highest and lowest strength for uni-ply fibre orientation are $+45^\circ$ and 0° respectively. The reason for $+45^\circ$ fibre orientation having the greatest strength is due to fibres at $+45^\circ$ experiencing an on-axis tensile load where the fibres have a great tensile strength. At the same time, a compressive load also acts transversely to the fibres where it tends to close the gap between debonded fibres from the matrix. The specimen with $+30^\circ$ fibre orientation also gives good ultimate shear strength and this orientation would also be advantageous for combined torque, axial and bending load applications.

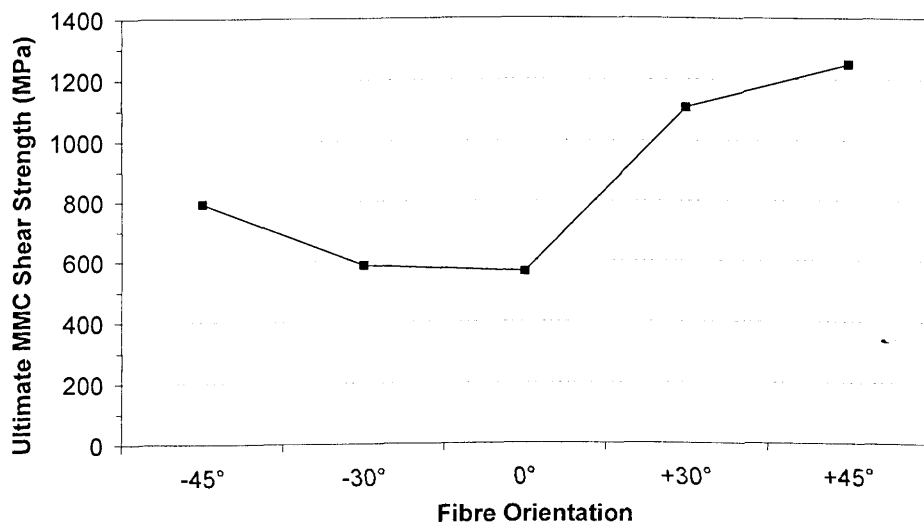


Figure 3.47 Ultimate shear strength of MMC at room temperature (Uni-ply)

Figure 3.48 shows the ultimate shear strength of MMC for cross-ply fibre orientation at room temperature. Clearly there is a trend on the ultimate shear

strength of MMC from 0° to $\pm 45^\circ$ fibre orientation where $\pm 45^\circ$ being the highest. Note that having the -30° fibre plies in the $\pm 30^\circ$ specimen decreased the strength by 7% compare to the $+30^\circ$ unidirectional specimen. For $\pm 45^\circ$ specimen, the -45° fibre plies decreased the strength by 5% compare to the $+45^\circ$ specimen. The decrease is due to the fact that the negative fibre plies act as a fibre weak plane for the specimen and will lead to earlier failure hence strength.

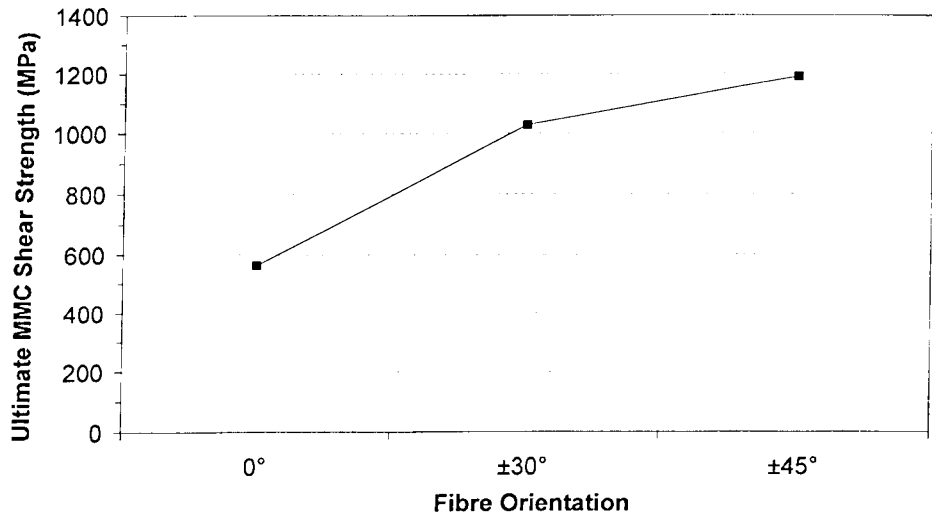


Figure 3.48 Ultimate shear strength of MMC at room temperature (Cross-ply)

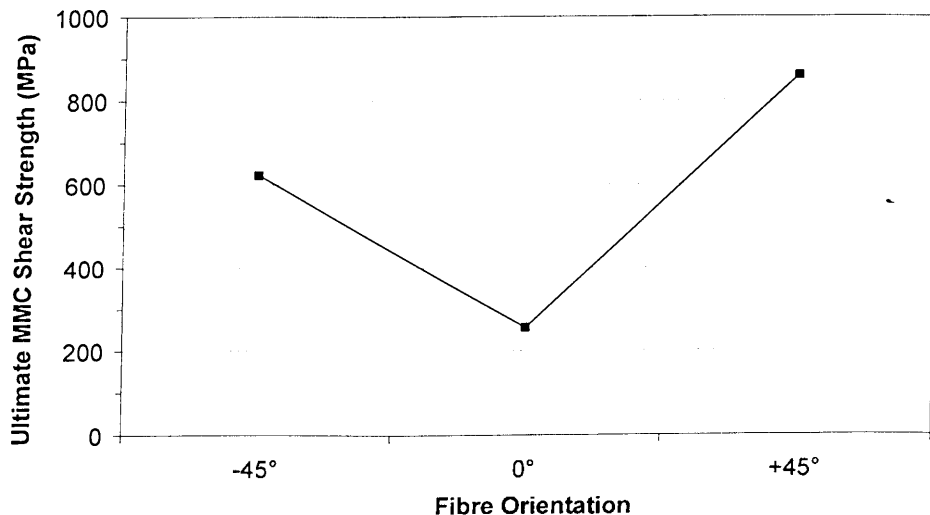


Figure 3.49 Ultimate shear strength of MMC at 350°C (Uni-ply)

Figure 3.49 shows the ultimate shear strength of MMC for uni-ply fibre orientation at 350°C. Specimen with +45° fibre orientation gives the highest strength at 859 MPa which is 38% higher than the -45° specimen. 0° specimen tested at 350°C gives a very poor ultimate MMC shear strength of 256 MPa, which is 55% lower than the specimen tested at room temperature. Hence, the temperature affects the strength greatly for 0° specimen. Although the +45° specimen gives the highest strength at 350°C, the strength dropped 31% compared to the specimen tested at room temperature. For -45° specimen, the strength dropped by 21% when tested at 350°C.

Hence, it is concluded that fibres laid at positive direction, in particular +45° direction subjected to a counter-clockwise torque, give good ultimate shear strength. Fibres laid at 0° should be avoided for all cases in torque application. Having some fibre plies at negative direction for cross-ply fibre orientation will decrease the strength marginally. However, if the fibre plies are only laid in the negative direction, the strength will definitely be poor due to the fibre weak plane.

3.8.4 Ductility

Ti-6-4 is a very ductile material and the ductility of TiMMC is very much dominated by the matrix material. The fibre is a brittle material and has low strain to fracture when tested separately in a uniaxial tensile test. To determine the ductility of a TiMMC specimen, it can be judged by evaluating the shear strain to fracture of the specimen when it fractures. For specimens of 0°, ±45°, -45° and +45° fibre orientation tested at both room temperature and 350°C, no

trend was observed in term of ductility. Hence, each case is unique and will be discussed separately.

For the specimens with 0° fibre orientation, the ductility increased by almost 200% when testing at 350°C compare to room temperature. It is obvious that the behaviour is dominated by the matrix material. For specimens with 30° fibre orientation, the highest ductility is measured for the $+30^\circ$ specimen at 4.04%; lowest ductility is measured for the -30° specimen at 2.09%. Ductility for -30° specimen is low because of its poor ultimate shear strength, which leads to failure at a lower load.

For specimens with 45° fibre orientation, tested at room temperature, the $+45^\circ$ specimen gives the highest ductility at 3.62% and the lowest is the -45° specimen at 1.38%. As with the -30° specimen, the low ductility of -45° specimen is due to its poor ultimate shear strength. At room temperature, cross-ply specimens such as $\pm 30^\circ$ and $\pm 45^\circ$ have ductility of 3.01% and 2.93% respectively.

For specimens with 45° fibre orientation tested at 350°C , the ductility of the -45° specimen is the lowest but it increased by 38% compare to room temperature of 1.38%. The highest ductility is measured for the $+45^\circ$ specimen at 2.84%. However, the ductility of $+45^\circ$ and $\pm 45^\circ$ specimens decreased by 22% and 36% respectively compared to room temperature. Clearly the ductility of $+45^\circ$ and $\pm 45^\circ$ specimens are dominated by the fibres due to the $+45^\circ$ fibre plies within the material. The $+45^\circ$ fibres take all of the on-axis tensile load under pure torsion,

thus decreasing the ductility. On the other hand, the ductility of -45° specimen is dominated by the matrix due to the absence of fibres at $+45^\circ$ direction.

3.9 Summary

In this chapter, details of the experimental work have been presented; from the design of specimens and components to the inspection stage prior to testing. The design of the specimens has been changed at the middle of the program due to the higher strength of the specimen than expected. The inspections of the specimens provide accurate information on the MMC and cladding thicknesses. This information was used to calculate the effective shear modulus, proof shear strength and ultimate shear strength for MMC. Test matrix within VITAL Phase 1 was also presented and showed specimens with different fibre orientation, tested at both room temperature and 350°C .

The torsion shaft rig and relevant equipment used for the testing were also described. Load, displacement and strain data were recorded during the tests. For specimens tested at 350°C , a custom built split tube furnace was used, which enclosed the whole specimen within the heating chamber. Repeated torsion test was applied to each specimen with an increasing maximum torque until failure. Trapezoidal load profile was used for all tests in which the load is ramped up at a constant rate and held for a period before ramping down at the same rate.

Methods of analysis for test results were presented. However, data such as torque, twist and strain need to be corrected to get the actual results. Then, test results for each specimen were discussed in detail to give the key material properties for that fibre orientation. Detailed discussions comparing the material

properties for different fibre orientation and test temperature were made, leading to the following key conclusions.

1. For pure torque applications, the $+45^\circ$ fibre orientation gives the highest torsional strength, good shear modulus and ductility at both room temperature and 350°C . However, if the torque is reversed, $+45^\circ$ specimen is now essentially a -45° specimen which the strength and ductility will drop greatly. Hence, for reversed torque applications, $\pm 45^\circ$ fibre orientation is more suitable. 0° orientation should be avoided for pure torque applications as it gives poor strength and ductility since the fibres are on a plane of maximum shear stress. Although the 0° specimen gave good ductility, the shear modulus and strength were reduced greatly.
2. The shear modulus for either cross-ply or uni-ply for a given fibre orientation are similar. However, the strength of the -30° and -45° were greatly reduced in comparison with the corresponding $+30^\circ$ and $+45^\circ$ cases. In contrast, the strength reduction for the corresponding cross-ply cases was marginal.

In Chapter 4, a comprehensive failure investigation for all tested specimens will be presented. This includes the inspections, such as the fractures surfaces, of post-tested specimens. The microstructure, fibre orientation, fibre regularity and fibre spacing will also be studied on polished samples through SEM imaging. Furthermore, the damage evolutions and the failure mechanisms for each specimen will also be discussed.

CHAPTER 4

FAILURE INVESTIGATION AND MATERIAL STUDIES

4.1 Introduction

The material properties obtained through various tests for different fibre orientation and temperature, have been presented in the previous chapter. After the specimens were tested, a comprehensive failure investigation was carried out to understand its damage mechanism. Specimens with different fibre orientation will lead to fracture at different planes. Its evolution to the ultimate failure will be discussed in details within this chapter.

The fractured surfaces of the specimen were studied through SEM imaging after being sent for cutting into smaller size samples through wire erosion to allow them to be placed into the microscope chamber. By looking at the fractured surfaces, one can distinguish the type of failure whether it is shear, tensile or mixed mode. This will enhance the understanding of its failure through the fractured plane. Mounted samples were polished according to the route supplied by TISICS Ltd and then etched to reveal the microstructure of the matrix material. Energy-dispersive X-ray (EDX) analysis was used to understand the chemical composition of the interface layer between the matrix and the outer carbon coating.

4.2 Damage Evolutions

The damage evolutions and the failure mechanism of each specimen will be discussed in detail within this section. Every specimen is unique in terms of fibre

orientation and test temperature. The fibre orientation is the key factor affecting the plane of fracture and this does not change with test temperature.

All the specimens in this test program were subjected to a counter-clockwise torque load viewed from above. For an element on the specimen surface orientated at 45° to the shaft axis, the torque load can be resolved into a tensile component and a compressive component which act perpendicular to each other. The tensile component is of particular interest here since it is more detrimental to the material than the compressive component. If the tensile component acts transversely or predominantly off-axis to the fibre direction, the fracture plane is likely to occur along the fibre direction and this is termed as the fibre weak plane. This is because TiMMC is very weak when subjected to tensile load transverse to the fibre direction. If a fibre weak plane does not exist for a particular specimen, a fracture plane will occur at the maximum shear stress plane which is at 0° or 90° to the tube axis. An example of this is a tube with uni-directional plies at $+45^\circ$.

However, it is impossible to identify the initiation point of crack that leads to the ultimate failure since the fracture of the specimen occurs instantaneously. For specimens that had been sent for X-ray inspection, no voids were observed. All specimens were also subjected to ultrasonic scans by Rolls-Royce prior to delivery and no anomalies were found. The weakest part of the specimen is at the plain section and from the axial symmetry of the fractures, it can be assumed that the crack initiates here and then propagates in opposite directions towards the two ends. However, once fracture occurs at the plain section, the load is no longer axis-symmetric pure shear, but a more complex stress field involving

shear, bending and tensile components. In some cases, this will lead to an asymmetric crack pattern or to secondary cracks in the specimens.

4.2.1 Room Temperature Test

4.2.1.1 UTC1 (0° Fibre Orientation)

UTC1 is a specimen with 0° fibre orientation tested at room temperature. An extensive post-test failure investigation and material studies was carried out for this specimen since it was the first TiMMC test. The material studies included investigation of the matrix microstructure between the cladding and the MMC ply and the chemical composition of the interphase layer. This will be discussed in detail later within this chapter.

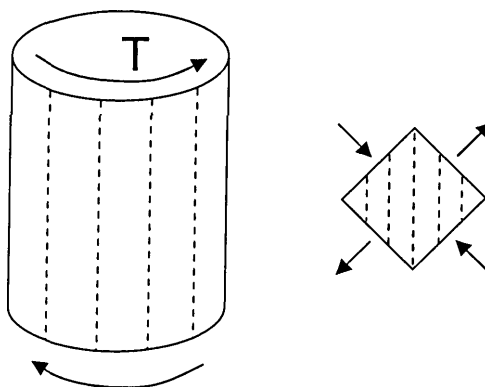


Figure 4.1 Schematic diagram of 0° specimen under torque load

Figure 4.1 shows a schematic diagram of a 0° specimen under torque load. It can be seen that the tensile component acting at 45° off-axis to the fibres. The fibre weak plane lies at the 0° direction which coincides with the maximum shear stress plane at 0°. Hence, the fracture plane will occur along the fibre direction which is clearly shown in Figure 4.2. Once the crack initiated at this plane in the centre of the plain section, it propagated towards each end and diverted

circumferentially almost at 90° when it reached the taper section. This is due to the larger section which the crack can no longer extend in the 0° direction.

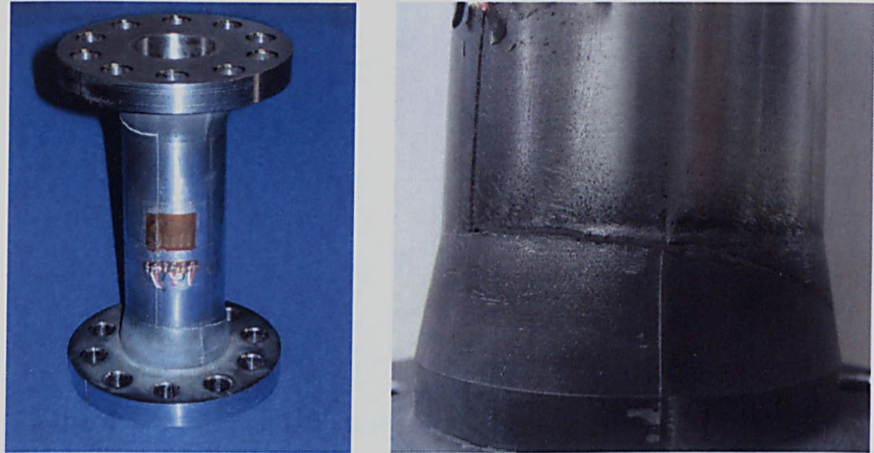


Figure 4.2 Fracture of UTC1 (0° fibre orientation, room temperature)

4.2.1.2 UTC5 ($\pm 30^\circ$ Fibre Orientation)

UTC5 is a specimen with $\pm 30^\circ$ fibre orientation tested at room temperature. Figure 4.3 shows a schematic diagram of a $\pm 30^\circ$ specimen under torque load. The tensile component acts at 60° off-axis to the -30° fibres, but only 15° off-axis to the $+30^\circ$ fibres. Hence, the fibre weak plane is at the -30° plane due to the greater off-axis angle which the tensile component acts on.

Figure 4.4 shows the final state of UTC5 after it failed where the fracture plane occurred at the -30° plane. Once the crack initiated, it propagated along the fibre direction at -30° and arrested when it reached the thicker taper section. Near the taper section at the top half of the specimen, secondary cracks parallel to the major crack were observed. Note that at this region, a secondary crack at 90° to the shaft axis was observed between the plain section and the taper section. This is the bond line where the plain section and the flange piece join during the

HIPping process. However, this slight defect has no significant effect on the material strength and it has been addressed to TISICS Ltd.

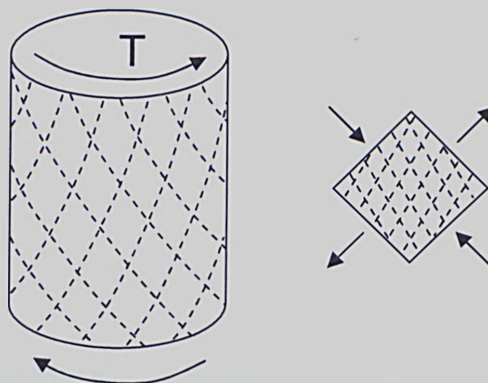


Figure 4.3 Schematic diagram of $\pm 30^\circ$ specimen under torque load



Figure 4.4 Fracture of UTC5 ($\pm 30^\circ$ fibre orientation, room temperature)

4.2.1.3 UTC6 (-30° Fibre Orientation)

UTC6 is a specimen with -30° fibre orientation tested at room temperature. Figure 4.5 shows a schematic diagram of a -30° specimen under torque load. As with the previous case (UTC5), the tensile component acts at 60° off-axis to the fibres, so the fibre weak plane is at the -30° plane.

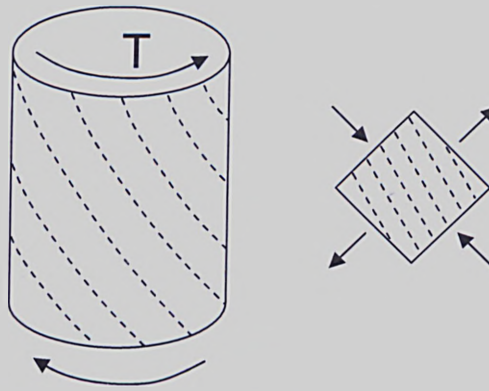


Figure 4.5 Schematic diagram of -30° specimen under torque load

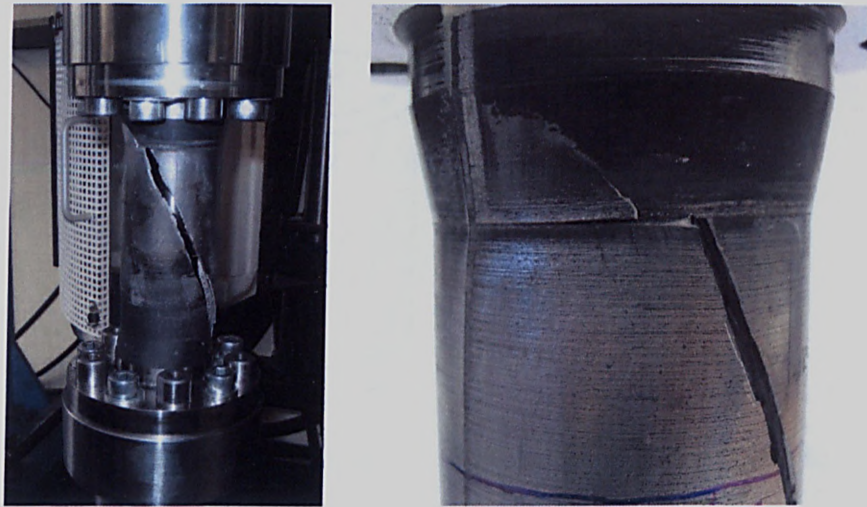


Figure 4.6 Fracture of UTC6 (-30° fibre orientation, room temperature)

Figure 4.6 shows the final state of UTC6 where the fracture plane was at the -30° plane. Similar to UTC5, the crack propagated along the fibre direction at -30° and arrested when it reached the thicker taper section. Note that near the taper section at the top half of the specimen, the crack diverts circumferentially at 90° briefly before diverts back to -30° direction again. It is obvious that the bonding between the flange pieces to the plain section is poor.

4.2.1.4 UTC7 (+30° Fibre Orientation)

UTC7 is a specimen with +30° fibre orientation tested at room temperature. Figure 4.7 shows a schematic diagram of a +30° specimen under torque load. The tensile component acts at 15° off-axis to the +30° fibres. However, this specimen is still strong although the tensile component acts off-axis to the fibres by a small angle. Hence, no fibre weak plane exists for this fibre orientation and the plane of fracture is at one of the maximum shear stress planes.

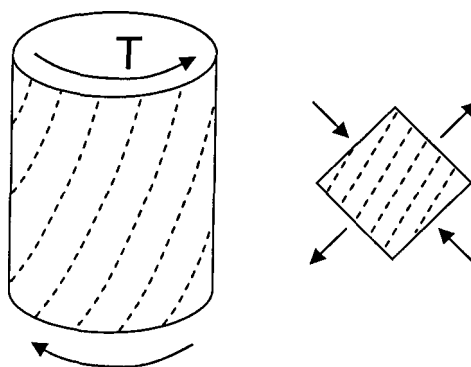


Figure 4.7 Schematic diagram of +30° specimen under torque load

Figure 4.8 shows the final state of UTC7 where the fracture occurred at 0° plane at the middle of the plain section. It is believed that the crack initiated here where 0° plane is one of the maximum shear stress planes. At the top half of the specimen, the crack divert slightly towards the negative direction before arresting at the transition section. At the bottom half of the specimen, the crack diverts sharply at almost 90° before the taper section due to its larger section. At 90° plane, it is the other maximum shear stress plane for this specimen. After the specimen had fractured, the load impose on the specimen was no longer a pure shear, therefore, the stress field at this stage is very complex which leads to an asymmetric crack pattern.

The reason that the crack occurs at the 0° plane at the middle of the plain section rather than 90° plane is because the distance between the $+30^\circ$ fibres is larger in this direction. This means that there is more matrix material between the fibres allowing the crack to grow more easily in this direction.

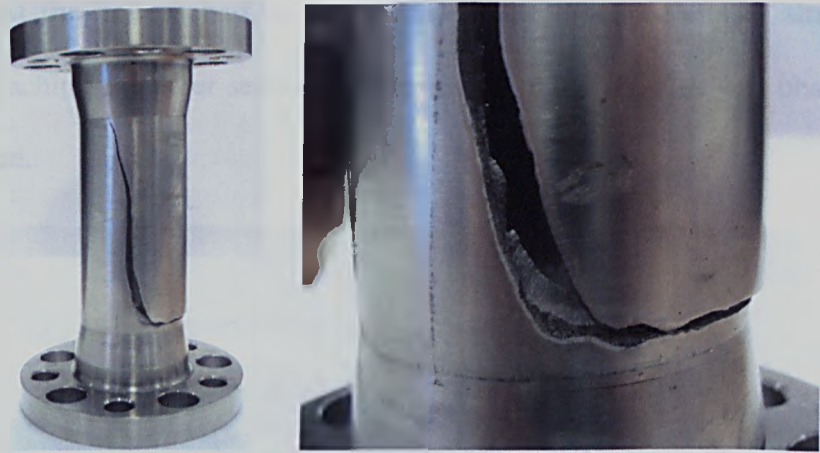


Figure 4.8 Fracture of UTC7 ($+30^\circ$ fibre orientation, room temperature)

4.2.1.5 UTC8 ($\pm 45^\circ$ Fibre Orientation)

UTC8 is a specimen with $\pm 45^\circ$ fibre orientation tested at room temperature. Figure 4.9 shows a schematic diagram of a $\pm 45^\circ$ specimen under torque load. The tensile component acts directly on-axis to the $+45^\circ$ fibres and transversely to the -45° fibres. Hence, the fibre weak plane is at the -45° plane.

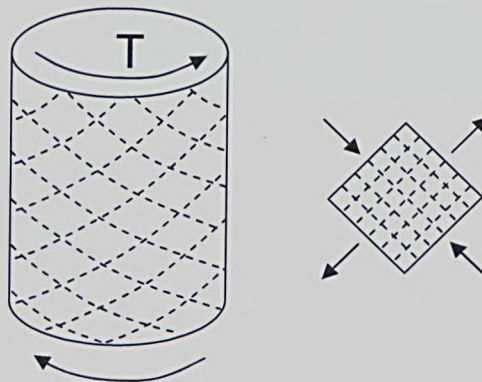


Figure 4.9 Schematic diagram of $\pm 45^\circ$ specimen under torque load

Figure 4.10 shows the final state of UTC8 where the fracture occurred at -45° plane. Once the crack initiated at the plain section, it propagated along the -45° plane at the plain section. At the top half of the specimen, the crack arrested at the taper section but a secondary crack at the $+45^\circ$ plane was observed at this region. At the bottom half of the specimen, the crack diverts to almost 90° before reaching the taper section. Delamination of MMC plies was observed at this region.

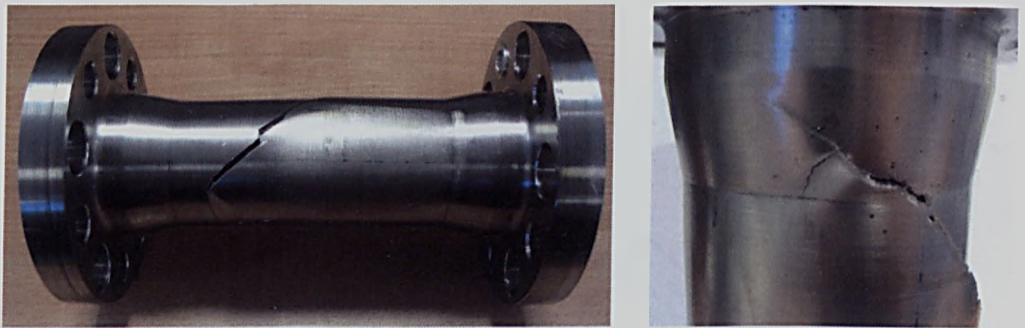


Figure 4.10 Fracture of UTC8 ($\pm 45^\circ$ fibre orientation, room temperature)

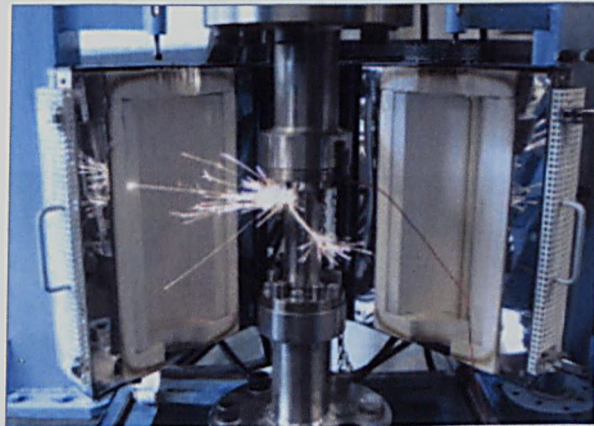


Figure 4.11 Spark along the crack plane at instant of fracture (UTC8)

An interesting phenomenon was observed during the test of UTC8. Figure 4.11 shows a frame from a video taken during the last cycle of the test where fracture occurs. A spark was observed along the -45° crack plane. This is the first time

this kind of phenomenon was observed when the specimen failed. It is believed that the spark was created where the material is rubbing each other, i.e. when the specimen failed, the fractured surfaces displace at the opposite direction radially.

4.2.1.6 UTC9 (-45° Fibre Orientation)

UTC9 is a specimen with -45° fibre orientation tested at room temperature. Figure 4.12 shows a schematic diagram of a -45° specimen under torque load. For this specimen, the tensile component acts transversely to the -45° fibres. Hence, the fibre weak plane is at the -45° plane.

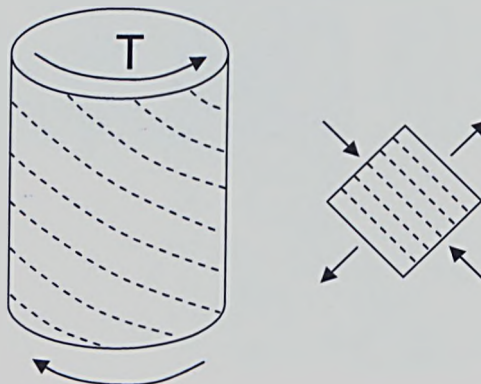


Figure 4.12 Schematic diagram of -45° specimen under torque load



Figure 4.13 Fracture of UTC9 (-45° fibre orientation, room temperature)

Figure 4.13 shows the final state of UTC9 where the fracture plane occurred at the -45° plane. Similar to other specimens, the crack propagated along the fibre direction at -45° and arrested when it reached the thicker taper section. An interesting feature was observed at the top half of the specimen where the secondary crack lies parallel to the major crack. Delamination of the MMC outer plies between the major and secondary cracks was seen. Figure 4.14 shows briefly there was a spark along the crack plane when the specimen fracture but this time, the fracture occur at the back of the specimen.

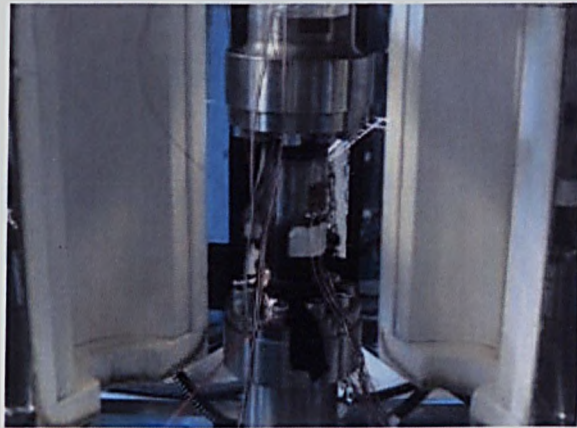


Figure 4.14 Spark along the crack plane at instant of fracture (UTC9)

4.2.1.7 UTC10 ($+45^\circ$ Fibre Orientation)

UTC10 is a specimen with $+45^\circ$ fibre orientation tested at room temperature.

Figure 4.15 shows a schematic diagram of a $+45^\circ$ specimen under torque load. The tensile component acts parallel to the $+45^\circ$ fibres. Hence, this will be the strongest specimen where stressing at the fibre direction gives the best strength. Therefore, no fibre weak plane exists for this fibre orientation and the plane of fracture is at one of the maximum shear stress planes.

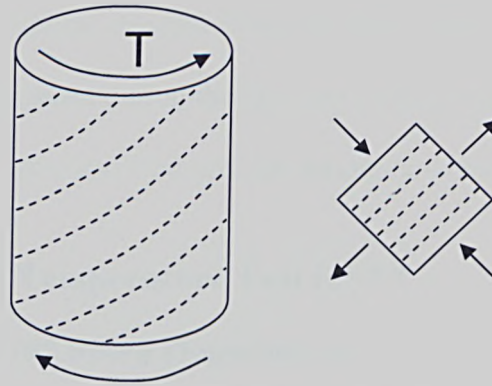


Figure 4.15 Schematic diagram of +45° specimen under torque load

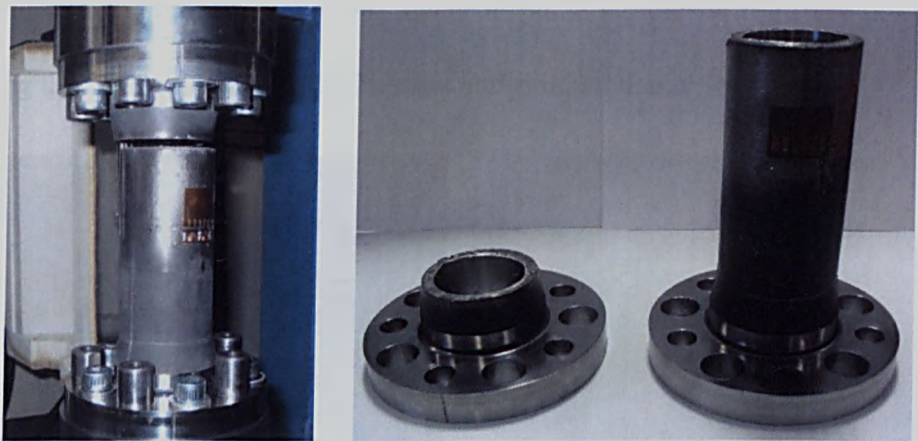


Figure 4.16 Fracture of UTC10 (+45° fibre orientation, room temperature)



Figure 4.17 Spark observed at instant of fracture (UTC10)

Figure 4.16 shows the final state of UTC10 where the fracture occurred at 90° plane between the plain section and the taper section, where 90° plane is one of the maximum shear stress planes. It is suspected that the axial location of the crack is due to the small stress concentration at this region. Despite this, the

specimen gave the highest strength of any of those tested. Figure 4.17 shows the frames from a video taken during the last cycle of the test where fracture occurs. There are lots of spark created around the specimen when the specimen failed.

4.2.2 Elevated Temperature Test (350°C)

4.2.2.1 UTC3 (0° Fibre Orientation)

UTC3 is a specimen with 0° fibre orientation tested at 350°C. Although it is certain that the fracture plane will occur at plane parallel to the fibre direction, testing the 0° specimen at 350°C shows additional damage features.

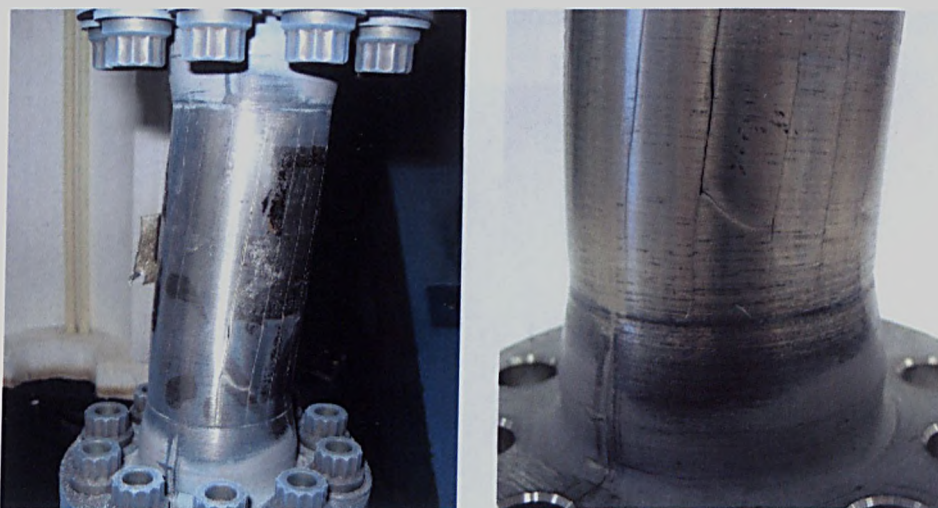


Figure 4.18 Fracture of UTC3 (0° fibre orientation, 350°C)

Figure 4.18 shows the final state of UTC3 after it failed. It is obvious that the major crack occurs at the 0° plane but numerous secondary cracks were observed parallel to the major crack round the plain section. The secondary cracks do not penetrate through into the bore and SEM images shown in a later section will justify this. From the calculation, the ultimate MMC shear strength for this specimen is much lower than the base material. Therefore, the weakest part is within the MMC plies where the crack tends to initiate here and then

propagate to the surface rather than into the bore. Note that near the bottom half of the specimen, the major crack diverts circumferentially before reaching the taper section. At this stage, the load is no longer pure shear where the specimen also shifted transversely. Very large deformation was observed at the last few cycles where the material behaviour is dominated by the matrix material.

4.2.2.2 UTC11 ($\pm 45^\circ$ Fibre Orientation)

UTC11 is a specimen with $\pm 45^\circ$ fibre orientation tested at 350°C . Similar to UTC8 tested at room temperature, the fibre weak plane is at the -45° plane due to the tensile component acts on the -45° fibres.



Figure 4.19 Fracture of UTC11 ($\pm 45^\circ$ fibre orientation, 350°C)

Figure 4.19 shows the final state of UTC11 where the fracture occurred along a -45° plane. The crack propagates along the -45° plane at the plain section and arrest at the taper section. The major crack is symmetric and no secondary cracks were observed. Since specimens were enclosed within the heating chamber for the high temperature tests, it was not possible to observe if there were any sparks at the instant of fracture.

4.2.2.3 UTC12 (-45° Fibre Orientation)

UTC12 is a specimen with -45° fibre orientation tested at 350°C. Similar to UTC9 tested at room temperature, the fibre weak plane is at the -45° plane due to the tensile component acts perpendicular to the fibres.



Figure 4.20 Fracture of UTC12 (-45° fibre orientation, 350°C)

Figure 4.20 shows the final state of UTC12 where the fracture occurred at -45° plane. The major crack also arrested at the taper section at both ends.

4.2.2.4 UTC13 (+45° Fibre Orientation)

UTC13 is a specimen with +45° fibre orientation tested at 350°C. Similar to UTC10, there is no fibre weak plane for this fibre orientation. Therefore, the fracture plane was expected to be at one of the maximum shear stress planes.

Figure 4.21 shows the final state of UTC13 where the crack is asymmetric. It is thought that the crack initiated close to the 0° maximum shear stress plane in the plain section and then propagated axially. In the top half of the specimen, the crack propagated at -15° until reaching the taper section. In the bottom half of

the specimen, the crack propagates at -80° . The crack pattern is unlike that obtained when this fibre orientation was tested at 20°C , where the fracture was on the 90° plane. Despite the asymmetric fracture behaviour, this fibre orientation gives the highest ultimate strength of any of those tested at 350° .

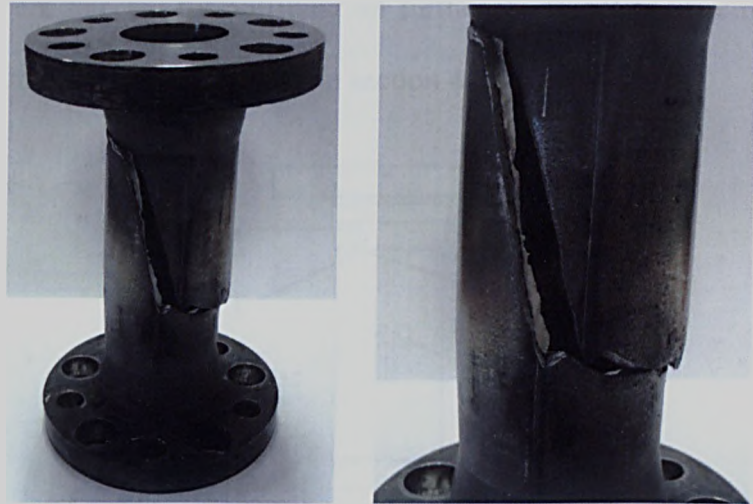


Figure 4.21 Fracture of UTC13 ($+45^\circ$ fibre orientation, 350°C)

4.3 Fractured Surfaces Studies

All tested TiMMC specimens were cut up using wire erosion to produce samples for studying the fracture faces. The smaller sized samples were examined using SEM where high magnification images were obtained and analyzed. These studies were used to identify whether the fracture was shear, tensile or mixed mode. The results from these studies will be presented in the following subsections. Each case includes a cutting plan that gives the reference number for the position of each sample.

4.3.1 UTC1 (0° Fibre Orientation)

Figure 4.22 shows a schematic diagram of the final state of UTC1. The location of each samples obtained from the specimens was shown on the diagram. The dotted red line is where the fracture occurred on the specimen. Sample 3 and sample 5 were selected for polishing for further investigation. The results of all polished samples will be presented in section 4.4.1.

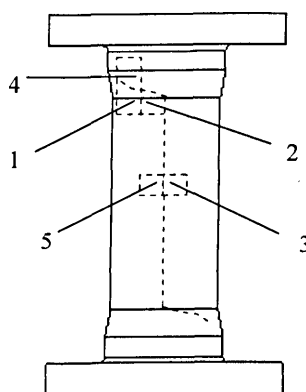


Figure 4.22 Cutting plan for UTC1 (0° fibre orientation, room temperature)

Figure 4.23 shows an image from the top of sample 1 where a broken fibre is visible. It is obvious that a crack developed through the fibre itself. The crack propagated from one side to the other side of the fibre through SiC and round the carbon core. Tensile failure was mainly observed in this region. Figure 4.24(a) shows a shear failure of the fibre and matrix of sample 2. It can be seen that the exposed matrix was sheared in the fibre direction, which is the maximum shear stress plane. Matrix cracking was observed on a number of matrix grooves as seen in Figure 4.24(b).

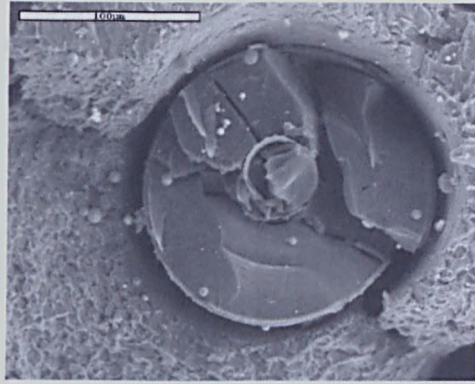


Figure 4.23 Broken fibre (UTC1, Sample 1)

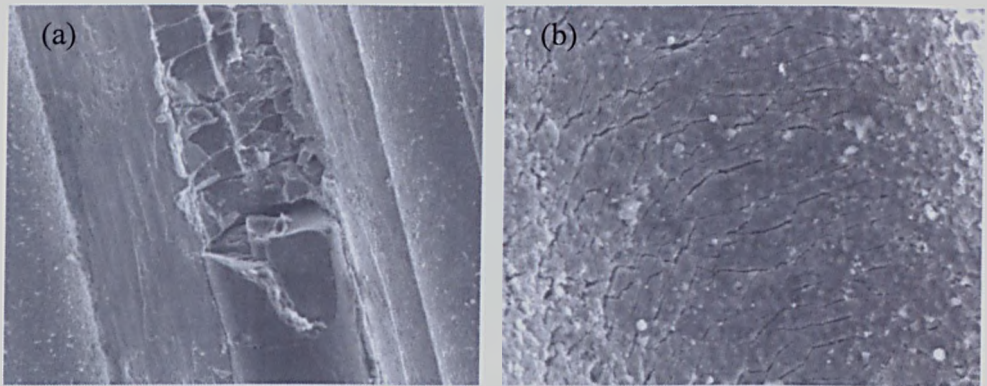


Figure 4.24 Fractured surface of UTC1, Sample 2 (Side)

(a) shear failure on matrix; (b) matrix cracking

At regions remote from the major crack, radial and circumferential cracks within the MMC plies were observed as shown in Figure 4.25. These images confirmed that the crack developed at a point where distance between the adjacent fibres was small. Once the fibres debonded from the matrix, the crack grew easily since there was less matrix material between the fibres. Then, the crack bridging process begins.

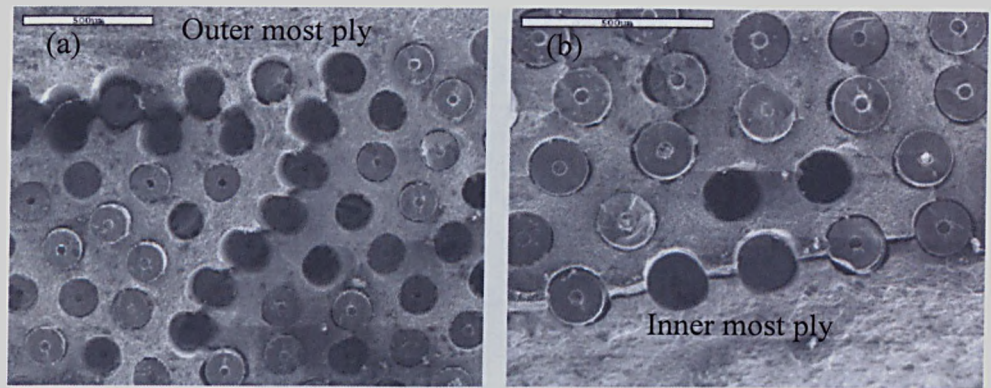


Figure 4.25 Fractured surface of UTC1, Sample 2 (Top)

(a) radial crack; (b) circumferential crack

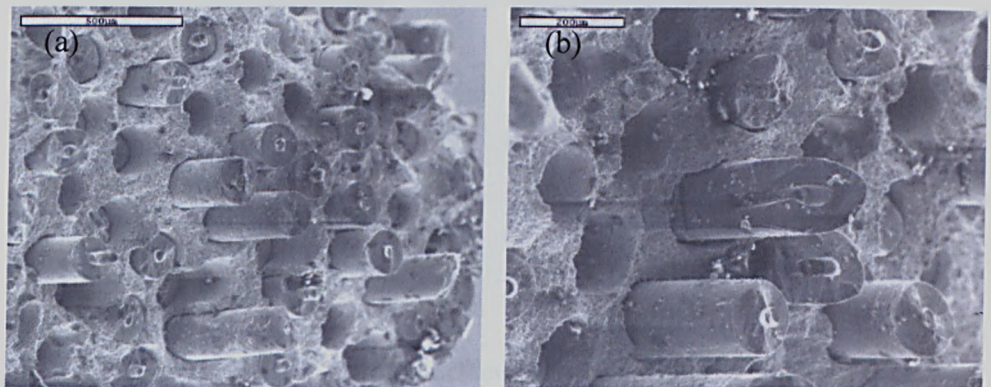


Figure 4.26 Fractured surface of UTC1, Sample 2 (Top)

(a) tensile failure of fibres; (b) shear failure of fibres

Figure 4.26 shows images of sample 2 from top where a mixed mode of tensile and shear failure of fibres were observed. Figure 4.27 shows an example where the fibres already debonded from the matrix and the matrix crack was observed where there is little matrix material between these two fibres. Due to the shear component at the fractured plane, tearing of carbon coating was observed on sample 5 as shown in Figure 4.28(a). Figure 4.28 (b) shows an image on the fractured surface of sample 5. The darker tubes represent the fibres and the brighter one is the matrix grooves where the fibres are attached at the opposite sample.

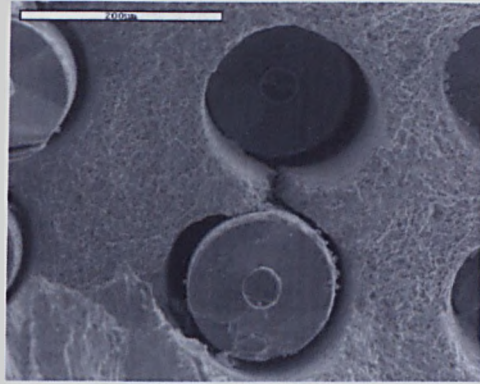


Figure 4.27 Crack developed through debonded fibres (UTC1, Sample 4)

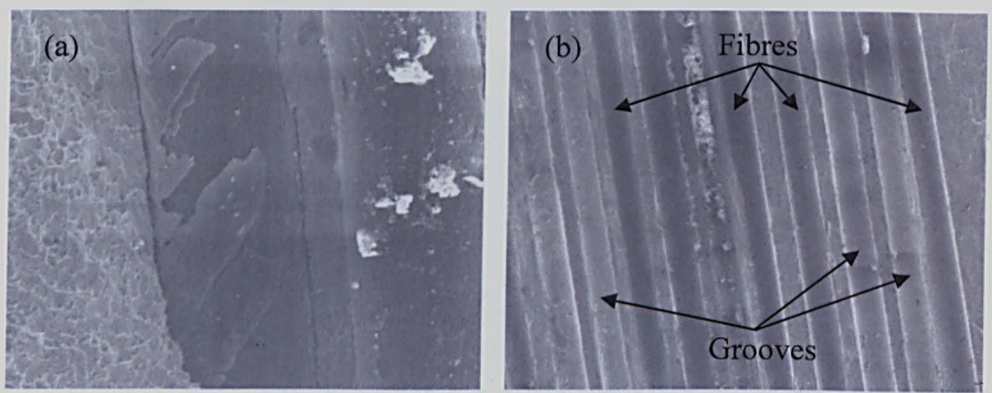


Figure 4.28 Fractured surface of UTC1, Sample 5 (Side)

(a) carbon coating on fibre; (b) fibres and grooves

4.3.2 UTC3 (0° Fibre Orientation)

Figure 4.29 shows a schematic diagram of the final state of UTC3 tested at 350°C. Only major crack is shown on the diagram as dotted red line. Note that there are a number of secondary cracks parallel to the major crack for this specimen. Fracture occurred at the 0° maximum shear stress plane. For this specimen, sample 3 was selected for polishing for further investigation.

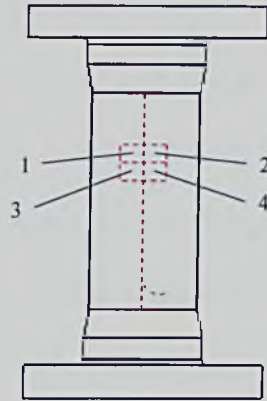


Figure 4.29 Cutting plan for UTC3 (0° fibre orientation, 350°C)

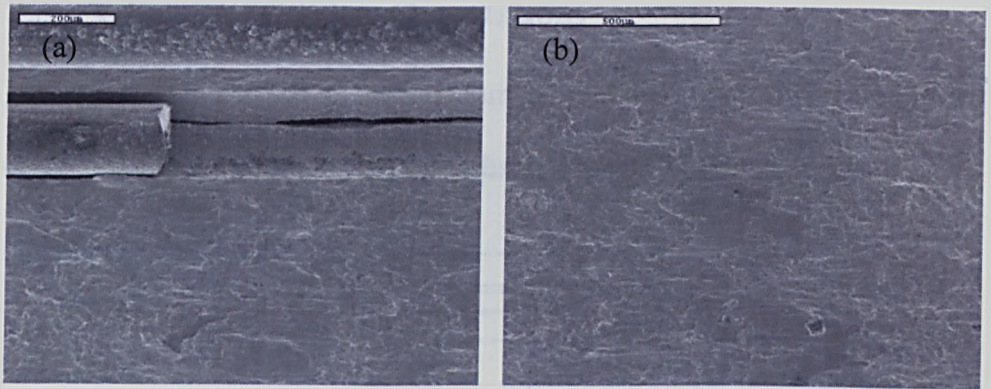


Figure 4.30 Fractured surface of UTC3, Sample 3

(a) and (b) shear failure on matrix

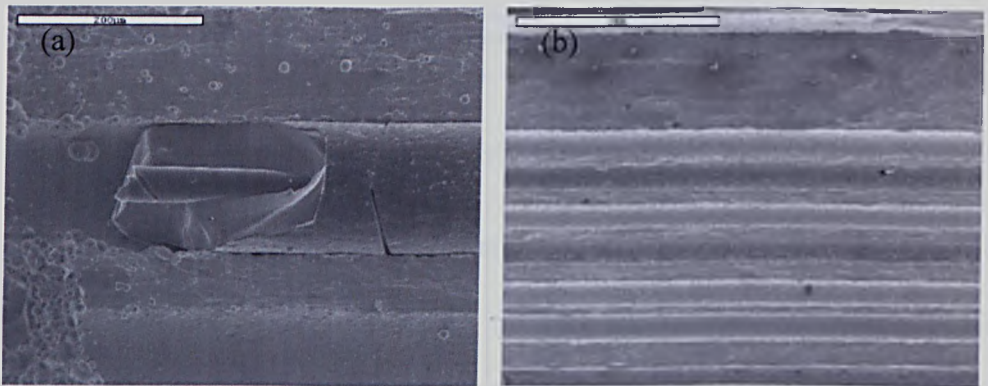


Figure 4.31 Fractured surface of UTC3, Sample 4

(a) broken fibre; (b) shear failure on matrix

Figure 4.30(a) shows the inner-most fibre ply and the matrix material at the inner cladding where shear failure was observed. The matrix is elongated in the direction parallel to the fibres. Matrix cracking at the inner-most ply was also observed. On the other hand, shear failure of matrix was also observed at outer cladding as shown in Figure 4.30(b). Consistent with the fracture occurring at the 0° maximum shear stress plane, shear failure of the fibre was observed as shown in Figure 4.31(a).

4.3.3 UTC5 ($\pm 30^\circ$ Fibre Orientation)

Figure 4.32 shows a schematic diagram of the final state of UTC5. For this specimen, sample 5 was selected for polishing for further investigation.

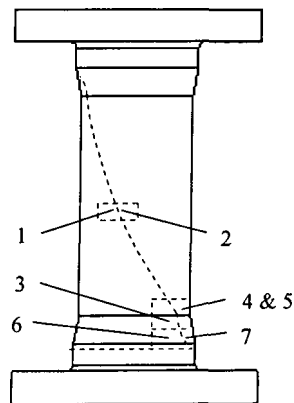


Figure 4.32 Cutting plan for UTC5 ($\pm 30^\circ$ fibre orientation, room temperature)

Figure 4.33(b) is an image of the fractured surface of sample 1 showing the $\pm 30^\circ$ cross-ply fibre plies. Here, the matrix grooves are for the -30° fibres. Figure 4.33(a) and Figure 4.34(a) show a matrix crack at the inner-most ply which is a $+30^\circ$ fibre ply. Figure 4.34(b) shows misalignment of the $+30^\circ$ fibre at the inner-most ply. This will encourage the crack growth since the distance between the fibres is smaller.

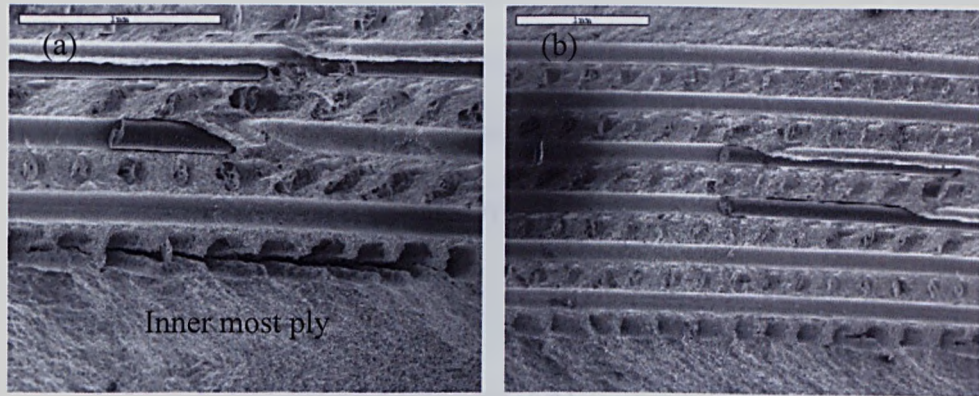


Figure 4.33 Fractured surface of UTC5, Sample 1

(a) crack at inner-most ply; (b) $\pm 30^\circ$ cross-ply fibre plies

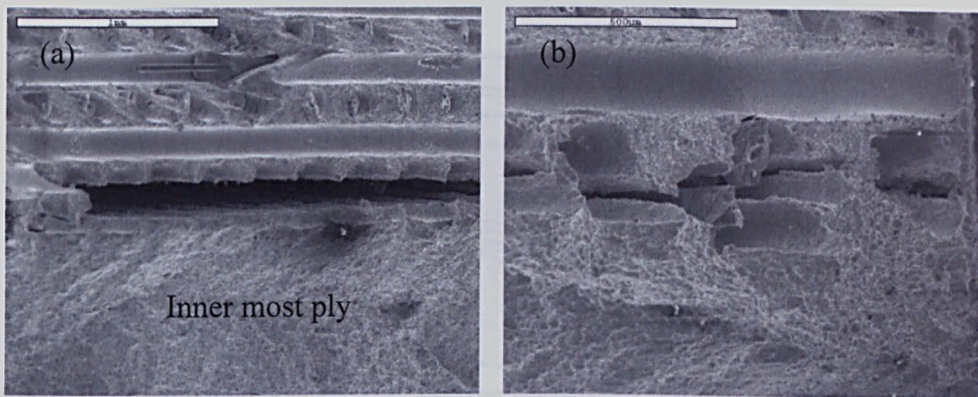


Figure 4.34 Fractured surface of UTC5, Sample 2

(a) crack at inner-most ply; (b) misalignment of fibre

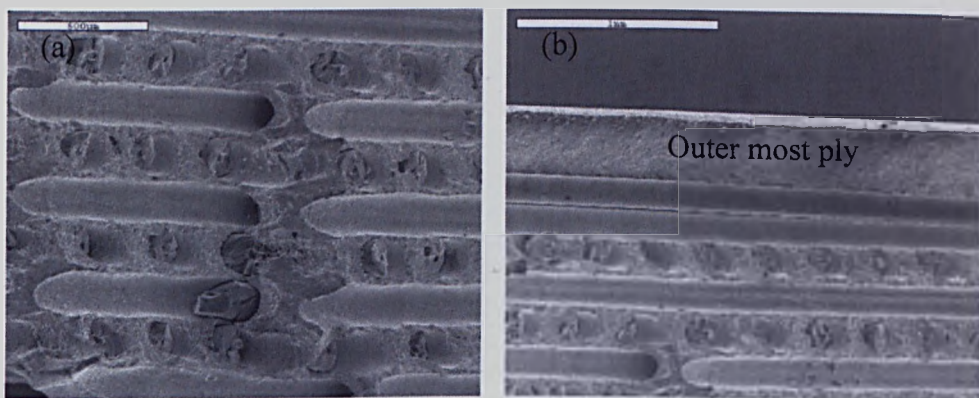


Figure 4.35 Fractured surface of UTC5, Sample 4 (a) step change on fractured

surfaces; (b) extra -30° fibre on top of outer-most ply

Figure 4.35(a) shows an image of sample 4 where unevenness on the fractured surface was observed. Shear failure of the matrix was also seen from the image. Again, misalignment of fibre was observed as shown in Figure 4.35(b). In this image, an extra -30° fibre running on top of another -30° fibre which will encourage cracks to grow at this region.

4.3.4 UTC6 (-30° Fibre Orientation)

Figure 4.36 shows a schematic diagram of the final state of UTC6. For this specimen, sample 3 was selected for polishing for further investigation.

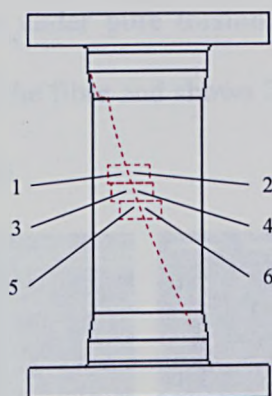


Figure 4.36 Cutting plan for UTC6 (-30° fibre orientation, room temperature)

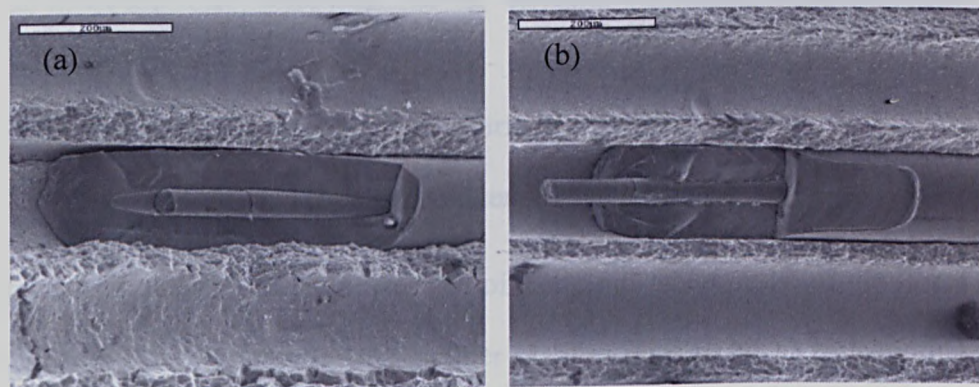


Figure 4.37 Fractured surface of UTC6, Sample 2

(a) and (b) shear failure of fibres

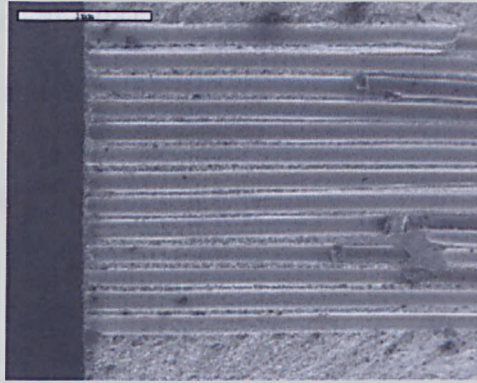


Figure 4.38 Fractured surface of UTC6, Sample 6

Figure 4.37 shows images of shear failure of fibre at -30° fractured plane with matrix grooves on top and bottom of it. A mix of tensile and shear component exist on the fractured plane under pure torsion. In Figure 4.37(a), it clearly illustrates the architecture of the fibre and shows 2 distinct layers of SiC, carbon core and inner carbon coating.

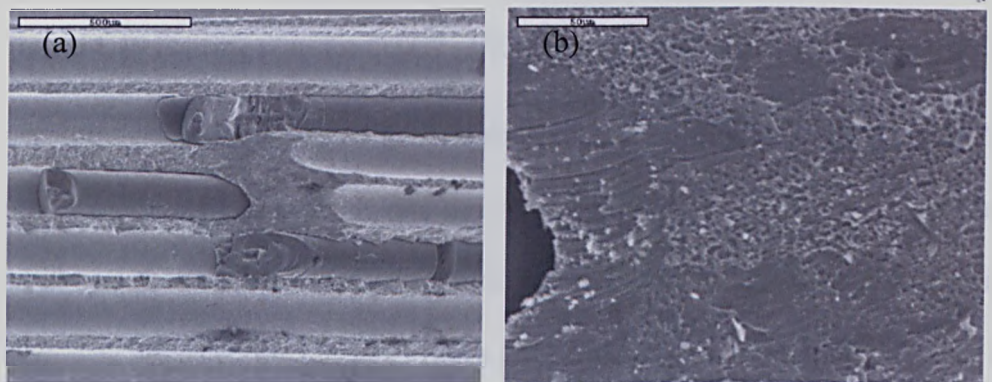


Figure 4.39 Fractured surface of UTC6, Sample 6

(a) and (b) shear and tensile failure on matrix

Figure 4.38 shows a fractured surface of sample 6 where most of the fibres are debonded. It also confirmed the number of fibre plies to be 13 by counting the matrix grooves. Good fibre uniformity was observed in this sample. Figure 4.39 shows a mix of shear and tensile failures of both fibres and matrix. It can be seen

that there are round dimples and some part has elongated shape which correspond to tensile and shear failure, respectively.

4.3.5 UTC7 (+30° Fibre Orientation)

Figure 4.40 shows a schematic diagram of the final state of UTC7. For this specimen, sample 4 was selected for polishing for further investigation.

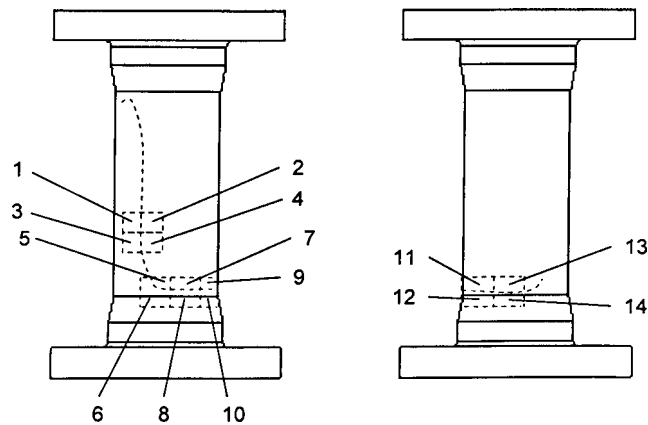


Figure 4.40 Cutting plan for UTC7 (+30° fibre orientation, room temperature)

Shear failure was observed on the fractured plane as shown in Figure 4.41. The dimples are elongated towards one direction rather than in round shape. Figure 4.42 shows the fractured surface of sample 3 where a mix of shear and tensile failure was observed for the +30° fibres. At sample 6 where the crack diverts to 90°, mainly tensile failure was observed here as shown in Figure 4.43. It can be seen that the fractured surfaces of the fibres are mostly flat.

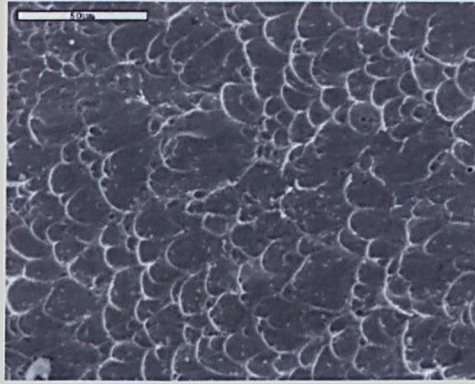


Figure 4.41 Shear dimples on matrix (UTC7, Sample 1)



Figure 4.42 Fractured surface of UTC7, Sample 3

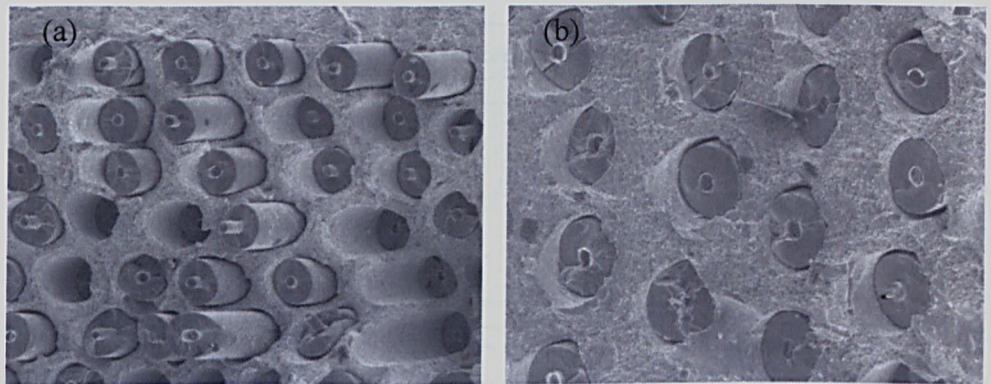


Figure 4.43 Fractured surface of UTC7, Sample 6

(a) and (b) tensile failure of fibres

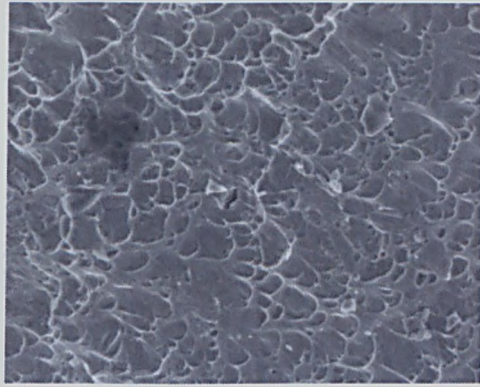


Figure 4.44 Dimples on matrix (UTC7, Sample 8)

In Figure 4.44, elongated dimples on the matrix were observed at sample 8 where it is directed outwards at 45° . This is because the crack surfaces moved in opposite radial directions when fracture occurred.

4.3.6 UTC8 ($\pm 45^\circ$ Fibre Orientation)

Figure 4.45 shows a schematic diagram of the final state of UTC8. For this specimen, sample 5 was selected for polishing for further investigation.

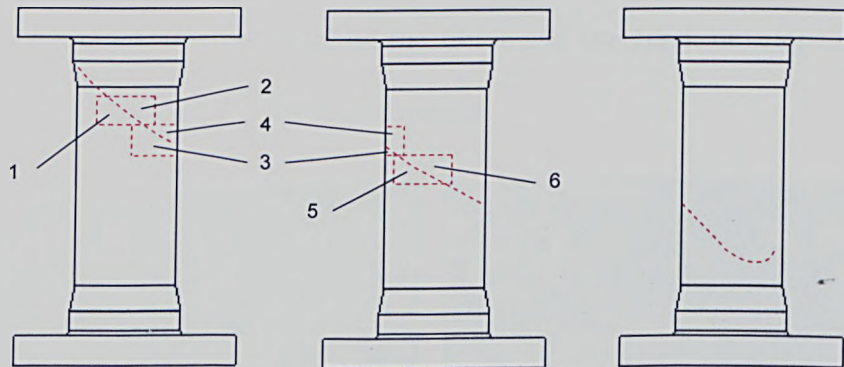


Figure 4.45 Cutting plan for UTC8 ($\pm 45^\circ$ fibre orientation, room temperature)

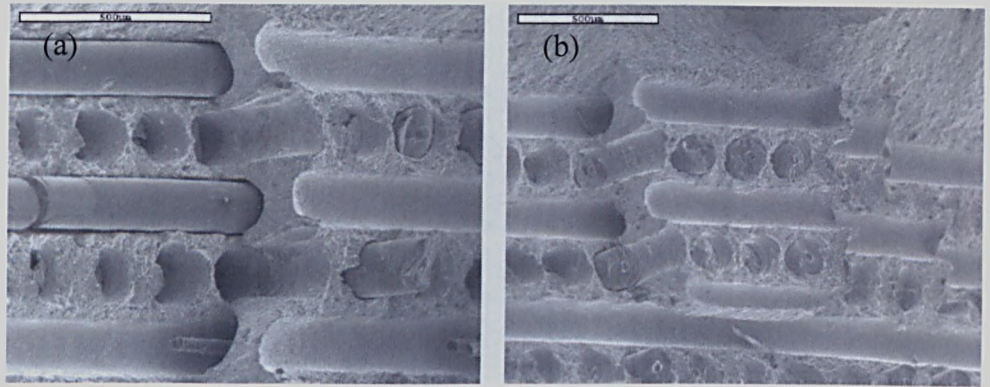


Figure 4.46 Fractured surface of UTC8, Sample 1 (a) and (b) step changes on fractured surfaces showing $\pm 45^\circ$ cross-ply fibre plies

Extensive step changes on fractured surfaces were observed on the top half of the specimen as shown in Figure 4.46. The unevenness on the fractured surfaces suggests the crack was developed at a later stage when fracture occurred. The images also show the cross-ply $\pm 45^\circ$ fibres running at 90° to each other.

Figure 4.47(a) shows a crack at the inner-most ply for sample 2. Within sample 2, a radial crack through the fibre plies was also observed as shown in Figure 4.47(b). No crack was observed on the fibres and the crack developed through the interphase between the fibres and matrix.

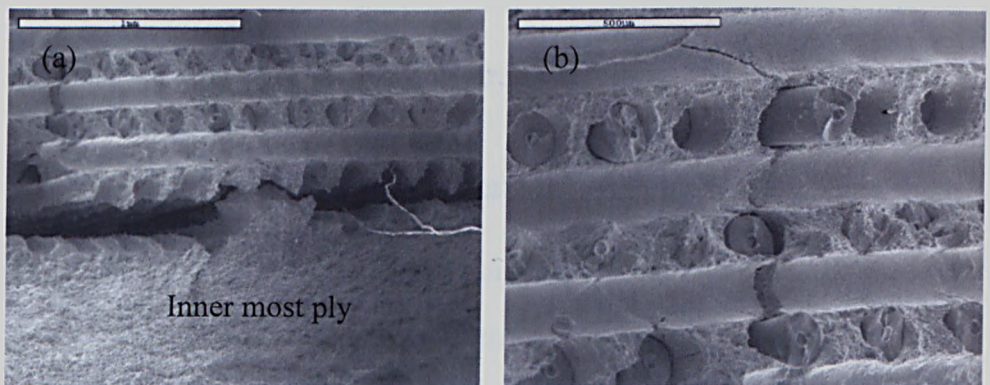


Figure 4.47 Fractured surface of UTC8, Sample 2

(a) crack at inner-most ply; (b) radial crack through fibres

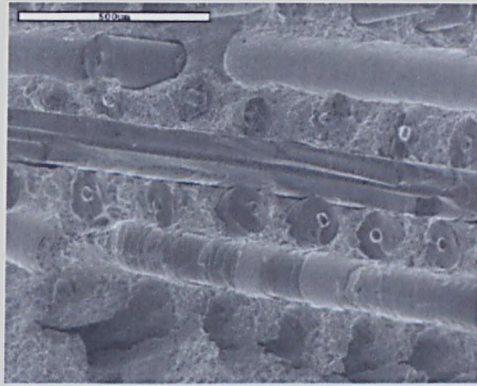


Figure 4.48 Tensile and shear failure of fibres (UTC8, Sample 2)

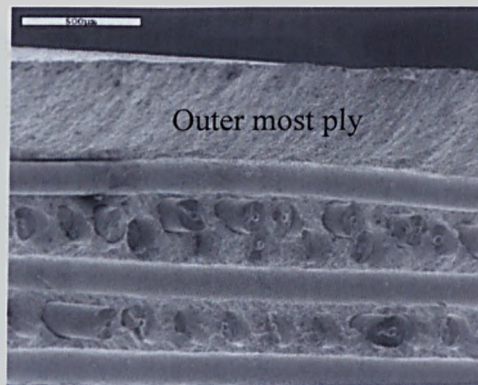


Figure 4.49 Misalignment of $+45^\circ$ fibres (UTC8, Sample 3)

Figure 4.48 shows tensile failure for the $+45^\circ$ fibres and shear failure of the -45° fibres. Some carbon coatings for the -45° fibre still remained on the matrix grooves. Figure 4.49 shows misalignment of a $+45^\circ$ fibre ply which pushed the outer-most -45° fibre ply slightly outward.

4.3.7 UTC9 (-45° Fibre Orientation)

Figure 4.50 shows a schematic diagram of the final state of UTC9. For this specimen, sample 4 was selected for polishing for further investigation.

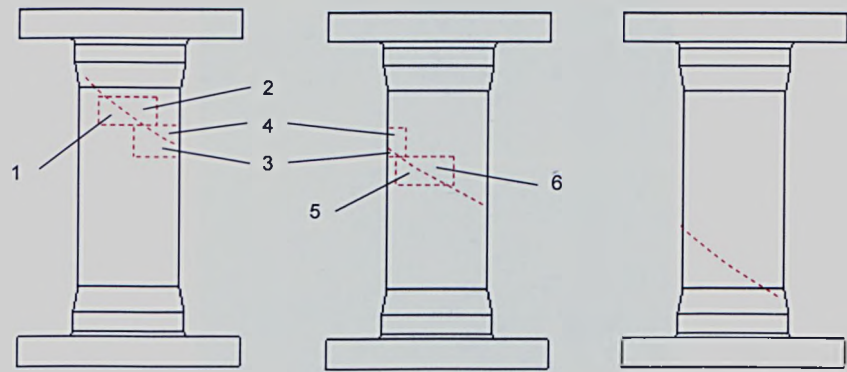


Figure 4.50 Cutting plan for UTC9 (-45° fibre orientation, room temperature)

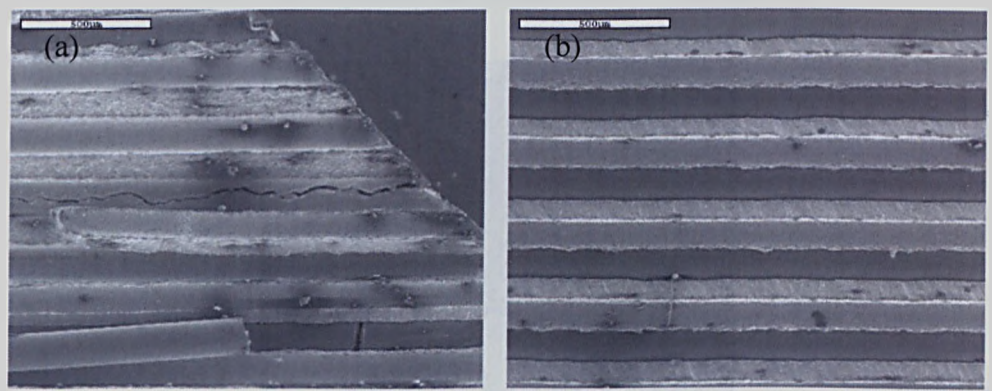


Figure 4.51 Fractured surface of UTC9, Sample 1 (a) crack on the matrix along the fibre; (b) delamination of fibre ply

As mentioned earlier, delamination of fibre plies was observed on samples 1 and 2. Figure 4.51(a) shows a matrix crack along the grooves in the -45° direction where the fibres had debonded. The fracture is due to the tensile component acting transversely to the fibre direction. Figure 4.51(b) shows an example of delamination. This is because a radial component exists here when the crack propagates to this region. From the image, it can be seen that the fibres within a ply are still intact. The brighter part shows the matrix material and the grooves which is very uniform.

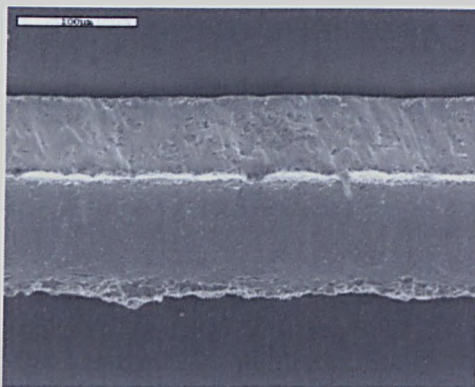


Figure 4.52 Magnified view showing shear failure of matrix where fibre plies delaminated (UTC9, Sample 1)

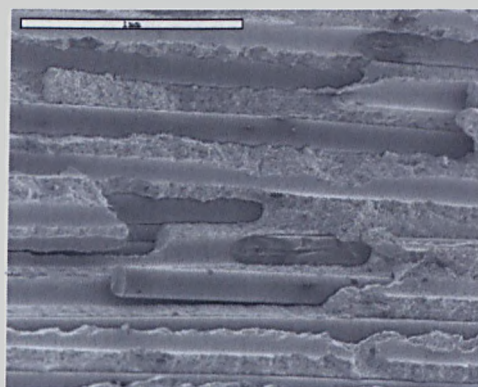


Figure 4.53 Step changes on fractured surface (UTC9, Sample 2)

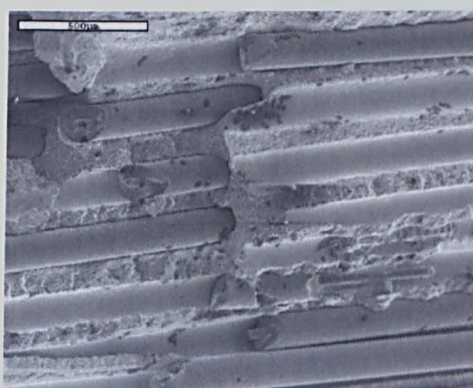


Figure 4.54 Step changes on fractured surface (UTC9, Sample 4)

Figure 4.52 shows a magnified view at the matrix where shear failure in the radial direction due to delamination is clearly illustrated. Figure 4.53 and Figure 4.54 show step changes on the fractured surfaces for samples 2 and 4. This

suggests that the crack did not initiate in this region, which is near the taper section.

4.3.8 UTC10 (+45° Fibre Orientation)

Figure 4.55 shows a schematic diagram of the final state of UTC10. For this specimen, sample 2 was selected for polishing for further investigation. The images from the polished samples will be presented later within this chapter.

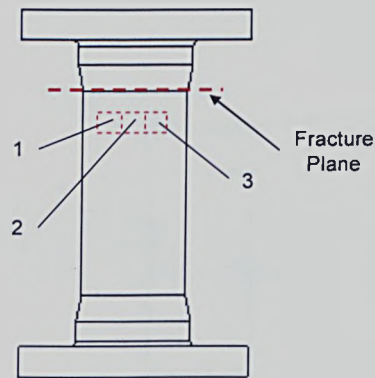


Figure 4.55 Cutting plan for UTC10 (+45° fibre orientation, room temperature)

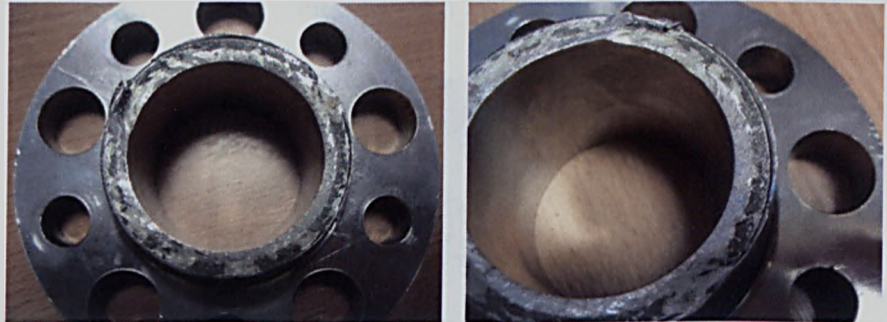


Figure 4.56 Fractured surfaces of UTC10, top half

No SEM images were taken on the fractured surfaces for this specimen because when fracture occurred, the fractured surfaces rubbed against each other and eliminated all failure evidence. Figure 4.56 shows the damaged surfaces of the top part of the specimen. An interesting feature was observed here where the

matrix was peeled off at the outer diameter near the end tip of the taper section. This suggests the bonding between the plain section and the flange piece was faulty.

4.3.9 UTC11 ($\pm 45^\circ$ Fibre Orientation)

Figure 4.57 shows a schematic diagram of the final state of UTC11 tested at 350°C . For this specimen, sample 4 was selected for polishing for further investigation.

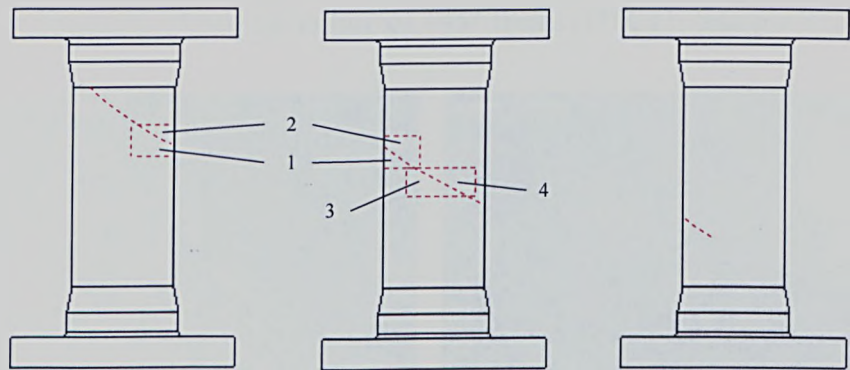


Figure 4.57 Cutting plan for UTC11 ($\pm 45^\circ$ fibre orientation, 350°C)

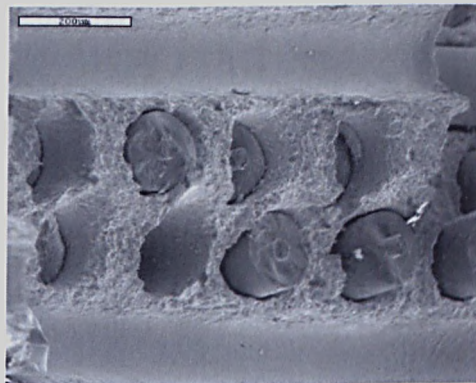


Figure 4.58 Double plies of $+45^\circ$ fibres (UTC11, Sample 1)

Figure 4.58 shows the fractured surface of sample 1 where double plies of $+45^\circ$ fibres can be seen. This could be due to the fibres movement during the HIPping

process. Figure 4.59 illustrates the tensile failure of the $+45^\circ$ fibres and that most of the -45° fibres on samples 2 have debonded.

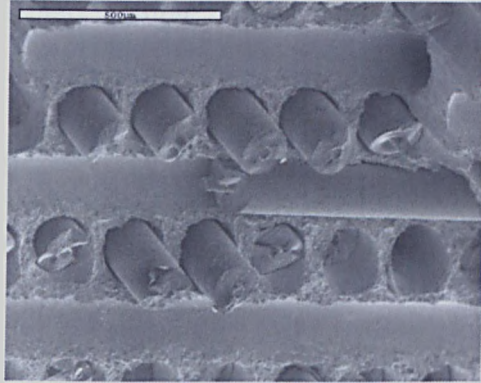


Figure 4.59 Tensile failure of $+45^\circ$ fibres (UTC11, Sample 2)

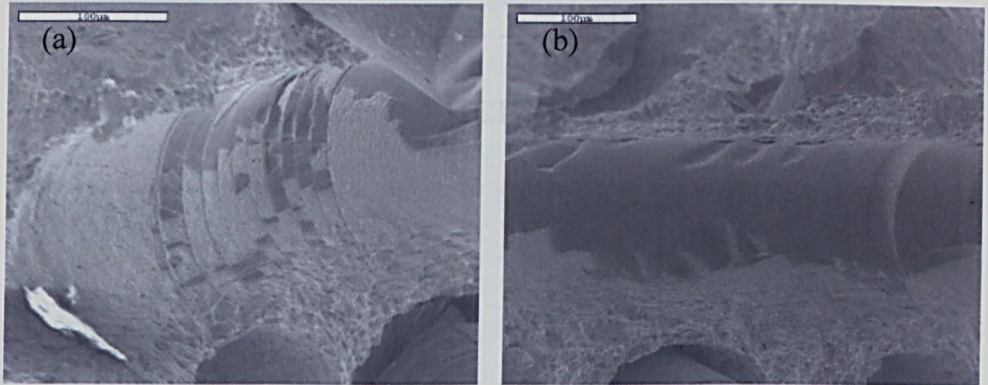


Figure 4.60 Fractured surface of UTC11, Sample 2

(a) and (b) patches of carbon coating left on fibre grooves

Figure 4.60 shows some of the carbon coating still remaining on the grooves where the fibres have debonded. An interesting feature of the carbon coating was observed on Figure 4.60(a) where there are a number of bands on the coatings. It is suspected that this is due to the repeated load cycles applied on the specimen. During loading, the -45° fibres are being pushed along the fibre axis while during unloading they are being pulled.

4.3.10 UTC12 (-45° Fibre Orientation)

Figure 4.61 shows a schematic diagram of the final state of UTC12 tested at 350°C. For this specimen, sample 2 was selected for polishing for further investigation.

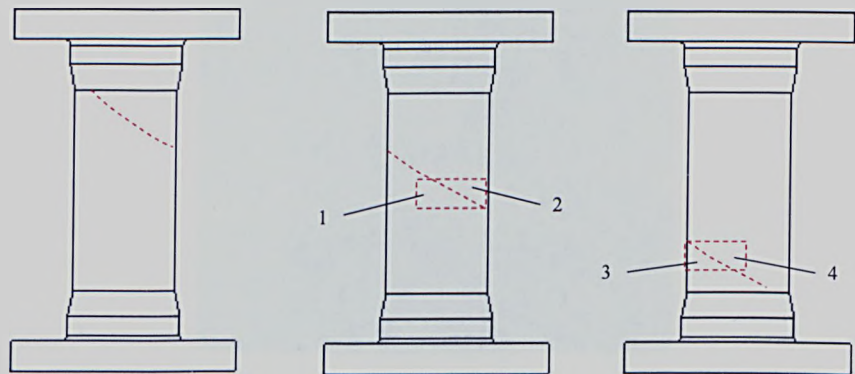


Figure 4.61 Cutting plan for UTC12 (-45° fibre orientation, 350°C)

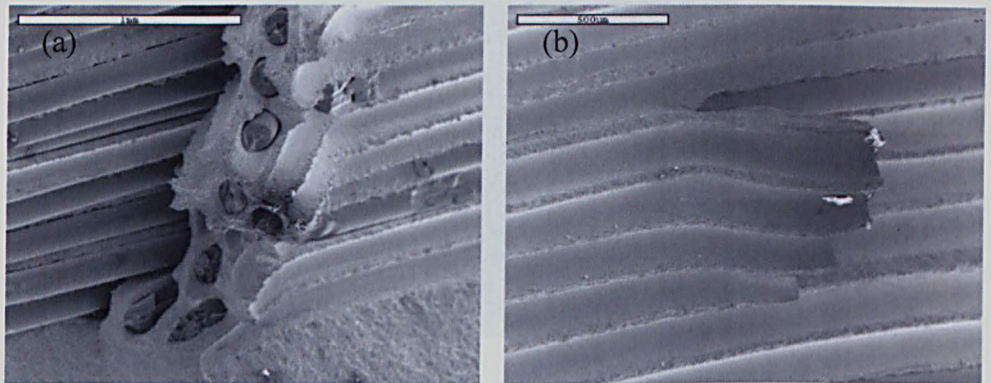


Figure 4.62 Fractured surface of UTC12, Sample 1

(a) and (b) section of material peeled off the fractured surface

Figure 4.62 shows the fractured surface of sample 1 where a section of material was peeled off. This suggests that an internal radial crack might have occurred just prior to fracture or that the distance between the fibres in the radial direction is small so that a crack could grow easily once fracture occurred. Severe cracking was observed on the carbon coating of one of the fibres which is shown

in Figure 4.63. It is suspected that this is due to the effect of temperature. The above phenomenon mentioned was not observed for the -45° specimen tested at room temperature. Figure 4.64 shows the fractured surface of sample 2 where matrix cracking on the groove was observed.

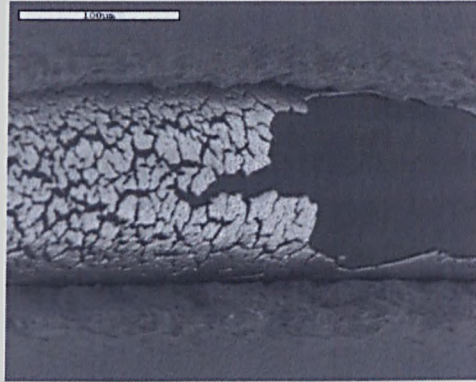


Figure 4.63 Cracking of carbon coating (UTC12, Sample 1)

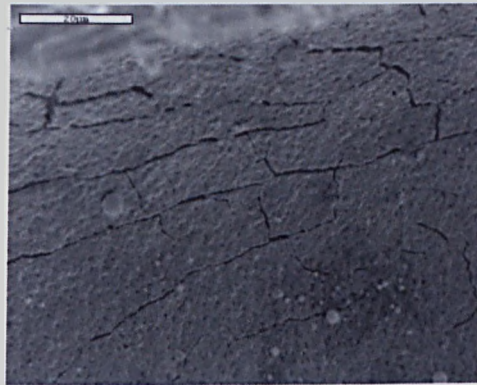


Figure 4.64 Cracking of matrix (UTC12, Sample 2)

4.3.11 UTC13 (+45° Fibre Orientation)

Figure 4.65 shows a schematic diagram of the final state of UTC13 tested at 350°C . For this specimen, sample 2 was selected for polishing for further investigation.

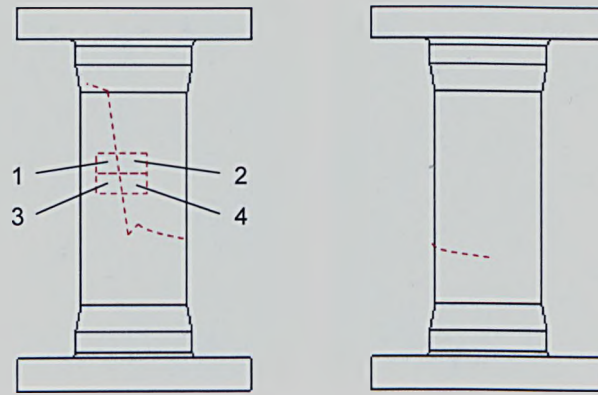


Figure 4.65 Cutting plan for UTC13 (+45° fibre orientation, 350°C)

Circumferential internal cracking was observed at the inner-most ply on sample 3, which is shown in Figure 4.66. As the fractured plane almost aligns at the 0° plane, shear failure is expected along the middle part of the plain section.

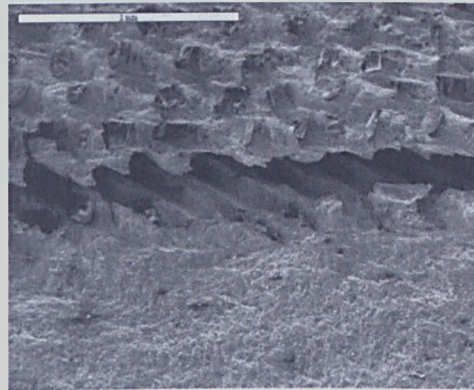


Figure 4.66 Crack at inner-most ply (UTC13, Sample 3)

Figure 4.67(a) shows the shear failure of the matrix material at the inner cladding and Figure 4.67(b) shows the dimples which are slightly elongated. On sample 4, severe cracking on the matrix grooves were observed on the fractured surface as shown in Figure 4.68.

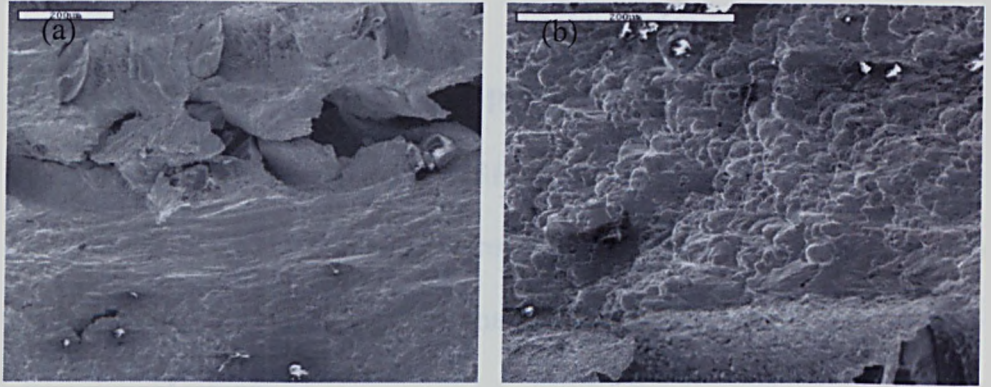


Figure 4.67 Fractured surface of UTC13, Sample 4

(a) shear failure on matrix (b) dimples on outer cladding

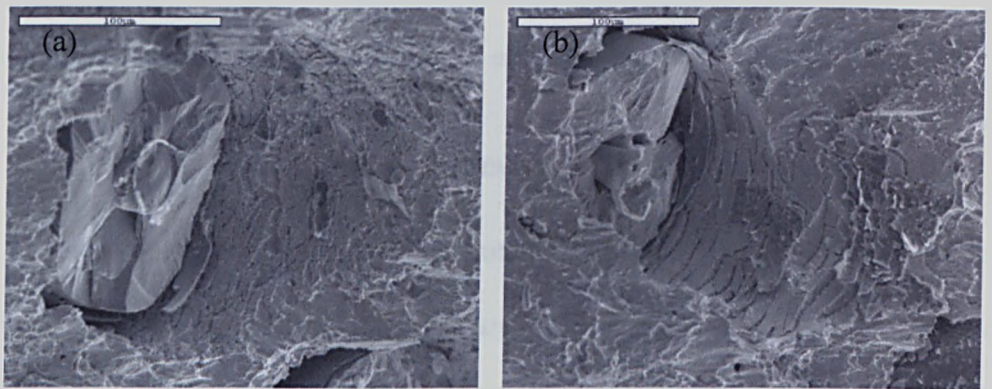


Figure 4.68 Fractured surface of UTC13, Sample 4

(a) and (b) cracking of matrix material

4.4 SEM Imaging

This section outlines the detailed material studies of samples taken from each tested specimen through SEM imaging. SEM images taken from the samples were analyzed and discussed in detail within this section. The samples were polished using a proprietary procedure developed by TISICS Ltd.. A description of available scanning electron microscopy techniques can be found in [39].

4.4.1 Imaging of Polished Samples

The equipment used for capturing SEM images is the JEOL 6400 SEM apparatus with tungsten filament electron gun. The apparatus is fitted with an Oxford Instruments ISIS EDX microanalysis comprising a Si(Li) detector and digital pulse processor.

Not all polished samples are etched, those which have been etched are mostly for microstructural studies, which will be covered in detail in section 4.4.2. Such samples are from monolithic specimens and part of it from UTC1.

4.4.1.1 UTC1 (0° Fibre Orientation)

UTC1 is a 0° tube specimen tested at room temperature. Figure 4.69 (a) is a view transverse to the fibre direction showing a SCS6 fibre of UTC1. This picture shows the constituent parts of the fibre, starting with the carbon core at the middle, the inner carbon coating, the first SiC sublayer, the second SiC sublayer and finally the outer carbon coating. According to Li. et al. [29], the first SiC sublayer contains 11% carbon, whilst the second SiC sublayer consists of SiC only. The image shows the different contrast of these sublayers. Figure 4.69 (b) and Figure 4.70 (a) show the view parallel to the fibre direction where the fibres are lying at different planes. Figure 4.70 (b) shows the axial view of MMC layer where the brighter region is the matrix grooves.

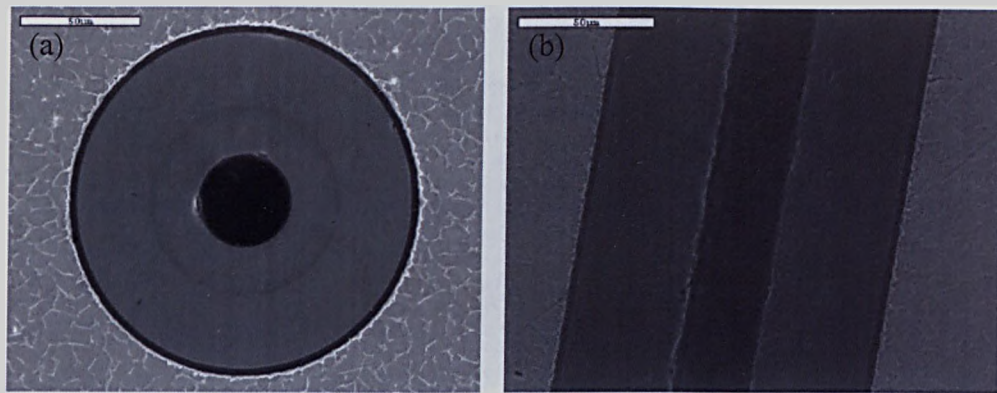


Figure 4.69 Polished and etched surface of UTC1 (a) Cross section of SCS6 fibre sample 5 (b) Transverse section of SCS6 fibre, sample 3

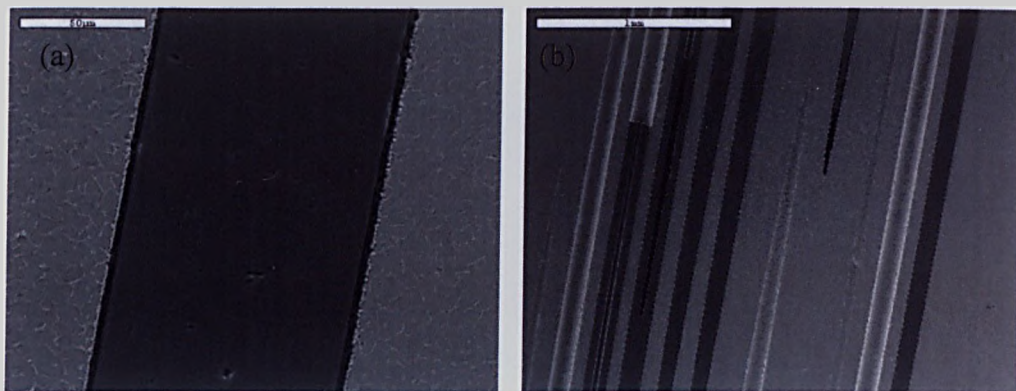


Figure 4.70 Polished and etched surface of UTC1, sample 3

(a) and (b) Transverse section of SCS6 fibre

4.4.1.2 UTC3 (0° Fibre Orientation)

UTC3 is a 0° tube specimen tested at 350°C. Numerous secondary cracks parallel to the major crack were observed. Sample 2 from this specimen was polished and it revealed exactly what happen internally. Figure 4.71 shows one of the secondary cracks that extend through the MMC layer and outer cladding, but not through the inner cladding. Figure 4.72 (a) and (b) is a magnified view of the secondary crack near the outer and inner cladding, respectively. The crack divert circumferentially before reaching the inner cladding.

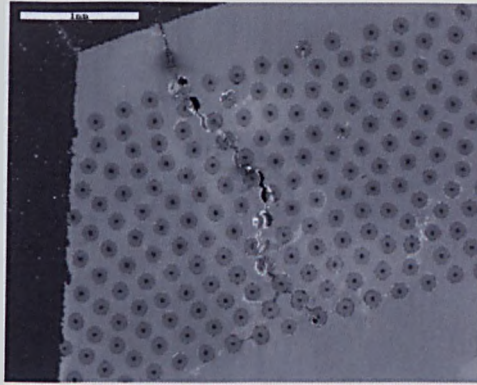


Figure 4.71 Polished surface of UTC3, sample 2
showing the secondary crack at radial direction

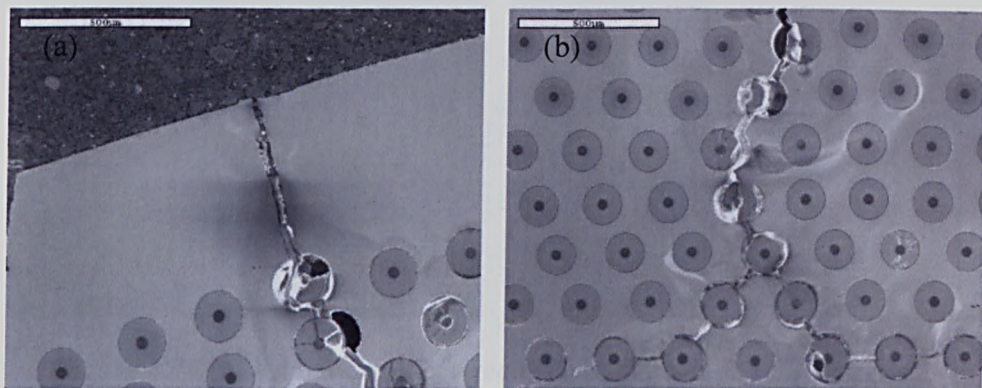


Figure 4.72 Magnified views of Figure 4.71

(a) outer cladding and outer MMC plies (b) inner MMC plies

Figure 4.73 shows the fibre distribution within the material and a hexagonal fibre array was observed in most places. Remote from the major and secondary cracks, internal radial crack at the MMC layer was observed as shown in Figure 4.74. This indicates that the weakest part for this fibre orientation is at the MMC layer. It is impossible to observe this crack externally if the sample has not been polished. The magnified view shows that the crack follows a path where the distances between the adjacent fibres are smallest.

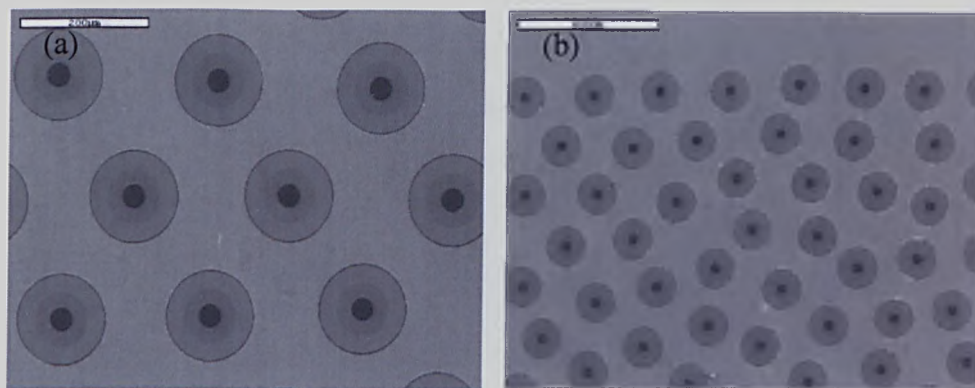


Figure 4.73 (a) and (b) Fibre distribution of UTC3, sample 2

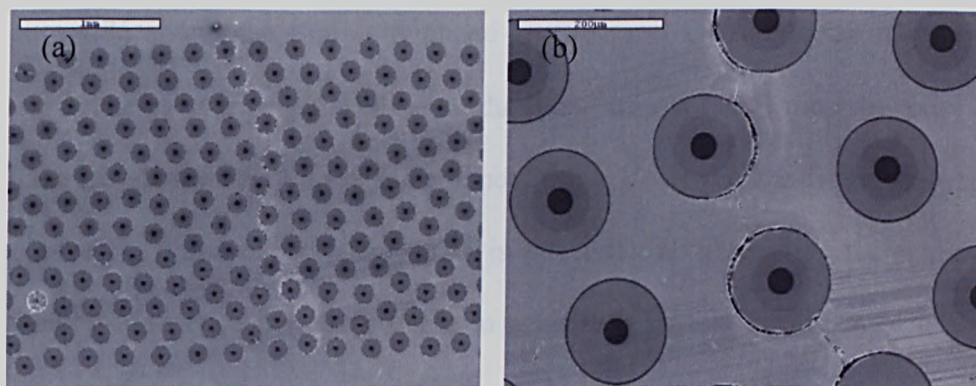


Figure 4.74 (a) Radial crack between MMC plies in UTC3, sample 2

(b) Magnified view of (a)

4.4.1.3 UTC5 ($\pm 30^\circ$ Fibre Orientation)

UTC5 is a $\pm 30^\circ$ tube specimen tested at room temperature. Figure 4.75 (a) and (b) show the fibre distribution at the inner MMC plies and outer MMC plies, respectively. For all cross-ply specimens, the inner-most ply is the positive ply. For this sample from UTC5, good fibre uniformity was observed in most places. However, missing fibres at the outer-most ply was seen at one location as shown in Figure 4.75 (b). The missing fibres might be due to the fibre ply lay up process or due to fibre movement during the HIPping process.

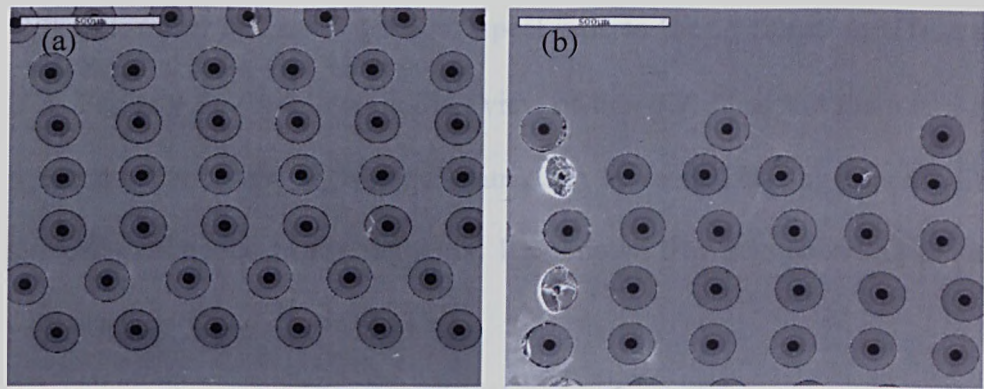


Figure 4.75 (a) and (b) Fibre distribution of UTC5, sample 5

Figure 4.76 shows the fibres orientated at $+30^\circ$ and -30° direction in between plies. In theory, viewing the fibres at the plane transverse to the tube axis, one should see all fibres have the same aspect ratio. However, the fibres shown do not have the same aspect ratio. This is because the fibre plies were laid up manually and hence it is impossible to achieve a perfect specimen at a given fibre orientation. Also, the plane of polishing might not have been exactly perpendicular to the tube axis.

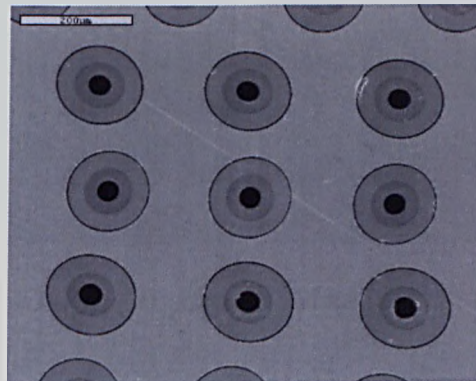


Figure 4.76 Magnified view of fibre plies for UTC5, sample 5

4.4.1.4 UTC6 (-30° Fibre Orientation)

UTC6 is a -30° tube specimen tested at room temperature. Figure 4.77 shows the good fibre uniformity for this specimen. Figure 4.78 (a) shows a -30° fibre but it

is still look rather similar in term of aspect ratio to the 0° fibres on UTC1 and UTC3. Figure 4.78 (b) is a magnified view of the -30° fibre and there is a gap between the carbon coating and the matrix can be seen. This suggests the fibre has already debonded from the matrix. It is known that the debonding process occurs at an early stage during loading.

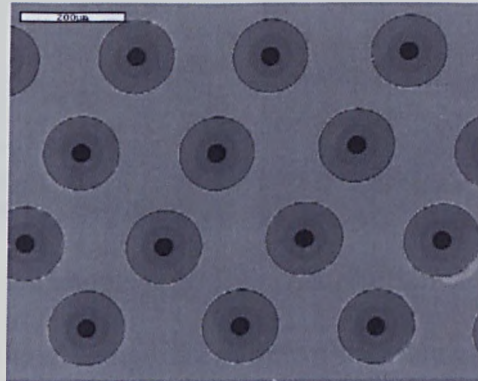


Figure 4.77 Fibre distribution of UTC6, sample 3

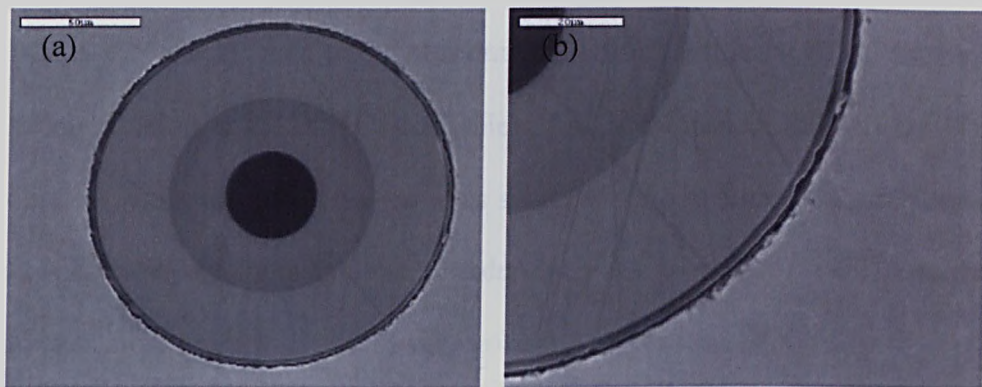


Figure 4.78 (a) -30° fibre (b) Magnified view of (a)

4.4.1.5 UTC7 ($+30^\circ$ Fibre Orientation)

UTC7 is a $+30^\circ$ tube specimen tested at room temperature. Figure 4.79 (a) shows good fibre uniformity in most places with a hexagonal fibre array. The shape of fibres is similar to -30° fibres as seen on UTC6. Figure 4.79 (b) shows a missing fibre in one of the plies. The extra gap in the fibre ply will promote the

movement of adjacent fibres during the HIPping process and could have allowed a crack to develop here due to closeness of the fibres to each other as seen on the picture.

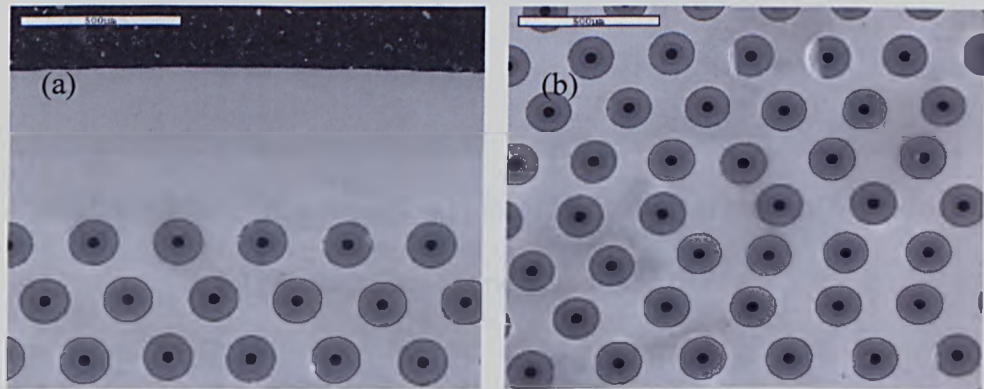


Figure 4.79 UTC7, sample 4 (a) Fibre distribution at outer MMC plies

(b) Missing fibre at one of the fibre ply

4.4.1.6 UTC8 ($\pm 45^\circ$ Fibre Orientation)

UTC8 is a $\pm 45^\circ$ specimen tested at room temperature. Figure 4.80 (a) shows the fibre distribution at the outer MMC plies. Again, the aspect ratio of the fibres should be same, but is not the case, as seen from the picture. Manufacturing a cross-ply tube specimen is much harder than for a unidirectional specimen. However, fibre uniformity is still very good in most places.

Figure 4.80 (b) shows a missing fibre at one of the -45° fibre ply and it is clearly seen some fibres are nearly touching each other. Samples from $\pm 45^\circ$ specimens are rather hard to polish without damaging some fibre edges. From the pictures above, if the fibre is orientated at $+45^\circ$, then the edges on the left of the fibre are thinner and are easily damaged during the polishing process. The bright contrasts on the pictures indicate this. Vice versa for fibres orientated at -45° direction.

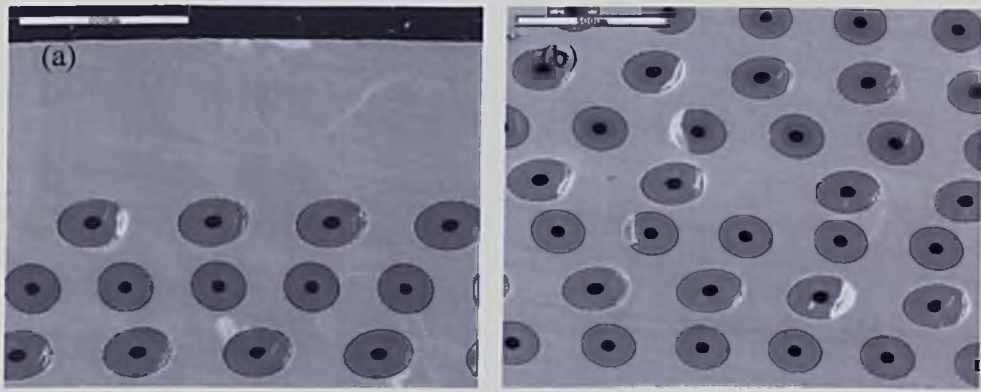


Figure 4.80 UTC8, sample 5 (a) Fibre distribution at outer MMC plies

(b) Missing fibre at one of the -45° fibre ply

4.4.1.7 UTC9 (-45° Fibre Orientation)

UTC9 is a -45° tube specimen tested at room temperature. Figure 4.81 shows the fibre distribution at the MMC plies. Again, good fibre uniformity was observed.

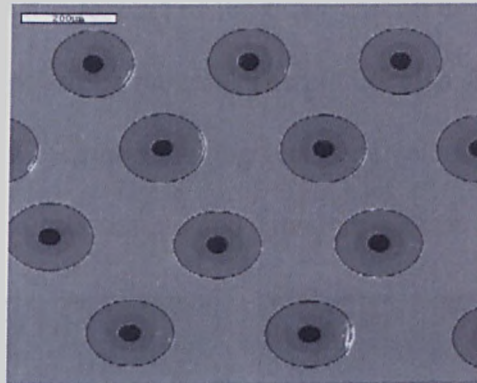


Figure 4.81 Fibre distribution of UTC9, sample 4

Although all fibres are nominally orientated in the -45° direction, the shape of the fibres is not identical as seen on Figure 4.82 (a). Missing fibre was observed in one of the fibre plies as seen on Figure 4.82 (b). Some fibres in this area are very close to each other, making it one of the weaker regions for this specimen; though failure did not occur here.

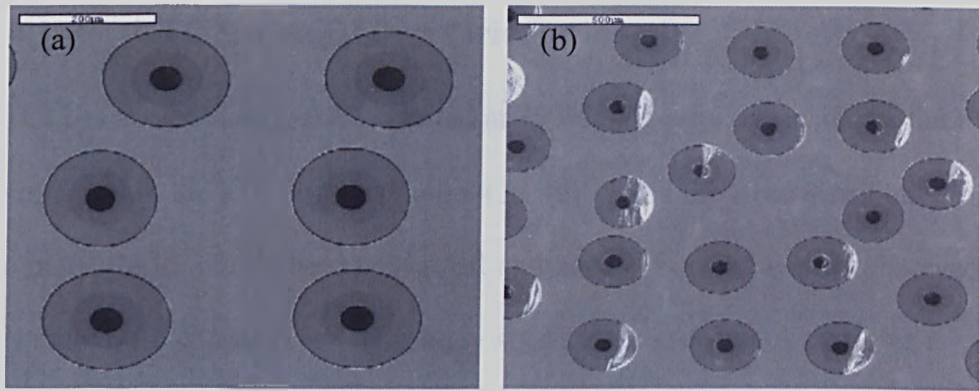


Figure 4.82 (a) -45° fibres (b) Missing fibres at one of the -45° ply

4.4.1.8 UTC10 ($+45^\circ$ Fibre Orientation)

UTC10 is a $+45^\circ$ tube specimen tested at room temperature. Figure 4.83 (a) shows the fibre distribution in the MMC plies. Very good fibre uniformity was observed. Figure 4.83 (b) shows a magnified view of a $+45^\circ$ fibre showing the thinner edges at the left side. Part of the outer carbon coating and SiC has been ripped off during the polishing process. The picture also shows the rough texture of the matrix where the carbon coating has been removed. This is due to the reaction between the carbon coating and Titanium matrix.

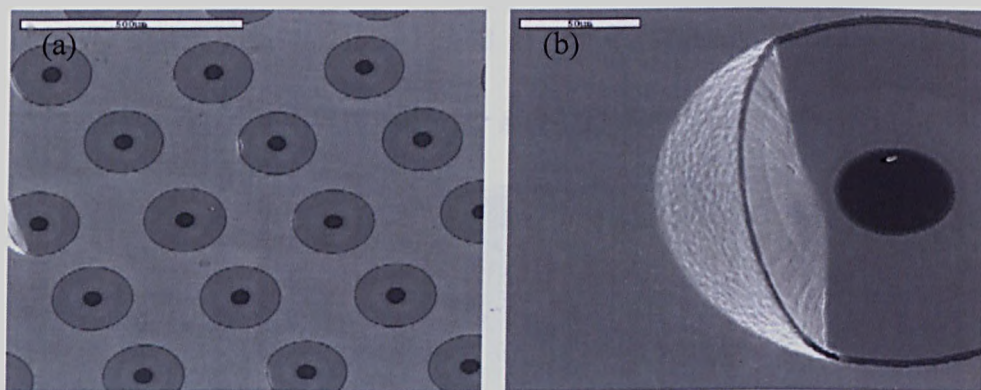


Figure 4.83 (a) Fibre distribution of UTC10, sample 2 (b) $+45^\circ$ fibre

4.4.1.9 UTC11 ($\pm 45^\circ$ Fibre Orientation)

UTC11 is a $\pm 45^\circ$ tube specimen tested at 350°C . Figure 4.84 (a) shows the fibre distribution in the MMC plies. Figure 4.84 (b) shows the fibre distribution near the outer MMC plies where hexagonal and square fibre array was observed at this region. As expected for a cross-ply specimen, the shape of all fibres is very similar.

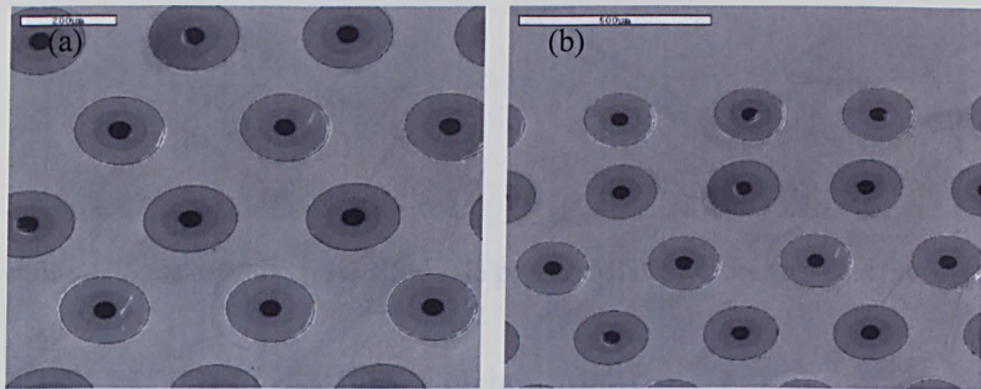


Figure 4.84 (a) Fibre distribution of UTC11, sample 4

(b) Fibre distribution at outer MMC plies

4.4.1.10 UTC12 (-45° Fibre Orientation)

UTC12 is a -45° tube specimen tested at 350°C . Figure 4.85 shows the fibre distribution of the MMC plies with very good fibre uniformity in most places.

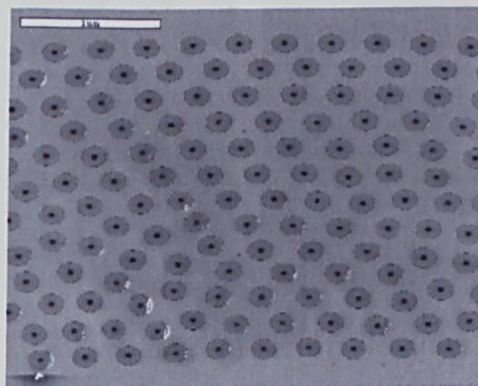


Figure 4.85 Fibre distribution of UTC12, sample 2

Figure 4.86 (a) and (b) show a location where missing fibres were observed in the middle of MMC plies and inner-most ply, respectively. As observed previously, regions with missing fibres can result in the surrounding fibres being very close to each other, which could cause a crack to develop.

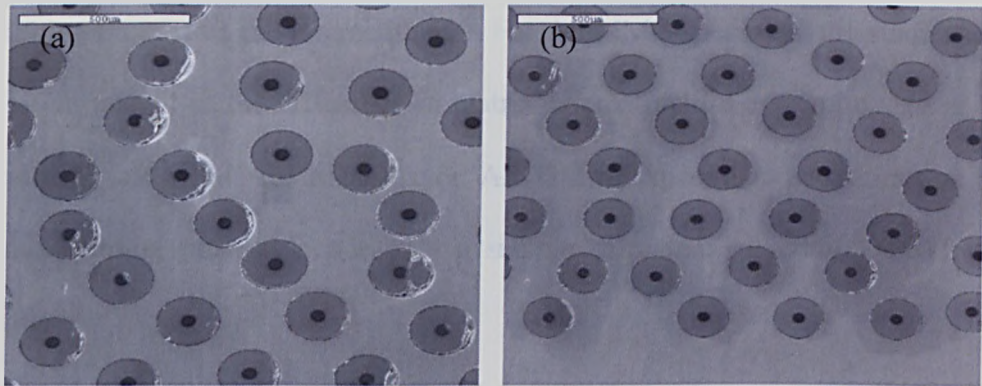


Figure 4.86 (a) Missing fibre at middle ply (b) Missing fibres at inner-most ply

4.4.1.11 UTC13 (+45° Fibre Orientation)

UTC13 is a +45° tube specimen tested at 350°C. Figure 4.87 (a) shows the fibre distribution at the MMC plies and good fibre uniformity was observed in most places. Figure 4.87 (b) shows a missing fibre at the inner-most MMC ply, with resulting non-uniform fibre distribution.

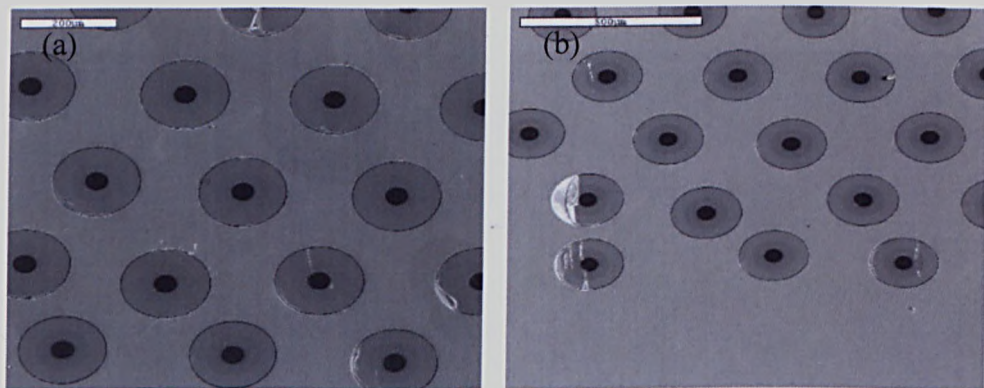


Figure 4.87 UTC13, sample 2 (a) Fibre distribution at middle plies

(b) Missing fibre at inner-most ply

4.4.2 Microstructural Studies

Microstructural studies were carried out on samples taken from both monolithic specimens (solid Ti-6-4 and HIPped Ti-6-4) and UTC1 with 0° fibre orientation. Studies on the monolithic specimens provided an understanding of the effect of HIPping process on the microstructure. For the MMC specimen, the studies also gave an insight of the difference in matrix microstructure and grain size in the claddings and within the MMC layer. All TiMMC specimens went through the same HIPping process, hence only a sample from one of them (UTC1) was studied.

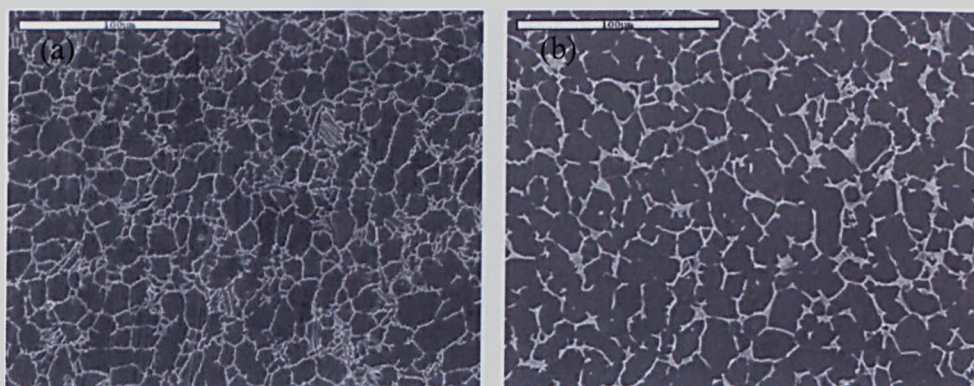


Figure 4.88 Microstructure of matrix material at transverse direction

(a) Solid Ti-6-4, sample 1 (b) HIPped Ti-6-4, sample 1

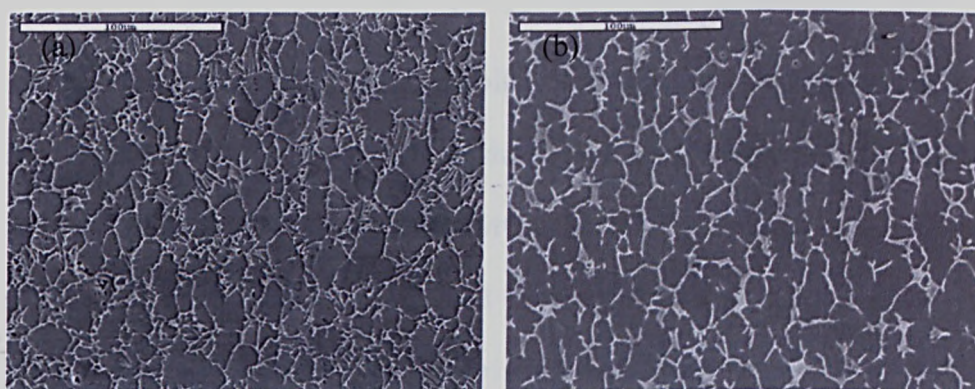


Figure 4.89 Microstructure of matrix material at axial direction

(a) Solid Ti-6-4, sample 2 (b) HIPped Ti-6-4, sample 2

Figure 4.88 (a) and (b) show images of the microstructure for solid and HIPped samples on a plane perpendicular to the tube axis. The microstructure is typical for Ti-6-4, showing equiaxed alpha phase (dark contrast) with beta phase (bright contrast) around the grain boundaries. The grain size of the HIPped sample is larger compared to the solid sample. This is an effect of the HIPping process on the microstructure where the grains grow during the heating stage. The larger grains give a lower elastic modulus, which confirms the experimental result presented earlier. A similar observation was found for samples polished on a plane parallel to the tube axis, as shown in Figure 4.89. However, the grains look slightly elongated on this plane.

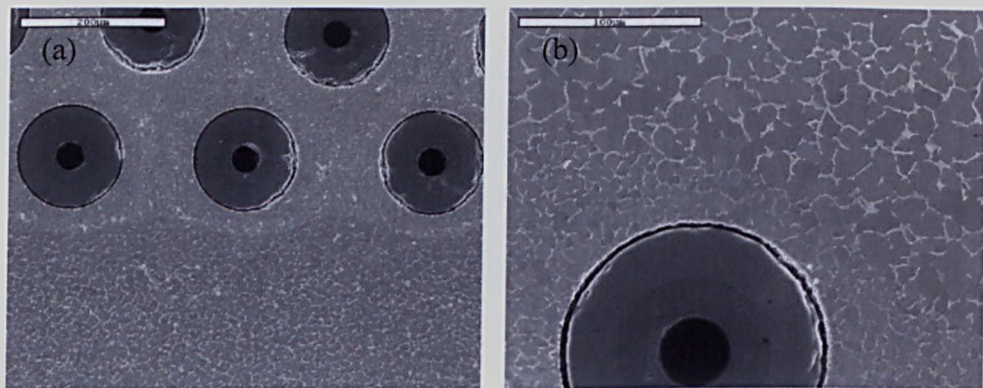


Figure 4.90 Difference in matrix microstructure, UTC1, sample 5

(a) Inner cladding and MMC layer (b) Outer cladding and MMC layer

Samples 3 and 5 from UTC1 were polished at the transverse plane and axial plane, respectively. Figure 4.90 (a) shows the matrix microstructure at the interphase region between the inner MMC plies and inner cladding. It is obvious that distinct regions can be established between the cladding and MMC plies. This is due to the difference in the matrix microstructure resulted from different manufacturing routes.

The fibre was originally supplied as matrix coated fibre (MCF) where Ti-6-4 is coated onto SCS6 fibre using the Electron Beam Physical Vapour Deposition (EBPVD) process. In EBPVD, Titanium, Aluminium and Vanadium are all evaporated at the same time and the alloy coating is then deposited onto the fibre surface. During the production of the tube specimen, the MCF was incorporated into the monolithic Titanium outer cladding and supported on a monolithic Titanium mandrel which provided the inner cladding. The mandrel and outer cladding is conventional Ti-6-4, obtained from extruded bar stock. Figure 4.90 (b) is a magnified view at the interphase region between the outer-most MMC ply and outer cladding.

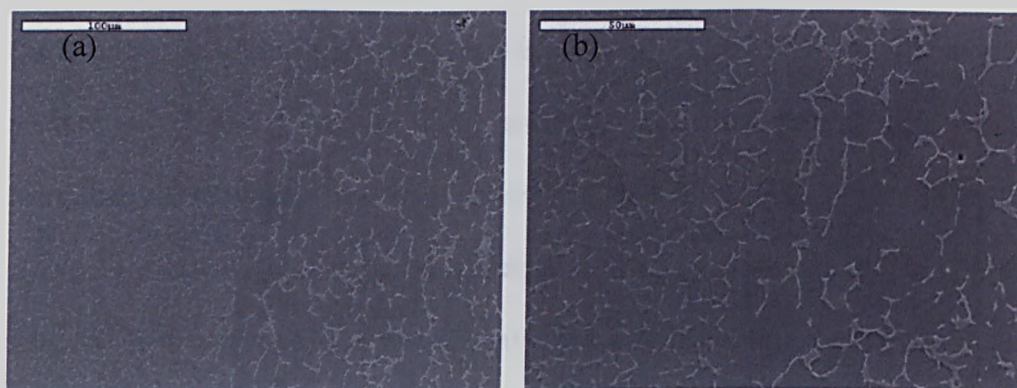


Figure 4.91 Microstructure of matrix material between MMC layer and outer cladding for UTC1, sample 3 (a) View at axial direction
(b) Magnified view of (a)

Figure 4.91 (a) shows the matrix microstructure on a plane parallel to the tube axis. This is the interphase region between the matrix at MMC outer-most ply and outer cladding. Distinct regions were observed due to the different grain size. Figure 4.91 (b) is a magnified view which shows slightly elongated grains in the cladding. This is similar to the observation from the monolithic samples on this plane.

4.5 Energy-dispersive X-ray Analysis

Energy-dispersive X-ray (EDX) analysis has been carried out on sample 5 from UTC1 with 0° fibre orientation. The analyzed surface is transverse to the fibre direction. The objective of this work is to identify the chemical elements at the interphase layer between the outer carbon coating and matrix. As a result of the reaction between carbon and Titanium, the interphase layer is created. The energy spectrum of X-ray radiation is acquired and it is used to identify the chemical elements on the scanned sample. Two methods were used here; line scanning and chemical mapping. These allowed a qualitative analysis of the chemical elements at the interphase layer.

The apparatus used for EDX analysis was a Philips XL30. This has a lanthanum hexaboride (LaB_6) electron gun and Oxford Instruments ISIS EDX microanalysis software. It is more powerful than a JEOL 6400, which is unable to detect the carbon content on the material due to its low atomic number ($Z=6$). Elements with a low atomic number have low efficiency and are hard to detect in a low power SEM machine.

4.5.1 Line Scanning

An almost perfect fibre was identified within sample 5 of UTC1. Then, three separate line scans were made across the interphase region. The images of the line scans are shown in Figure 4.92 (a), (b) and Figure 4.93 at location #1, #2 and #3, respectively.

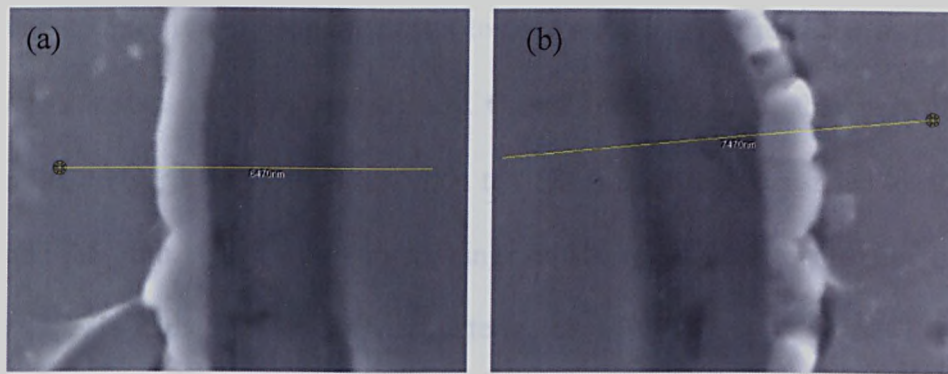


Figure 4.92 Line scanning at interphase region (a) Location #1 (b) Location #2

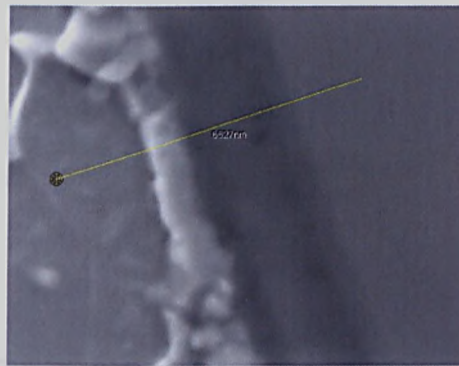


Figure 4.93 Line scanning at interphase region, location #3

These images give an overview of the constituent materials around the interphase region and how they vary physically at different locations. The brightest region next to the carbon coating is the interphase layer.

Location	Thickness (nm)	
	Interphase	Carbon Coating
#1	890	2344
#2	955	2371
#3	812	2313

Table 4.1 Thicknesses of interphase layer and carbon coating

The thickness of the interphase layer and carbon coating can be measured from the images as they have different contrast. The measured thicknesses obtained from each scan are given in Table 4.1. The results show that the thickness of

carbon coating is very consistent but lower than the value reported in [7, 29] which is 3.5 μm and 3 μm , respectively. On the other hand, the thickness of the interphase layer varies between 955nm to 812nm at different scanned locations around the fibre, which is within the range of 500 to 1000nm reported by Duda et al. [17]. Although the matrix material used in [17] was Ti-6242, it is reasonable to expect a similar value for Ti-6-4.

The line scanning results are shown in Figure 4.94-4.96, for scans #1, #2 and #3, respectively.

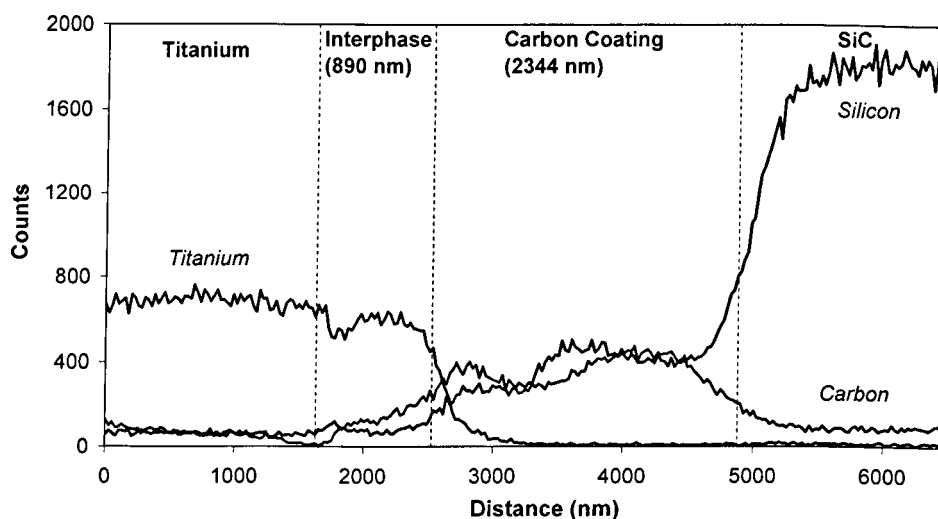


Figure 4.94 Elements distribution at location #1

As expected, the matrix region shows a very high content of Titanium, but the carbon content starts to build up within 500 nm of the interphase layer, especially in scan #2 and #3. In the interphase layer, the Titanium content drops and the carbon content increases when it gets closer to the carbon coating for all scans. The Silicon content is lower than Titanium and Carbon at the interphase layer. Many researchers [17, 33, 37] have speculated that this interphase layer is Titanium Carbide, which is less than a micron thick. The layer is thought to be

brittle in nature and may affect the strength of the bond between the matrix and the fibre. However, the properties for this interphase layer are unknown.

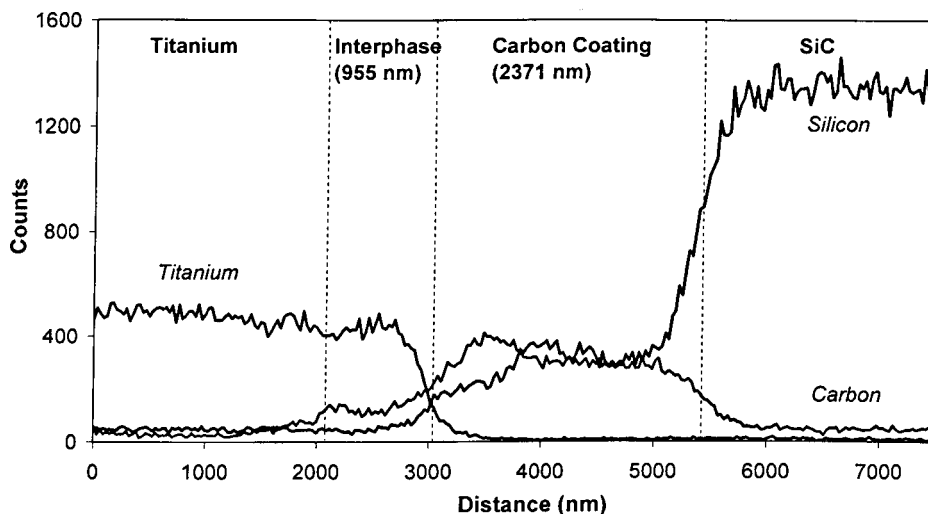


Figure 4.95 Elements distribution at location #2

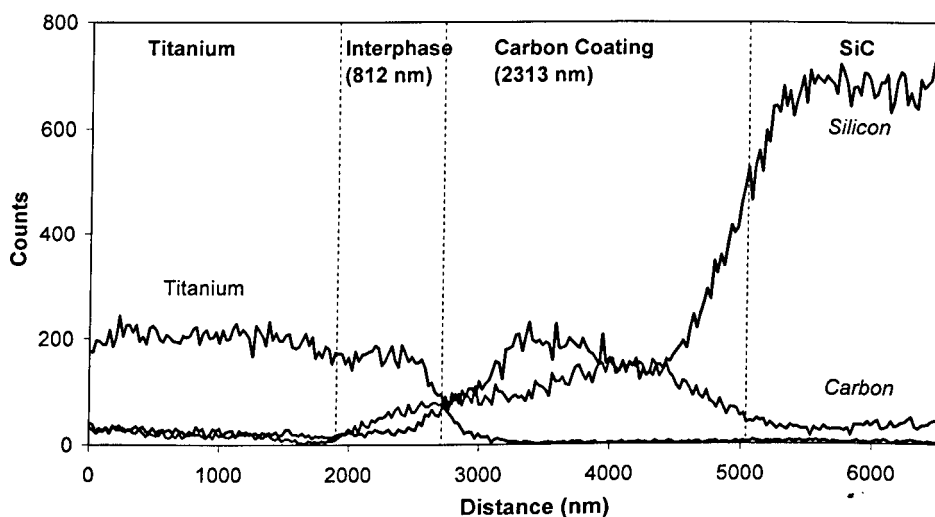


Figure 4.96 Elements distribution at location #3

Both the Silicon and Carbon are observed in the carbon coating, but there is no Titanium in this region. However, the content of the Silicon and Carbon varies at different locations in different scans. Scan #1 and #2 shows a greater amount of Carbon at the beginning while scan #3 has equal amount of Carbon and Silicon.

Li et al. [29] reported that there is a 35% Silicon Carbide content in the carbon coating and these scan results confirm that observation.

4.5.2 Chemical Mapping

In addition to the line scanning method, chemical mapping was carried out on the same sample to identify the various chemical elements in the sample, especially the interphase layer. Similar to line scanning, the energy spectrum of X-ray radiation is acquired during the mapping process, but this is done over an area of interest rather than along a line. The peaks in the spectrum for different elements are identified using the X-ray energy spectrum. Then, the information was used during the mapping process to identify which element in that particular area. The chemical maps for different elements can then be outputted using the software.

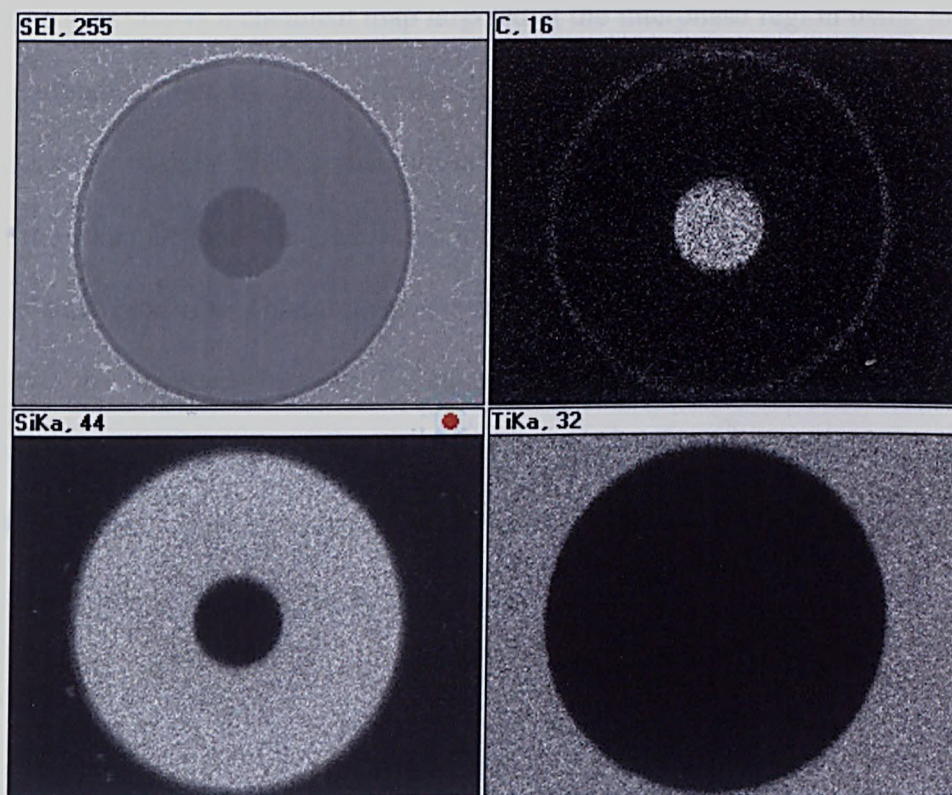


Figure 4.97 Chemical map of a SCS6 fibre and surrounding matrix

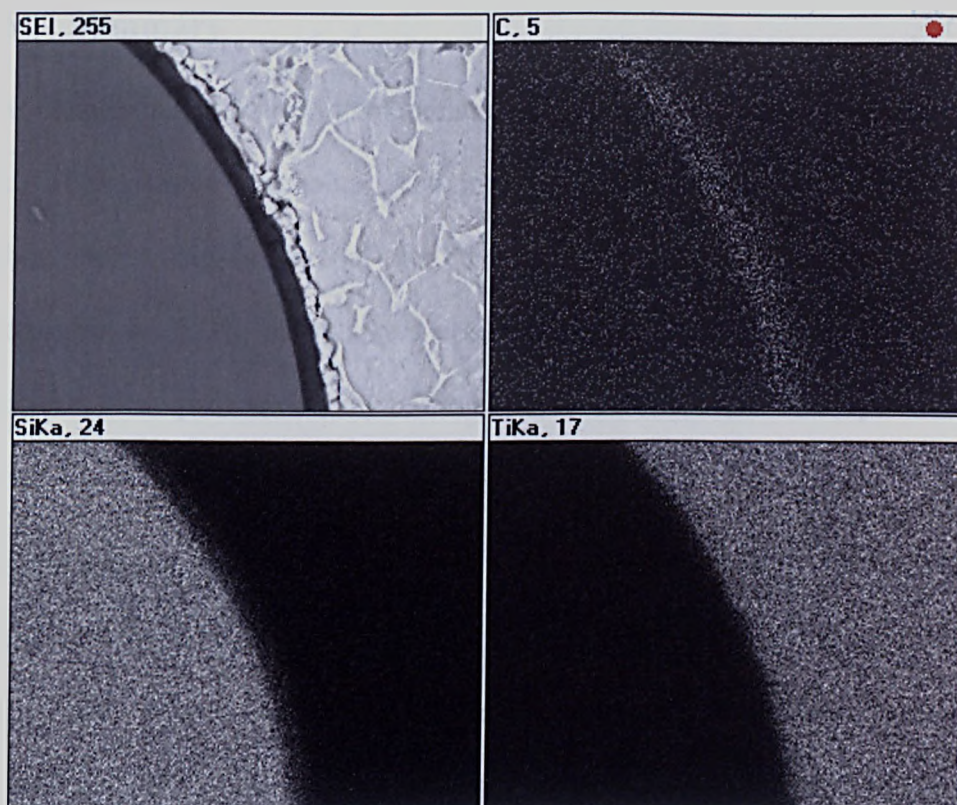


Figure 4.98 Chemical map at interphase region

Figure 4.98 shows a chemical map targeted at the interphase region using higher magnification. For the Carbon map, it can be seen that the ring with bright contrast is slightly thicker than those in the SEM image. This suggests the Carbon exist beyond the outer carbon coating which is where the interphase layer lies. From the Titanium map, beside the very bright region of Titanium matrix, the boundary between the matrix and the outer carbon coating is not distinct. This suggests some Titanium exist between the outer carbon coating and the matrix, where the interphase layer lies. The results are entirely consistent with the findings of the line scanning method.

4.6 Summary

This chapter has described a comprehensive failure investigation carried out on each of the tested specimens. The investigation included understanding the failure mechanism, studies of the fractured surfaces, polished surfaces and microstructure. EDX analysis was also carried out on sample 5 from UTC1, which enable a qualitative study of the chemical elements in the interphase layer between the fibre and matrix.

The failure mechanism of a TiMMC tube depends strongly on the fibre orientation. Hence, all specimens tested here had unique features. However, it is still possible to predict the plane of fracture for any given TiMMC tube, based on the knowledge gained from the experiments. Individual plies exhibit good strength if they are loaded in tension or compression parallel to the fibre direction. However, they are much weaker if they are subjected to either tensile loads perpendicular to the fibre direction or to shear loads in the plane of the fibre. These constitute fibre weak planes. For a TiMMC tube under pure torsion these lie at -45° to the tube axis for transverse tension and 0° and 90° for shear loads. Fibre orientations including plies at these angles (0° , -45° and $\pm 45^\circ$) will fail on the fibre weak plane. The -30° and $\pm 30^\circ$ tubes fail on the -30° plane, which carries a high tensile component. The $+30^\circ$ and $+45^\circ$ tubes do not have a fibre weak plane and they fail on either the 0° or 90° maximum shear stress planes.

Testing the tubes at 350°C does not affect the plane of fracture. The initial damage for all specimens is the debonding process between the fibres and matrix

at lower loads. However, this has no affect to their failure mechanism which is dependent on fibre orientation.

Small samples were cut from the tube to study their fractured surfaces. SEM images of the fractured plane show whether shear, tensile or mixed mode failure occurred. Where the distance between the fibres was small due to missing fibres and fibre relocation in the inner-most ply, circumferential cracks within the MMC plies were observed. Some radial cracks were also observed. The images of fractured surfaces for all samples confirmed that during failure, a large amount of energy was released when the fibres and matrix broke into pieces.

SEM images from polished samples confirmed the manufacture quality of all specimens was good, with good fibre uniformity. UTC3 with 0° fibre orientation tested at 350°C revealed internal cracks between the MMC plies which shows it was the weakest part of the material.

Polished and etched samples from monolithic specimens confirmed the larger grain size on the HIPped samples. This leads to the lower modulus measured on the HIPped Ti-6-4 tube compared to the solid Ti-6-4 tube. Samples from UTC1 also show the difference in microstructure between the cladding and within MMC layer. This is due to the different manufacturing routes experienced by the matrix, which is supplied as MCF (using Ti-6-4 coated onto the fibre using the EBPVD process) and the cladding material, which is conventional Ti-6-4 obtained from extruded bar stock.

EDX analysis using line scanning and chemical mapping methods confirmed that the interphase layer mainly comprised Titanium and Carbide. The measurements correlate well to those reported in [17].

Chapter 5 describes the prediction of TiMMC material properties using the FE method. Numerical models such as the unit cell models and the tube models were developed using the ABAQUS software package and Rolls-Royce in-house FE package – SC03. Effective MMC shear moduli for tube models with different fibre orientations were predicted and compared with the experimental results presented in Chapter 3.

CHAPTER 5

PREDICTION OF TIMMC MATERIAL PROPERTIES USING FINITE ELEMENT METHOD

5.1 Introduction

Finite Element (FE) models have been developed for comparison with the experimental results presented in Chapter 3, in order to assess how well the models are able to predict the material behaviour. The reason for this is to use the model to avoid unnecessary testing of components in order to reduce costs and timescales.

Two different finite element software packages were used here, i.e. the ABAQUS software package and a Rolls-Royce in-house FE package - SC03. Unit cell models were developed to predict the global orthotropic elastic properties for a TiMMC. The material constants (Young's moduli, shear moduli and Poisson's ratios) obtained through the ABAQUS and SC03 unit cell models, were used to define the orthotropic elastic properties, for MMC core layer in the tube models and this will be discussed in detail in a later section. A 360-degree, fully parametric tube model was developed in ABAQUS and a cyclic symmetry tube model was developed in SC03. Using both FE packages allowed an assessment of which package gives the best prediction

5.2 Prediction of Global Orthotropic Elasticity

To define an orthotropic material model for use in FE analysis, Young's moduli, shear moduli and Poisson's ratios related to each global direction are needed, as indicated in Table 5.1. For Poisson's ratio, ν_{12} is the ratio of strain in the 2-

direction to the strain in the 1-direction when a strain is applied at 1-direction, etc. For shear modulus, G_{12} is the ratio of shear stress τ_{12} over shear strain γ_{12} , where γ_{12} is a rotation towards the 2-direction of 1-axis, etc. These constants can be determined from the results of unidirectional 0° unit cell models, developed both in ABAQUS and SC03. The SC03 model was used to predict the Young's moduli and Poisson's ratios and the ABAQUS model was used to predict the shear moduli. The reason for using the ABAQUS model in this case is because the SC03 FE system can not impose a "planes remains plane" boundary condition under shear condition.

Young's Moduli	E_1, E_2, E_3
Poisson's Ratio	$\nu_{12}, \nu_{13}, \nu_{23}$
Shear Moduli	G_{12}, G_{13}, G_{23}

Table 5.1 Material constants for an orthotropic material model (ABAQUS)

These material constants were used to define the orthotropic material properties for the MMC core layer in the tube models. Although both ABAQUS and SC03 required 9 material constants in order to define an orthotropic material model, the Poisson's ratios and shear moduli needed are in different directions. Table 5.2 shows the material constants needed in SC03.

Young's Moduli	E_x, E_y, E_z
Poisson's Ratio	$\nu_{xy}, \nu_{yz}, \nu_{zx}$
Shear Moduli	G_{xy}, G_{yz}, G_{zx}

Table 5.2 Material constants for an orthotropic material model (SC03)

5.3 Unit Cell Models

A micromechanical analysis, such as unit cell model, is a very useful design tool, for the study of fibre-reinforced composite materials, and in particular, for a

monofilament MMC. A typical geometric model, used for the micromechanical analysis, is a repeating unit of matrix material containing an embedded single fibre. This is based on the assumption that a periodic fibre packing array exists and the region of interest is reduced via periodicity arguments [34]. The idealised fibre packing arrays can be either square or hexagonal.

ABAQUS	SC03
Ti-6-4	
E	E
v	v
SiC	
E	E
v	v
Carbon Core	
E	E
v	v
Carbon Coating	
E₁	E_x
E₂	E_y
E₃	E_z
v₁₂	v_{xy}
v₁₃	v_{yz}
v₂₃	v_{zx}
G₁₂	G_{xy}
G₁₃	G_{yz}
G₂₃	G_{zx}

Table 5.3 Material constants of constituent materials for ABAQUS and SC03

For the unit cell models developed here, it was assumed that a perfect bond existed between the matrix and the fibre. Two types of unit cell models have been developed; these are the unidirectional 0° unit cell model and the cross-ply ±45° unit cell model. The fibre for the unidirectional unit cell models is orientated at the axial direction and the fibres for cross-ply ±45° unit cell model are orientated at right angles to each other. The loading conditions and boundary

conditions in these unit cell models are intended to simulate a tube subjected to a pure torque loading.

The unit cell models have four constituent materials specified; these are the titanium matrix, silicon carbide, carbon core and carbon coating materials, respectively. The material properties data for the carbon core, silicon carbide and carbon coating were provided by Rolls-Royce and are obtained from SC03 material files. The shear modulus for the titanium matrix was obtained from the results of a torsion test on a HIPped, monolithic specimen; the Poisson's ratio was obtained from SC03 material files. Table 5.3 presents the material constants of the constituent materials needed in both ABAQUS and SC03 analyses. However, the values for each constant are not included as it is Rolls-Royce proprietary data. The material properties for the carbon coating are defined as an orthotropic material model, which is defined differently in ABAQUS and SC03 analyses. For SC03, subscript z represents the radial direction of the carbon coating and subscript x and y represent the axial and tangential direction, respectively. For ABAQUS, subscript 1 represents the radial direction and subscript 2 and 3 represent the tangential and axial direction, respectively. The Young's modulus for carbon coating in the fibre radial direction is a lot lower than that in the axial and tangential direction. This is because the carbon coating is characterised by multiple sublayers, which are arranged parallel to one another, and are bonded by relatively weak van der Waals forces in the radial direction [29]. The material properties are based on the local material directions specified in the model. The Poisson's ratios used in ABAQUS need to be changed accordingly, based on the straining direction and the contraction at the

transverse direction. ν_{12} and ν_{13} in ABAQUS are equivalent to ν_{zx} in SC03 and ν_{23} is equivalent to ν_{xy} , allowing for the fact that the weak direction for the carbon coating in ABAQUS and SC03 models are the 1-direction and z-direction, respectively.

The fibre volume fractions for the unit cell models were identical to the MMC core layer in the actual tubes, i.e. 35%. The fibre orientations can be altered in ABAQUS by specifying the orientation angle in the input file. For SC03, the fibre orientations of the MMC layer are defined through the material direction option.

5.3.1 Unidirectional 0° Unit Cell Model

Within this section, the development of the unidirectional, 0°, unit cell models in ABAQUS and SC03 is described. Note that the aspect ratio for each of the unit cell models is different; this will be discussed in detail. The material constants for MMC orthotropic material model, obtained from the ABAQUS and SC03 results, are then presented. These are the bulk orthotropic material properties for Ti-6-4 titanium matrix reinforced with SCS6 fibres, with a fibre volume fraction of 35%.

5.3.1.1 SC03 Unit Cell Model

A two quarter-fibre, unidirectional, 0°, unit cell model, with a 35% fibre volume fraction, as shown in Figure 5.1, was developed in SC03. In SC03, only tetrahedral elements can be created in the model, unlike ABAQUS which has a more comprehensive elements library. For this model, it is assumed that the fibre arrangement is hexagonal and the fibres are aligned axially (0°).

As mentioned earlier, results from this model can only be used to determine the Young's moduli and Poisson's ratios. Hence, another unidirectional single fibre unit cell model was developed, in ABAQUS, to evaluate the shear moduli, in different directions. The ABAQUS model will be discussed in detail in a later section.

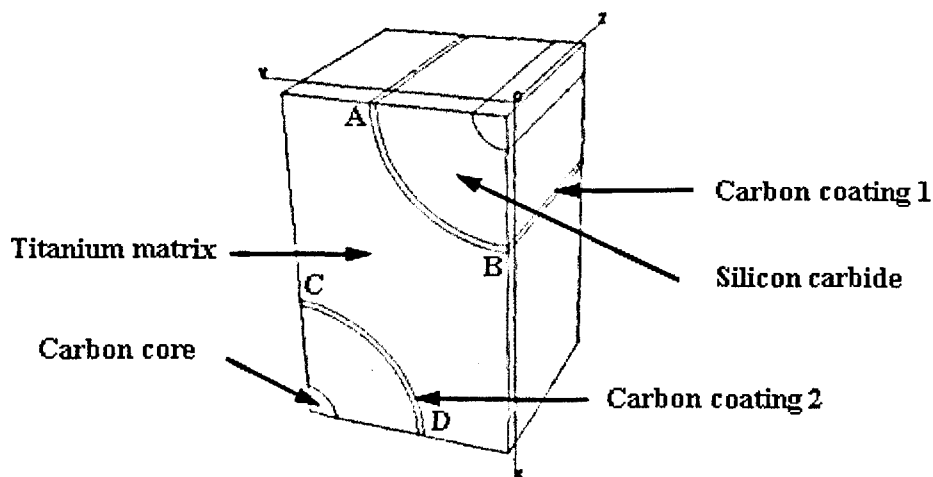


Figure 5.1 SC03 2 quarter-fibre unit cell model

Although SC03 has a model generation capability, it was decided to create the model using Pro/Engineer because of the greater familiarity with this software. All models in SC03 have a file extension “.PM”. To enable a conversion from a Pro/Engineer model to a SC03 model, an intermediate file called a STEP file (“.STP”) needs to be used. The STEP file is outputted from Pro/Engineer and software called “Cadverter” from Theorem Solutions Ltd, was used to convert a STEP file to “.PM” file.

Since this unit cell model has seven domains (2 carbon core, 2 SiC, 2 carbon coatings and 1 titanium block), it is necessary to create each domain separately,

in Pro/Engineer, as a part file using the dimensions presented in Table 5.4. The part files are then assembled to form the model, as shown in Figure 5.1.

	Dimensions (μm)
Radius of carbon core	16.5
Thickness of SiC	49
Thickness of carbon coating	3.5
Width	116.6
Length	116.6
Height	183.2

Table 5.4 Dimension for SC03 unidirectional 0° unit cell model

Figure 5.2 shows a schematic diagram on how the unit cell model is extracted from a macro model based on the hexagonal array fibre arrangement. The unit cell model can be further simplified, using symmetry conditions and hence a representative volume element for the macro model is obtained.

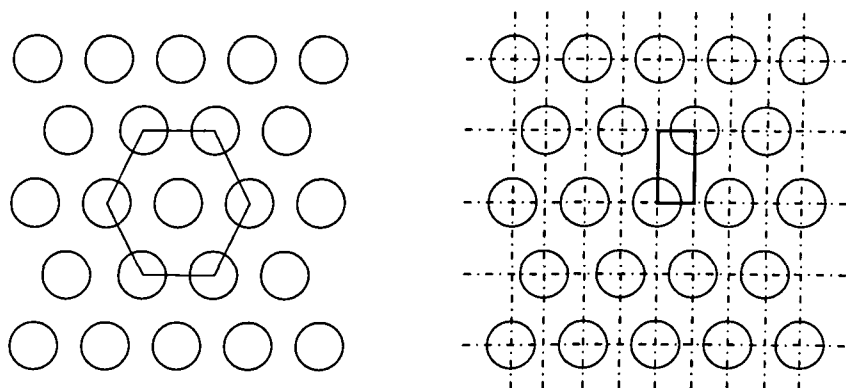


Figure 5.2 Schematic diagram showing the basis of the SC03 unit cell model

A typical aspect ratio for this kind of unit cell model is 1 to 2 (width to height) as there are two quarter-fibres in the vertical direction. However, a more realistic aspect ratio is 2 to π , which can be further justified through the change of geometry of the matrix coated fibres (MCFs) before and after the HIPping process. Figure 5.3 is a schematic diagram showing the changes in geometry for the MCFs. During the HIPping process of the tube specimen, the inner and outer

diameters of the tube, subjected to a hydrostatic pressure (P), and the circumferential direction was constrained by the adjacent MCFs. The void between the MCFs will then diminish progressively during the process at high temperature and pressure as the matrix material creeps. Before the process, the area of each MCF is $\frac{\pi D^2}{4}$. After the process, the area of the MCF is $D \cdot H$.

Equating both terms will give the width (D) over height (H) with a ratio of 4 to π and hence the ratio of 2 to π for this unit cell model which have two quarter fibres.

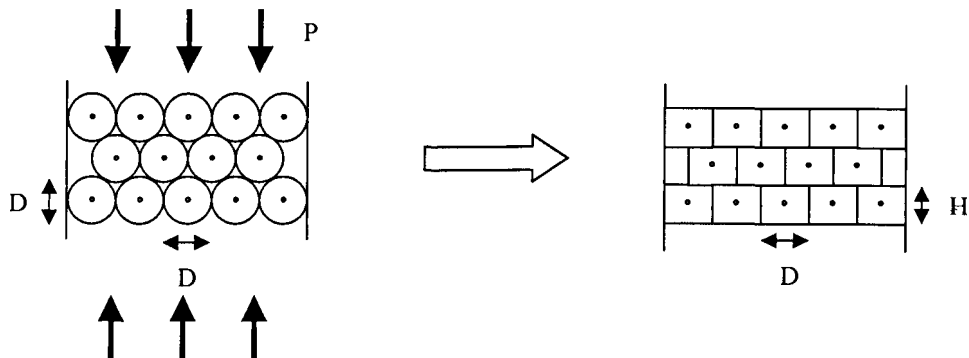


Figure 5.3 Physical geometry of MCFs before and after HIPping process

The dimensions of this unit cell model are given in Table 5.4. The dimensions of the SCS6 fibre were obtained from the paper reported by Li et al. [29]. The ratio of the width to the height give an aspect ratio of 2 to π .

The material properties used for the constituent materials are obtained from Rolls-Royce. Note that the carbon coating is orientation dependent. In SC03, the material orientation for any given domain is specified using the orientation sub-menu in “domain control”. There are several ways in which the orientation can be specified; the direction cosine method was used here. Using this method, the material x-axis and material y-axis are specified using the general Cartesian

coordinates X, Y or Z. Table 5.5 shows the general expressions used to define the material orientation, for both carbon coatings. Please refer to Appendix C for further details on how to define the material orientation in SC03.

	Carbon Coating 1	Carbon Coating 2
	Material x-axis	
x-coordinate	0	0
y-coordinate	0	0
z-coordinate	1	1
	Material y-axis	
x-coordinate	Y	0.1166-Y
y-coordinate	-X	X-0.1832
z-coordinate	0	0

Table 5.5 General expressions of material axes for carbon coatings

(SC03 0° unit cell model)

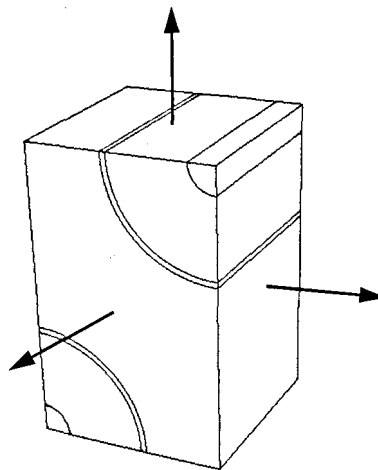


Figure 5.4 Loading arrangement on unit cell model

To evaluate the compliance matrix, 0.1% strains were applied, in each of the global directions, sequentially; the loading arrangement is shown in Figure 5.4. The faces opposite the loading faces were constrained in the loading directions. The applied forces were reacted on the constrained faces, for each load case. Using the reaction forces and area of the faces, bulk stresses were obtained. Coefficients in the compliance matrix were then computed by inverting the

stress matrix and multiplying it by the strain matrix. The material constants obtained are the Young's moduli and Poisson's ratios related to each global direction. Equation (5.1) shows the generalized Hooke's law used for these calculations.

$$\begin{Bmatrix} \varepsilon_x \\ \varepsilon_y \\ \varepsilon_z \end{Bmatrix} = \begin{bmatrix} \frac{1}{E_x} & -\frac{\nu_{yx}}{E_y} & -\frac{\nu_{zx}}{E_z} \\ -\frac{\nu_{xy}}{E_x} & \frac{1}{E_y} & -\frac{\nu_{zy}}{E_z} \\ -\frac{\nu_{xz}}{E_x} & -\frac{\nu_{yz}}{E_y} & \frac{1}{E_z} \end{bmatrix} \begin{Bmatrix} \sigma_x \\ \sigma_y \\ \sigma_z \end{Bmatrix} \quad (5.1)$$

Young's Moduli	E_x	E_y	E_z
	154.3 GPa	154.9 GPa	203.2 GPa
Poisson's Ratio	ν_{yx}	ν_{zx}	ν_{xy}
	0.30	0.27	0.30
	ν_{zy}	ν_{xz}	ν_{yz}
	0.27	0.20	0.20

Table 5.6 Material properties predicted using the SC03 unit cell model

Table 5.6 shows the Young's moduli and Poisson's ratios obtained by using the unit cell model. Note that z-direction is the fibre direction which gives a much higher bulk Young's modulus, compared to the transverse direction. In the case for the tube model in SC03, the Poisson's ratios needed are ν_{xy} , ν_{yz} and ν_{zx} where z-direction is the shaft axis. However, it is not necessarily the case for the ABAQUS tube model where the Poisson's ratios needed are ν_{12} , ν_{13} and ν_{23} . If, in the ABAQUS tube model, the shaft axis was in the 3-direction, then ν_{12} is equivalent to ν_{xy} , ν_{13} is equivalent to ν_{xz} and ν_{23} is equivalent to ν_{yz} . The shear moduli are also different for the two cases; this will be discussed in the next section.

5.3.1.2 ABAQUS Unit Cell Model

A single fibre unidirectional unit cell model, shown in Figure 5.5, was developed in FEMGV. FEMGV is a FE package which includes model generation, FE calculation and results post processing capabilities. However in the present application, FEMGV was only used to generate the FE models; the FE calculations and the post processing of the results were carried out in ABAQUS. Note that all ABAQUS models were generated using FEMGV. ABAQUS input files were created in FEMGV and the input files was edited manually, using a text editor, before the FE calculations were performed. Typically the sections which were edited are the material properties, boundary conditions, load conditions, orientations and results output.

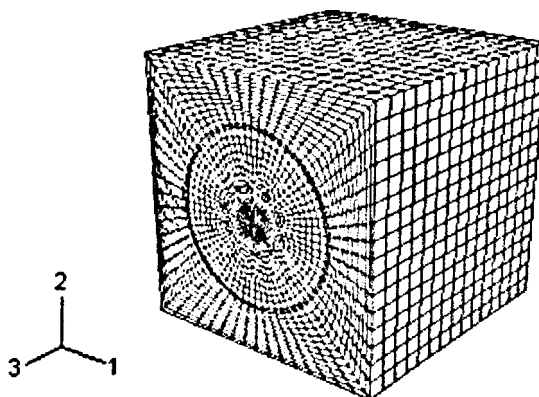


Figure 5.5 ABAQUS single fibre unit cell model

This unit cell model was used to evaluate the shear moduli related to different directions. The shear moduli are required for both the ABAQUS tube model and the SC03 cyclic symmetry tube model in order to define an orthotropic material model for the MMC core layer. As in the other unidirectional, 0° , unit cell model, four constituent materials were specified. Only 20-noded quadratic brick elements (C3D20R) were used in this model and the total number of elements is

approximately 22,000. The fibre arrangement was assumed to form a square array and hence the unit cell model has an aspect ratio of 1 to 1. This represents a unit cell model with a cubic shape, as shown in Figure 5.5. By using a cubic shape, unit cell model, it was easier to implement “planes remain plane” boundary conditions under a shear loading condition compared to the two quarter fibre model previously described.

Results from this model were used to determine the shear moduli G_{12} , G_{13} , G_{23} and G_{31} ; the shear moduli required for the ABAQUS orthotropic analyses are G_{12} , G_{13} , G_{23} . The additional shear modulus, G_{31} , is needed in the SC03 analysis. In SC03, cyclic symmetry tube model, if the shaft axis was in the 3-direction, then G_{xy} is equivalent to G_{12} , G_{yz} is equivalent to G_{23} and G_{zx} is equivalent to G_{31} .

As an example, for the case of the determination of G_{23} , the loads were applied on the front face in 2-direction and on the top face on 3-direction, as shown in Figure 5.6. The loads were applied using “dummy nodes” which were specified at the centre of the faces, as shown in Figure 5.7. Every node on the face is constrained to have the same displacement as the dummy node, via a linear multi-point constraints EQUATION available in ABAQUS. This linear multi-point constraint facility is defined in the form of an equation and it requires that the linear combination of nodal variables is equal to zero, that is:-

$$A_1 u_i^P + A_2 u_j^Q + \dots + A_N u_k^R = 0 \quad (5.2)$$

Where u_i^P is a nodal variable at node P , degree of freedom i , and A_i is the coefficients that define the relative motion of the node. A linear multi-point

constraint equation is defined in ABAQUS by specifying the number of terms in the equation ($1, 2, \dots, N$), the corresponding nodes or node sets (P, Q, R, \dots) and the corresponding degrees of freedom (i, j, k, \dots). As an example, if it is required that the top face is constrained to have the same deformation as the dummy node 108386 in 3-direction, then all of the nodes on the top face will move an equal amount to that of the dummy node (108386) in the 3-direction, using the equation for this linear multi-point constraint, i.e.:-

$$u_3^{TOP} = u_3^{dummy} \quad (5.3)$$

$$u_3^{TOP} - u_3^{dummy} = 0 \quad (5.4)$$

Hence, there are only 2 terms in this equation, with top face and the dummy node constrained in the 3-direction. The coefficients for top face and the dummy node are 1 and -1, respectively. The example below shows how this linear multi-point constraint appears in an ABAQUS input file. The first data line is the number of terms for this equation. The second data line specified the node or node set, degree of freedom and coefficient in sequence for both terms.

```
*EQUATION
2
TOP, 3, 1.0, 108386, 3, -1.0
```

Therefore, whatever load is applied to the dummy node, the load will be distributed appropriately to the whole face. The boundary conditions were applied such that the top and bottom faces were constrained in the 2-direction and the left and right faces were constrained in the 1-direction. Additional constraints in the 3-direction were needed for the bottom face to prevent rigid body motion of the model. To ensure that the front and back faces remain plane after loading, linear multi-point constraints EQUATION's were imposed on

these faces. An additional linear multi-point constraints EQUATION was also imposed at the mid plane (TOPMID), highlighted by the dotted line on Figure 5.7, and to the top face. It was to allow a displacement of 0.5 units for the mid plane, if the top face is displaced by 1 unit. A portion of the ABAQUS input file to define these constraints is shown below:-

```
*****
*EQUATION
2
TOP,3,1.0,108386,3,-1.0
*EQUATION
2
FRONT,2,1.0,108384,2,-1.0
*EQUATION
2
TOPMID,3,2.0,108386,3,-1.0
*****
*BOUNDARY
TOP,2,2
*BOUNDARY
BOTTOM,2,2
*BOUNDARY
BOTTOM,3,3
*BOUNDARY
LEFT,1,1
*BOUNDARY
RIGHT,1,1
*****
```

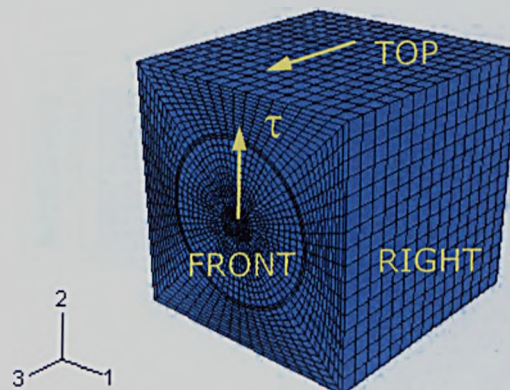


Figure 5.6 Loading arrangement for the G_{23} model

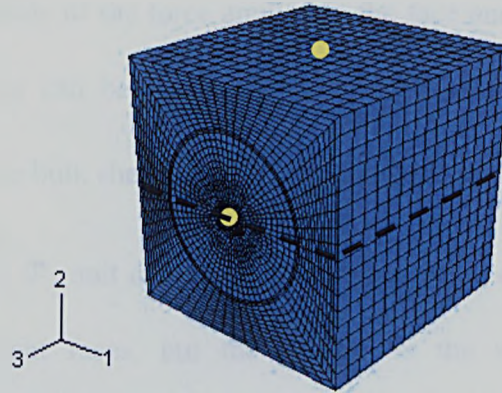


Figure 5.7 Position of dummy nodes and mid plane for the G_{23} model

Figure 5.8 shows the results in the form of a contour plot for displacement in 3-direction (U_3). The shear strain γ_{23} can be calculated using the following formula,

$$\tan \gamma_{23} = \frac{U_3}{H_2} \quad (5.5)$$

assuming γ is small,

$$\gamma_{23} = \frac{U_3}{H_2} \quad (5.6)$$

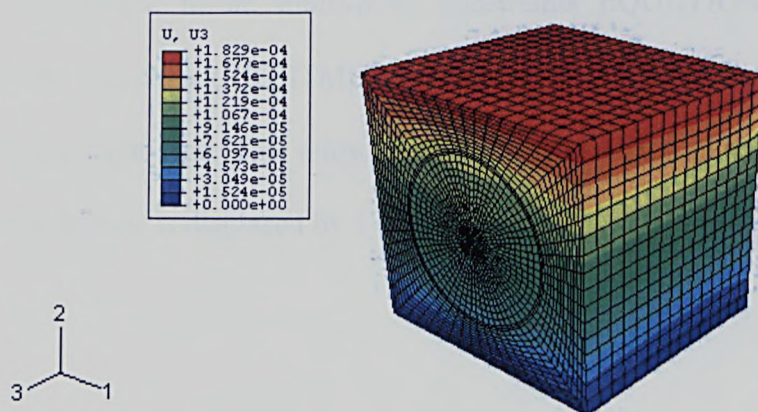


Figure 5.8 Displacement contour plot (U_3)

Knowing the magnitude of the force applied to the face and the area of the face, the bulk shear stress can be calculated. The effective shear modulus G_{23} is simply the ratio of the bulk shear stress, τ_{23} to the shear strain, γ_{23} .

For other ABAQUS, 0° , unit cell models, the application of load is in different directions on different faces, but the process is the same. The boundary conditions are also different to ensure that the unit cell simulates the deformations which occur for the particular set of loads. The following is a summary of the loading and boundary conditions used for the remaining three ABAQUS, 0° , unit cell models.

For the case of the determination of G_{12} , the load is applied to the top and right faces via dummy nodes at the centre of the faces, as shown in Figure 5.9. Linear, multi-point constraints EQUATION's were defined for these faces, which are constrained by the dummy node (TOP) and dummy node (RIGHT), respectively. The front and back faces are constrained in the 3-direction; left and right faces are constrained in the 1-direction and left face is also constrained in the 2-direction. Additional, linear, multi-point constraints EQUATION's are also imposed to the mid plane (RIGHTMID) highlighted by the dotted line on Figure 5.10 and to the right face. This allows a displacement of 0.5 units for the mid plane if the right face is displaced by 1 unit.

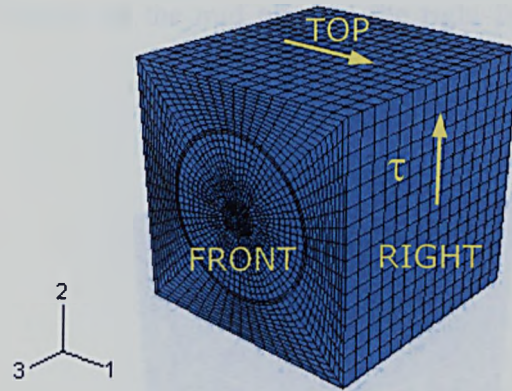


Figure 5.9 Loading arrangement for the G_{12} model

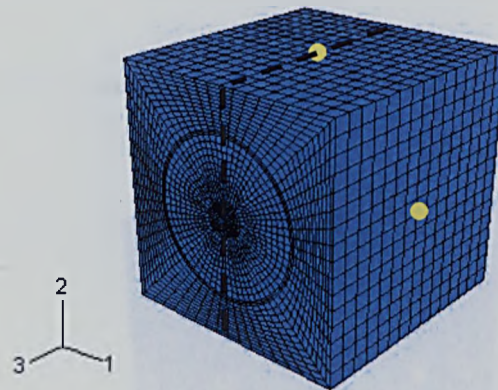


Figure 5.10 Position of dummy nodes and mid plane for the G_{12} model

For the case of the determination of G_{13} , the load was applied to front and right faces via dummy nodes at the centre of the faces, as shown in Figure 5.11. Linear, multi-point constraints EQUATION's were defined for these faces which are constrained by the dummy node (FRONT) and dummy node (RIGHT), respectively. The top and bottom faces were constrained in the 2-direction; left and right faces were constrained in the 1-direction and the left face was also constrained in the 3-direction. Additional, linear, multi-point constraints EQUATION's were also imposed to the mid plane (RIGHTMID1), highlighted by the dotted line on Figure 5.12, and the right face. This allows a

displacement of 0.5 units for the mid plane if the right face is displaced by 1 unit.

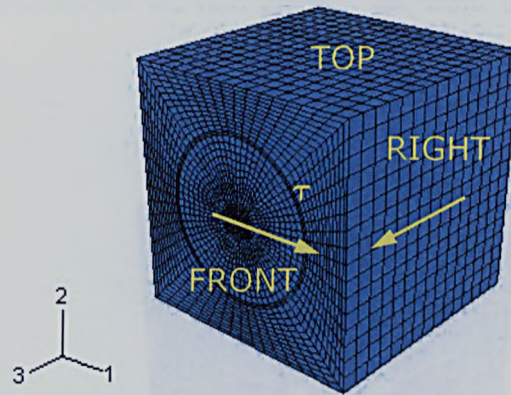


Figure 5.11 Loading arrangement for the G_{13} model

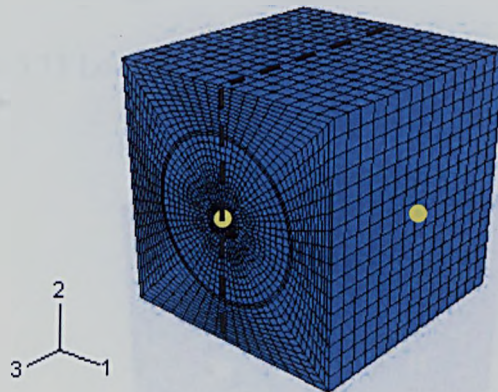


Figure 5.12 Position of dummy nodes and mid plane for the G_{13} model

For the case of the determination of G_{31} , the load is applied to the front and right faces via dummy nodes at the centre of the faces, as shown in Figure 5.13. Linear, multi-point constraints EQUATION's were defined for these faces, which are constrained by the dummy node (FRONT) and dummy node (RIGHT), respectively. The top and bottom faces were constrained in the 2-direction; front and back faces were constrained in the 3-direction and the back face was also constrained in the 1-direction. Additional, linear, multi-point

constraints EQUATION's were also imposed at the mid plane (FRONTMID), highlighted by the dotted line on Figure 5.14, and the front face. This allows a displacement of 0.5 units for the mid plane if the front face is displaced by 1 unit.

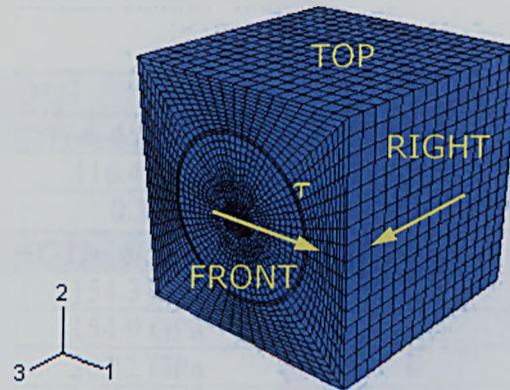


Figure 5.13 Loading arrangement for the G_{31} model

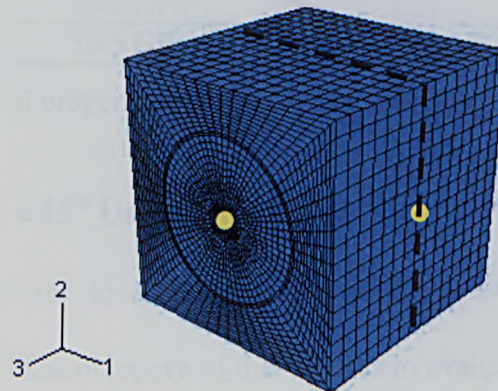


Figure 5.14 Position of dummy nodes and mid plane for the G_{31} model

5.3.1.3 Predicted orthotropic material properties for MMC

Having all of the material constants, determined from the results of unit cell model analyses, an orthotropic material behaviour model can now be specified for the tube model. Table 5.7 shows the material constants used in the ABAQUS tube model and SC03 cyclic symmetry tube model. To use these material

properties for the MMC layer, the shaft axis must be in the 3-direction or z-direction for the ABAQUS or SC03 cases, respectively. In ABAQUS, the fibre orientation can be specified in the SOLID SECTION option in the input file. For SC03, the fibre orientation can be altered through the material direction facility available under the “domain control” menu.

ABAQUS		SC03	
Ti-6-4 (Isotropic Material Model)			
E	116.4 GPa	E	116.4 GPa
ν	0.32	ν	0.32
MMC Layer (Orthotropic Material Model)			
E_1	154.3 GPa	E_x	154.3 GPa
E_2	154.9 GPa	E_y	154.9 GPa
E_3	203.2 GPa	E_z	203.2 GPa
ν_{12}	0.30	ν_{xy}	0.30
ν_{13}	0.20	ν_{yz}	0.20
ν_{23}	0.20	ν_{zx}	0.27
G_{12}	50.3 GPa	G_{xy}	50.3 GPa
G_{13}	50.5 GPa	G_{yz}	50.5 GPa
G_{23}	50.5 GPa	G_{zx}	62.1 GPa

Table 5.7 Material properties for Ti-6-4 and MMC layer for tube models

5.3.2 Cross-ply $\pm 45^\circ$ Unit Cell Model

This section describes the development of the cross-ply $\pm 45^\circ$ unit cell model in ABAQUS and SC03. The objective of this work is to evaluate the effective shear modulus for TiMMC with a fibre volume fraction of 35%, for a $\pm 45^\circ$ fibre orientation, based on the results obtained from unit cell analyses.

Figure 5.15 is a schematic diagram showing how the cross-ply $\pm 45^\circ$ unit cell model is extracted from the FE tube model. Figure 5.15(a) shows a tube model with $\pm 45^\circ$ fibre orientations; the arrow indicates the fibre direction and shows that the fibres are at right angles to each other from ply to ply, as shown in Figure 5.15(b). Using symmetry conditions, a representative unit cell model can

be extracted, as shown in Figure 5.15(c). For a shaft under pure torsion, the principal stresses act at $+45^\circ$ and -45° to the shaft axis, which are the on-axis directions for the fibres. Hence, a positive torque load causes the $+45^\circ$ fibre plies to experience a tensile load and causes the -45° fibre plies to experience a compressive load.

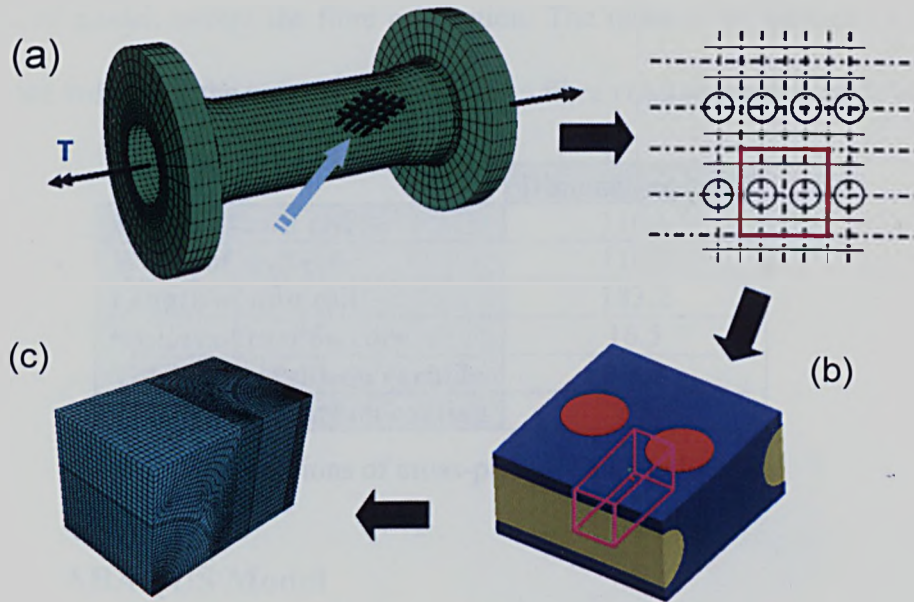


Figure 5.15 Idea of $\pm 45^\circ$ unit cell model

Therefore, the unit cell model comprises of two quarter-fibre orientated at right angle to each other. The aspect ratio for this model is also 2 to π and it contains four constituents' materials, i.e. the carbon core, the silicon carbide, the carbon coating and the titanium matrix. It is assumed that there is a perfect bond between the fibre and the matrix and hence the predicted effective shear modulus may be higher than the experimental result. The ABAQUS model is the same as in SC03 in term of geometry, boundary conditions and material properties. The main difference is that the mesh for the SC03 case used 10-node tetrahedral elements and that for the ABAQUS case used 20-noded, quadratic

brick elements. All of the analyses carried out used linear elastic room temperature material properties, obtained from both SC03 material file and VITAL experimental.

Table 5.8 shows the dimensions used for the cross-ply $\pm 45^\circ$ unit cell model. Essentially, the dimensions are the same as the two quarter-fibre, unidirectional 0° unit cell model, except the fibre orientation. The ratio of the volume of the fibre to the volume of the unit cell model gives a fibre volume fraction of 35%.

	Dimensions (μm)
Height of unit cell	116.6
Width of unit cell	116.6
Length of unit cell	183.2
Radius of carbon core	16.5
Thickness of silicon carbide	49.0
Thickness of carbon coating	3.5

Table 5.8 Dimensions of cross-ply $\pm 45^\circ$ unit cell model

5.3.2.1 ABAQUS Model

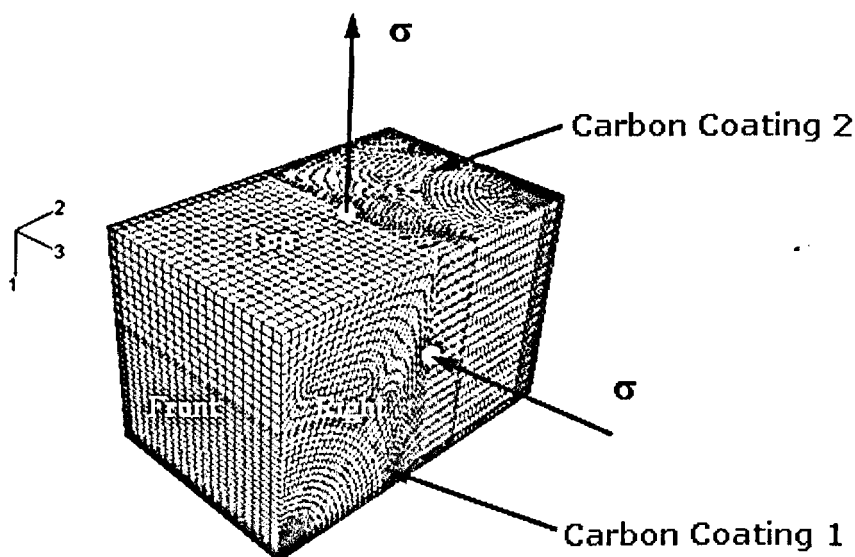


Figure 5.16 Cross-ply $\pm 45^\circ$ unit cell model (ABAQUS)

Figure 5.16 shows the loading arrangement used for the ABAQUS model, which simulates a $\pm 45^\circ$ tube model under pure torsion. The loads are applied through dummy nodes specified at the centre of the top and right faces via linear multi-point constraint EQUATION's as in the ABAQUS unidirectional 0° unit cell model. The boundary conditions are such that the left and right faces are constrained in the 2-direction, the bottom face is constrained in the 1-direction and the back face is constrained in the 3-direction. For this model, the aspect ratio is also 2 to π (height to length).

The material properties used for this model are obtained from Rolls-Royce. It should be noted that the material properties for carbon coatings are the same, but the material orientation is different. Local axis systems for material were specified for both of the carbon coatings by defining cylindrical systems in the ABAQUS input file. As an example, the input file has the following command lines within the ORIENTATION section:-

```
*ORIENTATION, SYSTEM=CYLINDRICAL, NAME=OR1
0.1166237, 0.000, 0.000, 0.1166237, 0.000, 0.1166237
1, 0.000
*ORIENTATION, SYSTEM=CYLINDRICAL, NAME=OR2
0.000, 0.183192, 0.1166237, 0.1166237, 0.183192, 0.1166237
1, 0.000
**
```

For a cylindrical system, it is necessary to specify the Cartesian x, y and z-coordinates of point A and point B on the polar axis. The coordinates for these two points are specified in sequence, as shown on the second command line after *ORIENTATION in the input file. OR1 and OR2 are the local cylindrical systems for carbon coating 1 and carbon coating 2, respectively, which has a different local axis. If additional rotation about the local direction is needed, this

can be specified in the third command line. However, no additional rotation is needed in this case. A cylindrical system has 1-direction as the radial direction, 2-direction as the tangential direction and 3-direction as the axial direction. Figure 5.17 illustrates the cylindrical orientation used in the model.

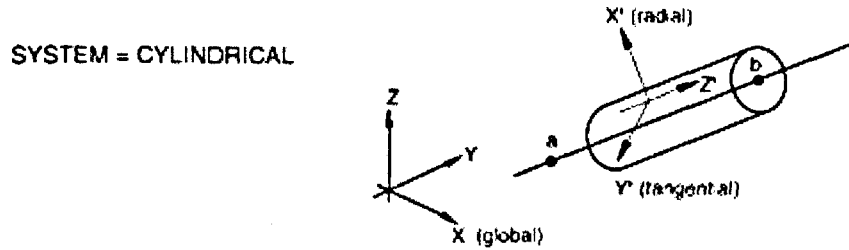


Figure 5.17 Cylindrical orientation in ABAQUS

Since the behaviour of the unit cell model is linear elastic, a nominal load of 5N was used in the analysis. After the analysis, the bulk effective shear modulus for $\pm 45^\circ$ fibre orientation was obtained from the ratio of the bulk shear stress to bulk shear strain. Bulk shear stress is defined as the load applied on the top or right face to the area of that face. Bulk direct strain is defined as the displacement in the top face in the 1-direction or displacement of right face in the 3-direction, to the height or width, respectively. Hence,

$$G_{eff} = \frac{\tau_{bulk}}{\gamma_{bulk}} \quad (5.7)$$

$$\tau_{bulk} = \frac{F}{A} \quad (5.8)$$

$$\varepsilon_{bulk} = \frac{\delta}{L} \quad (5.9)$$

$$\gamma_{bulk} = 2 \times \varepsilon_{bulk} \quad (5.10)$$

The bulk shear strain is twice the bulk normal strain under pure shear (pure torsion) condition. The effective shear modulus for $\pm 45^\circ$ fibre orientation is 73.1GPa. Please refer to Appendix B for the relation between the shear strain and direct strain under pure shear condition.

5.3.2.2 SC03 Model

A cross-ply $\pm 45^\circ$ unit cell model was also developed in SC03, which is used to compare the results with the ABAQUS model. The unit cell model as shown in Figure 5.18 is identical to the ABAQUS unit cell model except the definition for the carbon coatings, mesh and load. The loading arrangement is similar to the ABAQUS model, where a displacement was chosen to produce 0.1% strain on the top and right faces in the SC03 model instead of a force. The boundary conditions and material properties are identical to those used in the ABAQUS model.

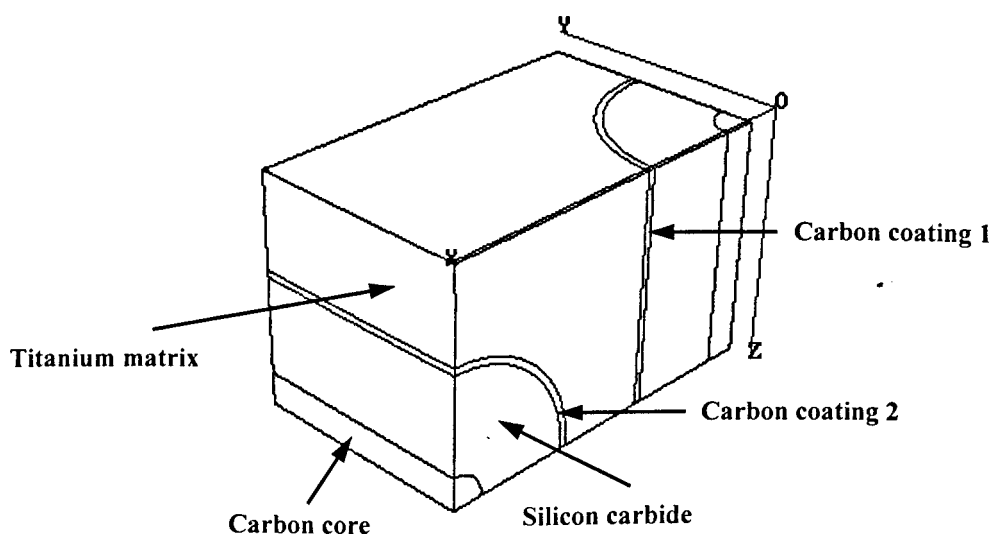


Figure 5.18 Cross-ply $\pm 45^\circ$ unit cell model (SC03)

Note that the procedure used to create this model is similar to that used for the SC03 0° unit cell model. The dimensions of each domain are the same also,

except for the titanium block. It has a different design as the fibres are orientated at right angle to each other, unlike the 0° unidirectional unit cell model, which has fibres orientated in the axial direction.

The method used for material orientation, for carbon coatings, is similar to that used for the SC03 0° unit cell model. However, the Cartesian coordinate systems are slightly different, due to the orientation of the carbon coatings. Table 5.9 shows the general expressions used to define the material orientation for each of the carbon coatings. Appendix C contains further details on how to define the material orientation in SC03.

	Carbon Coating 1	Carbon Coating 2
	Material x-axis	
x-coordinate	0	0
y-coordinate	0	1
z-coordinate	1	0
	Material y-axis	
x-coordinate	Y	Z-0.1166
y-coordinate	-X	0
z-coordinate	0	0.1832-X

Table 5.9 General expressions of material axes for carbon coatings
(SC03 cross-ply $\pm 45^\circ$ unit cell model)

After the analyses, the average reaction forces on the restrained faces (left and bottom) were calculated. The shear stress is the ratio of the reaction force to the area of the restrained face and the bulk shear strain is twice the bulk normal strain. Hence,

$$R_{ave} = \frac{R_{left} + R_{bottom}}{2} \quad (5.11)$$

$$\tau_{bulk} = \frac{R_{ave}}{A_{left/bottom}} \quad (5.12)$$

$$G_{eff} = \frac{\tau_{bulk}}{2 \times 0.001} \quad (5.13)$$

The effective shear modulus, calculated for this SC03 unit cell model for $\pm 45^\circ$ fibre orientation, is 72.0GPa.

5.4 Tube Models

This section describes the methods used to evaluate the bulk MMC shear modulus, for different fibre orientation using FE tube models. By varying the fibre orientation of the layers in the MMC model, the overall effective MMC shear modulus will change. The bulk shear modulus of the MMC layer is evaluated by removing the effect of the inner and outer titanium cladding on the plain section of the tube. The fibre orientations of interest here are, 0° , $+30^\circ$, -30° , $+45^\circ$, -45° , $\pm 30^\circ$ and $\pm 45^\circ$. All analyses which were carried out were linear elastic using the room temperature material properties data presented in Table 5.7.

5.4.1 ABAQUS Parametric Tube Model

A fully parametric 360-degree tube model shown in Figure 5.19 was created using FEMGV. The benefit of using a parametric model is that different shaft geometries can be easily generated by simply altering the parameters within the model. In general, all specimens in VITAL phase 1 have a similar geometry. However, the thicknesses of the cladding and MMC layer are slightly different for each specimen. Hence, this parametric tube model will be useful in generating a specific model for each test specimen. This enables a most accurate comparison of the numerical and experimental results to be made. Also, VITAL phase 3 comprises a number of buckling specimens which are of larger size but

having the same basic design. The parametric model can be used to generate quickly the buckling models. Hence saving the time required for pre-processing.

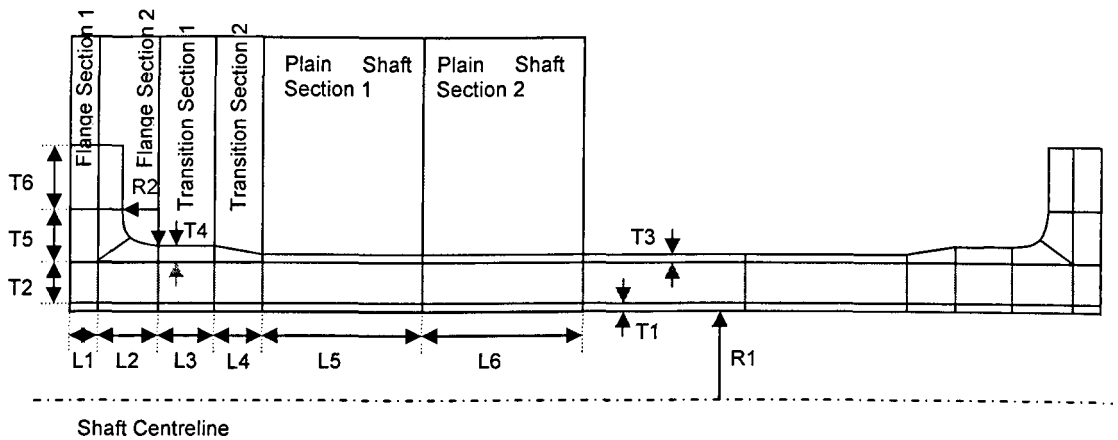


Figure 5.19 Schematic diagram of a tube showing the parameters

Independent Parameter	Inner Radius of Shaft	R1
	Flange Radius	R2
	Ti Cladding Thickness	T1
	TiMMC Thickness	T2
	Thickness of transition end flange	T3
	Extra Flange Thickness	T4
	Flange Section 1 Length	L1
	Transition Section 1 Length	L3
	Transition Section 2 Length	L4
	Shaft Section 1 Length	L5
	Shaft Section 2 Length	L6
	Dependent Parameter	Flange Section 2 Length ($L2 > R2$)
Flange Thickness ($R2 + T4$)		T5

Table 5.10 Definition of tube parameters

A schematic diagram, showing the parameters and different regions for the tube model, is shown in Figure 5.19. The parameters can be categorized as independent parameters or dependent parameters and their definitions are presented in Table 5.10. Dependent parameter L2 ensures that it can never be smaller than the flange radius R2 and T5 is the sum of the flange radius, R2 and

the thickness of transition end flange, T4. Other parameters are independent which can be altered freely without affecting the design of the tube.

For the various specimen used in VITAL phase 1, the parameters which had to be altered were the thickness of inner and outer cladding (T1 & T3), thickness of MMC layer (T2) and inner radius of tube (R1). By assuming that the flange diameter (110mm) and the diameter of transition section 1 (56mm) remain unchanged, it is necessary for the thickness of the transition end flange (T4) and the flange thickness (T5) to be changed accordingly. Other parameters remain unchanged for all test specimens. Table 5.11 shows the specific dimensions for each tube model, based on measurement taken from the test specimens. The units for all the parameters are mm.

$$T4 = \frac{D_{transition1}}{2} - R1 - T1 - T2 \quad (5.14)$$

$$T5 = R2 + T4 \quad (5.15)$$

	UTC1	UTC5	UTC6	UTC7	UTC8	UTC9	UTC10
R1	18.755	20.0	20.075	20.435	20.0	20.12	20.04
R2	3						
T1	2.37	2.30	2.04	2.09	2.28	2.38	2.45
T2	2.91	2.23	2.28	2.335	2.21	2.21	2.22
T3	0.965	0.47	0.48	0.485	0.51	0.49	0.49
T4	3.965	3.47	3.605	3.14	3.51	3.29	3.29
T6	24						
L1	12						
L3	9.14						
L4	12.86						
L5	25						
L6	25						
L2	6						
T5	6.965	6.47	6.605	6.14	6.51	6.29	6.29

Table 5.11 Dimensions for ABAQUS tube models

As with other ABAQUS models, 20-noded quadratic brick elements (C3D20R), with reduced integration, were used. This model contains approximate 14,000 elements. The inner and outer cladding were modelled using 1 element in the radial direction and the MMC core layer were modelled using 2 elements in the radial direction. The torque load was applied using a dummy node in the tube model. The dummy node was created at the centre of the flange face, at one end on the tube axis. Then, all the nodes on the flange face were constrained to the dummy node via Multi-point Constraints (MPC). There are different types of MPCs within ABAQUS; the MPC type BEAM was used here. This constraint provides a rigid beam which connects every node on the face to the dummy node, which constraint their displacement and rotation in all directions. Therefore, whatever load is applied on the dummy node, the load will be distributed appropriately to the whole face. Below is the command lines extracted from the input file, showing the definition of MPC type BEAM. Node set LOAD which is the face of the flange is constrained to the dummy node 65361 via MPC type BEAM.

```
**  
*MPC  
BEAM, LOAD, 65361  
**
```

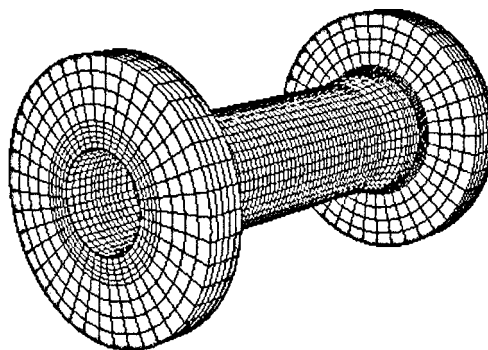


Figure 5.20 ABAQUS parametric tube model.

By applying a torque through the dummy node (i.e. a rotation for the dummy node), the torque will be distributed throughout the flange face. The flange face, at the other end of the shaft was constrained to be encastred, such that over the whole face all displacement and rotation degrees of freedom are zero. Figure 5.20 shows the parametric tube model used for the ABAQUS analyses.

The material properties used for the titanium matrix and for the MMC core layer for the model are given in Table 5.7. The titanium matrix is an isotropic material and the MMC layer are represented by an orthotropic material behaviour model. In ABAQUS, there are two ways in which to specify the fibre orientation for the MMC layer. It can be achieved by specifying the orientation in the SOLID SECTION or in the ORIENTATION section facilities. Below are the SOLID SECTION command lines for the MMC layer, extracted from an input file for specimen UTC1. This model has a 0° fibre orientation.

```
*SOLID SECTION, ELSET=PHY2, COMPOSITE, STACK DIRECTION=2,
ORIENTATION=OR1
0.000194, , TCM, +0.0
```

The first line indicates that it is a composite solid section with its layer stacking direction in the global 2-direction. This solid section also has a material orientation name of OR1 which is define later in the input file. In the data lines,

the first column represents the layer thickness. UTC1 has 15 fibre plies, with each ply having a thickness of 0.194mm. Note that the dimension units for the tube model are in meters (m). The second column represents the number of integration points to be used through the layer and it must be an odd number. If no value is specified, the default value is one integration point. The third column is the name of the material forming this layer which had been defined in the material section. The last column is the orientation angle ϕ (in degrees) for that layer, where $-90.0 \leq \phi \leq 90.0$, measured positive counter clockwise, relative to the local direction. The local direction is defined in the ORIENTATION section, as follow:-

```

**
*ORIENTATION, SYSTEM=CYLINDRICAL, NAME=OR1
0.000, 0.000, 0.000, 0.000, 0.000, 0.180
1, 0.000
**

```

The first line defines the orientation system used, which in this case is a cylindrical type with the name of OR1. The way in which the cylindrical coordinate system is defined has been presented earlier in this chapter for the ABAQUS unit cell model. In this model, the local direction chosen is the 1-direction, which is the radial direction. The fibre orientation can also be specified in OREINTATION, by specifying an additional rotation value on the local direction in the second data line. However, in the case of the tube model, it was decided to use the first method, because this enables the cross-ply for the MMC layer to be easily defined. The second method only allows unidirectional, off-axis, fibre orientation to be specified. Hence, using the first method, no additional rotation is needed in ORIENTATION. Nonetheless, the ORIENTATION definition is still needed to create a local coordinate system for

the model. This will allow the radial stress, tangential stress and axial stress to be outputted correctly in ABAQUS Viewer during the post-processing stage.

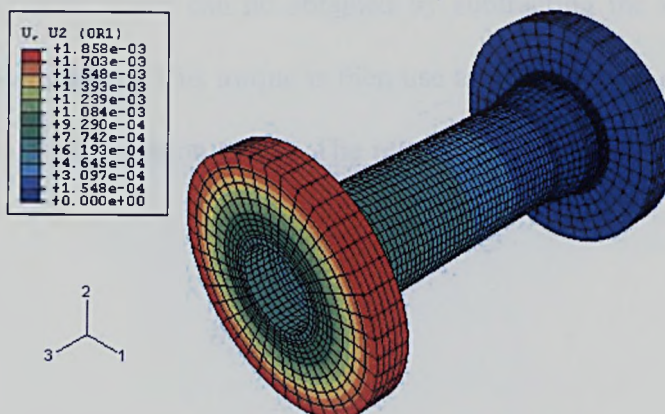


Figure 5.21 Tangential displacement contour plot of tube model

Since the analysis is linear elastic, the actual torque load used is not important; a torque load of 4800Nm was specified. In ABAQUS Viewer, the results can be outputted in the local coordinate system, via the Results > Options > Transformation > User-specified option and by selecting the coordinate system OR1. The tangential displacements are then plotted, via the Results > Field Outputs > U option and by selecting component U_2 . After the analysis, the relative tangential displacement, at the outer diameter, of the plain section was obtained using “Probe Values” in ABAQUS Viewer. Figure 5.21 shows a tangential displacement contour plot for the tube model. OR1 as seen in the legend confirmed that the displacements are plotted with a cylindrical coordinate system, having 2-direction in the tangential direction. Knowing the radius of the plain section, the twist angle of the plain section is easily calculated using equation (5.16). The next stage is to calculate the torque carrying capacity of the inner and outer titanium cladding using equation (5.17). With the rotation of the plain section, polar second moment of area for the titanium cladding, shear

modulus of HIPped titanium and length of the plain section, the torque carrying capacity is calculated. Based on the total torque applied to the model, the torque carried by the MMC layer can be obtained by subtracting the torque carrying capacity of the cladding. This torque is then use to calculate the effective MMC shear modulus using equation (5.18). The results obtained are discussed later in this chapter.

$$\theta_{PS} = \frac{S_1 - S_2}{R_{PS}} \quad (5.16)$$

$$T_{cladding} = \frac{G_{Ti} J_{cladding} \theta_{PS}}{L_{PS}} \quad (5.17)$$

$$G_{MMC} = \frac{T_{MMC} L_{PS}}{J_{MMC} \theta_{PS}} \quad (5.18)$$

5.4.2 Cyclic Symmetry Tube Model

5.4.2.1 ABAQUS Cyclic Symmetry Tube Model

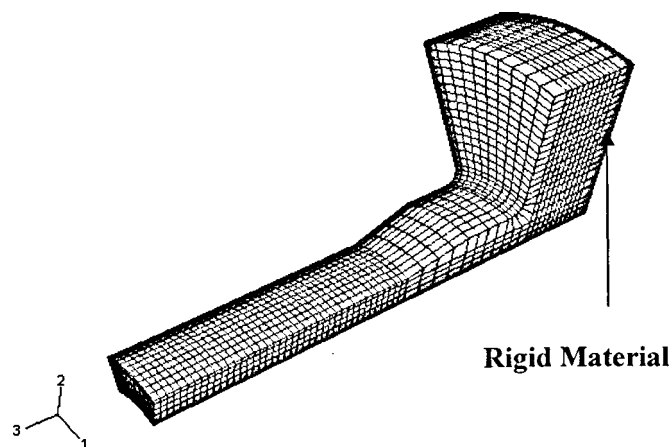


Figure 5.22 ABAQUS cyclic symmetry tube model

The cyclic symmetry tube model represents a 1/10th sector of the full tube model and it is further reduced to half the length, as both ends are identical. As

with the full tube model, 20-noded quadratic brick elements (C3D20R), with reduced integration, were used; the model contains approximately 4500 elements. Figure 5.22 shows the ABAQUS, cyclic symmetry tube model.

For the cyclic symmetry tube model, the dimensions are based on those shown in Table 5.11 and the material properties are the same as those used in the full tube model. However, additional boundary conditions must be imposed in order to create the cyclic symmetry of the model. The cyclic symmetry boundary condition is defined through MPC type CYCLSYM, which is used to enforce proper constraints on the radial faces bounding a segment of a cyclic symmetric structure. In the data line for MPC type CYCLSYM, the 2nd and 3rd columns represent the node sets (CYC1 & CYC2) of the respective radial faces. The end face, on the plain section, is encastre. However, in order to apply a torque load using this model, it is necessary to attach a rigid material to the flanged end, as indicated in Figure 5.22. The reason for this is that, each node can only have one MPC and since MPC type CYCLSYM is already specified for the radial faces of the model, MPC type BEAM can not be imposed at the flange face. Otherwise the edge of the radial faces would have two MPC's. By having the additional rigid material, the torque load can be applied through the face of the rigid material, which will, in turn be transmitted to the cyclic symmetry tube model. The modulus for the rigid material was set to be six orders of magnitude higher than that of the Titanium matrix.

```
*MPC
CYCLSYM,CYC1,CYC2

*****
** MATERIAL DEFINITIONS *
*****
**
```

```

*MATERIAL, NAME=TIM
*ELASTIC, TYPE=ISO
116.424E+09, 0.320, 000.0E+00
**
*MATERIAL, NAME=TMCM
*ELASTIC, TYPE=ENGINEERING CONSTANTS
154.3172E+9, 154.9341E+9, 203.1527E+9, 0.2997, 0.2043,
0.2043, 50.259E+9, 50.459E+9
50.459E+9
**
*MATERIAL, NAME=RIGID
*ELASTIC, TYPE=ISO
200.00E+15, 0.320, 000.0E+00
**

```

The procedure for obtaining the effective MMC shear modulus is the same as that described for the ABAQUS tube model. However, it should be noted that, it is necessary to remove the rigid material in ABAQUS Viewer, to ensure that the outputted results are correctly displayed. This can be done under the menu, Tools > Display Groups > Create and by selecting PHY3 for the rigid material element set and then clicking remove. As for the calculation, the length of the plain section is half the full model and the polar second moment of area is 1/10th of that for the full model. The results obtained using the cyclic symmetry model will be discussed later in this chapter.

5.4.2.2 SC03 Cyclic Symmetry Tube Model

This section outlines the methodology used to evaluate the effective MMC shear modulus, for different fibre orientations, using the cyclic symmetry tube model in SC03. The fibre orientations to be modelled are the same as those modelled using the ABAQUS tube model. As with the SC03 unit cell models, this cyclic symmetry tube model was created in Pro/Engineer, using a similar procedure and the file was then converted to a SC03 model.

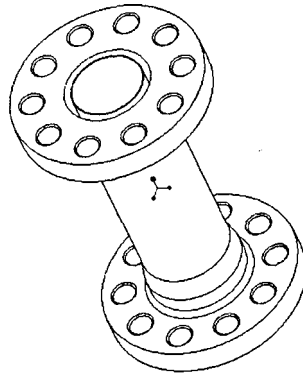


Figure 5.23 Titanium part

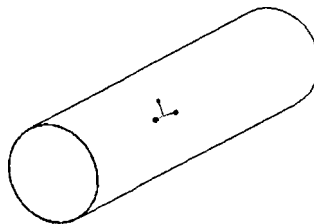


Figure 5.24 MMC layer

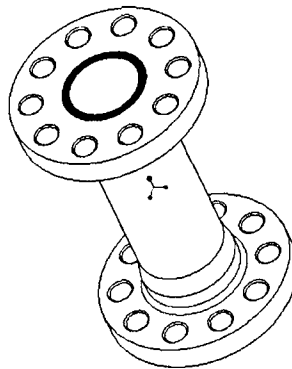


Figure 5.25 Tube model assembly

Since the tube model is made up of different materials, separate domains need to be created so that different material properties can be specified. Hence, the titanium part which comprised of two domains and the MMC layer were created separately, in Pro/Engineer, as shown in Figure 5.23, Figure 5.24, respectively. The parts are then assembled together in order to form a complete tube model (Figure 5.25). Only four domains were created for the MMC layer, because the

meshing operation will fail if the layer is too thin. Although there are only 4 domains for the MMC layer, a cross-ply laminate can still be defined. For example, in the case of a cross-ply, 45° laminate, the lay-up of $[\pm 45_2]$ is equivalent to $[\pm 45_8]$ as long as the total layers thickness is the same. This has been verified using the laminate analysis program “WINLAM” developed at the University of Nottingham. The assembled model has six domains; two are used for the titanium matrix and the other four are used for the MMC core layer.

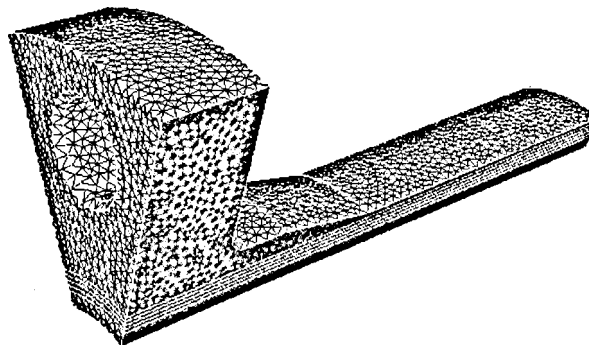


Figure 5.26 Half 1/10th cyclic symmetry tube model (SC03)

In order to create the cyclic symmetry tube model, a similar procedure was used. However, all of the parts were rotated 1/10th of a full revolution. Also, only half of the length of the tube model was modelled. The cyclic symmetry tube model in SC03, with the mesh, is shown in Figure 5.26.

The material properties used in this model are obtained from Rolls-Royce. However, the orthotropic material properties for the MMC core layer are orientation dependent. The material axis can be specified, for different layers, through general coordinates X, Y, Z, R or θ . The general expressions represent the material direction of a point for a particular domain in the Cartesian coordinate systems. Table 5.12 shows the general expressions used for different fibre orientation. Material x-axis is transverse to the fibre direction (z-axis) and

material y-axis is the radial direction for all cases; refer to Appendix C for further details on how to define the material orientation in SC03.

Fibre Orientation	0°	+30°	-30°	+45°	-45°
	Material x-axis				
x-coordinate	Y	Y	Y	Y	Y
y-coordinate	-X	-X	-X	-X	-X
z-coordinate	0	Rtan30	-Rtan30	R	-R
	Material y-axis				
x-coordinate	X	X	X	X	X
y-coordinate	Y	Y	Y	Y	Y
z-coordinate	0	0	0	0	0

Table 5.12 General expressions of material axes

To apply a torque load for this cyclic symmetry tube model, in SC03, traction needs to be specified on the flange face. The unit of the traction is MPa or N/mm². For example, a torque load of 4800Nm in a full tube model is equivalent to 240Nm on this cyclic symmetry tube model. In order to determine the traction needed for the given torque load, an arbitrary traction was first specified and the solution obtained. After the analysis, the torque/moment imposed on the model is obtained by restoring the traction display using the Display > Discrete Data Display option in SC03, which is shown in Figure 5.27. Note that the shaft axis for this model is the z-direction. M_z which is the moment about the z-axis gives the value of the torque load for the traction applied in Nmm. Using the torque value, the applied traction and the total area of the flange face, the effective radius of the applied traction can be obtained using equation (5.20). Then, for any torque load, an accurate traction can be calculated.

$$T = F \times r \quad (5.19)$$

$$T = \sigma \times A \times r \quad (5.20)$$

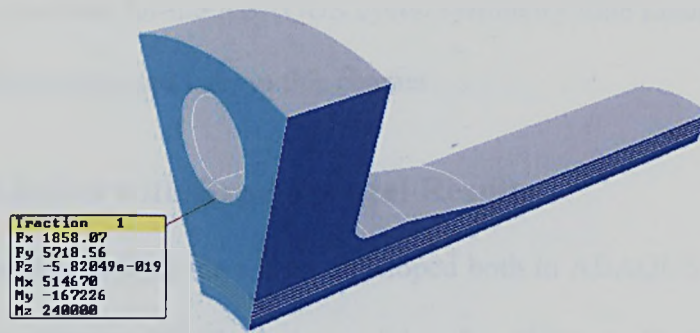


Figure 5.27 Torque/moment on cyclic symmetry tube model

Cyclic symmetry boundary conditions were imposed on the model, via Structural > Joints option and by selecting cyclic. Six radial faces on six domains are then selected and the end face of the plain section is constraint in radial and axial directions.

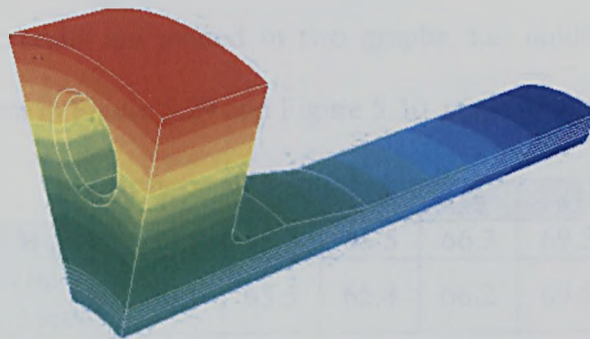


Figure 5.28 Circumferential displacement plot of the model

Once the analysis is completed, circumferential displacement contours can be plotted, as shown in Figure 5.28. This can be done, via the Results > Contour Types > Displacement > Circumferential Displacement option. The relative circumferential displacement of the plain section is obtain, via the Results > Get Values option. By clicking on the surface of the plain section, the circumferential displacement is displayed in a separate box; note that the units are mm. The procedure used to calculate the effective MMC shear modulus is

the same as that used for the ABAQUS cyclic symmetry tube model. The results obtained will be discussed later in this chapter.

5.5 Validation with Experimental Results

Various numerical models have been developed both in ABAQUS and SC03, to evaluate the effective MMC shear modulus for different fibre orientations. Within this section, numerical results obtained from the finite element models and experimental results obtained from the VITAL test program will be presented and discussed.

Table 5.13 summarizes the effective MMC shear modulus for different fibre orientations at room temperature. To give a better view for the results and draw conclusions, the results are plotted in two graphs, i.e. unidirectional ply and cross-ply, as shown in Figure 5.29 and Figure 5.30, respectively.

	0°	+30°	-30°	±30°	+45°	-45°	±45°
ABAQUS Tube Model	50.1	65.5	65.5	66.3	69.5	71.7	72.5
ABAQUS Cyclic Symmetry Tube Model	50.1	65.5	65.4	66.2	69.5	71.7	72.4
SC03 Cyclic Symmetry Tube Model	61.7	68.9	68.9	68.9	69.3	71.5	72.2
ABAQUS Unit Cell Model	62.1	–	–	–	–	–	73.1
SC03 Unit Cell Model	–	–	–	–	–	–	72.0
Experiment Results (VITAL)	62.8	66.6	68.4	67.3	68.2	68.6	70.5

Table 5.13 Summary results of effective MMC shear modulus
at room temperature

Results from the ABAQUS tube model and cyclic symmetry tube models were used to obtain predictions of shear modulus for all cases. In general, the correlation is good. However, for the 0° fibre orientation, the shear modulus predicted by ABAQUS is 19% less than that from the SC03 cyclic symmetry

tube model. Also, the measured shear modulus for the 0° fibre orientation is very close to the SC03 cyclic symmetry tube model and the ABAQUS unit cell model. For the $+45^\circ$ and -45° fibre orientations, the ABAQUS tube model and the cyclic symmetry tube model predicted similar results to the SC03 cyclic symmetry tube model. Comparing predictions with the experimental results, the predictions generally show a good agreement. For the $+30^\circ$ and -30° fibre orientations, the ABAQUS models predict slightly lower shear modulus than to the SC03 models. As can be expected, there will be some variability in the experimental results. It is also concluded that ABAQUS appears to have some inaccuracies when dealing with the 0° fibre orientation for tube models. The only difference between the 0° fibre orientation and other fibre orientation for the tube models is that the orientation angle in the input file is different. The big increase in shear modulus, when changing the orientation angle from 0° to 30° , is surprising.

A graph showing the variation of the shear modulus predicted from the numerical models and from experimental results, for cross-ply fibre orientation is shown in Figure 5.30. The various shear moduli predicted, or measured, for the $\pm 30^\circ$ or $\pm 45^\circ$ fibre orientations exhibit very good agreement. In general, the results all lie within 4% of each other. For the $\pm 45^\circ$ fibre orientation, all numerical models predicted a higher shear modulus when compared with the test results. This is probably due to the fact that a perfect bond is assumed for all numerical models. Further, the $\pm 45^\circ$ fibre orientation is harder to manufacture, due to the difficulty of the wrapping process for MMC plies around the mandrel, leading to the MMC being more prone to defects. However, the measured shear

modulus for the 0° fibre orientation was higher than all numerical models as this fibre orientation is the easiest to manufacture compared with the others.

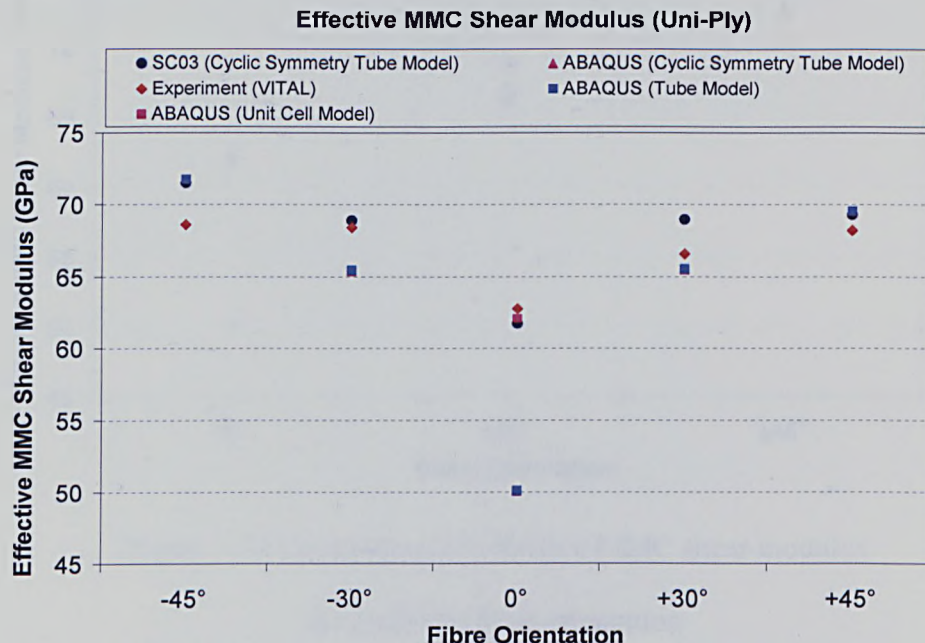


Figure 5.29 Comparison of effective MMC shear modulus for unidirectional fibre orientation

In conclusion, Figure 5.29 clearly shows a trend for the variation of the shear modulus of unidirectional MMCs, with fibre orientation for orientations varying from -45° to $+45^\circ$. The results are consistent except for the ABAQUS tube and cyclic symmetry tube models with the 0° fibre orientation. The highest shear modulus is achieved with the $\pm 45^\circ$ fibre orientation, both in the numerical models and the experimental results. Figure 5.30 shows a similar trend when the shear modulus increases with fibre orientation for fibre orientations from 0° to $\pm 45^\circ$. Beyond 45° , it is expected that the shear modulus will decrease. To obtain the highest shear modulus, the fibres should be aligned in the principal stress directions, i.e. at 45° to the tube axis for pure torsion.

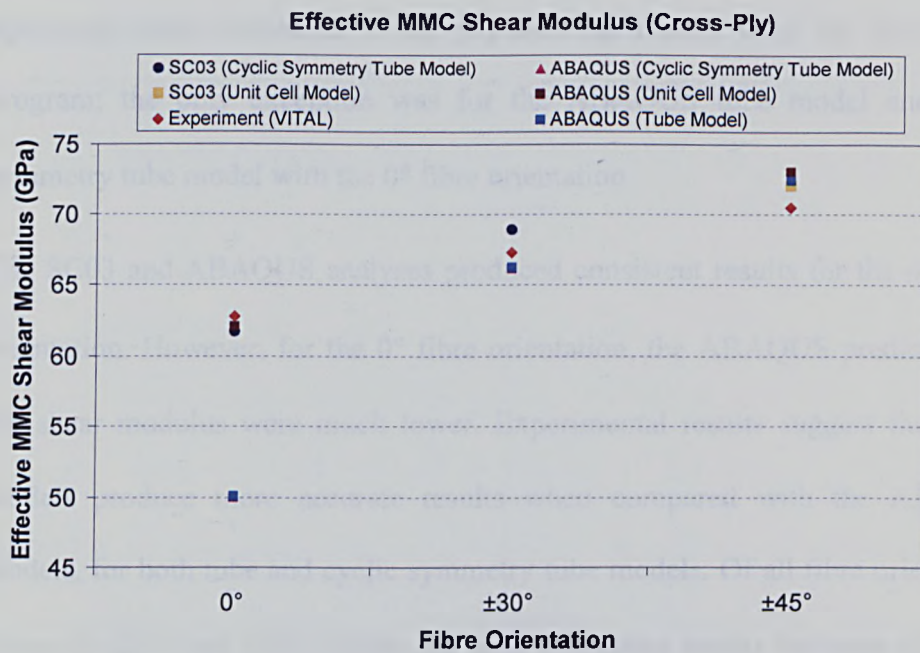


Figure 5.30 Comparison of effective MMC shear modulus
for cross-ply fibre orientation

5.6 Summary

Various numerical models have been developed using the ABAQUS and SC03 FE analysis packages. These include unit cell models, tube models and cyclic symmetry tube models. Unit cell models are used to determine 9 elastic constants which define the orthotropic elastic properties for the MMC layer. These include three Young's moduli, three Poisson's ratios and three shear moduli. Some of the unit cell models were also used to evaluate the effective MMC shear modulus for fibre orientations of 0° and $\pm 45^\circ$.

The calculated material constants are then used to define the properties of the MMC core layer for the tube model and cyclic symmetry tube model. The effective MMC shear moduli were calculated for 0° , $+30^\circ$, -30° , $+45^\circ$, -45° , $\pm 30^\circ$ and $\pm 45^\circ$ fibre orientations. The predicted results obtained, show a good

agreement when compared to the experimental results from the VITAL test program; the only exception was for the ABAQUS tube model and cyclic symmetry tube model with the 0° fibre orientation.

The SC03 and ABAQUS analyses produced consistent results for the 45° fibre orientation. However, for the 0° fibre orientation, the ABAQUS predictions of the shear modulus were much lower. Experimental results suggest that SC03 models produce more accurate results when compared with the ABAQUS models, for both tube and cyclic symmetry tube models. Of all fibre orientation, cross-ply $\pm 30^\circ$ and $\pm 45^\circ$ exhibit the most consistent results between all of the numerical model results and the experimental results.

Chapter 6 describes the methodology of the TiMMC torsional buckling analysis using FE method. The buckling shaft model can be used to perform buckling calculation of shafts, with any geometries and any fibre orientations. The aim of this calculation is to evaluate the buckling torque, failure mode shape and to obtain the torque vs. twist curve.

CHAPTER 6

TIMMC TORSIONAL BUCKLING ANALYSIS USING FINITE ELEMENT METHOD

6.1 Introduction

The orthotropic elastic material properties for MMC core layer have been predicted using unit cell models in Chapter 5. Subsequently, the material properties were implemented in tube models to evaluate the effective MMC shear modulus for different fibre orientations. Since, TiMMC is a potential material for aero engine drive shafts, it is necessary to understand how the MMC affects other important component failure modes such as buckling. Moreover, with increasing demand for higher performance from the component, for use of lighter materials, leading to thinner walled shafts increase the tendency for buckling instability to occur.

However, until now, nothing has been reported within the literature by any researchers, to describe the buckling behaviour of TiMMC shafts subjected to pure torsion. Nonetheless, theoretical predictions, based on general shell theory, were made by Bauchau et al. [40] for graphite/epoxy composite shafts. The theoretical model, which includes elastic coupling effects and transverse shearing deformations, agreed well with measured torsional buckling loads. Also, Tennyson et al. [41] developed an analytical model to evaluate the compressive buckling strength of sandwich cylinders with axisymmetric shape imperfections and Bert et al. [42] presented a theoretical approach for determining the buckling torque of circular hollow composite shafts, using

various thin-shell theories. The theoretical models were compared with results from experiments and good agreement was achieved.

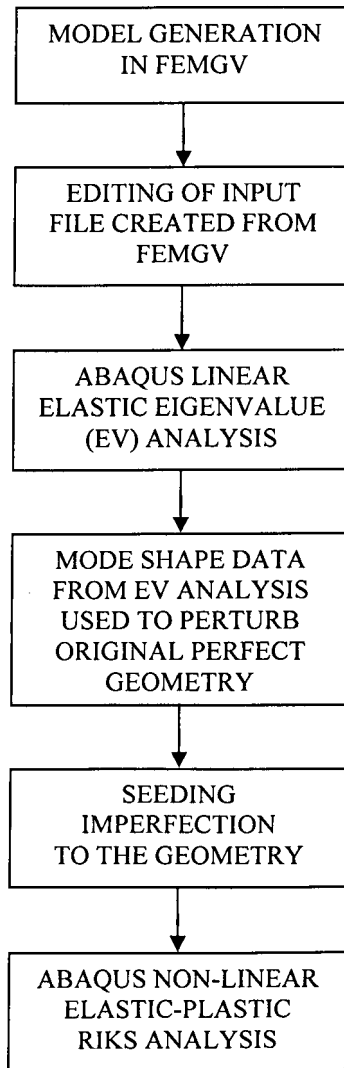


Figure 6.1 FE buckling analysis route

Within phase 3 of the VITAL project, 3 TiMMC shafts will be manufacture and tested at room temperature, to investigate the buckling behaviour. However, the experimental results can not be included in this thesis due to delays in the delivery of the shafts. This chapter outlines the methodology used for the TiMMC torsional buckling FE analysis based on the approach proposed by Robotham [43, 44]. The aim of the buckling analysis is to perform a fully non-

linear FE analysis of a shaft, using the ABAQUS FE package, in order to obtain the buckling load, mode shapes and torque vs. twist curve.

Figure 6.1 outlines the analysis route for a FE shaft buckling analysis. Detailed descriptions of each step will be presented within this chapter, including model generation in FEMGV, editing of the input file to define the model, linear elastic eigenvalue (EV) analysis and elastic-plastic Riks analysis.

6.2 Analysis Algorithms

In ABAQUS, EV and Riks algorithms can be used for the prediction of buckling behaviour. However, in order to fully understand the buckling behaviour, both algorithms were used here. The EV algorithm was used, as a first step, to estimate the critical buckling load and mode shapes. Then, a mode shape was selected from the EV results to perturb the perfect geometry for a subsequent elastic-plastic Riks analysis. Details of each algorithm will be presented in the following sub-sections.

6.2.1 Elastic Buckling (Eigenvalue Algorithm)

The eigenvalue algorithm was used for linear elastic buckling prediction. This algorithm assumed the response is linear before buckle occurs. For example, the Euler column responds very stiffly when subjected to a compressive axial load, until a critical load is reached. Then, it bends suddenly and exhibits a much lower stiffness. The EV analysis is required as a step towards the more general collapse or elastic-plastic Riks analysis. It can be used in two ways. First, the analysis estimates the critical buckling load. Second, the mode shapes from the EV buckling analysis provides the necessary data for the complete elastic-plastic Riks buckling analysis.

The concept of the EV algorithm is based on the determination of singularities in a linear perturbation of the structure's stiffness matrix. The estimated critical buckling load is only valid if the linear perturbation is a realistic reflection of the shaft before it buckles. Therefore, this method is only suitable for very stiff shafts or structures which exhibit very small elastic deformations before they buckle. In many cases, the post-buckling response is unstable and may strongly depend on imperfections of the structure. Thus, the actual collapse load may be significantly lower than the critical buckling load predicted by the EV analysis. The Riks algorithm, which is detailed in the next sub-section, can be used to predict the complete buckling characteristic, including the post-buckling response.

In the ABAQUS input file, the following command lines are used to perform the EV analysis:-

```
*STEP, PERTURBATION
*BUCKLE
a, b, c, d
```

Where:

- a = number of eigenvalues to be estimated
- b = maximum eigenvalue of interest
- c = number of vectors used in the iterations
- d = maximum number of iterations

The number of eigenvalues estimated for all of the analyses was 4. The analysis also provides mode shapes corresponding to each EV, which can be used to perturb the perfect geometry for the Riks buckling analysis. Buckling mode shapes are normalized vectors and do not represent the actual magnitudes of deformation at critical load. However, the mode shapes predicted show the likely

failure mode of the structure. The EV calculated is a “load multiplier”, where the original load applied in the analysis is multiplied by the EV to give the estimate of the buckling load.

6.2.2 Elastic-Plastic Buckling (Riks Algorithm)

TiMMC material exhibits material nonlinearity characteristic, hence, the linear elastic EV analysis is not suitable. For structures which exhibit snap-through behaviour, i.e. the elastic deformation result in large geometry changes prior to collapse, the Riks algorithm can be used to investigate the problem further. Such structures tend to reach a maximum sustainable load, which then increases and decreases in post-buckling behaviour. When zero stiffness is reached at the point of maximum load, the Newton-Raphson method used in the regular ABAQUS *STATIC analysis procedure predicts an unbounded displacement increment. This prevents further prediction of the load-displacement characteristics. By using the Riks algorithm it is possible to overcome the problem of zero stiffness.

The Riks algorithm determines the static equilibrium at the end of each increment. Unlike a normal static analysis, the load magnitude is a solution variable and thus can increase or decrease during the analysis, to satisfy static equilibrium. To control the progress of the analysis, some measure of the response, which increases monotonically during the analysis, must be introduced. Since both the load and the displacement can either increase or decrease during the analysis, neither is suitable for this purpose. As a consequence, another quantity must be selected, which measures the progress of the solution. The “arc length” is used for this purpose. The “arc length” is the

length along the static equilibrium path, in the load-displacement space, which is used to control the automatic time incrementation algorithm.

Static analysis of post-buckling problems using the “arc length” method provides valuable information about the characteristics of structures in the unstable regime. The method works well if the equilibrium path in the load-displacement space is smooth and does not branch. Otherwise, convergence and incrementation problems may occur. This means that the method should always be applied to imperfect geometries.

The Riks method often follows an EV analysis to provide complete information about the collapse of a structure. To overcome the discontinuous nature of the response, at the point of bifurcation, obtained from the EV analysis, a small initial imperfection is introduced into a perfect geometry. Such imperfections are introduced into the model by perturbing the geometry using the lowest buckling mode shape. This ensures that the response in the buckling mode is achieved before the critical load is reached. Essentially, this also converts a pure bifurcation problem into a snap-through problem. Details of the process for seeding imperfections to the geometry are presented in Section 6.3.4. The elastic-plastic material properties which need to be specified for a Riks analysis are presented in Section 6.3.3.

In the ABAQUS input file, the following command lines are used to perform the Riks analysis:-

```
*STEP, NLGEOM, INC=50
*STATIC, RIKS
a, b, c, d, e, f, g, h
```

Where:

a = initial increment in arc length

- b = total arc length scale factor
- c = minimum arc length increment
- d = maximum arc length increment
- e = maximum value of Load Proportionality Factor (LPF)
- f = node number being monitored
- g = degree of freedom being monitored
- h = value of total displacement or rotation at the node and degree of freedom that, if exceeded during an increment, ends the step at the current increment

Geometric nonlinearity is activated by specifying NLGEOM after the *STEP command, where INC represent the maximum number of increments for the step. When using the Riks method, if none of the termination criteria are specified or are not exceeded, the analysis will stop after the maximum number of increments is reached. The analysis will also terminate when the solution fails due to excessive distortion. The Load Proportionality Factor (LPF) used in the Riks method is detailed in Section 6.3.7.

6.3 Analysis Approach

6.3.1 Design and Model Generation

The design process used for the TiMMC buckling test shafts is identical to that for the VITAL phase 1 tubes tested within this project. However, the overall size of the buckling shafts is larger, with a larger plain section length, larger outer diameter and thinner wall. Table 6.1 is the VITAL phase 3 test matrix, which shows the geometries and fibre orientations of the 3 buckling shafts. Note that there are only 2 sets of geometries here, as B2 and B3 are identical in size except for the fibre orientation. B1 has 6 MMC plies while B2 and B3 have 4 MMC plies at the core layer. All buckling shafts are to be tested at room temperature.

Test Reference	B1	B2	B3
Fibre Orientation	$\pm 45^\circ$	$\pm 45^\circ$	$+45^\circ$
Outer Diameter	82	82	
Inner Diameter	77	78	
Plain Section Length	300	300	
Wall Thickness	2.5	2.0	
MMC Thickness	1.5	1.0	

Table 6.1 VITAL phase 3 test matrix

From the experimental results presented in Chapter 3, it can be seen that specimens with $\pm 45^\circ$ and $+45^\circ$ fibre orientations gave the highest strengths and high shear moduli. Therefore, the same fibre orientations were selected for the buckling shafts. Since the VITAL demonstrator TiMMC shaft has an outer diameter of 82mm, the buckling shafts use the same size. This is of benefit to TISICS Ltd. who will manufacture the demonstrator shaft and need to investigate the manufacturability of it. The demonstrator shaft has a $\pm 45^\circ$ fibre orientation with 16 MMC plies and a length of 1.2m. All buckling shafts have an inner and outer cladding of 0.5mm.

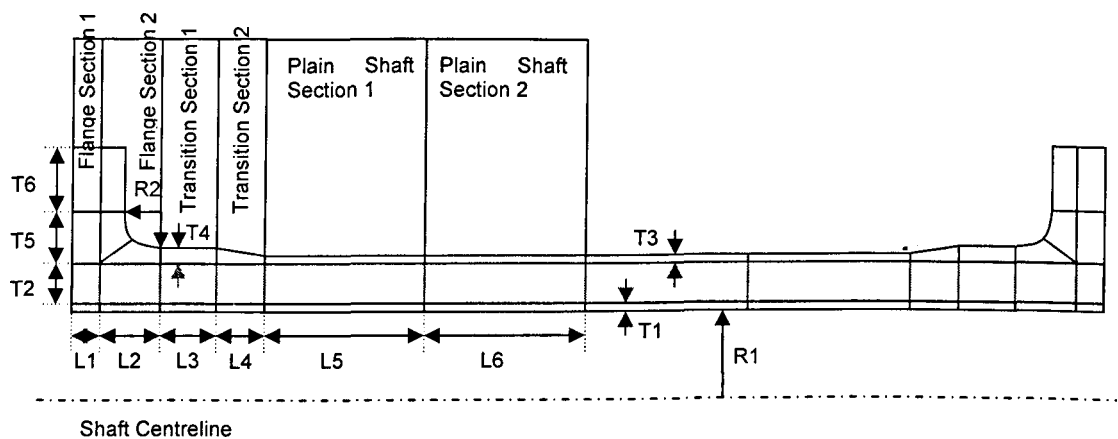


Figure 6.2 Schematic diagram of a shaft model with respective parameters

A fully parametric 360-degree tube model has been developed in FEMGV as shown in Figure 6.2. By changing the parameters accordingly, the buckling

models can be regenerated with ease. The definition of each parameter used is presented in Table 6.2.

Independent Parameter	Inner Radius of Shaft	R1
	Flange Radius	R2
	Ti Cladding Thickness	T1
		T3
	TiMMC Thickness	T2
	Thickness of transition end flange	T4
	Extra Flange Thickness	T6
	Flange Section 1 Length	L1
	Transition Section 1 Length	L3
	Transition Section 2 Length	L4
	Shaft Section 1 Length	L5
	Shaft Section 2 Length	L6
Dependent Parameter	Flange Section 2 Length ($L2 > R2$)	L2
	Flange Thickness ($R2 + T4$)	T5

Table 6.2 Definition of shaft parameters

Parameters	Models	
	B1	B2 & B3
R1	38.5	39.0
R2	3.0	
T1	0.5	
T2	1.5	1.0
T3	0.5	
T4	3.0	
T6	24.5	
L1	22	
L3	9.14	
L4	12.86	
L5	75	
L6	75	
L2	6.0	
T5	6.0	

Table 6.3 Parameters of buckling models

Table 6.3 shows the parameters used for the buckling models. Changes in R1, T1, T2 and T3 alter the diameter, while changes in L5 and L6 alter the plain section length of the models. The magnitudes of these parameters are significantly larger than those used for the phase 1 tube models. Major

differences between 2 sets of geometries are R1 and T2 which alter the inner radius and MMC thickness, respectively.

6.3.2 Elements

Similar to the phase 1 tube models, 20-node quadratic brick elements (C3D20R), with reduced integration, were used for the buckling models. ABAQUS [45] recommends the use of stress/displacement element in the modelling of linear and non-linear mechanical analyses, which involve plasticity and large deformations. Therefore, the brick type element was selected for the buckling analyses. The mesh of the model was refined in FEMGV, as shown in Figure 6.3. Finer meshes were used in the plain section, where the buckling failure occurs.

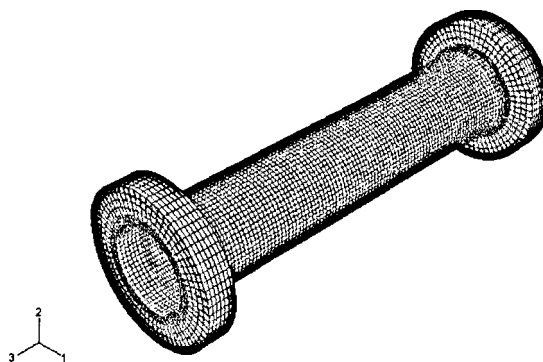


Figure 6.3 FE buckling model with fine mesh

This model contains approximately 27,000 brick elements. As this is a TiMMC shaft model which is made up of inner cladding, outer cladding and MMC layer, at least one element through the thickness is needed for each constituent material. Therefore, there are 3 elements through the wall thickness. Unlike models with monolithic material, 1 element through the thickness is sufficient; increase in the number of elements would significantly increase the analysis run

times and is computationally expensive. Moreover, in general, elastic-plastic analysis results in long analysis run times. For the buckling model developed here, the linear elastic EV analysis took approximately 1.5 hours, while the elastic-plastic Riks analysis took approximately 13 to 20 hours. The platform used is a PC with 3.4GHz processor and 3.0GB memory.

6.3.3 Material Models

For an EV analysis, only elastic material properties are needed while for a Riks analysis elastic-plastic material properties are required. The material models used for both analyses are presented in the next two sub-sections.

6.3.3.1 Elasticity Material Model

Both EV and Riks analyses required elasticity material properties. Isotropic elastic material properties were used for the titanium cladding. For the MMC layer, orthotropic elastic material properties were used. The elasticity material models used for the buckling models are identical to those used for the tube models presented in Chapter 5. Table 6.4 shows the material properties used where the 3-direction is the shaft axis.

In the ABAQUS input file, the following command lines are used to specify the fibre orientation of the shaft model:-

```
*SOLID SECTION, ELSET=PHY2, COMPOSITE, STACK DIRECTION=2,
ORIENTATION=OR1
0.00025, , TMCM, +45.0
0.00025, , TMCM, +45.0
0.00025, , TMCM, +45.0
0.00025, , TMCM, +45.0
```

The command lines under the *SOLID SECTION command define the MMC layers and their properties. The command lines shown above represent 4 MMC

layers orientated at $+45^\circ$ direction with 0.25mm thick for each layer. A positive angle means a counter-clockwise direction relative to the local direction, which is specified under the *ORIENTATON command. For further details regarding the definition of the local direction, refer to Chapter 5. TCM is the material name for the MMC layers, defined earlier in the input file.

ABAQUS	
Ti-6-4 (Isotropic Material Model)	
E	116.4 GPa
ν	0.32
MMC Layer (Orthotropic Material Model)	
E_1	154.3 GPa
E_2	154.9 GPa
E_3	203.2 GPa
ν_{12}	0.30
ν_{13}	0.20
ν_{23}	0.20
G_{12}	50.3 GPa
G_{13}	50.5 GPa
G_{23}	50.5 GPa

Table 6.4 Elastic material properties for Ti-6-4 and MMC layer

6.3.3.2 Plasticity Material Model

In addition to the elastic material properties, a Riks analysis requires the plasticity properties for the materials. Different plastic material properties were used for the titanium and the MMC layer.

For the titanium cladding, an Isotropic Elastic-Plasticity model was used, which is very common for classical metal plasticity. This model uses the von Mises yield function with the associated flow rule and isotropic hardening was selected. The plasticity material model is defined by giving the value of the stress as a function of uniaxial equivalent plastic strain. It is a requirement in ABAQUS, that the plastic data is in the form of true stress and true strain.

However, material test data is often supplied using nominal stress and nominal strain, which is based on the initial geometry. Hence, a conversion is needed for the plastic data from the nominal stress/strain values to the true stress/strain values.

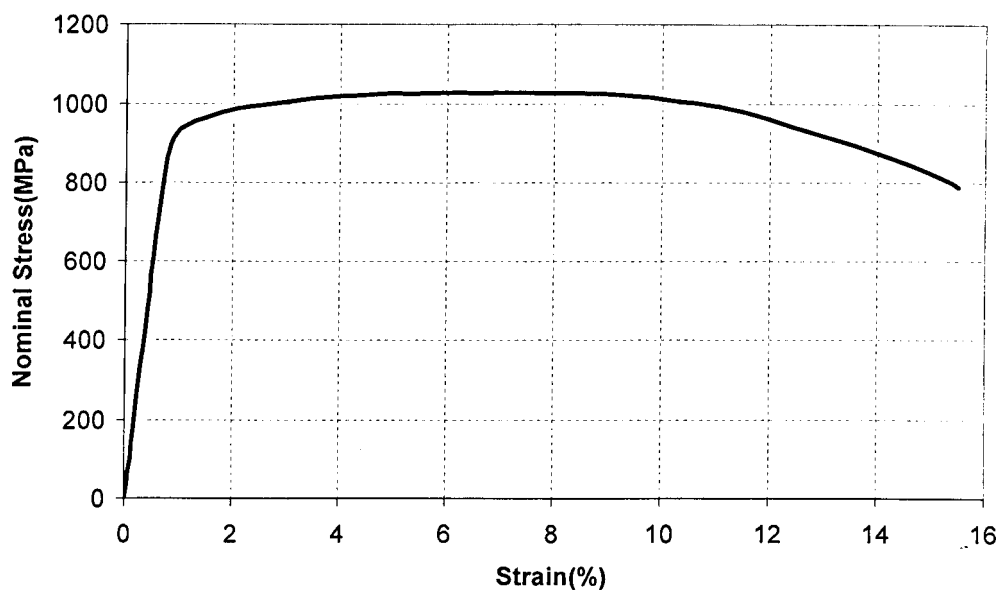


Figure 6.4 Room temperature tensile stress vs. strain curve
for annealed Ti-6-4 rod

The nominal stress/strain data for titanium was obtained from the engineering tensile stress strain curve as shown in Figure 6.4. The curve was generated from a tensile test conducted on an annealed Ti-6-4 rod and is published on the IMI datasheet. To convert the nominal stress/strain to true stress/strain, equations 6.1 and 6.2 were used, in which ϵ_{nom} and σ_{nom} are the nominal strain and nominal stress, respectively. ABAQUS requires true stress and true plastic strain in order to interpret the data correctly. However, the strain values obtained from the material test data are total strains. Therefore, the converted true strain values need to be separated into the elastic and plastic components. The procedure to obtain the values required and the derivations of the equations are detailed in

Appendix D. The relationship between true stress/strain and nominal stress/strain are:-

$$\varepsilon = \ln(1 + \varepsilon_{nom}) \quad (6.1)$$

$$\sigma = \sigma_{nom} (1 + \varepsilon_{nom}) \quad (6.2)$$

The material data for the plasticity material model are defined in the input file under the *PLASTIC command. As mentioned in Appendix D, the first piece of data given defines the initial yield stress of the material. Therefore, this should be associated with a plastic strain value of zero. Figure 6.5 shows the plastic part component of the converted true stress vs. true strain curve from Figure 6.4. This curve was used to define the plasticity material data for Ti-6-4. Note that, the first data point is the initial yield stress with zero plastic true strain. These data are in tabulated form in the ABAQUS input file.

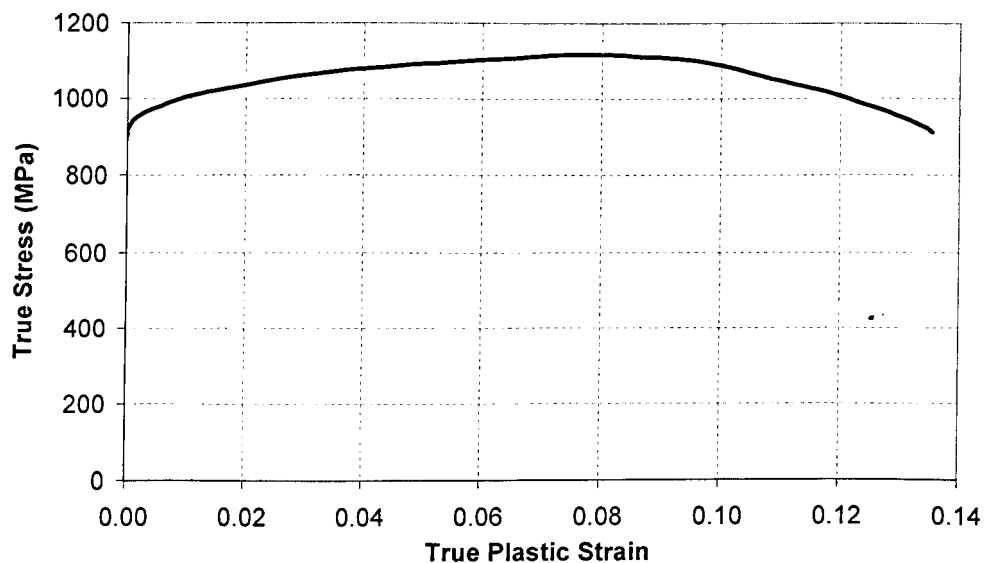


Figure 6.5 True stress vs. true plastic strain curve for Ti-6-4

For the plastic material model for the MMC layer, a different approach was used. Since the MMC layer exhibit different yield behaviours in different

directions, user-defined stress ratios that are applied in Hill's potential function were specified in the model. Hill's potential function can be used to model anisotropic yield behaviour, which is a simple extension of the von Mises function. This material model can be used in conjunction with the *PLASTIC option and is expressed, in terms of rectangular Cartesian stress components, as:-

$$f(\sigma) = \sqrt{F(\sigma_{22} - \sigma_{33})^2 + G(\sigma_{33} - \sigma_{11})^2 + H(\sigma_{11} - \sigma_{22})^2 + 2L\sigma_{23}^2 + 2M\sigma_{31}^2 + 2N\sigma_{12}^2} \quad (6.3)$$

where F, G, H, L, M, N are constants obtained from the results of tests carried out on the material, in various directions. They are defined as:-

$$F = \frac{(\sigma^0)^2}{2} \left(\frac{1}{\bar{\sigma}_{22}^2} + \frac{1}{\bar{\sigma}_{33}^2} - \frac{1}{\bar{\sigma}_{11}^2} \right) = \frac{1}{2} \left(\frac{1}{R_{22}^2} + \frac{1}{R_{33}^2} - \frac{1}{R_{11}^2} \right) \quad (6.4)$$

$$G = \frac{(\sigma^0)^2}{2} \left(\frac{1}{\bar{\sigma}_{33}^2} + \frac{1}{\bar{\sigma}_{11}^2} - \frac{1}{\bar{\sigma}_{22}^2} \right) = \frac{1}{2} \left(\frac{1}{R_{33}^2} + \frac{1}{R_{11}^2} - \frac{1}{R_{22}^2} \right) \quad (6.5)$$

$$H = \frac{(\sigma^0)^2}{2} \left(\frac{1}{\bar{\sigma}_{11}^2} + \frac{1}{\bar{\sigma}_{22}^2} - \frac{1}{\bar{\sigma}_{33}^2} \right) = \frac{1}{2} \left(\frac{1}{R_{11}^2} + \frac{1}{R_{22}^2} - \frac{1}{R_{33}^2} \right) \quad (6.6)$$

$$L = \frac{3}{2} \left(\frac{\tau^0}{\bar{\sigma}_{23}} \right)^2 = \frac{3}{2R_{23}^2} \quad (6.7)$$

$$M = \frac{3}{2} \left(\frac{\tau^0}{\bar{\sigma}_{13}} \right)^2 = \frac{3}{2R_{13}^2} \quad (6.8)$$

$$N = \frac{3}{2} \left(\frac{\tau^0}{\bar{\sigma}_{12}} \right)^2 = \frac{3}{2R_{12}^2} \quad (6.9)$$

Where

$$R_{11} = \frac{\bar{\sigma}_{11}}{\sigma^0} \quad (6.10)$$

$$R_{22} = \frac{\bar{\sigma}_{22}}{\sigma^0} \quad (6.11)$$

$$R_{33} = \frac{\bar{\sigma}_{33}}{\sigma^0} \quad (6.12)$$

$$R_{12} = \frac{\bar{\sigma}_{12}}{\tau^0} \quad (6.13)$$

$$R_{13} = \frac{\bar{\sigma}_{13}}{\tau^0} \quad (6.14)$$

$$R_{23} = \frac{\bar{\sigma}_{23}}{\tau^0} \quad (6.15)$$

However, due to the form of the yield function described by equation (6.3), all ratios must be positive. If the constants F , G , and H are positive, the yield function is always well defined.

The anisotropic yield behaviour is modelled through the use of yield stress ratios R_{ij} . The yield stress ratios are defined with respect to a reference yield stress σ^0 , such that if σ_{ij} is applied as the only nonzero stress, the corresponding yield stress ($\bar{\sigma}_{ij}$) is $R_{ij}\sigma^0$. Local orientation must be used to define the direction of anisotropy. In the case of the shaft, a cylindrical coordinate system was used where the 1, 2 and 3 directions refer to radial, tangential and axial directions, respectively. The reference yield stress (σ^0) used here is 200MPa which is specified under the *PLASTIC command and $\tau^0 = \sigma^0 / \sqrt{3}$. The yield stress ratios are defined under the *POTENTIAL command directly after the *PLASTIC command.

For example, a shaft with 0° fibre orientation, the 1-direction is the radial direction. If the material is being stressed in this direction, it will behave like a coupon specimen being stressed with the fibre direction being at 90° . Hence the yield stress from a 90° coupon test was used as the yield stress $\bar{\sigma}_{11}$. The stress ratio R_{11} is obtained by dividing the yield stress by the reference yield stress σ^0 . For the 2-direction which is tangential to the fibre direction, the yield stress $\bar{\sigma}_{22}$ is also the yield stress of a “ 90° coupon”. Hence, the yield stress ratios, R_{22} , will be the same as R_{11} . For the 3-direction which is parallel (axial) to the fibre direction, the yield stress $\bar{\sigma}_{33}$ is the yield stress from a 0° coupon test. The coupon yield stresses were obtained from the coupon tests [26] which has a fibre volume fraction of 35%. The yield stresses for 90° and 0° coupons are 266.2 MPa and 1337.2 MPa, respectively.

Parameters	Magnitude	Remarks
Ref. Yield Stress	$\sigma^0 = 200$ MPa	Choose any value
	$\tau^0 = 115.47$ MPa	$\tau^0 = \sigma^0 / \sqrt{3}$
R_{11}	1.331	Yield stress from 90° coupon test data
R_{22}	1.331	Yield stress from 90° coupon test data
R_{33}	6.686	Yield stress from 0° coupon test data
R_{12}	4.884	0.2% proof strength from UTC1
R_{13}	4.884	0.2% proof strength from UTC1
R_{23}	4.884	0.2% proof strength from UTC1

Table 6.5 Reference yield stresses and stress ratios for MMC layer

For shear stress ratios (R_{12} , R_{13} and R_{23}), these ratios are defined using the 0.2% proof strength from UTC1 tube specimen with 0° fibre orientation. Investigation shows that the shear stress ratios have no effect on the buckling behaviour for a 45° fibre orientation shaft. This is because the buckling behaviour is strongly dominated by the on-axis stress ratio, i.e. R_{33} . The effect of the shear stress

ratios on the buckling results is presented in detailed in Section 6.4.2. The 0.2% proof strength of UTC1 is 564 MPa where the shear stress ratios were calculated using equations (6.13), (6.14) and (6.15) with the reference shear yield stress of 115.47 MPa. Table 6.5 shows the reference yield stresses and stress ratios used to define the anisotropic yield behaviour of the MMC layer.

Below are the command lines used to define the elastic-plastic material properties for the MMC layer. The orthotropic material properties were defined using the *ELASTIC command, which is identical to those specified for the tube model. The reference yield stress and the associated plastic strain were defined using the *PLASTIC command. Using the *POTENTIAL command, the stress ratios were specified, in sequence. As was the case with the tube model, the fibre orientation for each MMC layer can be change under the *SOLID SECTION command.

```
*MATERIAL, NAME=TMCM
*ELASTIC, TYPE=ENGINEERING CONSTANTS
154.3172E+9, 154.9341E+9, 203.1527E+9, 0.2997, 0.2043,
0.2043, 50.259E+9, 50.459E+9
50.459E+9
*PLASTIC
200000000.0, 0.0
*POTENTIAL
1.331, 1.331, 6.686, 4.884, 4.884, 4.884

*SOLID SECTION, ELSET=PHY2, COMPOSITE, STACK DIRECTION=2,
ORIENTATION=OR1
0.00025, , TMCM, 0.0
0.00025, , TMCM, 0.0
0.00025, , TMCM, 0.0
0.00025, , TMCM, 0.0
```

6.3.4 Imperfections

The introduction of imperfection has two effects on the analyses. First, it simulates the effect of inevitable manufacturing variations that would be present

on an actual shaft. Secondly, it helps the FE analysis to overcome any numerical problems arise with the use of perfect geometry.

As mentioned earlier, a small initial imperfection needs to be specified in the Riks analysis. This is to overcome the discontinuous nature of the response at the point of bifurcation. There are two approaches used in order to introduce an imperfection into a perfect geometry; there are loading or geometric imperfections. For loading imperfections, a fictitious “trigger load” is used to initiate the instability. For geometric imperfections, the EV mode shapes from, previous EV analysis, are used as the basis of the imperfection. For all analyses carried out here, the latter approach was used. The lowest buckling mode shape is assumed to provide the most critical imperfection, which is scaled and added to the perfect geometry to create the perturbed mesh.

Imperfection is activated in ABAQUS, using the `*IMPERFECTION` command. The following is an example of the command lines in which the `FILE` parameter indicates the name of the result file from where the EV mode shape is to be read from. In this case, the name of the result file is “buckling_shaft” which has a file extension “.fil”. This file needs to be in the same directory as the ABAQUS input file. The `STEP` parameter indicates the step number which is the mode shape number in the result file. The mode shape associated with the lowest EV, i.e. shape 1, was used here. The second command line shows the step number and the scaling factor which is measured in meters. For the case of torsional buckling of a shaft, the scaling factor/level of imperfection was based on a percentage of shaft wall thickness [44]. The level of imperfection used in the buckling analysis was chosen based on the guidance from [44], where the author

discusses the different imperfection values. If the shaft model did not exhibit a buckling failure, the level of imperfection was then increased further.

```
*IMPERFECTION, FILE=buckling_shaft, STEP=1  
1, 0.00005
```

6.3.5 Boundary Conditions

As with the tube models, the flange surface of the shaft model opposite to the loading flange face was constrained to be encastre. This is to prevent rigid body motion.

6.3.6 Loading

Also, as with the tube models, pure torsion was applied through a dummy node at one end of the shaft. Every node at this flange face was “constrained” to the dummy node via the MPC command.

6.3.6.1 EV Analysis

The magnitude of the load specified in the input file for the EV buckling analysis is not important as it is scaled by the “load multiplier”. Therefore, a nominal torsion load of 100 Nm was specified for all EV analyses. It is a one-step analysis procedure which contains a number of iterations in order to reach convergence for the EV prediction.

6.3.6.2 Riks Analysis

The Riks analysis follows the EV analysis. However, the sign of the load for Riks analysis is important and this depends on the sign of the eigenvalue/mode shape chosen. If the 1st mode shape from the EV analysis was chosen and the associated eigenvalue has a negative value, then the load for the Riks analysis

must have the same sign, i.e. -100 Nm. On the other hand, if the 1st mode shape was chosen with a positive eigenvalue value, then the load for the Riks analysis must have a positive sign.

If this is not done, the results can be misleading because the imperfection has a particular rotational direction. If it is applied in the opposite sense to the torsional loading, the imperfection will have the opposite effect which acts as an artificial stiffener to the structure; this will lead to a buckling load that is too high.

6.3.7 Monitoring the Analysis

During an EV analysis, the user can monitor the progress by looking at the “.msg” file. This file gives the current estimates for the eigenvalues requested and the iteration number that the analysis is currently on. The analysis is completed once the solution has converged for the number of eigenvalues requested. However, there is a possibility that some of the eigenvalues have negative sign. This indicates that the shaft model will buckle if it is loaded at the reverse direction.

The procedure for a Riks analysis is incremental and iterative. Hence, it attempts to follow the load-deflection path of the shaft and attempts to find static equilibrium in each increment. This involves several iterative steps within each increment. During a Riks analysis, the user can monitor the progress by looking at the “.msg” file. This file gives details of each increment and iteration and how it is progressing. Warning messages are written in this file if the analysis is diverging, which is very useful. Also, by looking at the “.sta” file, the user can check the current status of the analysis. Information such as the Load

Proportionality Factor (LPF) for each increment and the accumulated LPF are written in this file.

The accumulated LPF indicates how much load is being applied in the current increment. As a quick check, the actual load is simply obtained by multiplying the load specified in the Riks analysis input file by the accumulated LPF. Table 6.6 gives an example of the status file showing the progress of a Riks analysis.

STEP	INC	ATT	SEVERE DISCON ITERS	EQUIL ITERS	TOTAL ITERS	TOTAL TIME/ FREQ	STEP TIME/ LPF	INC OF TIME/LPF	DOF MONITOR	IF RIKS
1	1	1	0	3	3		0.5	0.5		R
1	2	1	0	3	3		1	0.5		R
1	3	1	0	4	4		1.75	0.75		R
1	4	1	0	4	4		2.88	1.125		R
1	5	1	0	4	4		4.56	1.688		R
1	6	1	0	4	4		7.09	2.531		R
1	7	1	0	4	4		10.9	3.797		R
1	8	1	0	4	4		16.6	5.696		R
1	9	1	0	4	4		25.1	8.543		R
1	10	1	0	5	5		37.9	12.82		R
1	11	1	0	5	5		48.5	10.51		R
1	12	1	0	4	4		56.4	7.928		R
1	13	1	0	4	4		64.2	7.828		R
1	14	1	0	5	5		75.8	11.55		R
1	15	1	0	5	5		87.1	11.34		R
1	16	1	0	6	6		97.5	10.35		R
1	17	1	0	8	8		96.5	-0.988		R
1	18	1	0	8	8		88	-8.477		R
1	19	1	0	6	6		79.7	-8.328		R
1	20	1	0	5	5		72.7	-6.98		R

Table 6.6 An example of the status file for a Riks analysis

The increment of the LPF gives an indication of how well it is converging. There are 3 things which could possibly happen. First, if the increment starts getting smaller, then the load is near to its maximum. Second, if the increment becomes negative, the load had reversed and the analysis is in the post-buckling phase. Finally, if the increment continually gets smaller and does not go negative, then there is a problem with the analysis as it is not converging. After some time and continuous iterations, the analysis will halt judging a converged solution is impossible. If there are problems with the analysis, then the “.msg” file gives

details which indicate what is going wrong. Normally the problem can be cured by reducing the minimum time increment used within the Riks analysis. This will allow a smaller time increment within the analysis. However, the problem may be more difficult to solve and may require, for example, mesh refinement and/or checks to ensure that the mesh is fully connected.

6.4 Results and Discussions

Having established the analysis approach, the results for the buckling shaft models, i.e. the VITAL phase 3 shafts, are presented in this section. The effects of the shear stress ratios and fibre orientation on the buckling behaviour are also presented.

All shaft models have a plain section length of 300mm, outer diameter of 82mm, with inner and outer cladding thicknesses of 0.5mm; refer to Table 6.1 for the dimensions of the VITAL phase 3 shaft models.

6.4.1 Analysis of Results

After the Riks analysis is completed, torque vs. twist curve can be obtained. The torque data can be obtained, through the LPF, from the status file. The LPF is multiplied by the applied load to obtain the actual load applied to the shaft model. Twist data can be obtained, through the “.dat” file. The rotation of the dummy node, which is the rotation of the shaft as a whole, is written in the file after each increment. With these data, the complete torque vs. twist curve can be plotted and analyze. The results of main interest are the peak load and the buckling failure mode.

6.4.2 Effect of Shear Stress Ratios

Due to the lack of experimental data, it is not possible to obtain the shear stress ratios for the MMC layer at this stage. Nonetheless, the 0.2% proof strength obtained from the results from the UTC1 (0° fibre orientation) test was used to estimate the shear stress ratio. The shear stress ratio was obtained by dividing the 0.2% proof strength by the reference shear yield stress. This is a “representative” shear stress ratio and was used for the buckling calculation, in the belief that precise knowledge of this ratio would not affect the numerical results obtained from an FE analysis. To assess its suitability, the effect of varying the shear stress ratios was investigated to establish how it affects the MMC buckling behaviour.

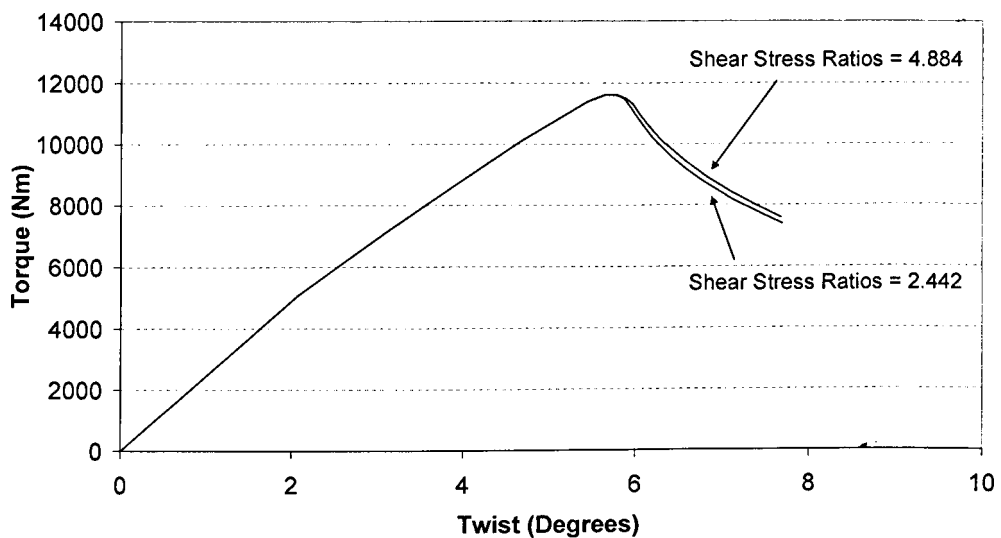


Figure 6.6 Torque vs. twist curve of shaft model B2 ($\pm 45^\circ$ fibre orientation) with different shear stress ratios

The nominal shear stress ratio has a value of 4.884. Initially, this “representative” shear stress ratio was used for R_{12} , R_{13} and R_{23} , where the stress ratios R_{11} , R_{22} and R_{33} , were calculated from the coupon test results. Then, the

buckling calculations were carried out for shaft models with $+45^\circ$ and $\pm 45^\circ$ fibre orientations. To investigate the effect of shear stress ratios to the peak load, the shear stress ratios were reduced by 50% to 2.442 and the calculations were repeated.

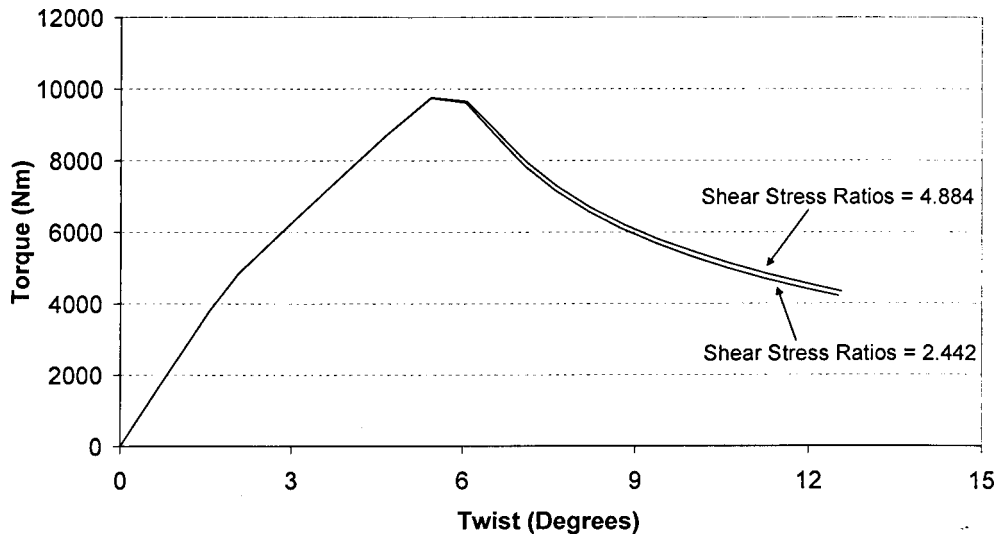


Figure 6.7 Torque vs. twist curve of shaft model B3 ($+45^\circ$ fibre orientation) with different shear stress ratios

Figure 6.6 shows the buckling results of B2 shaft model which has a $\pm 45^\circ$ fibre orientation. The peak load remains unchanged even though the shear stress ratio was reduced by 50%. However, very slight differences in the post-buckling behaviour were observed but this is considered to be negligible. Similar behaviour was predicted for the B3 shaft model. The finite element results are shown in Figure 6.7 and B3 for which there is a $+45^\circ$ fibre orientation. These results indicate that the magnitude of shear stress ratios has a negligible effect on the buckling behaviour of the MMC shaft with 45° fibre orientations. This is because the buckling behaviour for this fibre orientation is dominated by the on-axis stress ratio R_{33} , where the 45° direction is the principal stress direction for a

shaft in torsion. Thus, in this case, accurate determination of the magnitude of R_{33} , which defines the fibre on-axis yield stress, is vitally important whereas accurate knowledge of R_{12} , R_{13} and R_{23} is not important.

Figure 6.8 shows the buckling results for the 0° fibre orientation shaft models using the B2/B3 geometries. It can be seen that a reduction in the shear stress ratios, by 50% causes the peak load to drop by 24%. Moreover, the analysis with the reduced shear stress ratios failed to achieve the limit point for buckling.

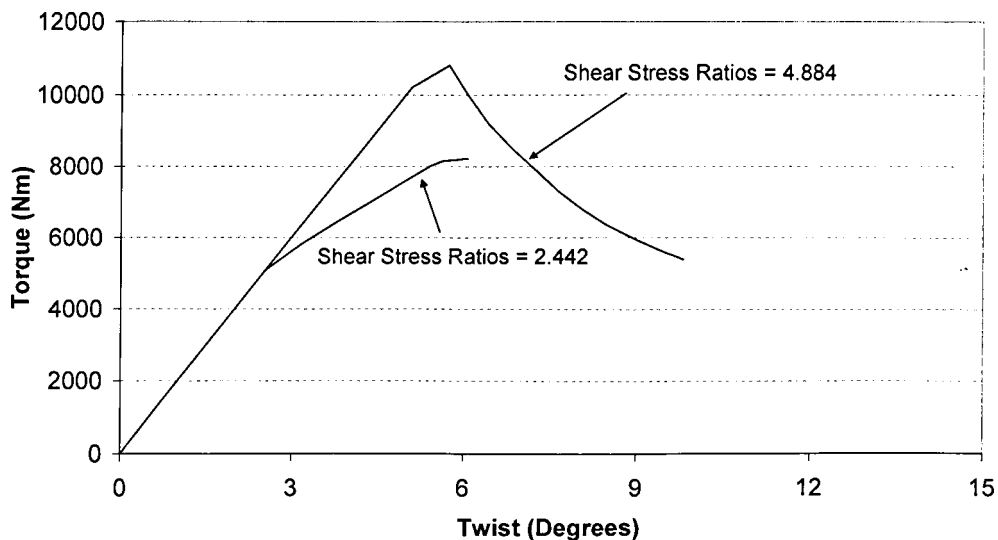


Figure 6.8 Torque vs. twist curve of shaft model (0° fibre orientation) using B2/B3 geometry with different shear stress ratios.

6.4.3 Effect of Fibre Orientation

The torque vs. twist curves for all of the VITAL phase 3 shaft models are shown in Figure 6.9. Initially, a 1% imperfection (representative imperfection level) was seeded to all of the shaft models. Shaft B1 failed to achieve the limit point for buckling due to the relatively thick wall dimension. The results for the 10% imperfection show that a higher imperfection level helps to achieve the limit

point for buckling. There were no problems encountered with the buckling calculations for the shaft models B2 and B3 for which a 1% imperfection was seeded.

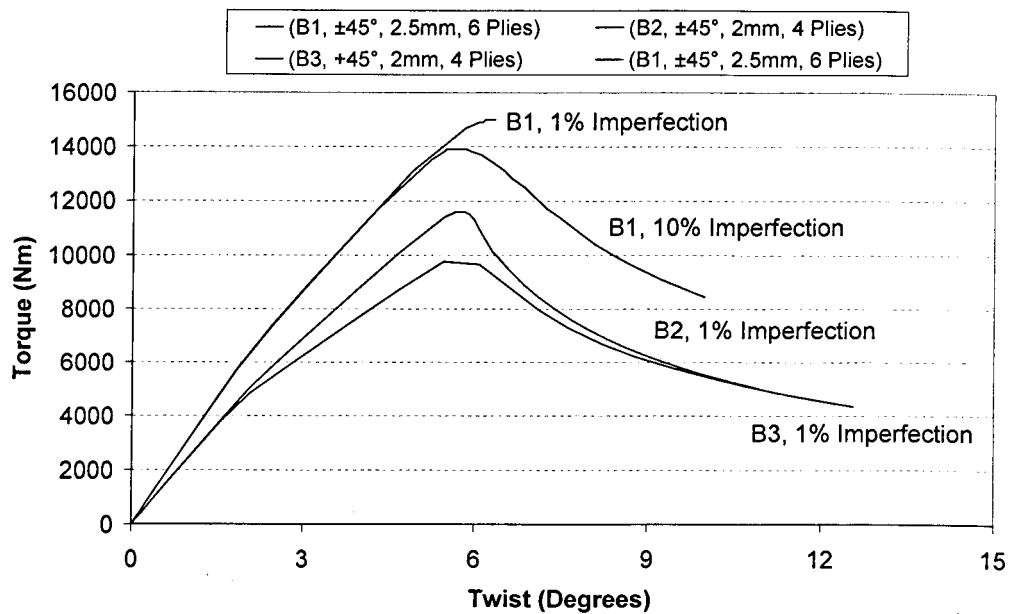


Figure 6.9 Torque vs. twist curves of VITAL phase 3 shaft models

The legend shown in Figure 6.9 provides the shaft reference, fibre orientation, wall thickness and number of MMC plies, respectively. As expected, B1 which has a thicker wall has the highest peak load at 13900 Nm, followed by B2 and B3 at 11600 Nm and 9650 Nm, respectively. All of the results for the shaft models exhibited similar behaviour, in one respect, irrespective of what the fibre orientation and geometry were. The load displacement paths for all of the models exhibited a bilinear behaviour before the peak load/limit point was achieved. B1 has a higher initial stiffness compare to B2 and B3 due to the difference in the number of MMC plies. Comparing the results of B2 and B3, there is a greater reduction in stiffness for B3 before the peak load is achieved. Although B2 and B3 having the same geometry, B3 has a lower peak load

compare to B2. This suggested that shaft models with cross-ply fibre orientation (B1 and B2) can sustain a higher load before they buckle. Moreover, it is likely that it is easier to develop lobes in the plain section for shafts with uni-ply fibre orientations. The buckling failure modes will be discussed in detail later in this section.

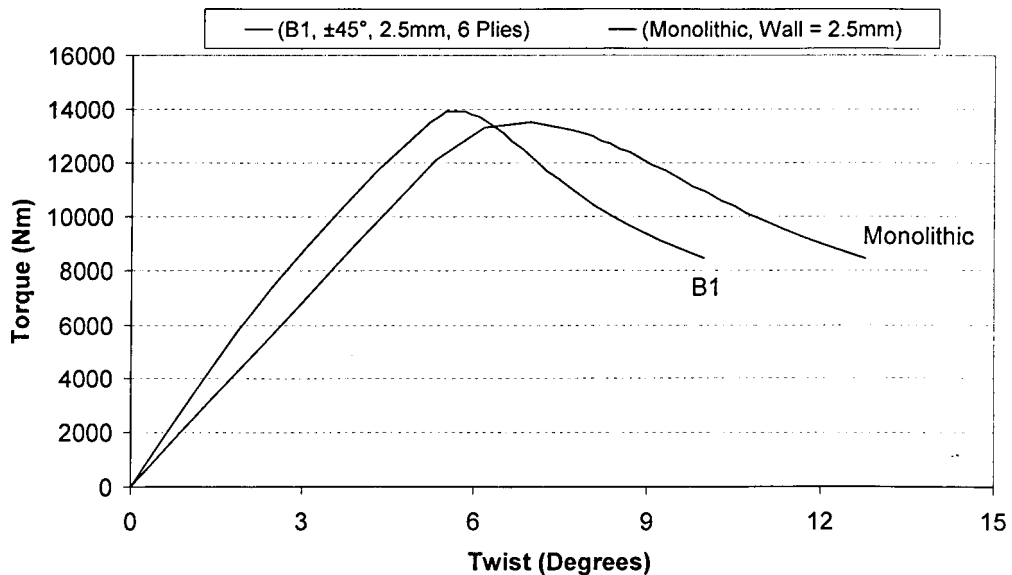


Figure 6.10 Torque vs. twist curves of B1 and monolithic shaft models

In addition to the buckling calculations carried out for the MMC shafts, the buckling behaviour of monolithic Ti-6-4 shafts, using the same geometries as the MMC shafts, were also carried out. Figure 6.10 shows the torque vs. twist curves obtained for the MMC and monolithic shaft models using the B1 geometry. Although the MMC shaft model has a higher stiffness, having MMC plies in the shaft models did not increase the peak load significantly. Similar observations can be made for the shaft models with the B2/B3 geometry; the torques vs. twist curves are shown in Figure 6.11. The peak load for B2 with $\pm 45^\circ$ fibre orientation is slightly higher than the monolithic shaft model. However, the peak load of B3 with $+45^\circ$ fibre orientation is slightly lower compared with that of the

monolithic shaft model. Again, the results indicate that by reinforcing the shafts with MMC, did not cause a significant increase in the resistance to buckling. However, these results and conclusions can only be verified by comparison with experimental results, which are not available at this stage.

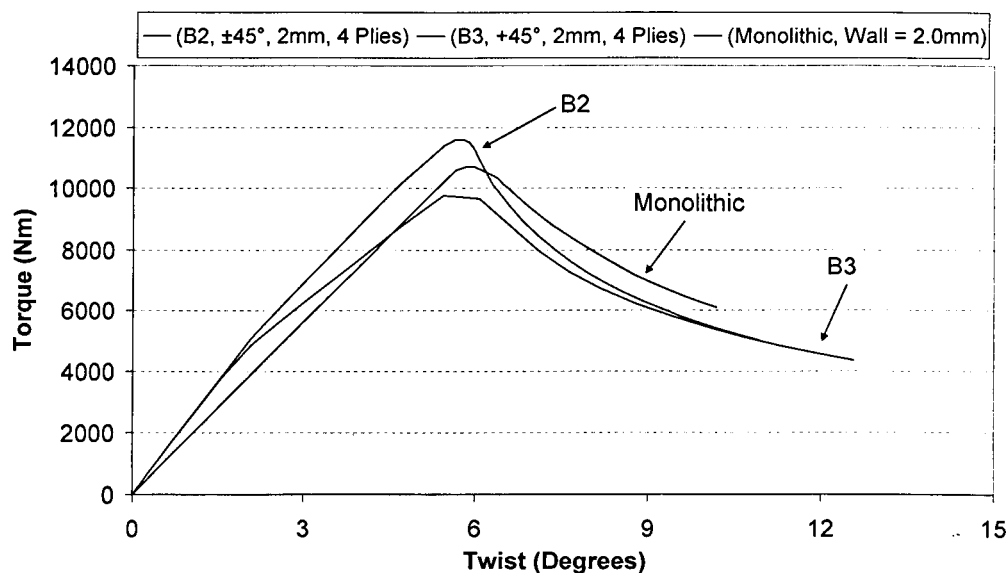


Figure 6.11 Torque vs. twist curves of B2, B3 and monolithic shaft models

Figure 6.12, Figure 6.13 and Figure 6.14 show the FE prediction of the buckling failure modes for shaft models B1, B2 and B3, respectively. All of the shaft models buckled in the middle of the plain section, where 3 circumferential lobes were developed. Two of the shaft models have cross-ply and one has uni-ply fibre orientations. However, the direction of circumferential lobes does not depend on the fibre orientation, but they do depend on the direction of the torque load. For example, B2 and B3, which have a $\pm 45^\circ$ and a $+45^\circ$ fibre orientation, respectively, both have lobes which are at almost 45° clockwise to the 3-direction. The torque loads (rotation) specified for B1, B2 and B3 were all positive, i.e. counter-clockwise looking down the shaft from the left hand end.

Figure 6.15 shows the direction in which a positive torque load was applied; the 3-direction is the shaft axis. If an element on the shaft was orientated at 45° , the torque load (pure shear) can be resolved into tensile and compressive components, which perpendicular to each other. For a shaft subjected to buckling failure, it is the direction of the compressive component which determines the direction of the lobes.

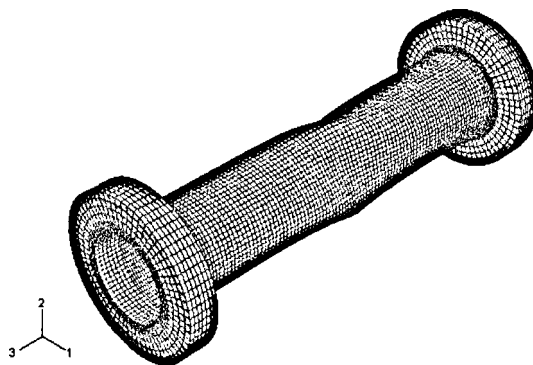


Figure 6.12 Buckling failure mode of B1 ($\pm 45^\circ$, Wall = 2.5mm)

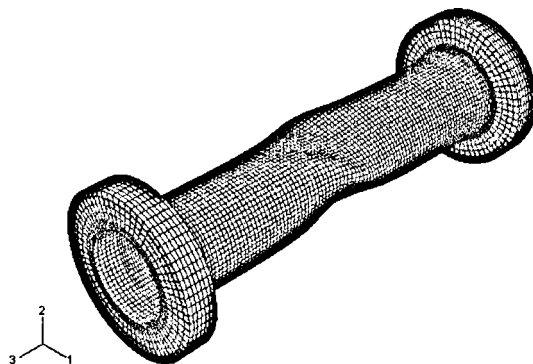


Figure 6.13 Buckling failure mode of B2 ($\pm 45^\circ$, Wall = 2.0mm)

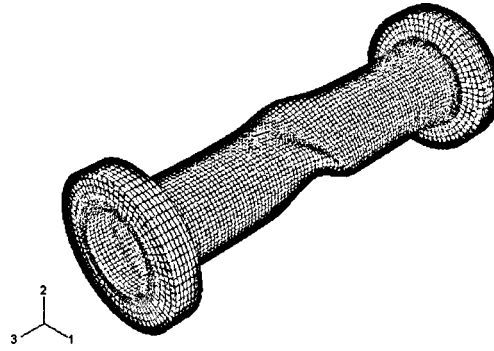


Figure 6.14 Buckling failure mode of B3 (+45°, Wall = 2.0mm)

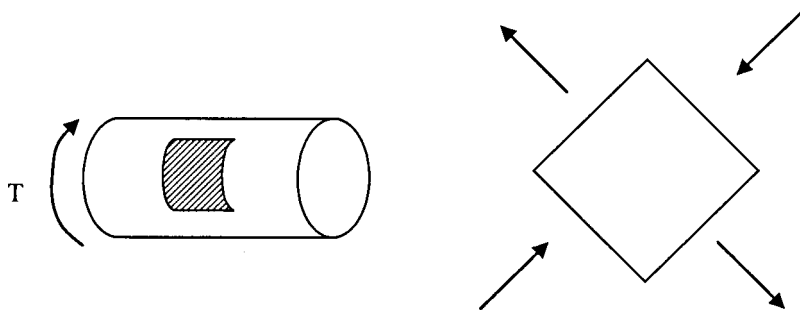


Figure 6.15 Schematic diagram showing a positive torque load on the model

6.5 Summary

In order to understand the buckling behaviour of MMC shafts, a procedure for modelling, using the ABAQUS FE analysis packages, has been developed. All numerical models were based on the VITAL phase 3 geometries and fibre orientations. From the buckling calculations, peak loads, failure mode shapes and torque vs. twist curves were obtained. The methodology developed can be used for any shaft geometry with any fibre orientations. The geometry of the shaft model can be altered using the parametric model facility and the fibre orientations can be altered by editing the ABAQUS input file.

Each buckling analysis comprised of two steps, i.e. a linear elastic EV analysis followed by a non-linear elastic plastic Riks analysis. The mode shape obtained from the EV analysis was used to perturb the perfect geometry for the Riks

analysis. Imperfections were seeded in the geometries for the Riks analyses, in order to simulate the inevitable presence of real manufacturing variations, which would be present on an actual shaft. These imperfections also help in the FE analyses, enabling the solution to overcome any numerical problems which can arise with the use of a perfect geometry. The results from a Riks analysis provide complete information about the collapse of the shaft.

For both EV and Riks analyses, elastic material behaviour models were used in the models. The material properties for the titanium and MMC layer are identical to those in the tube models. For the Riks analysis, plastic material behaviour models were required in order to give the true structural response. For the titanium cladding, an Isotropic Elastic-Plastic model was used, which uses the von Mises yield function. For MMC layer, user-defined stress ratios that are applied in a Hill's potential function material model were specified. This is because the MMC layer exhibit different yield behaviours at different directions.

However, due to the lack of experimental data, a nominal shear stress ratio was calculated using the 0.2% proof strength from the UTC1 (0° fibre orientation) test results. The calculated shear stress ratio was used for all shear stress ratios R_{12} , R_{13} and R_{23} . Numerical investigations showed that the magnitude of the shear stress ratios is not important for shaft model with 45° fibre orientations. This is because the buckling behaviour is strongly dominated by the on-axis stress ratio, i.e. R_{33} .

Shaft model B1 has the highest peak load due to it having more MMC plies in the shaft than the other two shafts. For B2 and B3 shaft models, with identical geometries, the peak load of B2 with $\pm 45^\circ$ fibre orientation is slightly higher

than that of B3 with $+45^\circ$ fibre orientation. However, comparing the MMC shaft behaviour with that of the monolithic shaft models, it can be seen that reinforcing the shafts with MMC, did not produce a great change to the resistance to buckling failure. The buckling failure modes for all of the shaft models were similar; they failed at the middle of the plain section with 3 circumferential lobes. It is found that the direction of circumferential lobes does not depend on the fibre orientation but does depend on the direction of the torque load. This is because the compressive component of principal stress for shafts subject to pure torsion, is at 45° to the shaft axis, which pushes the shaft wall and creates radial displacement on the plain section.

In Chapter 7, further discussions and conclusions related to various aspects of the research will be presented. Future work within the VITAL project will also be described. Last but not least, the prospects for the use of TiMMC technology in the future will be discussed in detail.

CHAPTER 7

CONCLUSIONS AND FUTURE WORK

7.1 Introduction

It has been demonstrated in the experimental work, that TiMMC is a strong candidate for high performance shaft applications, when compared to the corresponding monolithic material. Their superior strength-to-weight and stiffness-to-weight ratios are the key advantages, where it is a potential next generation material in both aeronautical and automobile applications. Very limited work has been carried out to understand the torsional behaviour of TiMMC in the literature, whereas this thesis has made a distinct addition to the knowledge in this particular area.

To the author's best knowledge, the modelling method used within this project is the first of its kind. Unit cell models were used to determine the global orthotropic elastic material properties for TiMMC for a given fibre volume fraction. The material properties are then inputted as MMC layer in the tube model, where the fibre orientation for the tube can be altered, by editing the orientation angle in the ABAQUS input file. The buckling analysis method used, were based on those described by Robotham [44]. However, for the material definition of the MMC layer, the Hill's potential function was used, which defines the anisotropic yield behaviour, using user-defined stress ratios. The stress ratios and plasticity data were obtained, based on the experimental results, from the literature and those within the VITAL project.

On the other hand, the experimental program investigated the torsional behaviour of TiMMC, using lab-scale tube specimens, with different fibre orientations. Important material properties were obtained from the test, such as the shear modulus, static strength and stress-strain curves. Moreover, every test is unique and exhibits features which differ from those of the other tests. The comprehensive post-test investigation enhances the understanding of the failure mechanisms for each specimen. Detailed SEM images also reveal the failure modes (fibre fracture, matrix yielding and interface debonding), observed after final fracture.

This chapter draws the main conclusions, resulting from the research carried out within the VITAL program. Suggestions for future work and the future prospects of TiMMC technology are discussed in the following sub-sections.

7.2 Conclusions

Concise conclusions of the thesis are presented in this section. Although detailed summaries and conclusions were presented at the end of each chapter, for clarity the main conclusions are summarised as follow:-

1. A general review of various TiMMC systems and the advancement of the manufacturing routes were presented in Chapter 2. The tube specimens tested in this project, were manufactured using the matrix coated fibre method, from which high quality of component can be obtained. Uniform fibre distribution as seen on the as-fabricated specimens, results in virtually no defect in the component prior to loading. As for the characterisation of the material, understanding of the behaviour of TiMMC, with different fibre orientations, has been gained, through the testing of coupon specimens, by

various researchers [20, 26-28]. These provide basic information about the behaviour of the material under uniaxial loading, leading to an understanding of the material behaviour when subjected to torque loading (biaxial). Furthermore, having an understanding of the interface between the fibre and matrix is important as it plays a major role in the cause of failure and the damage mechanisms, especially when loaded in the transverse direction. Very often an aeroengine shaft is subjected to multiaxial loading, such as combined torque, bending and axial loads. Therefore, designers need to take this into account and tailor the TiMMC for the specific application, by means of fibre orientation and shaft features.

2. The experimental results from the VITAL, phase 1, tube testing were presented in Chapter 3. From the results, the highest shear modulus was obtained from specimens with 45° fibre orientation, regardless of whether they were for a uni-directional or cross-ply lay-up, under torque loading. This is because fibres orientated at 45° lie on the principal stress directions, where loading on-axis to the fibre direction gives the best performance. Testing at a temperature of 350°C , shows no significant modulus degradation for all specimens, except for the 0° fibre orientation where the behaviour is dominated by the matrix material. The highest strength is obtained from specimen with $+45^\circ$ fibre orientation for which the tensile component of the torque load aligns with the fibres. Specimens with negative fibre orientation result in early failure, hence low strength, because that is the fibre weak plane, for which loading off-axis to that plane is detrimental. However, for reversed torque application, $\pm 45^\circ$ fibre orientation

is the best option because it provides good strength for both torque directions. Typical aeroengine shafts are also subjected to axial loading in addition to torque loading. Therefore, 30° plies could be beneficial, which provide some strength in the axial direction as well as in bending. On the other hand, 0° plies are not considered, as it is where the fibre weak plane is aligned with the maximum shear stress plane for torque loading, leading to early failure.

3. Chapter 4 presented the failure investigation carried out for each tested specimen in order to understand its failure mechanisms. Each specimen failed in a different way, and through the studies, it was found that the failure mechanism is strongly dependent on the fibre orientation. The specimen will normally fail on the fibre weak plane, if it exists within the specimen. Otherwise, it will fail on the maximum shear stress plane under torque loading, i.e. 0° and 90° . Depending on the application, the fibre weak plane should always be avoided within the specimen, because it will severely degrade the material performance. The failure mechanisms observed for the specimens tested at elevated temperature are similar to those for the specimens tested at room temperature. Samples from post-tested specimens were also analysed through SEM imaging, and crack bridging was observed at locations where the distance between fibres was small. Nonetheless, good fibre uniformity was observed in all samples. This confirms that the manufacturing process used for TiMMC components, using the matrix coated fibre method, can produce good quality components. EDX analysis also confirmed the existence of a reaction zone layer, where

the chemical elements are mostly comprised of titanium and carbon. However, the properties of this reaction product are not known.

4. The development of the unit cell models and tube models were presented in Chapter 5. The predicted shear modulus using the tube models, in both ABAQUS and SC03 FE packages, with different fibre orientations, agreed very well with the experimental results. The only exception was the 0° fibre orientation result obtained with ABAQUS. Although only global orthotropic elastic material properties are predicted, the method can be used, to predict TiMMC material properties with any fibre volume fraction. It can also be extended to model different TiMMC systems, if the elastic material properties for each constituent material property are known. The modelling method presented in Chapter 5, was performed in order to understand the material at a micromechanical level, before prediction at the macromechanical level. This is because the interaction between each constituent material, at the macroscopic level, is often more complex.
5. In Chapter 6, the buckling behaviour of TiMMC shafts is investigated, using the VITAL phase 3 shaft geometries and fibre orientations. Anisotropic yield behaviour of the MMC layer was defined, using the stress ratios in Hill's potential function within ABAQUS. Also, it was found that the magnitude of the shear stress ratios in the Hill's model is not important, for shafts with 45° fibre orientation. This is because the buckling behaviour is dominated by the on-axis stress ratio, which defines the yield behaviour in the fibre direction. The buckling failure, which occurred at the plain section, resulted in circumferential lobes. It was found that the direction of the

circumferential lobes does not depend on the fibre direction but the torque direction. However, the numerical results can only be validated through comparison with experimental test results which are not available at the moment.

From the above it can be seen that the major aims of this project have been achieved. The torsional behaviour of TiMMC was studied in detail through numerical modelling and experimental work. A stress analysis method for TiMMC tube component has been established, as well as studies of buckling behaviour. The performance of TiMMC can be optimised by altering the fibre orientation, which results in superior material properties compared to those of the monolithic material. The results from the numerical models correlate well with the experimental results. Furthermore, the comprehensive failure investigation has enhanced the understanding of the failure mechanisms of TiMMC, with different fibre orientations. The research has strengthened the understanding of the torsional behaviour of TiMMC, which was previously very limited.

7.3 Future Works

The VITAL program runs until the end of 2008, and so further research work will add to that presented in this thesis. The major work comprises of fatigue tests of tube specimens and buckling tests of shaft components. Further to that, suggestions will be made to improve the numerical models.

7.3.1 Fatigue Tests

The results from VITAL phase 1 tube testing formed the material database for the TiMMC system used. Using these results, the VITAL phase 2 test matrix

was developed as shown in Table 7.1 for torsional fatigue tests. The sizes of the tube specimens are identical to those tested in phase 1.

Fibre Orientation	Test Temperature (°C)
0°	20
+45°	20
±30°	20
±45°	20
0°	350
+45°	350
±30°	350
±45°	350

Table 7.1 VITAL phase 2 test matrix

It is important to understand how the material performs under fatigue loading conditions, as an aeroengine component undergoes millions of cycles during service. The fatigue test will give an insight on its failure mechanism, and whether they are similar to those observed in the monotonically loaded tubes in phase 1. Moreover, through the tests, the endurance limit of each fibre orientation will be determined. Another important task is to identify the location of crack initiation in the specimen. It was not possible to identify the initiation sites for the specimens tested in phase 1, as failure occurred instantaneously. However, inspection of the specimens can be made during the fatigue tests, to identify the occurrence of damage (eg. crack initiation or roughening of the surface due to plastic deformation), which could be the evidence of crack initiation sites. Nonetheless, this is only possible for fatigue tests at room temperature, since the furnace encloses the whole specimen during the high temperature test.

7.3.2 Buckling Tests

As the wall thickness of the shaft gets thinner, it is possible that buckling failures could be the major failure mode. Hence, it is important to investigate the instability of shaft due to buckling. Based on the experience gained earlier, 3 shaft components of 45° fibre orientation have been ordered and will be tested. Table 7.2 shows the VITAL phase 3 test matrix; all the components will be tested at room temperature. The length of the plain section is twice that of the tube specimens and the outer diameter is the same as the TiMMC demonstrator shaft.

Fibre Orientation	MMC Plies	Wall Thickness (mm)	OD (mm)	Plain Section Length (mm)
±45°	6	2.5	82	300
±45°	4	2	82	300
+45°	4	2	82	300

Table 7.2 VITAL phase 3 test matrix

The experimental results will be use to validate the buckling model developed in Chapter 6. Load vs. twist curves, buckling torque and buckling failure modes will be compared. Since there is no TiMMC shaft buckling experimental results in the literature, the tests, which will be conducted within VITAL phase 3, are important and valuable. Also, it will be interesting to see whether buckling is the dominant failure mode for these components, as they are reinforced with brittle fibres, as the core layer.

7.3.3 Further Development on Numerical Models

At present, the numerical models, developed within this project, only predict the elastic material properties of TiMMC. However, the plasticity behaviour is also

important as it will allow the strength and the pre-failure response of the material to be predicted. Hence, a model which includes the elastic and plastic material data is necessary. However, the definition of plastic data for the MMC layer is complicated, compared to that for the monolithic material. Nonetheless, the experimental results can be used to estimate a set of plastic data for each fibre orientation.

The idea is to separate the compound stress-strain curve obtained from the tests. Given the stress-strain response of the monolithic material, the stress-strain response of the MMC layer can be obtained. Then, this data can be feed into the FE models for a given fibre orientation, of any geometry. This enables the fully elastic-plastic response to be determined. However, the accuracy of this calculation can not be guaranteed, as the data are obtained from a single torsion test for each fibre orientation, where it is not possible to assess the repeatability of the results. However, this will form the first step, towards the prediction of the global behaviour, up until failure.

For the buckling models, the experimental results can be used to fine tune the imperfection factor, and to subsequently match the numerical results to the experiment. The experimental results give an insight into the effects of manufacturing variations on the imperfection factor in the models, for each fibre orientation.

7.4 Future Prospects of TiMMC Technology

TiMMC technology has been shown to be a candidate material for high performance components, which require superior material properties and lightweight. For aeronautical applications, TiMMC is being used as the material

for blings within the compressor section in aeroengines. Also, TiMMC technology has been implemented as part of the primary structural landing gear, in the F16 military aircraft, by SP aerospace. However, for shaft applications, the technology is still in its early “proof-of-concept” stage, which is the research presented in this thesis. Once this is successful, the next stage is to demonstrate a system prototype in relevant environment.

However, testing of TiMMC components is very expensive, as a result of the high cost of raw material, especially the cost of the fibres. The matrix coated fibres cost approximately £17,000 per kg. As a reference, each tube specimen and buckling shaft component cost approximately £9,000 and £15,000, respectively. Given the size of these specimens, it is obvious that the cost to manufacture a full size TiMMC LP shaft would be very expensive, and the price would increase with an increase in the number of MMC plies. Nonetheless, accurate numerical models can be used, as a substitute to reduce the amount of testing.

Delay of specimens’ delivery was experienced throughout the research period. It is understood that, only TISICS Ltd. has the facility in the U.K. with the capability to manufacture TiMMC shaft component. Therefore, the availability of this material is very limited. Another option would be to go for suppliers in Europe or the U.S.A., but the availability of the required TiMMC system is not guaranteed. Therefore, the supply chain of TiMMC needs to be improved, to enable a smooth introduction to high performance applications of it.

REFERENCES

1. Korsia, M.J.-J., Environmentally Friendly Aero Engine (VITAL) Proposal Part B. 2004, SNECMA Moteurs.
2. Hooker, J.A. and P.J. Doorbar, *Metal matrix composites for aeroengines*. Materials Science and Technology, 2000. **16**: p. 725-731.
3. Askeland, D.R., *The Science and Engineering of Materials*. 2nd SI ed. 1990: Chapman and Hall. p. 447-454.
4. TIMET, *TIMETAL 6-4 Technical Data Sheet*. 2000, Titanium Metals Corporation.
5. Le Petitcorps, Y., et al., *MODERN BORON AND Si CVD FILAMENTS: A COMPARATIVE STUDY*. Composites Science and Technology, 1988. **32**(1): p. 31-55.
6. Upadhyaya, D., et al., *Coating and fiber effects on SiC-reinforced titanium*. JOM, 1994. **46**(11): p. 62-67.
7. Ning, X.J. and P. Pirouz, *Microstructure of SCS-6 SiC fiber*. Journal of Materials Research, 1991. **6**(10): p. 2234 - 2248.
8. Nutt, S.R. and F.E. Wawner, *SILICON CARBIDE FILAMENTS: MICROSTRUCTURE*. Journal of Materials Science, 1985. **20**(6): p. 1953-1960.
9. Chen, Z.Q., et al., *Effect of carbon additions on microstructure and mechanical properties of Ti-15-3*. Materials Science and Technology, 2004. **20**(3): p. 343 - 349.

10. Lissenden, C.J., M.J. Pindera, and C.T. Herakovich, *Stiffness degradation of SiC/Ti tubes subjected to biaxial loading*. Composites Science and Technology, 1994. **50**(1): p. 23-36.
11. Lissenden, C.J., C.T. Herakovich, and M.-J. Pindera. Inelastic deformation of titanium matrix composites under multiaxial loading. in Proceedings of the 1994 Symposium on Life Prediction Methodology for Titanium Matrix Composites, Mar 22-24 1994. 1996. Hilton Head Island, SC, USA: ASTM, Conshohocken, PA, USA.
12. Lissenden, C.J., C.T. Herakovich, and M.J. Pindera, *Response of SiC/Ti under combined loading. Part I: theory and experiment for imperfect bonding*. Journal of Composite Materials, 1995. **29**(2): p. 130-155.
13. Lissenden, C.J., B.A. Lerch, and C.T. Herakovich, *Response of SiC/Ti under combined loading part III: microstructural evaluation*. Journal of Composite Materials, 1996. **30**(1): p. 84-108.
14. Lissenden, C.J., M.-J. Pindera, and C.T. Herakovich. Response of SiC/Ti tubes under biaxial loading in the presence of damage. in Winter Annual Meeting of the American Society of Mechanical Engineers, Nov 8-13 1992. 1992. Anaheim, CA, USA: Publ by ASME, New York, NY, USA.
15. Newaz, G.M. and B.S. Majumdar, *Comparison of mechanical response of MMC at room and elevated temperatures*. Composites Science and Technology, 1994. **50**(1): p. 85 - 90.
16. Kruch, S. and P. Paulmier *VITAL Internal Report - Cylindrical Samples Phase 2 Test Results*. 2007, ONERA (Office National d'Etudes et de Recherches Aérospatiales).

17. Duda, C., et al., *Microstructural characterization of liquid route processed Ti 6242 coating of SCS-6 filaments*. Composites Part A: Applied Science and Manufacturing, 2004. **35**(5): p. 511.
18. Cheng, T.T., et al., *Microstructure of sigma 1140+ SiC fibres*. Materials Science & Engineering A: Structural Materials: Properties, Microstructure and Processing, 1999. **A260**(1-2): p. 139-145.
19. Shatwell, R.A., *Fibre-matrix interfaces in titanium matrix composites made with sigma monofilament*. Materials Science & Engineering A: Structural Materials: Properties, Microstructure and Processing, 1999. **A259**(2): p. 162-170.
20. Thomas, M.P. and M.R. Winstone, Effect of matrix alloy on longitudinal tensile behaviour of fibre reinforced titanium matrix composites. Scripta Materialia, 1997. **37**(12): p. 1855-1862.
21. Thomas, M.P. and M.R. Winstone, *Longitudinal yielding behaviour of SiC-fibre-reinforced titanium-matrix composites*. Composites Science and Technology, 1999. **59**(2): p. 297 - 303.
22. Wu, X., C. Cooper, and P. Bowen, *In-situ observations of titanium metal-matrix composites under transverse tensile loading*. Metallurgical and Materials Transactions A: Physical Metallurgy and Materials Science, 2001. **32**(7): p. 1851.
23. Partridge, P.G. and C.M. Ward-Close, *Processing of advanced continuous fibre composites: current practice and potential developments*. International Materials Reviews, 1993. **38**(1): p. 1-24.
24. Ward-Close, C.M. and C. Loader. *PVD processing of fibre reinforced composites*. 1994. Rosemont, IL, USA.

25. Peng, H.-X., *Manufacturing titanium metal matrix composites by consolidating matrix coated fibres*. Journal of Materials Science and Technology, 2005. **21**(5): p. 647-651.
26. Sun, C.T., et al., Investigation of the mechanical behaviour of SCS-6/Ti-6-4 metal-matrix composite at elevated temperatures. Composites Science and Technology, 1993. **49**(2): p. 183.
27. Sun, C.T., et al., *Mechanical characterization of SCS-6/Ti-6-4 metal matrix composite*. Journal of Composite Materials, 1990. **24**(10): p. 1029-1059.
28. Li, D.S. and M.R. Wisnom, *Unidirectional tensile stress-strain response of BP-SiC fiber reinforced Ti-6Al-4V*. Journal of Composites Technology & Research, 1994. **16**(3): p. 225-233.
29. Li, D.S. and M.R. Wisnom, Micromechanical modelling of SCS-6 fibre-reinforced Ti-6Al-4V under transverse tension-effect of fibre coating. Journal of Composite Materials, 1996. **30**(5): p. 561-588.
30. Cotterill, P.J. and P. Bowen, Transverse properties of a Ti-6-4 matrix/SiC fibre-reinforced composite under monotonic and cyclic loading. Journal of Materials Science, 1996. **31**(22): p. 5897-5905.
31. Upadhyaya, D., et al. Comparison of SCS6/Ti-6Al-4V and sigma SM1240/Ti-6Al-4V composite systems: a microstructural characterization. 1995. Rosemont, IL, USA: Minerals, Metals & Materials Soc (TMS).
32. Yang, C.J., S.M. Jeng, and J.M. Yang, *Interfacial properties measurement for SiC fiber-reinforced titanium alloy composites*. Scripta Metallurgica et Materialia, 1990. **24**(3): p. 469 - 474.

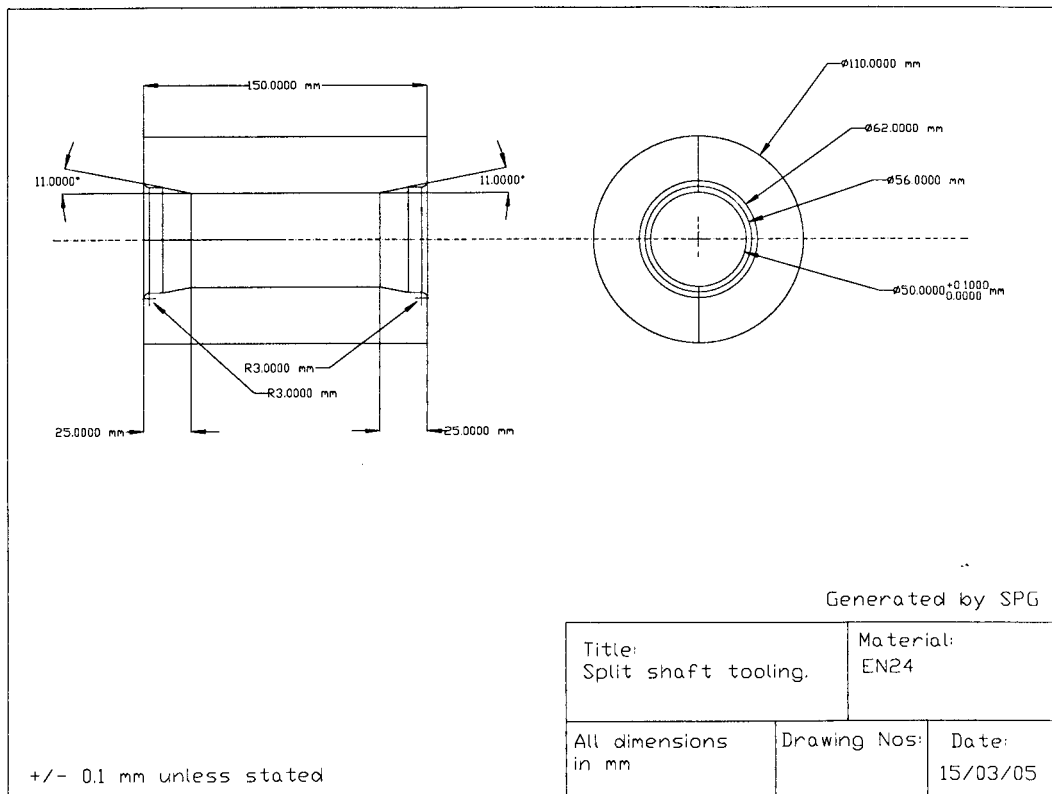
33. Wang, Q. and F.-P. Chiang, *Experimental characterization of interphase mechanical properties of composites*. Composites Part B:Engineering, 1996. **27**(2): p. 123 - 128.
34. Xie, M., et al. *Nonlinear behavior of unidirectional SCS-6/Ti-6Al-4V composite*. 1996. Atlanta, GA, USA: Technomic Publ Co Inc, Lancaster, PA, USA.
35. Li, D.S. and M.R. Wisnom, Factors controlling the transverse tensile properties of unidirectional SiC/Ti-6Al-4V. Composites Engineering, 1995. **5**(3): p. 235.
36. Aghdam, M.M. and S.R. Falahatgar, Micromechanical modeling of interface damage of metal matrix composites subjected to transverse loading. Composite Structures, 2004. **66**(1-4): p. 415.
37. Nimmer, R.P., et al., Micromechanical modeling of fiber/matrix interface effects in transversely loaded SiC/Ti-6-4 metal matrix composites. Journal of Composites Technology & Research, 1991. **13**(1): p. 3-13.
38. Shaw, L.L. and D.B. Miracle, Effects of an interfacial region on the transverse behavior of metal- matrix composites - a finite element analysis. Acta Materialia, 1996. **44**(5): p. 2043-2055.
39. Lawes, G., *Scanning Electron Microscopy and X-Ray Microanalysis*, ed. M.A. James. 1987: John Wiley & Sons.
40. Bauchau, O.A., T.M. Krafchack, and J.F. Hayes, *Torsional buckling analysis and damage tolerance of graphite/epoxy shafts*. Journal of Composite Materials, 1988. **22**(3): p. 258-270.

41. Tennyson, R.C. and K.C. Chan, *Buckling of imperfect sandwich cylinders under axial compression*. International Journal of Solids and Structures, 1990. **26**(9-10): p. 1017-1036.
42. Bert, C.W. and C.-D. Kim, *Analysis of buckling of hollow laminated composite drive shafts*. Composites Science and Technology, 1995. **53**(3): p. 343.
43. Robotham, W.S., *The Elastic-Plastic Buckling Behaviour of Shafts*. PhD Thesis, 2000, University of Nottingham.
44. Robotham, W.S., *Shaft Buckling Manual*. 2004, University of Nottingham Technology Centre in Gas Turbine Transmission Systems.
45. ABAQUS, ABAQUS Online Documentation. 2006.

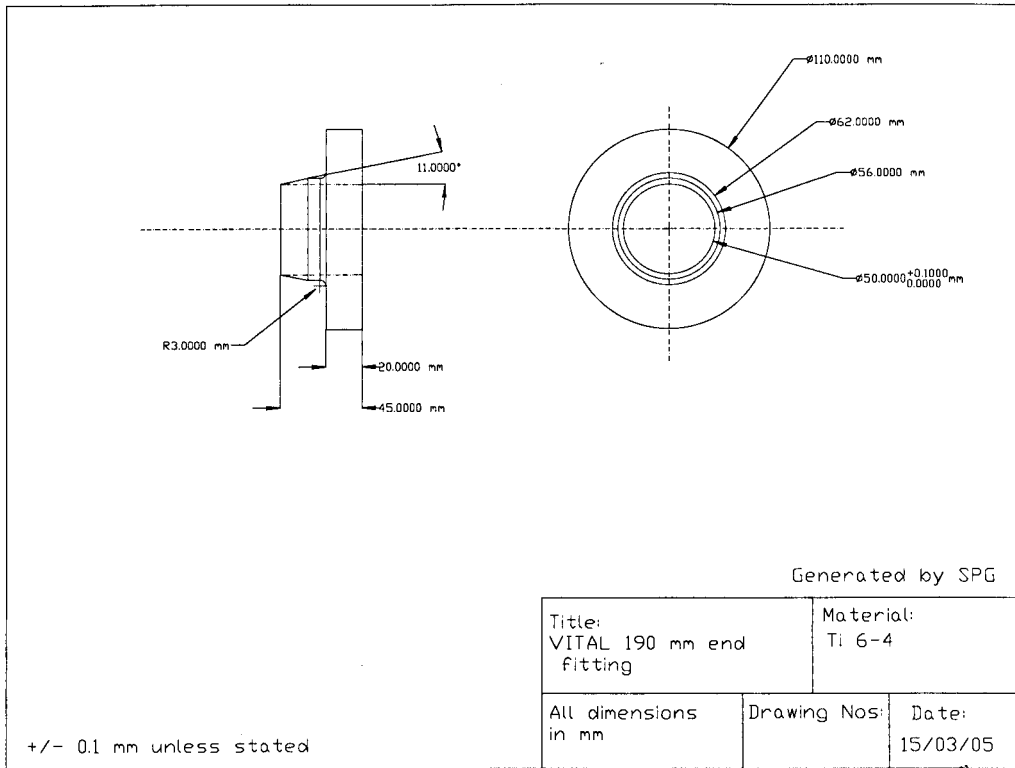
APPENDIX A:

DRAWINGS OF SHAFT TOOLING

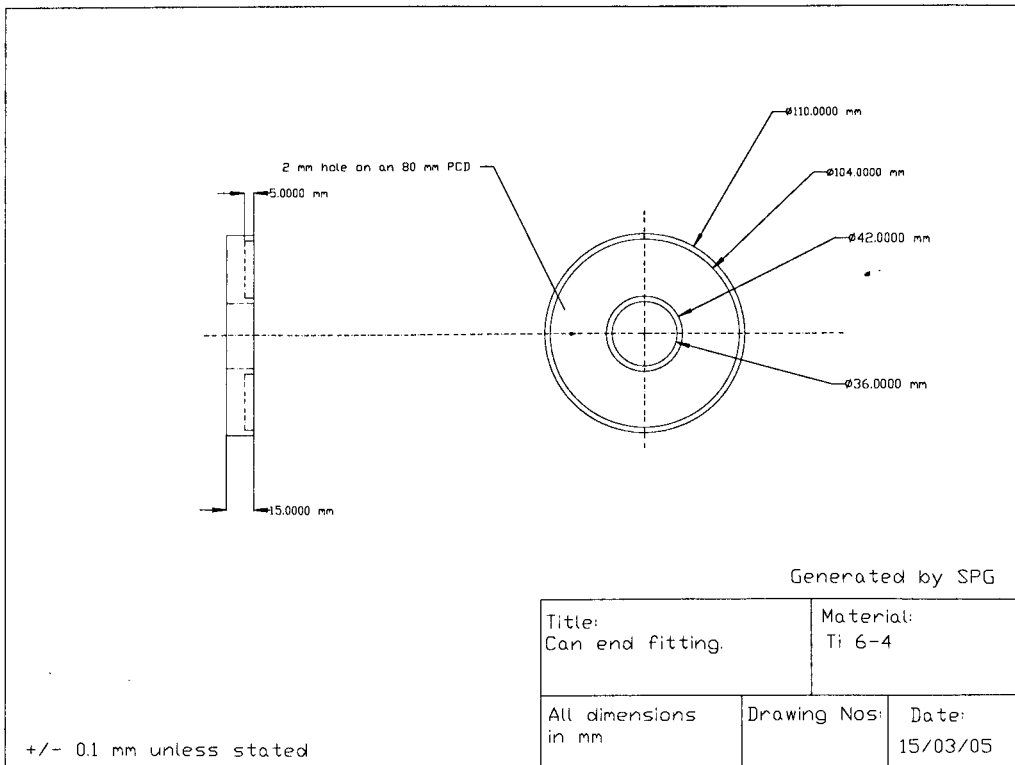
Split Tooling Design



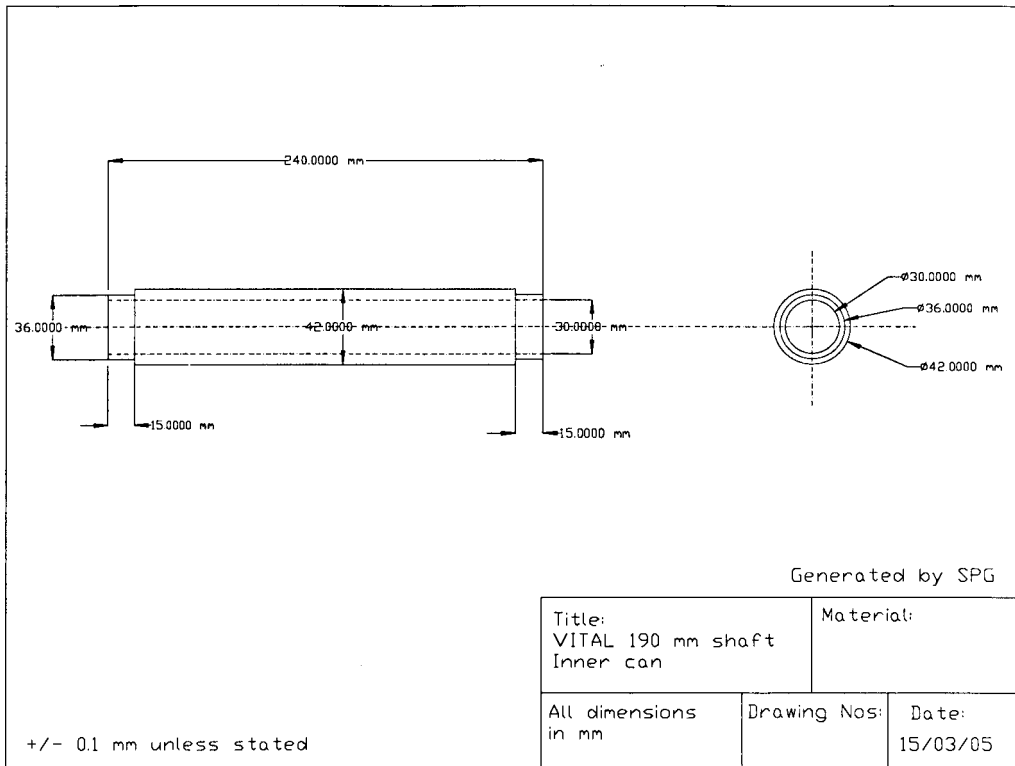
Titanium End Fittings



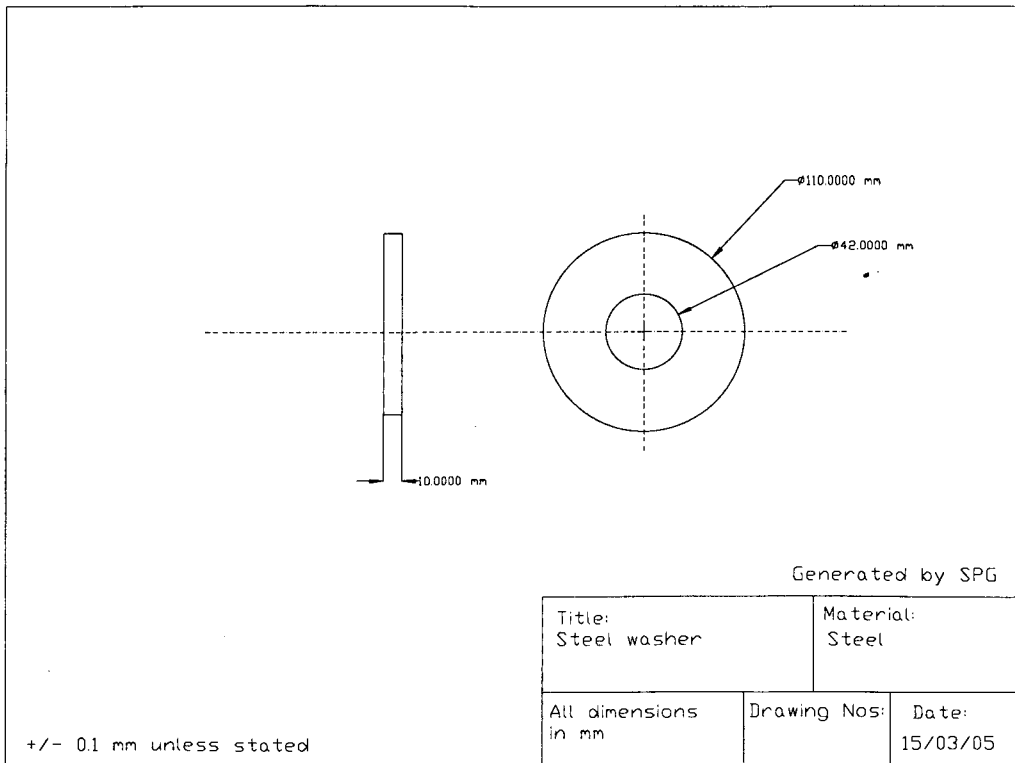
HIP Can End Fitting



Inner Mandrel



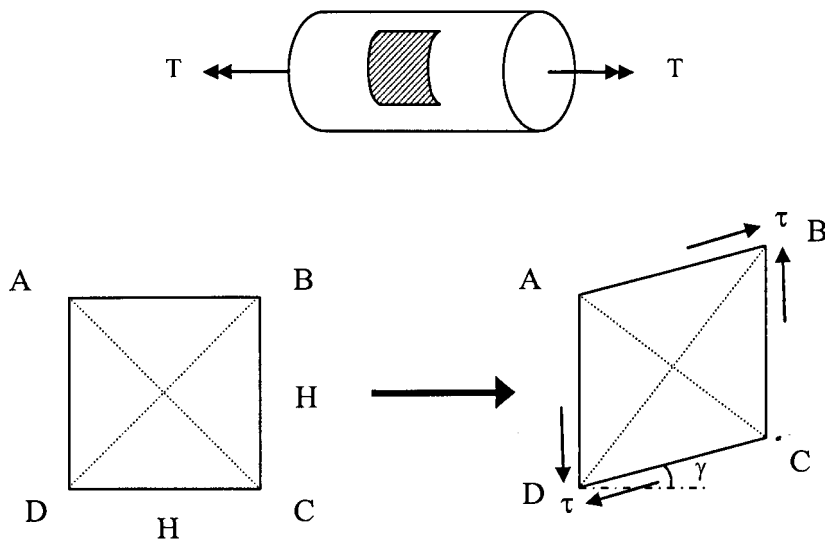
Steel Washer



APPENDIX B:

RELATION BETWEEN DIRECT STRAIN TO SHEAR STRAIN

Consider an element of material which is taken out from the surface of a shaft. When subjected to a pure torque loading, a pure shear condition is created and the element will deform in the manner shown in the figure below. Before deformation, each side of the element has a length of H . After the deformation, angle ADC has a value of $\frac{\pi}{2} - \gamma$ and angle DAB has a value of $\frac{\pi}{2} + \gamma$. The relationship between the shear strain, γ , and the direct strain, ϵ_{\max} , is derived below.



Initial length of DB,

$$L_{BD} = \sqrt{H^2 + H^2} = \sqrt{2}H \quad (\text{B.1})$$

After deformation, the direct strain in the direction BD is the ratio of extension to the initial length of BD, i.e.,

$$\varepsilon_{\max} = \frac{\delta}{L_{BD}} \quad (\text{B.2})$$

$$\delta = \varepsilon_{\max} L_{BD} \quad (\text{B.3})$$

The final length of BD is the summation of initial length and the extension of the diagonal direction.

$$L_{BD}^{Final} = L_{BD} + \varepsilon_{\max} L_{BD} \quad (\text{B.4})$$

$$L_{BD}^{Final} = \sqrt{2}H(1 + \varepsilon_{\max}) \quad (\text{B.5})$$

Now, consider the triangle DAB. Using cosine rule,

$$L_{BD}^2 = H^2 + H^2 - 2H^2 \cos\left(\frac{\pi}{2} + \gamma\right) \quad (\text{B.6})$$

$$\left[\sqrt{2}H + \sqrt{2}H\varepsilon_{\max}\right]^2 = 2H^2 \left[1 - \cos\left(\frac{\pi}{2} + \gamma\right)\right] \quad (\text{B.7})$$

$$2H^2 + 4H^2\varepsilon_{\max} + 2H^2\varepsilon_{\max}^2 = 2H^2 \left[1 - \cos\left(\frac{\pi}{2} + \gamma\right)\right] \quad (\text{B.8})$$

$$1 + 2\varepsilon_{\max} + \varepsilon_{\max}^2 = 1 - \cos\left(\frac{\pi}{2} + \gamma\right) \quad (\text{B.9})$$

For small strain, $\varepsilon_{\max}^2 = 0$ and $\sin \gamma = \gamma$, also

$$\cos\left(\frac{\pi}{2} + \gamma\right) = -\sin \gamma, \text{ hence,} \quad (\text{B.10})$$

$$1 + 2\varepsilon_{\max} = 1 + \gamma \quad (\text{B.11})$$

$$\text{i.e. } \gamma = 2\varepsilon_{\max} \quad (\text{B.12})$$

Hence, the above derivation shows that, under pure shear condition, the shear strain γ is twice the direct strain ε_{\max} .

APPENDIX C:

PROCEDURE TO DEFINE MATERIAL ORIENTATION IN SC03

Cyclic Symmetry Tube Model

In the cyclic symmetry tube model, the MMC layer is assumed to consist of an orthotropic material model, the properties of which are orientation dependent. From the material properties shown in Table C.1, it can be seen that the stiffest direction is the z-direction, as seen from the Young's modulus. For a tube model with 0° fibre orientation, the fibres are aligned to the tube axis. Hence, the tube axis in the model must be orientated in the global Z-direction if this set of material properties is used. An example of this, for a cyclic symmetry tube model is shown in Figure C.1.

Material Constants	Values
E_x	154.3 GPa
E_y	154.9 GPa
E_z	203.2 GPa
ν_{xy}	0.30
ν_{yz}	0.20
ν_{zx}	0.27
G_{xy}	50.3 GPa
G_{yz}	50.5 GPa
G_{zx}	62.1 GPa

Table C.1 Orthotropic material properties for MMC layers in SC03

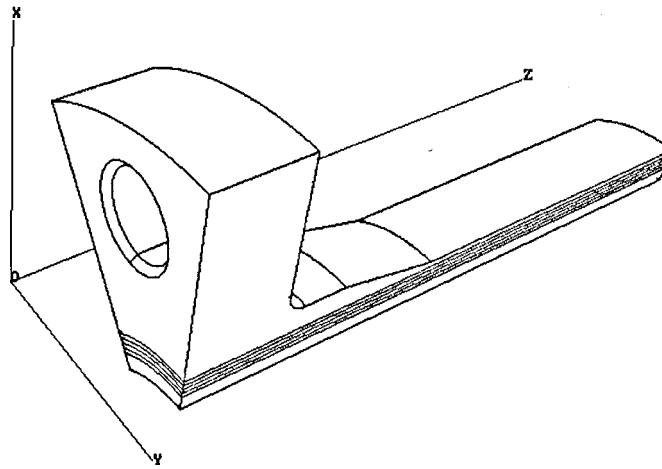


Figure C.1 SC03 cyclic symmetry model showing global axes

Hence, for the 0° fibre orientation, the material z-axis is the same as that of the global Z-direction (tube axis). The material x and y-axes are perpendicular to the material z-axis. It was decided that for all cases, the material x-axis will be chosen to be in the tangential direction, i.e. transverse to the fibre direction (material z-axis), and the material y-axis will be in the radial direction. However, the two perpendicular directions are not necessary the global X-direction and Y-direction since the MMC layer is a domain with a cylindrical shape. Hence, the material orientation system used here is a cylindrical coordinate system. As mentioned in Chapter 3, the positive angle is measured clockwise to the tube axis for all test specimens. However, for the definition of orientation angle in ABAQUS, positive angle is measured counter-clockwise to the local direction as described in Chapter 5. It was decided that for all tube models, both in ABAQUS and SC03, the positive angle is measured counter-clockwise to the tube axis for consistency.

The direction cosine method is used to define the material orientation. Using this method, it is only necessary to specify the Cartesian coordinates for the material

x and y-axes directions; the material z-axis is calculated, automatically, within the program; it is orthogonal to both the material x- and y-directions. The Cartesian coordinates of the material axes are defined using the general expression in X, Y, Z, R or θ . The general expression needs to satisfy all points in the domain which result the material axes pointing at a particular direction consistently. The procedure used to obtain the general expression for the 0° , $+30^\circ$, -30° , $+45^\circ$ and -45° material orientations are described in the following.

0° Material Orientation

To obtain a general expression for a 0° fibre orientation, first, two points on the MMC layer which coincide with the global X and Y-axes are identified. These two points are A (0, 1, 0) and B (1, 0, 0), as shown in Figure C.2, and the Cartesian coordinates of these points are obtained by assuming the radius of the cylinder is 1 unit.

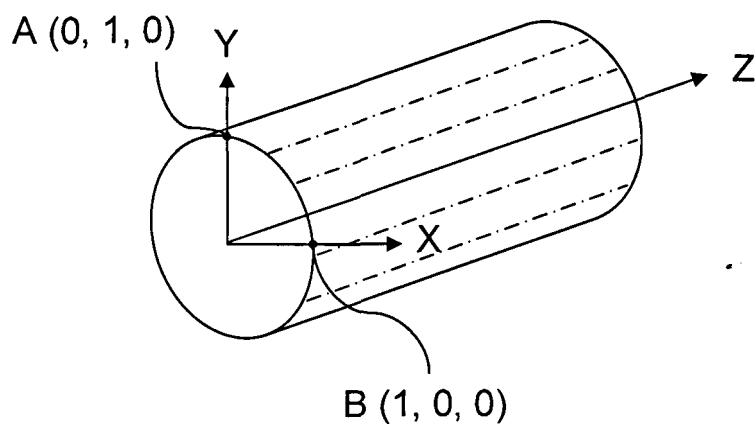


Figure C.2 Schematic diagram for 0° fibre orientation tube model

As mentioned earlier, global Z-axis (tube axis) is the material z-axis. By taking point A as the origin of the local coordinate system, the material x-axis is in the same direction as the global X-axis. Therefore, the material y-axis is also in the

same direction as the global Y-axis. For a material x-axis pointing in the same direction as the global X-axis, the Cartesian coordinate for that direction will be $(1, 0, 0)$; for a material y-axis pointing in the same direction as the global Y-axis, the Cartesian coordinate for that direction will be $(0, 1, 0)$.

Now, take point B as the origin of the local coordinate system. Then, the material x-axis will now be in the direction of the negative global Y-axis. This is because the local coordinate system is rotated about the material z-axis when moving from point A to point B. This will ensure the material x-axis always points in the tangential direction. Therefore, the material y-axis is now in the direction of the global X-axis. For a material x-axis pointing in the direction of the negative global Y-axis, the Cartesian coordinate, for that direction, will be $(0, -1, 0)$; for a material y-axis pointing in the direction as the global X-axis, the Cartesian coordinate, for that direction, will be $(1, 0, 0)$. A diagram showing the material axes, for points A and B, are shown in Figure C.3.

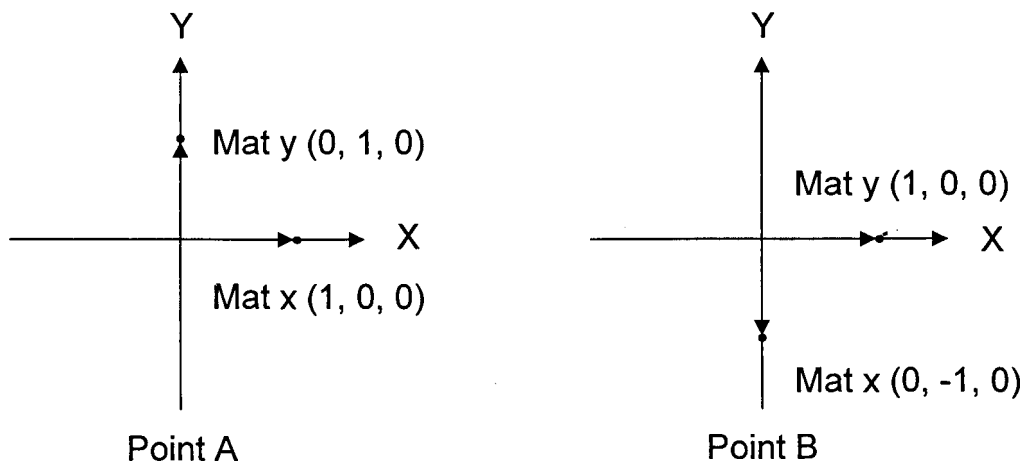


Figure C.3 Material x and y-axes for point A and B (0°)

By combining the global Cartesian coordinates and the direction Cartesian coordinates of the material x and y-axes for both point A and point B, a general

expression can be derive which satisfies these conditions. For point A, the global Cartesian coordinate is $(0, 1, 0)$ and the material x-axis is in the direction of $(1, 0, 0)$. A general expression of $[Y, -X, 0]$ will lead to the material x-axis at point A pointing in the global X-direction. This can be confirmed by substituting the global Cartesian coordinates to the general expression which give a direction of $(1, 0, 0)$. This general expression also applies to point B for the material x-axis direction where the material x-axis at point B points in the negative global Y-direction. For the material y-axes, a similar procedure is used. A general expression $[X, Y, 0]$ is derived for material y-axes orientation which satisfies the material y-axes directions for points A and B.

+30° Material Orientation

Figure C.4 shows a schematic diagram for a +30° fibre orientation tube model. Using a similar method to that used for the 0° model, points A $(0, 1, 0)$ and B $(1, 0, 0)$ on the MMC layer, which coincide with the global X and Y-axes, are identified. The Cartesian coordinates of these points are obtained by assuming the radius of the cylinder is 1 unit.

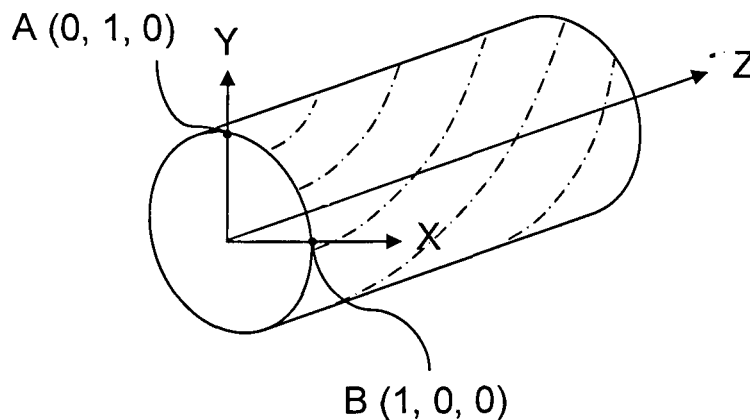


Figure C.4 Schematic diagram for +30° fibre orientation tube model

The procedure used to define an off axis unidirectional material orientation is more complicated than that for the 0° material orientation. This is because the material x and y-axes do not lie on the same plane in the global coordinate system. It is convenient to illustrate the material axes on a different plane for better understanding.

Considering the global X-Y plane shown in Figure C.5, the material y axes, for points A and B, are pointing in the global Y and X-directions, respectively which is the radial direction. This is identical to the case of the 0° fibre orientation. Hence the general expression $[X, Y, 0]$ will satisfy the material y-axes directions for points A and B, which may be confirmed by substituting its global Cartesian coordinates into the general expression.

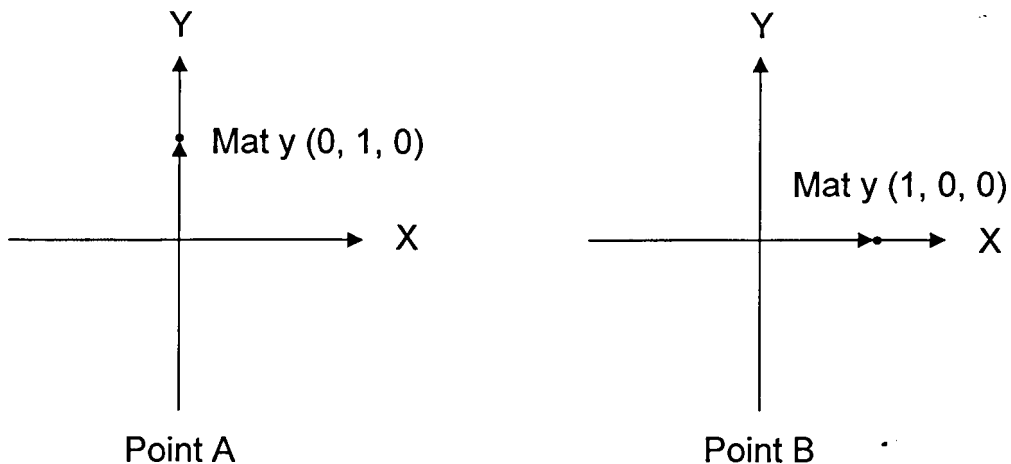


Figure C.5 Material y-axes for point A and B ($+30^\circ$)

The material x-axes, for points A and B, are shown in Figure C.6. Note that material x-axes for points A and B are shown in the X-Z and Y-Z planes, respectively. The material z-axis is the fibre direction, which is no longer the global Z-direction (tube axis). For points A and B, the material z-axis is rotated 30° in a counter clockwise direction relative to the global Z-direction, and the

material x-axis is perpendicular to the material z-axis. For point A, the material x-axis is pointing in a direction 30° counter clockwise to that of the global X-direction. This forms a right angled triangle of 30° , such that the opposite side of the oblique angle (30°) is 1 and the hypotenuse is equal to 2. Hence, the Cartesian coordinates for this material x-axis direction is $(\sqrt{3}, 0, 1)$. For point B, the Cartesian coordinates for the material x-axis direction is $(0, -\sqrt{3}, 1)$. Hence, a general expression $[Y, -X, R \tan \theta]$ will satisfy the material x-axes directions for points A and B, which can be confirmed by substituting the global Cartesian coordinates into the general expression. Note that θ is the material orientation angle and $R = \sqrt{x^2 + y^2}$.

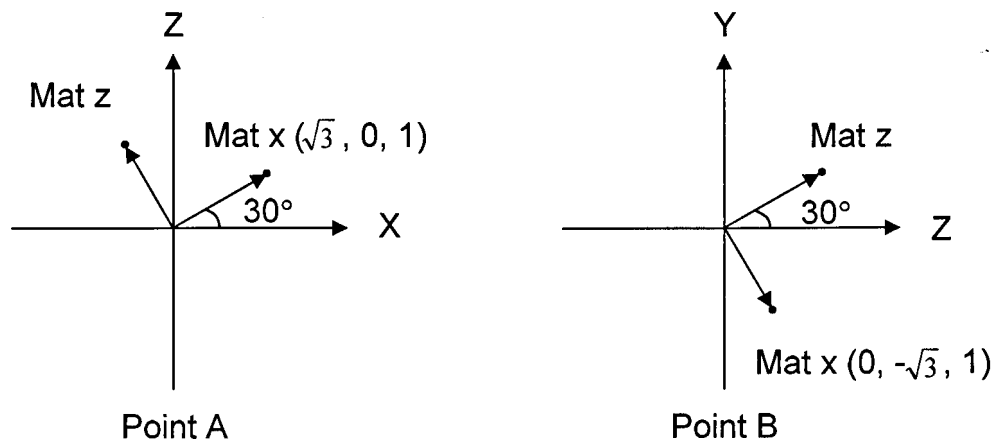


Figure C.6 Material x-axes for point A and B ($+30^\circ$)

-30° Material Orientation

Figure C.7 shows a schematic diagram for a -30° fibre orientation tube model. Using a similar method to that used for the 0° model, points A $(0, 1, 0)$ and B $(1, 0, 0)$ on the MMC layer, which coincide with the global X and Y-axes, are

identified. The Cartesian coordinates of these points are obtained by assuming the radius of the cylinder is 1 unit.

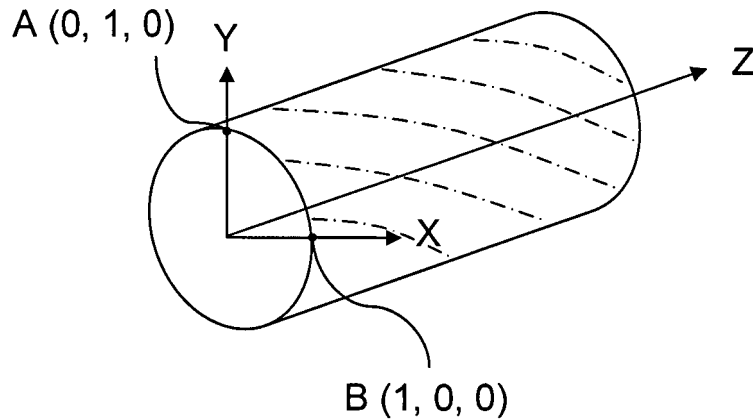


Figure C.7 Schematic diagram for -30° fibre orientation tube model

Considering the global X-Y plane shown in Figure C.8, the material y axes, for points A and B, are pointing in the global Y and X-directions, respectively, which is the radial direction. This is identical to the case of the 0° fibre orientation. Hence the general expression $[X, Y, 0]$ will satisfy the material y-axes directions.

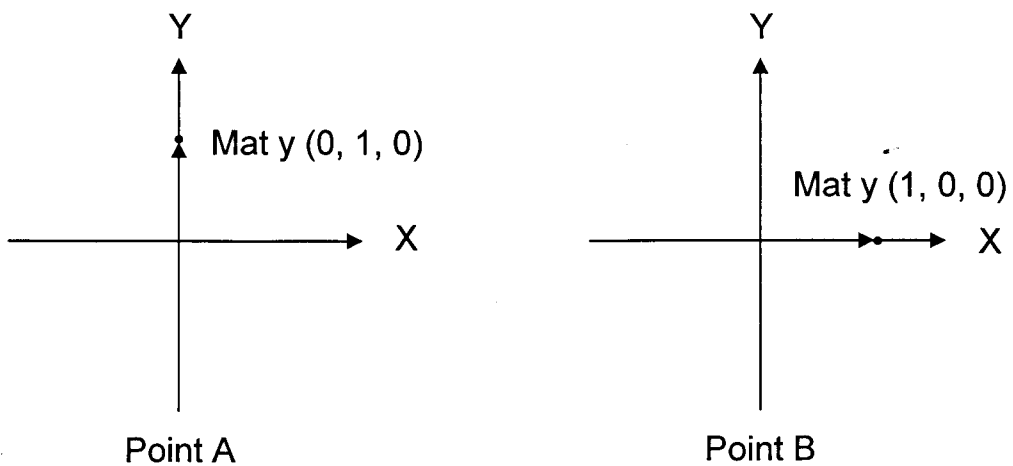


Figure C.8 Material y-axes for point A and B (-30°)

The material x-axes, for points A and B, are shown in Figure C.9. Note that material x-axes for points A and B are shown in the X-Z and Y-Z planes, respectively. For points A and B, the material z-axis is rotated 30° in a clockwise direction relative to the global Z-direction, and the material x-axis is perpendicular to the material z-axis. For point A, the material x-axis is pointing in a direction 30° clockwise to that of the global X-direction. Hence, the Cartesian coordinates for this material x-axis direction are $(\sqrt{3}, 0, -1)$. For point B, the Cartesian coordinates for the material x-axis direction is $(0, -\sqrt{3}, -1)$. Hence, a general expression $[Y, -X, -R \tan \theta]$ will satisfy the material x-axes directions for points A and B.

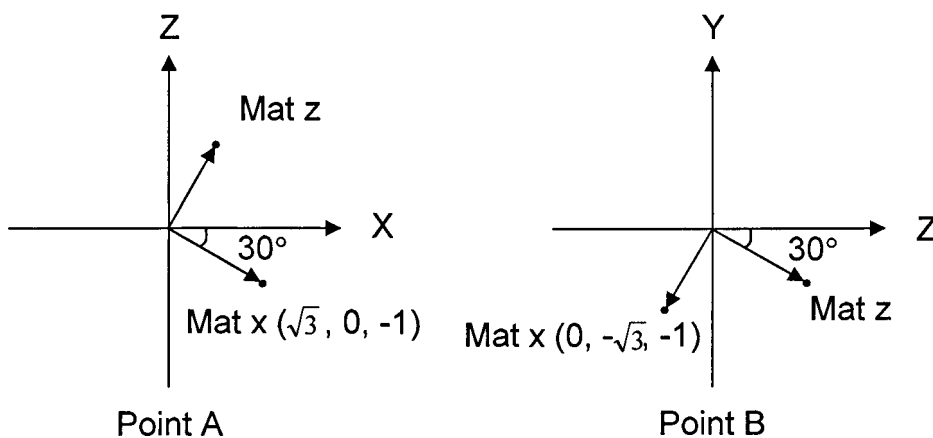


Figure C.9 Material x-axes for point A and B (-30°)

+45° Material Orientation

Figure C.10 shows a schematic diagram for a $+45^\circ$ fibre orientation tube model. Using a similar method to that used for the 0° model, points A $(0, 1, 0)$ and B $(1, 0, 0)$ on the MMC layer, which coincide with the global X and Y-axes, are

identified. The Cartesian coordinates of these points are obtained by assuming the radius of the cylinder is 1 unit.

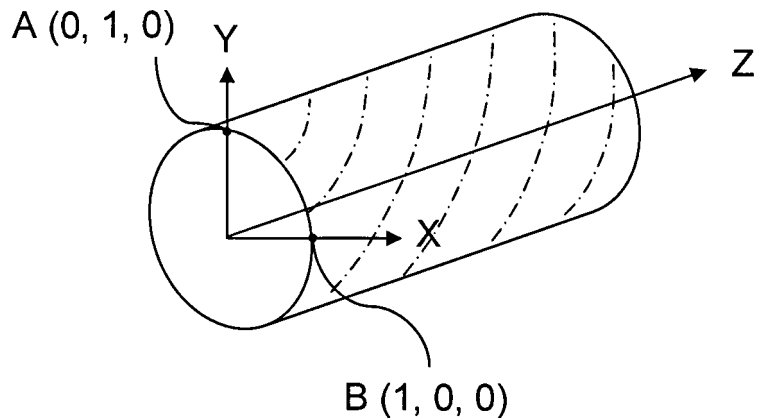


Figure C.10 Schematic diagram for +45° fibre orientation tube model

Considering the global X-Y plane shown in Figure C.11, the material y axes, for points A and B, are pointing in the global Y and X-directions, respectively, which is the radial direction. This is identical to the case of the 0° fibre orientation. Hence the general expression $[X, Y, 0]$ will satisfy the material y-axes directions.

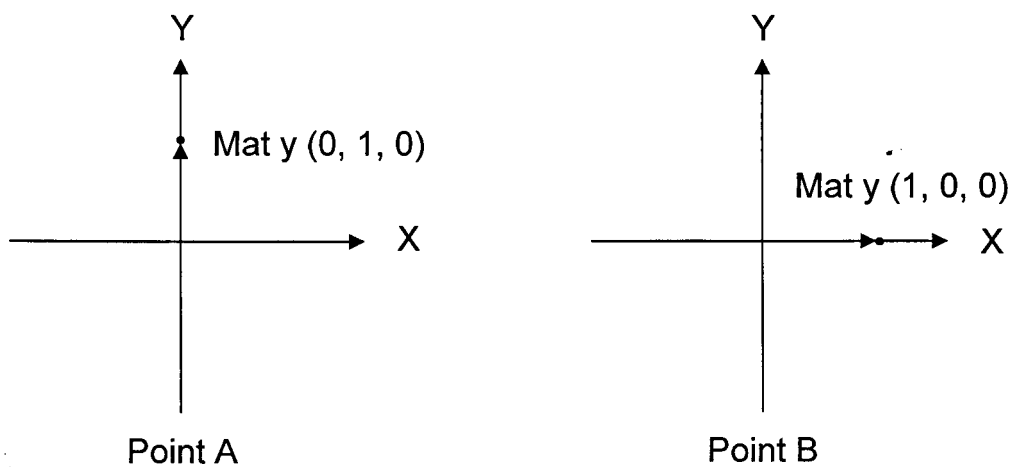


Figure C.11 Material y-axes for point A and B (+45°)

The material x-axes, for points A and B, are shown in Figure C.12. Note that material x-axes for points A and B are shown in the X-Z and Y-Z planes, respectively. For points A and B, the material z-axis is rotated 45° in a counter clockwise direction relative to the global Z-direction, and the material x-axis is perpendicular to the material z-axis. For point A, the material x-axis is pointing in a direction 45° counter clockwise to that of the global X-direction. This forms a right angled triangle of 45° such that the opposite side of the oblique angle (45°) is 1 and the hypotenuse is equal to $\sqrt{2}$. Hence, the Cartesian coordinates for this material x-axis direction is $(1, 0, 1)$. For point B, the Cartesian coordinates for the material x-axis direction is $(0, -1, 1)$. Hence, a general expression $[Y, -X, R]$ will satisfy the material x-axes directions for points A and B.

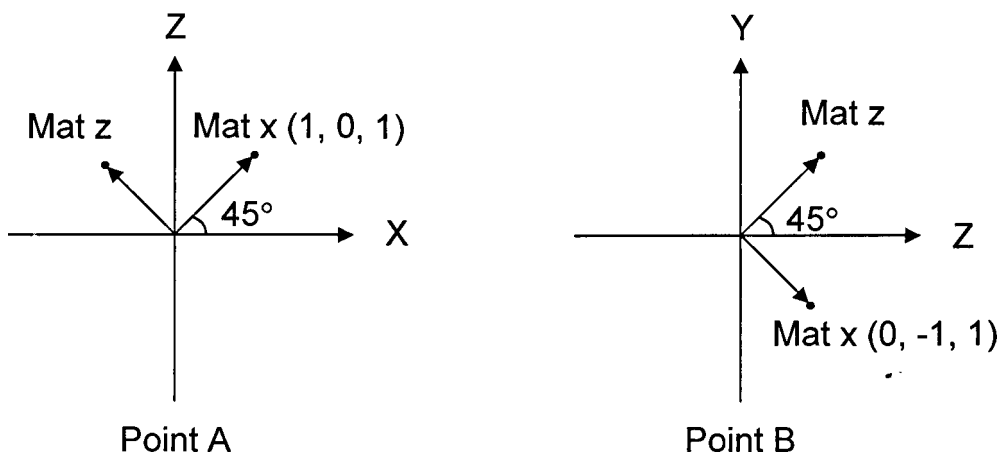


Figure C.12 Material x-axes for point A and B ($+45^\circ$)

-45° Material Orientation

Figure C.13 shows a schematic diagram for a -45° fibre orientation tube model.

Using a similar method to that used for the 0° model, points A $(0, 1, 0)$ and B $(1,$

0, 0) on the MMC layer, which coincide with the global X and Y-axes, are identified. The Cartesian coordinates of these points are obtained by assuming the radius of the cylinder is 1 unit.

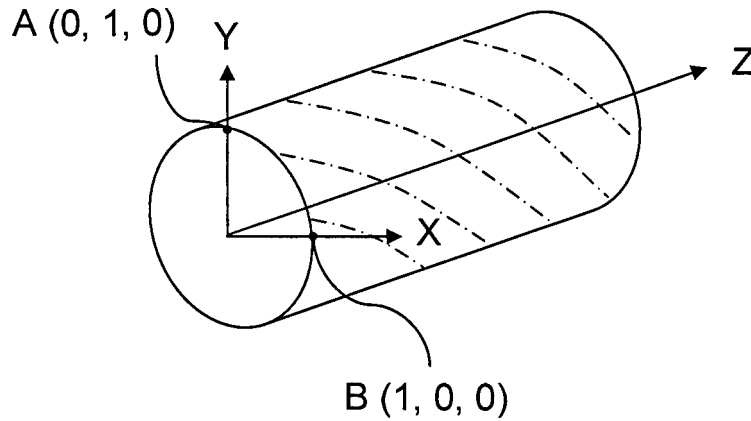


Figure C.13 Schematic diagram for -45° fibre orientation tube model

Considering the global X-Y plane shown in Figure C.14, the material y axes, for points A and B, are pointing in the global Y and X-directions, respectively, which is the radial direction. This is identical to the case of the 0° fibre orientation. Hence the general expression $[X, Y, 0]$ will satisfy the material y-axes directions.

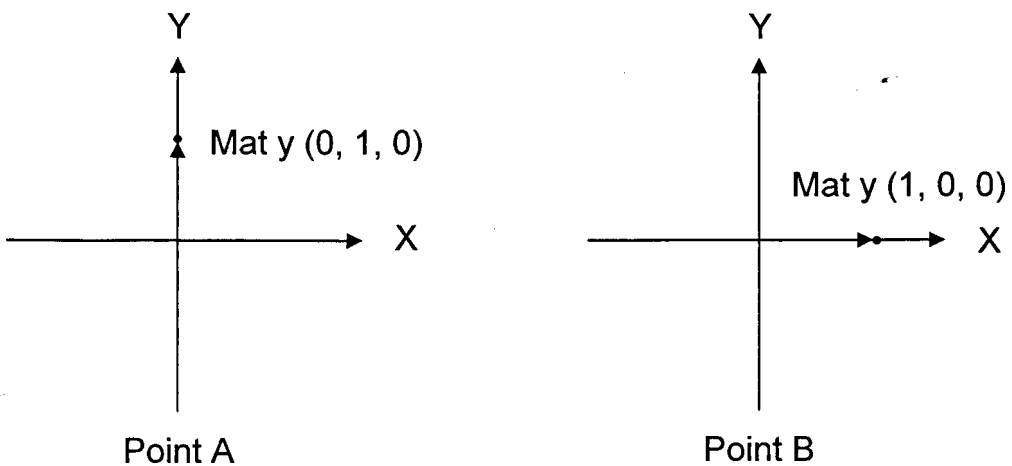


Figure C.14 Material y-axes for point A and B (-45°)

The material x-axes, for points A and B are shown in Figure C.15. Note that material x-axes for points A and B are shown in the X-Z and Y-Z planes, respectively. For points A and B, the material z-axis is rotated 45° in a clockwise direction relative to the global Z-direction, and the material x-axis is perpendicular to the material z-axis. For point A, the material x-axis is pointing in a direction 45° clockwise to that of the global X-direction. Hence, the Cartesian coordinates for this material x-axis direction is $(1, 0, -1)$. For point B, the Cartesian coordinates for the material x-axis direction is $(0, -1, -1)$. Hence, a general expression $[Y, -X, -R]$ will satisfy the material x-axes directions for points A and B.

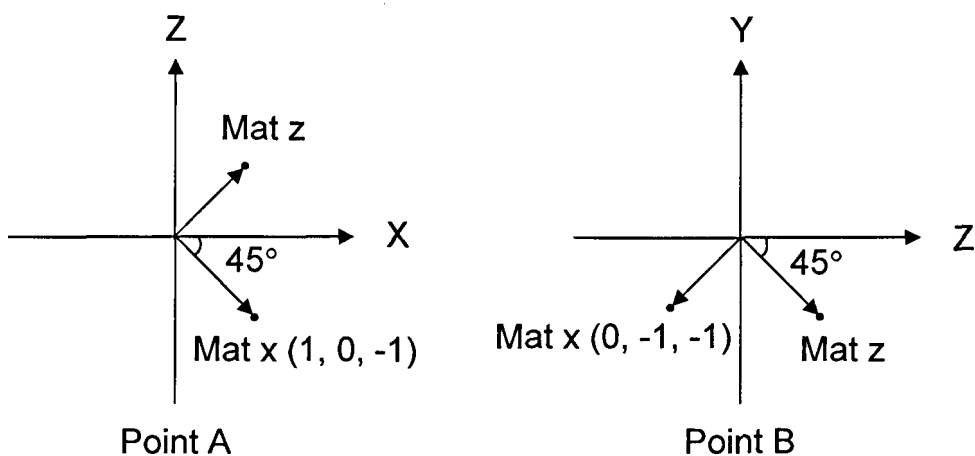


Figure C.15 Material x-axes for point A and B (-45°)

Table C.2 is a summary for the general expressions for the various material orientations, as used in SC03. The material x-axis is a direction which is tangential to the fibres; the material y-axis is the radial direction and the material z-axis is the fibre direction.

Fibre Orientation	0°	+30°	-30°	+45°	-45°
Material x-axis					
x-coordinate	Y	Y	Y	Y	Y
y-coordinate	-X	-X	-X	-X	-X
z-coordinate	0	Rtan30	-Rtan30	R	-R
Material y-axis					
x-coordinate	X	X	X	X	X
y-coordinate	Y	Y	Y	Y	Y
z-coordinate	0	0	0	0	0

Table C.2 General expression for material axes in SC03

Unit Cell Models

In the unit cell models, the carbon coating is an orthotropic material, which is orientation dependent. The material orientation for carbon coating, is also define using the direction cosine method in SC03, but only the material x and y-axes need to be specified. The weakest direction is the radial direction and the reason for this was described in Chapter 5. In other words, the material x and y-axes are the axial and tangential directions, respectively.

Unidirectional 0° Unit Cell Model

Figure C.16 shows a schematic diagram for a unidirectional, 0°, unit cell model, in SC03. Note the position of both carbon coatings, the general expression for the material x-axis is the same for both cases which is the axial direction (global Z-direction). Hence, the general expression for material x-axis is $(0, 0, 1)$.

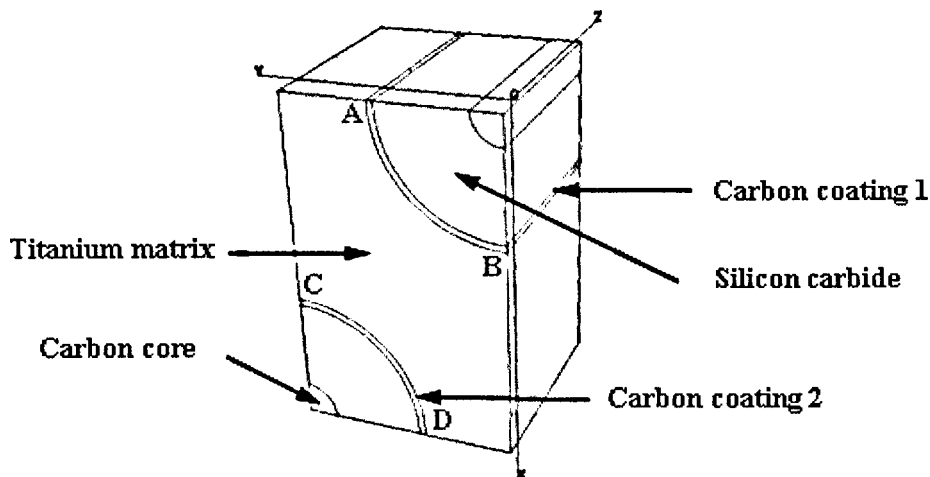


Figure C.16 SC03 2 quarter fibre unit cell model

For the material y-axis, first, the Cartesian coordinates for point A and B for carbon coating 1, as shown in Figure C.16, are identified. Based on the dimensions as shown in Table C.3, the Cartesian coordinates for point A are (0, 0.069, 0) and point B are (0.069, 0, 0). Note that the units in the model are millimetres (mm) and 0.069 is the radius of the carbon coating. Since material y-axis is orientated in the tangential direction, the material y-axes for point A and B, point in the global X-direction and the negative global Y-direction, respectively. Hence a general expression $[Y, -X, 0]$ will satisfy these conditions.

For carbon coating 2, the Cartesian coordinates for point C are (0.1142, 0.1166, 0) and for point D are (0.1832, 0.0476, 0). The exact coordinates can be obtained from the model through Model > Query Geometry in SC03. The material y-axes for points C and D, point in the negative global Y-direction and the global X-direction, respectively. Hence, a general expression $[0.1166-Y, X-0.183192, 0]$ will satisfy these conditions. The general expressions used for both carbon coatings are summarized in Table C.4.

	Dimensions (μm)
Radius of carbon core	16.5
Thickness of SiC	49
Thickness of carbon coating	3.5
Width	116.6
Length	116.6
Height	183.2

Table C.3 Dimension for SC03 unidirectional 0° unit cell model

	Carbon Coating 1	Carbon Coating 2
	Material x-axis	
x-coordinate	0	0
y-coordinate	0	0
z-coordinate	1	1
	Material y-axis	
x-coordinate	Y	$0.1166 \cdot Y$
y-coordinate	-X	$X - 0.1832$
z-coordinate	0	0

Table C.4 General expressions of material axes for carbon coatings

(SC03 0° unit cell model)**Cross-ply $\pm 45^\circ$ Unit Cell Model**

Figure C.17 shows a schematic diagram for a cross-ply, $\pm 45^\circ$, unit cell model, as used in SC03. Note the position of both carbon coatings, the general expression for the material x-axis is different for the two cases. For carbon coating 1, the material x-axis points in the global Z-direction whilst for carbon coating 2 it points in the global Y-direction. Hence, the general expressions for material x-axes, for carbon coatings 1 and 2, are $[0, 0, 1]$ and $[0, 1, 0]$, respectively.

For the material y-axis, first, the Cartesian coordinates for points A and B at carbon coating 1, as shown in Figure C.17, are identified. Based on its dimensions, which are similar to those for the 0° unit cell model, the Cartesian coordinates for point A are $(0, 0.069, 0)$ and point B are $(0.069, 0, 0)$. Since the material y-axis points in the tangential direction, the material y-axes for point A

and B will point in the global X-direction and negative global Y-direction, respectively. Hence a general expression $[Y, -X, 0]$ satisfies these conditions.

For carbon coating 2, the Cartesian coordinates for point C are (0.1832, 0, 0.0476) and for point D are (0.1142, 0, 0.1166). The material y-axes for points C and D, point in the negative global X-direction and the global Z-direction, respectively. Hence, a general expression $[Z-0.1166, 0, 0.1832-X]$ satisfies these conditions. The general expressions for each of the carbon coatings are summarized in Table C.5.

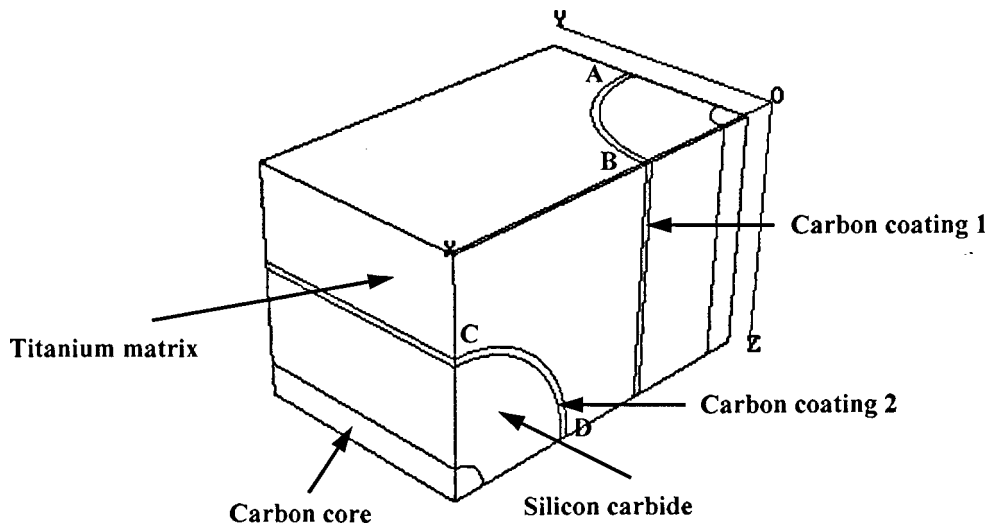


Figure C.17 SC03 cross-ply $\pm 45^\circ$ unit cell model

	Carbon Coating 1	Carbon Coating 2
Material x-axis		
x-coordinate	0	0
y-coordinate	0	1
z-coordinate	1	0
Material y-axis		
x-coordinate	Y	Z-0.1166
y-coordinate	-X	0
z-coordinate	0	0.1832-X

Table C.5 General expressions of material axes for carbon coatings

(SC03 cross-ply $\pm 45^\circ$ unit cell model)

APPENDIX D:**CONVERSION OF NOMINAL STRESS/STRAIN TO TRUE STRESS/STRAIN IN ABAQUS**

The derivations and conversions of nominal stress/strain to true stress/strain presented here are extracted from the ABAQUS documentation.

Strains in compression and tension are the same only if considered in the limit as, $\Delta l \rightarrow dl \rightarrow 0$ i.e.,

$$d\varepsilon = \frac{dl}{l} \quad (\text{D.1})$$

and

$$\varepsilon = \int_{l_0}^l \frac{dl}{l} \quad (\text{D.2})$$

$$= \ln\left(\frac{l}{l_0}\right) \quad (\text{D.3})$$

where

l = current length

l_0 = original length

ε = true strain or logarithmic strain.

The stress measure that is the conjugate to the true strain is called the true stress and is defined as

$$\sigma = \frac{F}{A} \quad (\text{D.4})$$

where

F = force in the material

A = current area

A ductile metal, subjected to finite deformations, will have the same stress-strain behaviour in tension and compression if true stress is plotted against true strain.

When defining plasticity data in ABAQUS, true stress and true strain must be used. ABAQUS requires these values in order to interpret the data correctly.

However, material test data is often supplied using values of nominal stress and strain. In such situations, conversion is needed for plastic material data from nominal stress/strain values to true stress/strain values.

The relationship between true strain and nominal strain is established by expressing the nominal strain as:

$$\varepsilon_{nom} = \frac{l - l_o}{l_o} \quad (D.5)$$

$$= \frac{l}{l_o} - \frac{l_o}{l_o} \quad (D.6)$$

$$= \frac{l}{l_o} - 1 \quad (D.7)$$

Adding unity to both sides of this expression and taking the natural log of both sides provides the relationship between the true strain and the nominal strain:

$$\ln\left(\frac{l}{l_o}\right) = \ln(1 + \varepsilon_{nom}) \quad (D.8)$$

$$\varepsilon = \ln(1 + \varepsilon_{nom}) \quad (D.9)$$

The relationship between true stress and nominal stress is formed by considering the incompressible nature of the plastic deformation and assuming the elasticity is also incompressible, so

$$l_o A_o = lA \quad (D.10)$$

The current area is related to the original area by

$$A = A_o \frac{l_o}{l} \quad (D.11)$$

Substituting this definition of A into equation (D.4) of true stress gives

$$\sigma = \frac{F}{A} = \frac{F}{A_o} \times \frac{l}{l_o} \quad (D.12)$$

$$= \sigma_{nom} \left(\frac{l}{l_o} \right) \quad (D.13)$$

where

$$\frac{l}{l_o} \text{ can also be written as } 1 + \epsilon_{nom}$$

Making this final substitution into equation (D.13) provides the relationship between true stress and nominal stress and strain:

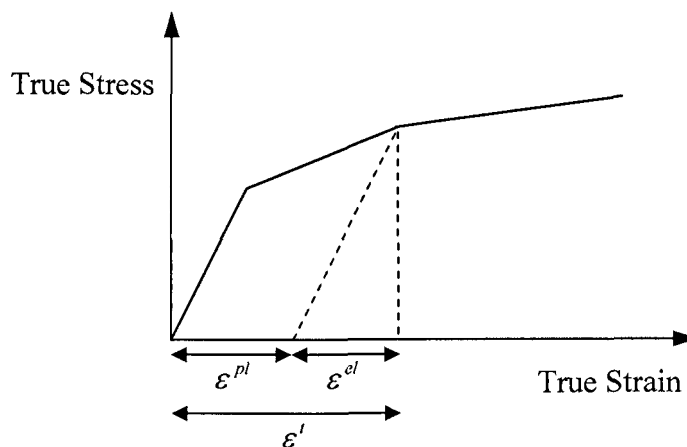
$$\sigma = \sigma_{nom} (1 + \epsilon_{nom}) \quad (D.14)$$

Hence equations (D.9) and (D.14) can be used to convert the data from nominal stress/strain values to true stress/strain values.

The classical metal plasticity model in ABAQUS defines the post-yield behaviour for most metals. ABAQUS approximates the smooth stress-strain behaviour of the material with a series of straight lines joining the given data

points. Any number of points can be used to approximate the actual material behaviour; therefore, it is possible to use a very close approximation of the actual material behaviour. The plastic data define the true yield stress of the material as a function of true plastic strain. The first piece of data given defines the initial yield stress of the material and, therefore, should have a plastic strain value of zero.

However, the strains provided in material test data are not likely to be the plastic strains in the material. Instead, it will probably be the total strains in the material. Therefore, the strains must be decomposed into the elastic and plastic strain components. The plastic strain is obtained by subtracting the elastic strain from the total strain as shown in equation (D.15). The elastic strain is defined as the value of true stress divided by the Young's modulus of the material, as shown in equation (D.16). The following schematic diagram shows the decomposition of the total strain into elastic and plastic components.



$$\varepsilon^{pl} = \varepsilon^t - \varepsilon^{el} \quad (D.15)$$

$$= \varepsilon^t - \frac{\sigma}{E} \quad (D.16)$$

where

ε^{pl} = true plastic strain

ε^t = true total strain

ε^{el} = true elastic strain

σ = true stress

E = Young's modulus

Therefore, equations (D.14) and (D.16) are used to obtain the true stress and true plastic strain, respectively, which are required by ABAQUS.